

AFOSR-TR- 83 - 0218

11

ADA 126803

RESEARCH ON NEW APPROACHES TO OPTICAL
SYSTEMS FOR INERTIAL ROTATION SENSING

FINAL REPORT

for

Grant No. AFOSR F49620-80-C-0040

Prepared for

Air Force Office of Scientific Research
Bolling Air Force Base



G. L. Report No. 3552

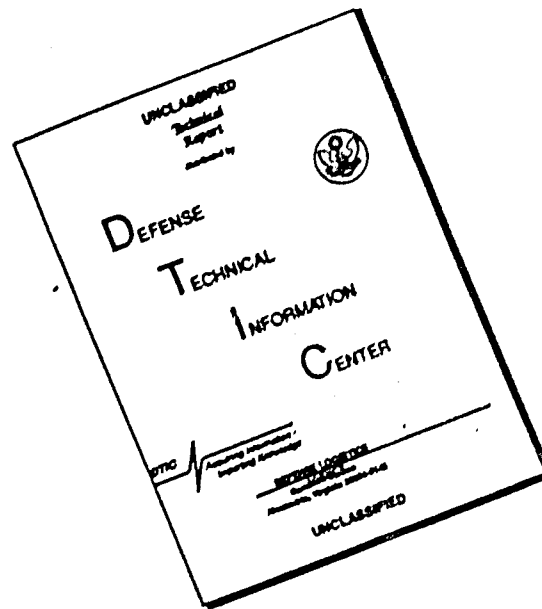
Approved for public release;
distribution unlimited.

DTIC FILE COPY

Edward L. Ginzton Laboratory
W. W. Hansen Laboratories of Physics
Stanford University
Stanford, California 94305

83 04 14 009

DISCLAIMER NOTICE



THIS DOCUMENT IS BEST QUALITY AVAILABLE. THE COPY FURNISHED TO DTIC CONTAINED A SIGNIFICANT NUMBER OF PAGES WHICH DO NOT REPRODUCE LEGIBLY.

UNCLASSIFIED

SECURITY CLASSIFICATION OF THIS PAGE (When Data Entered)

REPORT DOCUMENTATION PAGE		READ INSTRUCTIONS BEFORE COMPLETING FORM
1. REPORT NUMBER AFOSR-TR- 83-0218	2. GOVT ACCESSION NO. AD-A126	3. RECIPIENT'S CATALOG NUMBER F43
4. TITLE (and Subtitle) RESEARCH ON NEW APPROACHES TO OPTICAL SYSTEMS FOR INERTIAL ROTATION SENSING		5. TYPE OF REPORT & PERIOD COVERED Final Report 1-1-81 through 4-30-82
		6. PERFORMING ORG. REPORT NUMBER G.L. 3552
7. AUTHOR(s) Multiple authors		8. CONTRACT OR GRANT NUMBER(s) F49620-80-C-0040
9. PERFORMING ORGANIZATION NAME AND ADDRESS Stanford University Edward L. Ginzton Laboratory Stanford, California 94305		10. PROGRAM ELEMENT, PROJECT, TASK AREA & WORK UNIT NUMBERS 61102F 2305/62
11. CONTROLLING OFFICE NAME AND ADDRESS Director of Electronic and Material Sciences Air Force Office of Scientific Research, Attn: NE Building 410, Bolling AFB, D.C. 20332		12. REPORT DATE March 1983
		13. NUMBER OF PAGES 136
14. MONITORING AGENCY NAME & ADDRESS (if different from Controlling Office)		15. SECURITY CLASS. (of this report) UNCLASSIFIED
		15a. DECLASSIFICATION DOWNGRADING SCHEDULE
16. DISTRIBUTION STATEMENT (of this Report) Approved for public release; distribution unlimited.		
17. DISTRIBUTION STATEMENT (of the abstract entered in Block 20, if different from Report)		
18. SUPPLEMENTARY NOTES		
19. KEY WORDS (Continue on reverse side if necessary and identify by block number) Re-entrant Fiber Gyro, Inertial Rotation Sensing, Optical Sagnac Interferometer (passive, active, re-entrant, all-fiber, polarization effects, theory, noise, birefringence, reciprocity, unpolarized operation, multi-mode operation), Rayleigh Scattering, Bilateral Optical Amplifiers (noise, nonreciprocity), Fiber Components (polarizer, directional couplers)		
20. ABSTRACT (Continue on reverse side if necessary and identify by block number) This report describes progress in the investigation of novel fiber optic Sagnac loop configurations for inertial rotation sensing, "fiber gyros." One concept - the passive re-entrant Sagnac system (PRS), in which two identical optical sig- nals circulate around a multi-turn loop many times, with successive samplings of the difference signal after each transit of the total loop, has been success- fully tested in a rotating all fiber system (no bulk optics). Nineteen circula- tions were achieved, generating a sinusoidal output signal which represented several cycles of accumulating optical phase shift between the two counter-		

UNCLASSIFIED

UNCLASSIFIED

SECURITY CLASSIFICATION OF THIS PAGE(When Data Entered)

20.

rotating optical waves. This experiment demonstrated for the first time the successful operation of a re-entrant Sagnac system but also demonstrated the tremendous value of the various fiber components developed in this laboratory which enabled an all fiber system to be used for this recirculating mode of operation of a fiber gyro. Eventually a bilateral amplifier will be incorporated in the fiber loop permitting many more recirculations of the two injected optical signals. This device is known as the active re-entrant Sagnac system (ARS).

Detailed theoretical calculations have been made on a number of important relevant problems for both the PRS and ARS devices. These include calculations on the propagation of noise in PRS devices, amplifier and incoherent Rayleigh back-scattering noise and the effects of amplifier non-reciprocity in ARS devices, and possibly most important, a polarization analysis of re-entrant fiber optic gyros. The latter involved a coherence analysis which permitted treatment of cases of polarized, unpolarized and partially polarized input light and the effects of various configurations of polarizers. In addition to the analytic results obtained, this treatment also indicated the possibility and value of the use of completely unpolarized light in Sagnac systems. This result and application of the same mathematical techniques also showed that there were new possibilities for using multi-mode fiber in Sagnac sensors with the light distributed among all the modes. This new concept could potentially be very important.

Accession For
NATIS GRAFI ☒
NATIS TAB ☐
Unannounced
Justification

By
Distribution/
Availability Codes
Avail and/or
Special

Dist
A

UNCLASSIFIED

SECURITY CLASSIFICATION OF THIS PAGE(When Data Entered)

TABLE OF CONTENTS

I.	INTRODUCTION	1
II.	PROGRAM SUMMARY	4
III.	RE-ENTRANT FIBER GYRO EXPERIMENT	5
	A. Basic Sagnac System	5
	B. All-Fiber Interferometer	8
	C. Alignment Procedures for Re-Entrant Rotation Sensor	12
	1. Spatial Beam Alignment	14
	2. Loop I/O Coupler Alignment	14
	3. Splitter/Combiner Coupler Alignment	18
	4. Input Polarization Controller Alignment	21
	5. Loop Polarization Controller Alignment	22
	E. Typical Rotation Experiments	22
IV.	POLARIZATION ANALYSIS OF RE-ENTRANT FIBER OPTIC ROTATION SENSORS	26
	1. Co-Polarized With External Polarizer	36
	2. Cross Polarized With External Polarizer	48
	3. No Polarizer	49
	4. Co-Polarized With Internal Polarizer	61
	5. Unpolarized	68
	6. Partially Polarized	71
V.	PROPAGATION OF NOISE IN PASSIVE RE-ENTRANT PULSED FIBER OPTIC ROTATION SENSORS	84
VI.	AMPLIFIER AND INCOHERENT RAYLEIGH BACKSCATTERING NOISE IN ACTIVE RE-ENTRANT ROTATION SENSORS	106

1. Amplifier Noise	106
2. Noise Due to Incoherent Backscattering	115
VII. AMPLIFIER NONRECIPROCITY	122
VIII. MULTIMODE FIBER GYROS	130
IX. ANALYSIS OF SOURCE CHARACTERISTICS AND SCATTERING IN FIBER GYROS	133
X. REFERENCES	135
XI. PUBLICATIONS AND REPORTS	136
APPENDIX	

I. INTRODUCTION

This report covers research under Contract F49620-80-C-0040 for the period from January 1, 1981 through April 30, 1982. Work done during the period from January 1, 1980 through December 31, 1980 is covered in an earlier report,¹ and is not treated in the present report.

The objective of this research program has been to investigate the characteristics of new fiber optic configurations for inertial rotation sensing with the aim of extending the sensitivity threshold and basic stability of such systems. The program has involved basic device research, including both theoretical analyses and experimental demonstrations of some specific configurations, and the introduction of some novel concepts in the use of optical fibers in these systems.

The principal approach which has been studied theoretically and experimentally is referred to as a re-entrant Sagnac system which, like the conventional fiber gyro uses a multiturn fiber sensing coil, but which uses recirculating optical pulses as opposed to the single pass cw light of the conventional system, giving a multiplication of the phase shift due to rotation, and resulting in a device which is intrinsically an integrating rate gyro rather than a direct rate gyro. The re-entrant Sagnac system was introduced earlier under the AFOSR program, and an all fiber version had been constructed as of the beginning of the present reporting period.

The effort on re-entrant gyros during the reporting period followed two main directions. One involved the first experimental evaluation of the new system, which uses an integrated, all fiber circuit for the interferometer, which give results in very good agreement with expectation. The second was concerned with the first detailed theoretical analyses of error sources and operating ranges, as a basis of comparison for future detailed experimental studies of the device.

Another phase of work under the program has involved analyses of the effects of scattering, birefringence and modal propagation in fiber gyros of both recirculating

and conventional single pass types, resulting in disclosure of major sources of error in conventional gyros and basic techniques for circumventing them which have been crucial for the development of practical fiber gyros. This work is described in earlier reports, and has continued during the reporting period. This work has also had, as an outgrowth, proposals for new modes of operation of single pass fiber gyros. One of these, involving operation with unpolarized light in single mode fiber was described in the preceding report.¹ Another proposal using multimode fiber in a new way which has prospects for realizing fiber gyros with fewer components and lower cost, grew out of work during the reporting period and its analysis is described in this report.

One of the important new concepts involves recirculating two counterpropagating optical pulses in a fiber loop and monitoring the pulses as they pass the input/output junction. This concept we have referred to as the "passive re-entrant Sagnac system" (PRS). We envisage active operation of such loops, i.e. the incorporation of an amplifier in the loop, aimed at increasing the number of circulations and therefore the optical integration times of these devices by very large factors. We have referred to such an implementation as an "active re-entrant Sagnac system" (ARS).

The ARS approach possesses some features of both the ring laser gyro and the usual fiber gyro, and avoids some problems of both. Like the ring laser gyro it recirculates the optical energy many times around a closed sensing loop which contains a gain medium, it has automatic built-in signal processing with output in the form of a frequency having the same value as the beat frequency from the ring laser gyro, and it is an integrating rate gyro having inherently linear response. It is like the usual fiber gyro in that it can be realized in all-solid state form, contains

an N -turn fiber sensing loop, uses an external fixed-frequency optical source and is free of lock-in. Unlike either of the other two devices, however, optical pulses of several microseconds duration, rather than cw light, are injected into the sensing loop from the external source.

Another way in which the ARS device differs from conventional fiber gyros concerns the optimum total optical transit time in the sensing loop for maximum signal-to-noise ratio. The optimum **fiber** length in the loop is the same for both devices, within a factor of two, but in an ARS device the light will traverse this same loop a large number of times, thereby multiplying the Sagnac rotation-produced phase shift.

With regard to the integrating feature of the ARS gyro, successive readouts of the cumulative phase difference between the two recirculating signals generates a sinusoidal wave so that one can actually measure the integrated angular rotation of the system. This is ultimately what is required in most applications, such as inertial navigation. In contrast, conventional single pass rotation sensing gives a signal which is proportional to the phase shift per pass. That requires maintaining some precise and invariant proportionality factor between these signals and the corresponding value of rate of rotation. Then, integration is necessary to get the actual angle turned through as a function of time. This feature, that a single pass device provides only a measure of the instantaneous rate of rotation of the system, which must then be integrated, complicates the use of single pass fiber gyros, generally requiring electronic closed-loop operation. In the re-entrant device, which generates a sinusoidal waveform representing the integrated phase shift between the two counter-rotating signals, the number of cycles generated of course depends on the rate of rotation and the duration of the circulating pulses. The repeated circulations of the pulse must continue long enough to encompass many cycles of phase shift between the two recirculating signals.

The significance of the above distinctions between a conventional single pass device and a re-entrant device has become more apparent recently, partially as a result of our own work on single pass gyros¹³ under another program. We have been able to get, we think, the highest sensitivity achieved anywhere in such single pass devices, by refining the device and all its components, and optimizing the operating conditions. Some of those components have been of fundamental importance in the AFOSR program. Having achieved such high performance we are now more fully aware of the limitations of a single pass device.

At this time the ARS system appears to have important potential for use in vehicle navigation because of the built-in signal processing referred to above, which does not require electronic closed-loop operation to obtain a linear scale factor. Also, because of the long optical integration time afforded by pulse recirculation, it has potential for use in applications, such as in geodesy and geophysics, which can tolerate very large sensing loops and very long integration times to achieve extreme sensitivity to small rotation rates.

The principal component still needed in all of these cases is an optical amplifier. Development, under different contracts, of optical amplifiers using neodymium-based materials, organic dyes, and semiconductors, is presently underway. Results from this work will be available for use on the AFOSR program.

II. PROGRAM SUMMARY

Most of the work performed in this program during the reporting period (January 1 - April 30, 1981) has been concerned with the following items.

(1) Detailed measurements and analysis of an all fiber passive re-entrant rotation sensor including evaluation of the new form of signal processing, made possible by the re-entrant format, and studies of the error sources, characteristic of this configuration. Experimental results from the operation of this re-entrant rotation

sensor, described in more detail later, were in good qualitative and quantitative agreement with the theory. Nineteen recirculations of an optical pulse around an 830 meter long fiber loop have been consistently obtained.²

(2) A number of theoretical studies on the general performance characteristics of passive re-entrant fiber optic rotation sensors, including (a) the effects of polarization and birefringence on performance, and (b) the propagation and behavior of noise.

(3) Theoretical calculations on various problems expected with this kind of device. We have considered such topics as the sensitivity limits of active re-entrant systems due to amplifier noise, incoherent Rayleigh backscattering, and the effect of amplifier nonreciprocity.

(4) It is to be especially noted that the investigation of the whole problem of birefringence and polarization effects in fiber gyros revealed possible great advantages in two particular forms of operation - (a) controlled unpolarized operation of a fiber gyro and (b) the use of multimode fiber for rotation sensing.³

All this work is described in later sections and publications which are attached.

III. RE-ENTRANT FIBER GYRO EXPERIMENT

A. Basic Sagnac System

A re-entrant fiber rotation sensor such as described in the 1980 report (Interim Scientific Report, January 1, 1980 through December 31, 1980, Contract F49620-80-C-0010) was mounted on a rotating table for testing. The table had rotating joints for electrical power and signal output, thus enabling it to be rotated continuously. Mechanical tachometers allowed direct measurements of the angular velocity of the table.

The basic recirculating Sagnac system is shown in block form in Fig. III-1. The description and schematic figures in these subsection III.A and B are the same as in the previous annual report for Contract F49620-80-C-0010. They are repeated

here as a background to the description of the experimental work to be described, without requiring reference to earlier reports.

Light from a pulsed source is sent, via an optical junction, into a multiturn fiber sensing loop, where it makes multiple circulations around the loop. The laser is pulsed with an impulse somewhat shorter than the optical transit time once around the loop. A portion of the light recirculating in the loop is extracted by the junction and sent to an optical detector and associated video signal processor and display, which indicates the inertial rotation of the sensing loop about the axis perpendicular to its plane.

The junction has the property that light entering at *A* is split into two equal-amplitude parts at *B* and *C*, leading to waves propagating clockwise and counterclockwise, respectively, around the loop. It also has the property of closing the loop upon itself, in such a way that most of the light, once propagating around the loop, continues to do so in multiple transits. The junction also has the property that it couples a given portion of both counterpropagating light waves back out of the loop and sends them to the detector. The light pulses going to the detector are modulated in amplitude by the phase interference of the two waves, so that the received pulse amplitude varies sinusoidally with time at a rate dependent on the rotation of the loop in inertial space.

The frequency of this waveform provides a measure of the angular velocity of the system. The loop will contain an optical amplifier and other elements *G* in (Fig. III-1) to compensate for optical attenuation in the loop, but it is an essentially linear system, and as such is free of the mode locking phenomena experienced with ring laser gyros.

Consider a single pulse from the laser, leading to two pulses traveling in the loop, one clockwise and the other counterclockwise. After these pulses have traveled once around the *N*-turns of the loop, they are reintroduced into the loop for a

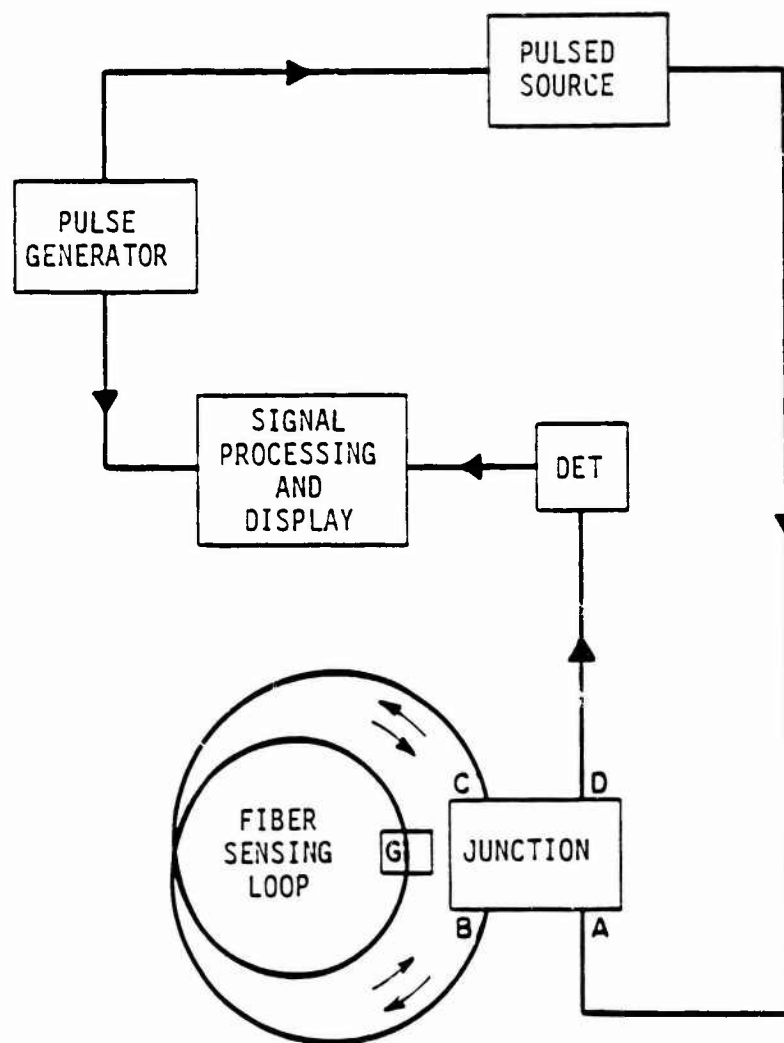


Fig. III-1. Basic schematic of recirculating system.

second transit, and this process is repeated until a large number of transits have been completed. An amplifier and saturable absorber in the loop would allow a large number of recirculations, giving large integration time of the rotation, and sensitivity to small rotation rates.

As the original pulses continue to recirculate around the loop, they generate a train of pulse samples at the detector. It is important to emphasize that the entire train of output pulses results from one single input pulse supplied by the laser. The effect of rotation is to shift the phases of the counterpropagating optical pulses relative to the inertial frame, in opposite directions. This relative phase shift is proportional to the rotation rate and also proportional to the length of time the pulses have been exposed to the rotation. As the pulses continue to circulate, they accumulate phase shift $\Delta\phi(t)$ which increases linearly with time t . The detector is phase sensitive and the output is sinusoidal in the argument $\Delta\phi(t)$. That is, for a fixed rotation rate, the output of the detector is a sinusoidal wave in time.

We refer to the system just described as an active recirculating Sagnac system if there is an amplifier in the sensing loop and the pulses are not attenuated. When operated as a passive recirculating system without the amplifier, the output pulse train is a damped sinusoid whose amplitude decreases exponentially with time.

B. All-Fiber Interferometer

The design for the optical junction in single mode fiber form is shown in Fig. III-2 where the terminals A , B , C and D correspond to the same symbols as in Fig. III-1. DC1 and DC2 are single-mode fiber directional couplers. These low loss couplers, developed in our laboratory, are a key factor in the performance of our rotation sensors. A brief description of their design is given at the end of this section. DC1 is a 3 dB coupler which splits the light pulses entering at A into two equal amplitude pulses at E and F , which enter coupler DC2 at opposite ends.

DC2 is a directional coupler with a coupling coefficient (coupling between *B* and *C* and between *E* and *F*) near unity. Thus a large fraction of the light at *E* and *F* returns to *F* and *E*, respectively, while a small fraction enters the loop to form counterclockwise and clockwise traveling pulses, respectively. Pulses once in the loop remain in the loop by crossing from one side of DC2 to the other following the path shown by the dashed arrow, with low insertion loss because of the high coupling coefficient between the two halves 1 and 2 of the coupler, and the low internal dissipative loss of the coupler.

Making high quality splices on single mode fibers is difficult because of the small core diameter. Commercially available multimode splicing equipment yields splice losses of 1-3 dB when used on single mode fibers. In order to determine base-line performance for recirculating systems, the junction of Fig. III-2 is designed to be fabricated, together with the sensing loop, with no fiber splices at all. This calls for coupler halves 1, 2, 3 and 4 to be fabricated directly on the ends of the single-mode fiber sensing loop as at (a) and then assembled as at (b).

A diagram of the overall passive re-entrant system is given in Fig. III-3. The system shown is passive, without an amplifier in the loop, pending completion of a Nd:YAG fiber amplifier which is now under development in this laboratory under another contract.

The optical source consists of a Nd:YAG laser operating at 1.06 microns, a telescope, acousto-optic beam deflecting modulator, and beam steering device leading up to the fiber input.

Polarization controllers PC1 and PC2 are necessary to compensate the system for the birefringence in the fiber, in order to balance the interferometer at zero rotation rate.

Adjustments of the fiber circuit are simple and straightforward, in sharp contrast to earlier models using bulk optic components. There are no optical alignments

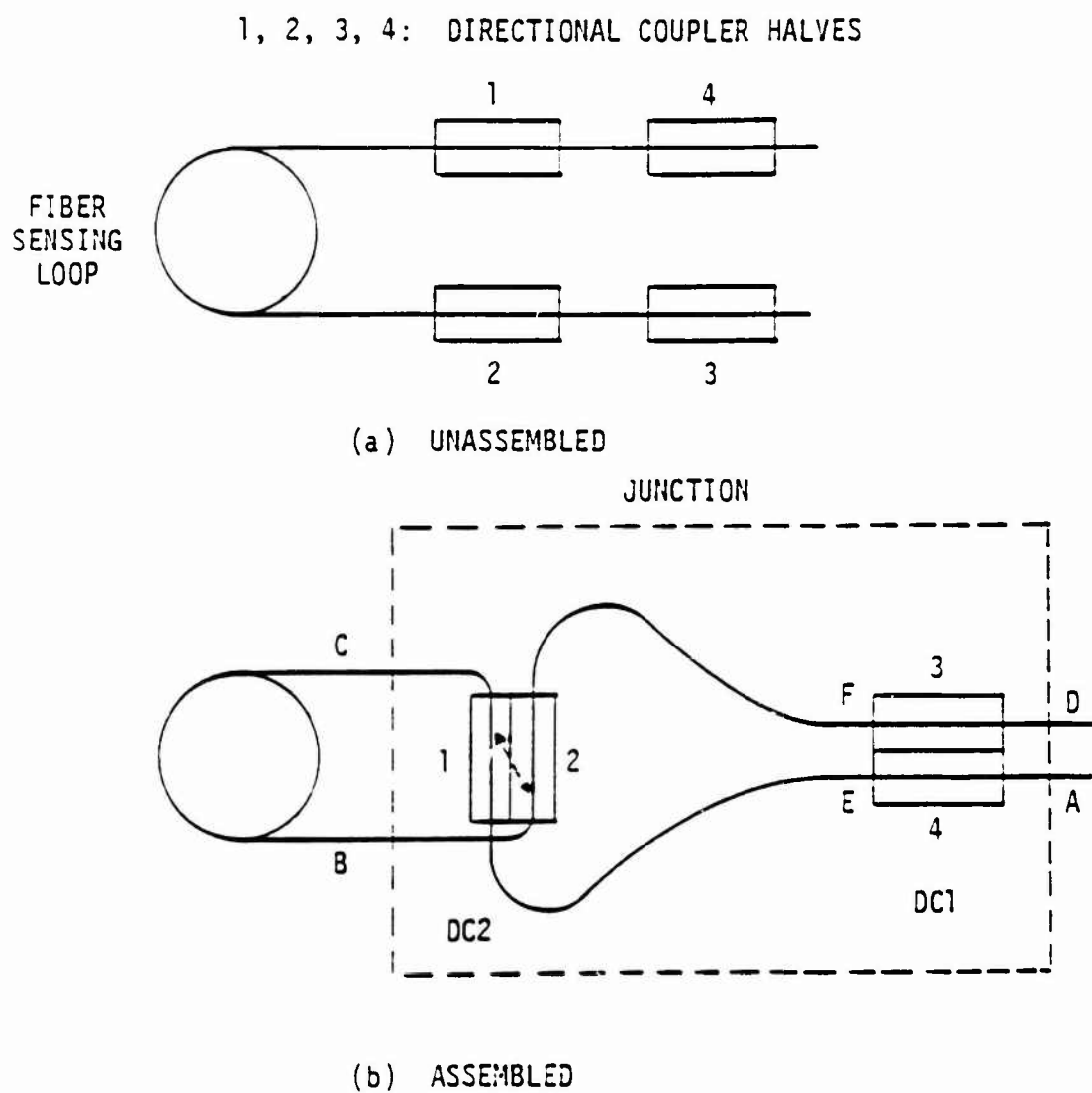


Fig. III-2. Schematic for spliceless sensing loop and junction assembly.

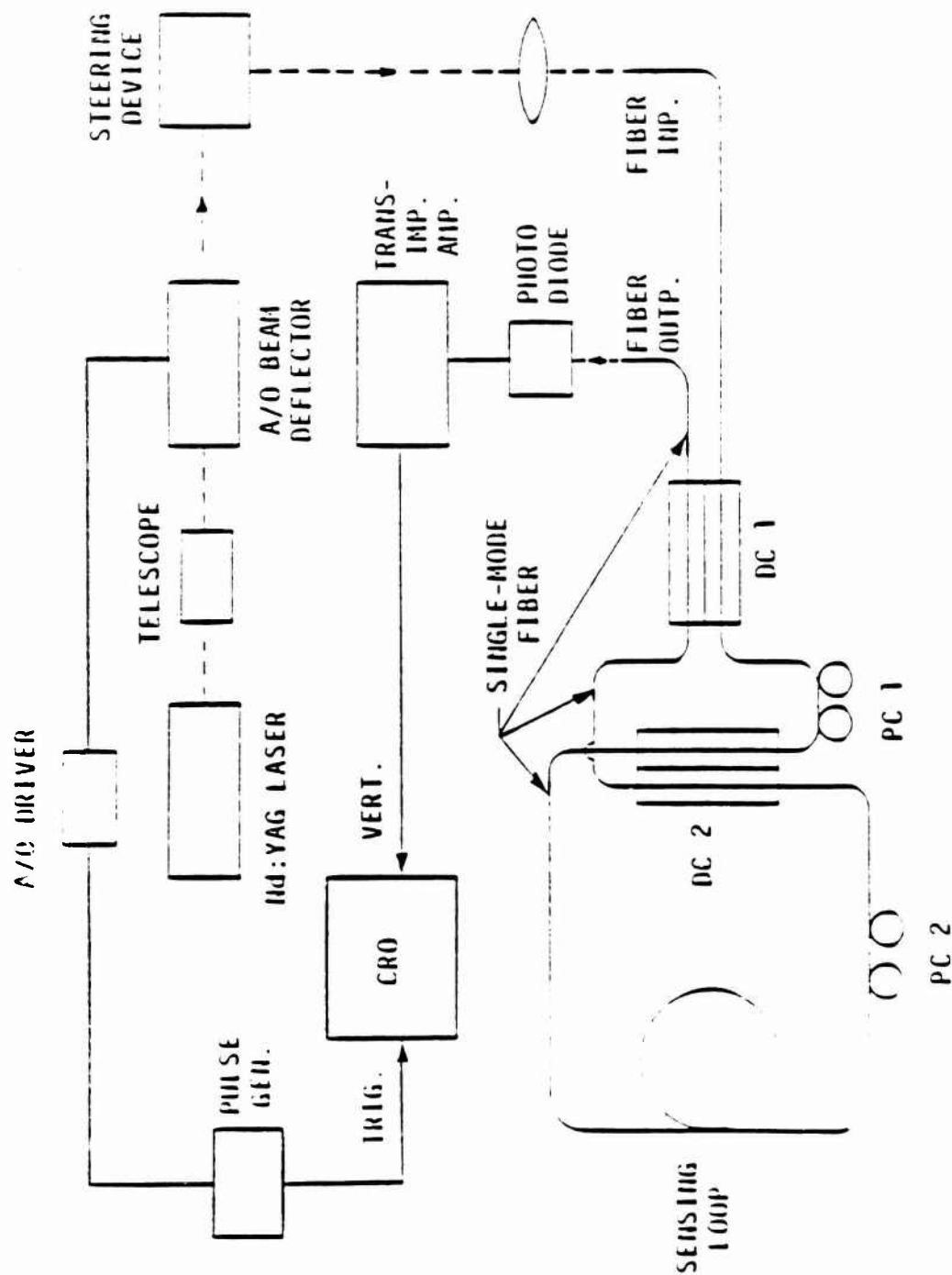


Fig. III-3. Schematic for PRS system with all-fiber interferometer.

to be made within the interferometer circuit, but only at the input and output ports.

A single-mode fiber-to-fiber, evanescent field directional coupler has been developed in this laboratory⁴ as noted above, and this design was followed in fabricating the couplers DC1 and DC2 on the fiber just described. In this coupler design, a fiber is bonded into a slot cut in a quartz substrate. The face of the block is polished to remove a significant portion of the cladding, allowing access to the evanescent fields of the guided mode. When two such substrates are placed in contact, strong coupling exists between the two fibers. This coupling is highly directional and can result in complete power transfer in a length of approximately 1 millimeter. The coupling can be varied and optimized by transverse displacement of the fibers. Fig. III-4 shows an assembled coupler with micrometers to control relative fiber displacement.

The loop of the rotation sensor was formed from an 830 meters length of Corning single mode fiber. The core diameter was 6 microns and the measured attenuation was 1.8 dB/km at a wavelength of 1.06 microns. The sensing loop diameter was 15 cm. With these dimensions for the fiber loop the conversion factor relating phase shift to rotation rate is 2.46 radians of phase shift for each radian/sec of rotation.

The loop coupler (DC2 in Fig. III-3) has a maximum coupling of 82%. This is sufficiently close to the optimal coupling value of 90% for our purposes. The splitter/combiner coupler (DC1) has a coupling ratio which is greater than 50%.

C. Alignment Procedures for Re-entrant Rotation Sensor

To achieve optimum performance in re-entrant fiber gyros care must be taken in the alignment of its components. The input end is positioned with respect to the coupling lens for optimum coupling of the laser beam to the fiber. Next, the loop coupler is set to obtain a maximum number of recirculations and the

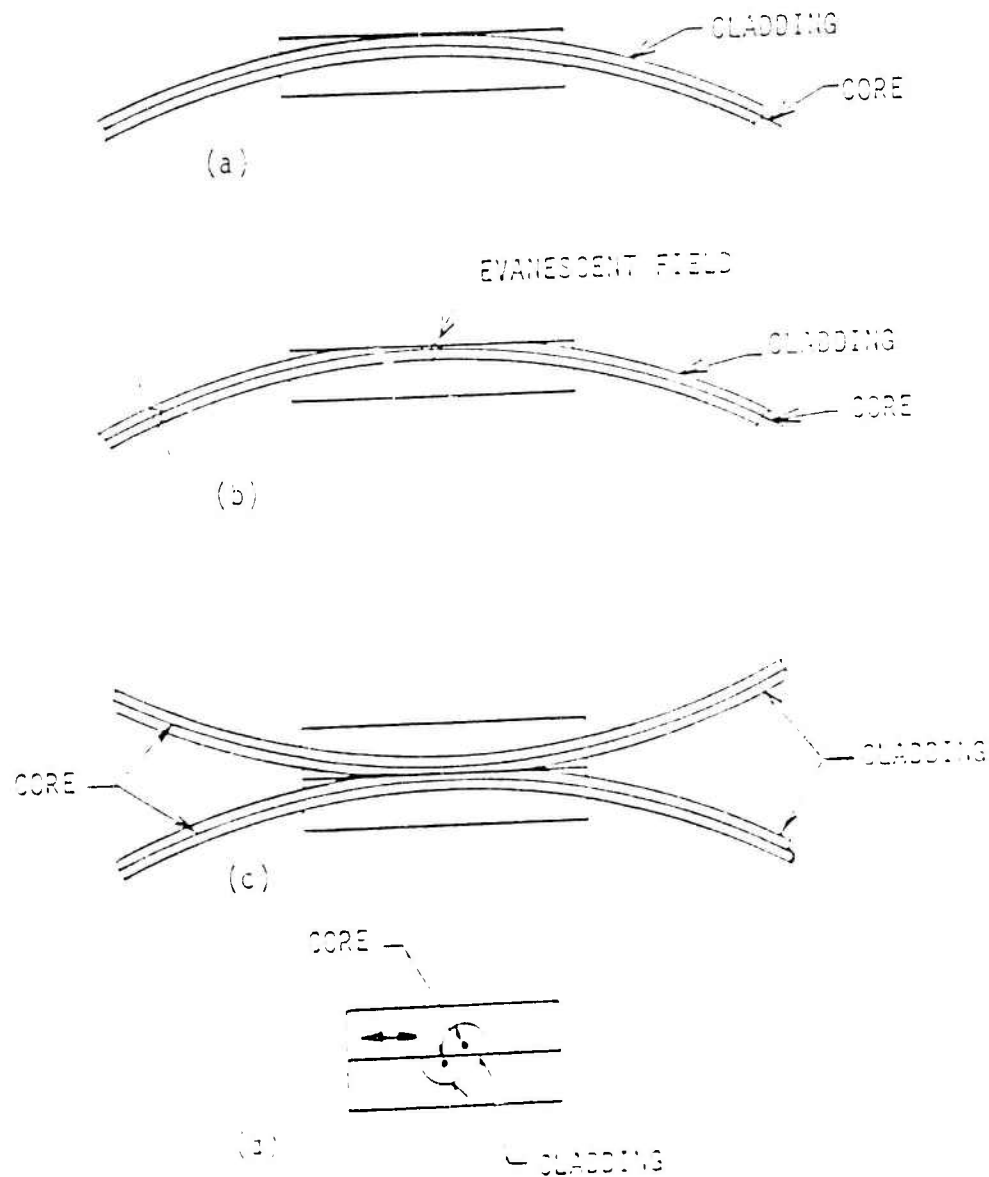


Fig. III-4. Fiber to fiber, evanescent field coupler. a. Fiber bonded into slot cut in fused silica substrate. b. Cladding partially removed to expose evanescent field. c. Assembled coupler side view. d. Tuning collar and view of transverse displacement of fibers.

splitter/combiner coupler must be set for a 50% coupling ratio. Due to natural birefringence in all single mode fibers the rotation sensor will support two polarization modes. To ensure good rotation sensitivity the input and loop polarization controllers must be adjusted so that only one mode is present throughout the fiber gyro. The details of the alignment algorithm which accomplishes these steps are given below.

Five alignments had to be performed to render the rotation sensor in Fig. III-5 operational. The spatial beam had to couple into the input fiber, the splitter/combiner coupler had to be adjusted for the maximum coupling ratio, and input and loop polarization controllers had to be adjusted to obtain the proper state of polarization at the splitter/combiner coupler.

1. Spatial Beam Alignment

The coupling of the spatial beam is accomplished by first misaligning the splitter/combiner coupler and the loop I/O coupler (Fig. III-5) and then monitoring the power at the output end of the fiber while the input end is positioned behind the coupling lens. Misaligning the couplers results in the equivalent of the configuration shown in Fig. III-6. The coupling ratio of the spatial beam into the fiber was estimated to be around 25%.

2. Loop I/O Coupler Alignment

The I/O coupler is initially aligned by visually positioning the two fibers on the top of each other with the aid of a microscope. The modulator is turned on to launch pulses in the fiber. The photo diode monitors the power exiting at the output end of the fiber. This detected power is displayed on the vertical axis of an oscilloscope with time on the horizontal axis. The optical circuit at this point is equivalent to that in Fig. III-7a.

Initially, the oscilloscope trace is similar to that in Fig. III-7b. The first pulse

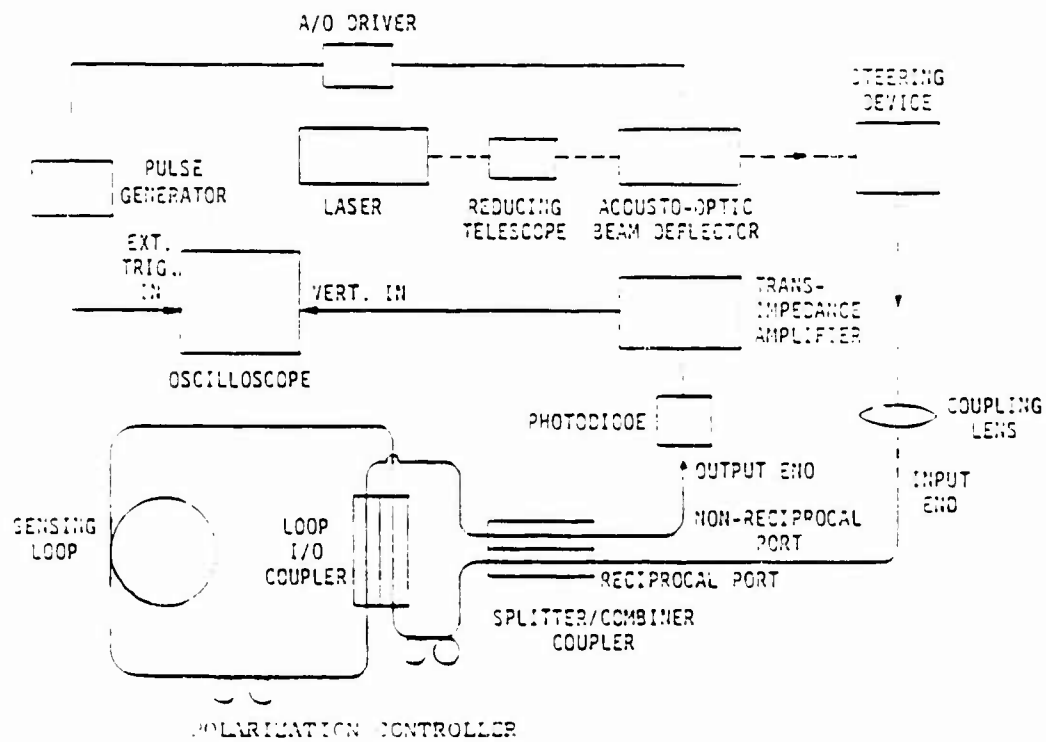
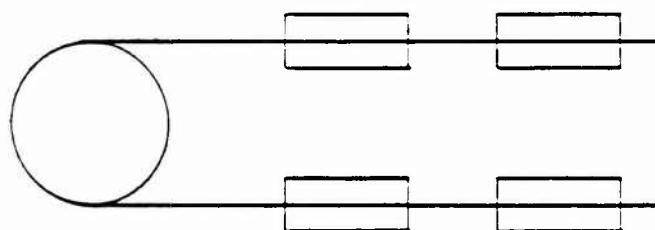
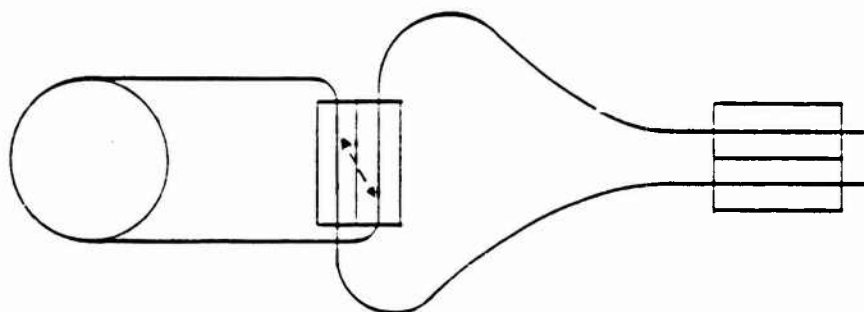


Fig. III-5. All fiber optic, passive re-entrant rotation sensor schematic.

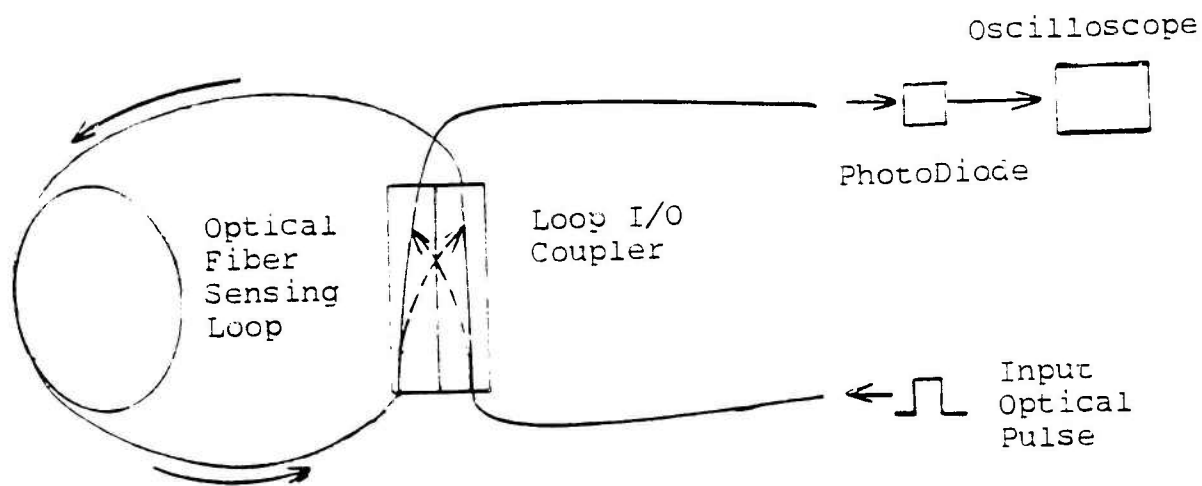


(a)

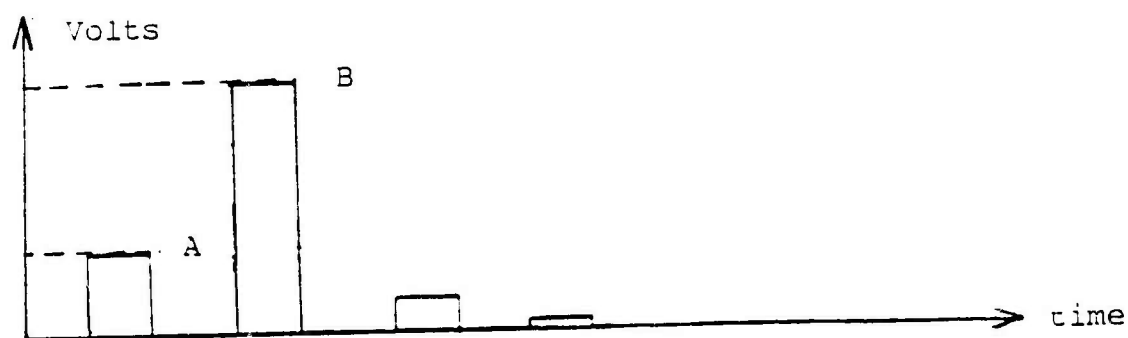


(b)

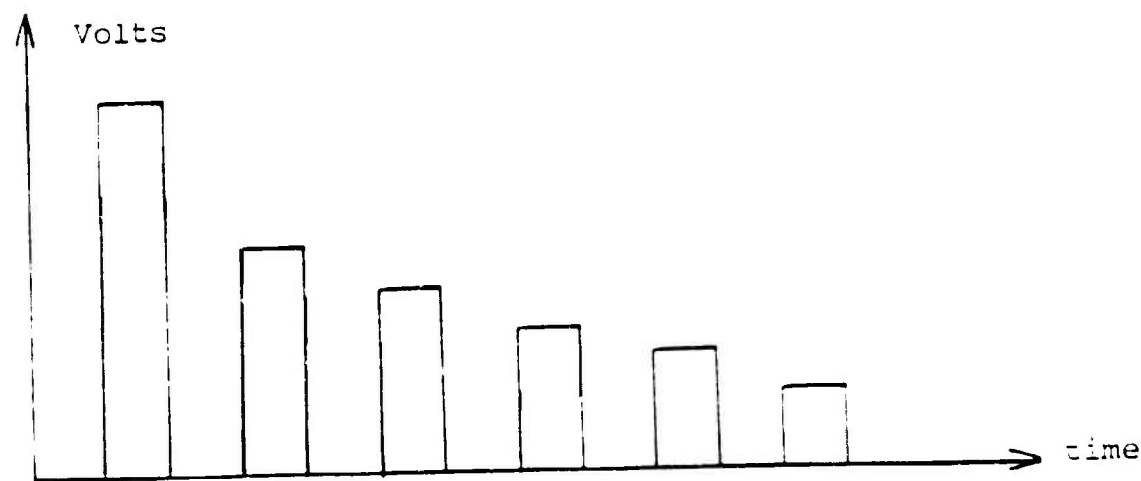
Fig. III-6. Fiber optic circuit for spliceless all fiber re-entrant rotation sensor. (a) Unassembled. (b) Assembled.



a)



b)



c)

Fig. III-7. Alignment procedure for loop I/O coupler. (a) Circuit configuration. (b) Oscilloscope display when loop I/O coupler is misaligned. (c) Oscilloscope display when loop I/O coupler is aligned.

is due to that portion of the input which is not coupled into the sensing loop, while succeeding pulses are due to first, second, and third recirculations around the sensing loop. The oscilloscope trace implies that the coupling ratio, δ , of the I/O coupler is low, i.e. a large portion of the recirculating power is also coupled out from the loop after each recirculation.

The pulse heights A and B for the first two pulses (Fig. III-7) can be expressed in terms of the loop I/O coupler coupling ratio as

$$\begin{aligned} A &= P_0 \delta \\ B &= P_0 (1 - \delta)^2 \exp(-\alpha L) \end{aligned} \quad (III - 1)$$

where P_0 is the input power and αL is the attenuation due to the fiber in the sensing loop. The coupling ratio, δ , can be obtained by measurement of A and B through the following equation:

$$\delta = 0.5[2 + (B/A) \exp(\alpha L)] - \sqrt{[1 + (B/2A) \exp(\alpha L)]^2 - 1} \quad (III - 2)$$

As the coupling of the loop I/O coupler increases, the first pulse increases while the second one decreases in height. In addition, more recirculations will be visible (Fig. III-7). Physically, less power is being coupled into the loop, but once in the loop it decays more slowly, because very little is coupled out after each recirculation. The optimum coupling for N recirculations is achieved varying the coupling until N^{th} pulse is a maximum.

3. Splitter/Combiner Coupler Alignment

The splitter/combiner coupler must now be aligned for 50% coupling to achieve maximum contrast of the pulses. This results from the use of the nonreciprocal port (Fig. III-5) of the splitter/combiner coupler. If the reciprocal port were used, then maximum contrast would always be obtained. Physically, this can be understood

by referring to the rotation sensor depicted in Fig. III-8. Power P_0 is assumed incident on the reciprocal port of the splitter/combiner coupler whose coupling ratio is δ . The portion of the clockwise wave which arrives at the nonreciprocal port has coupled across the coupler twice (Fig. III-8). The portion of the counterclockwise wave which arrives at the nonreciprocal port has gone straight through the coupler twice (Fig. III-8). The power of the clockwise and counterclockwise waves at the nonreciprocal port are:

$$\begin{aligned} P_{cw} &= \delta^2 P_0 \\ P_{ccw} &= (1 - \delta)^2 P_0 \end{aligned} \quad (III - 3)$$

Maximum contrast requires equal powers in the two waves, hence from the above equation $\delta = 50\%$. At the reciprocal port, each wave has coupled across and gone straight through the coupler once, hence the powers are automatically equal. Maximum power delivered to the reciprocal port, however, still requires a coupling ratio of 50%.

An ideal coupler introduces a 180 degree phase shift between the counterpropagating waves at the nonreciprocal port. The waves are in-phase at the reciprocal port. For real couplers (i.e. lossy couplers), the phase shift is less than 180 degrees. The detected power, at rest, at the nonreciprocal port of the splitter/combiner coupler in Fig. III-5 is approximately

$$P_{\text{detected}} = P_{cw} + P_{ccw} - 2\sqrt{P_{cw}P_{ccw}} \quad (III - 4)$$

where birefringence in the fiber has been neglected. Substituting Eq. III-3 in Eq. III-4 results in

$$P_{\text{detected}} = (1 - 2\delta)^2 P_0 \quad (III - 5)$$

When the coupling equals 50%, the detected power is approximately zero at the

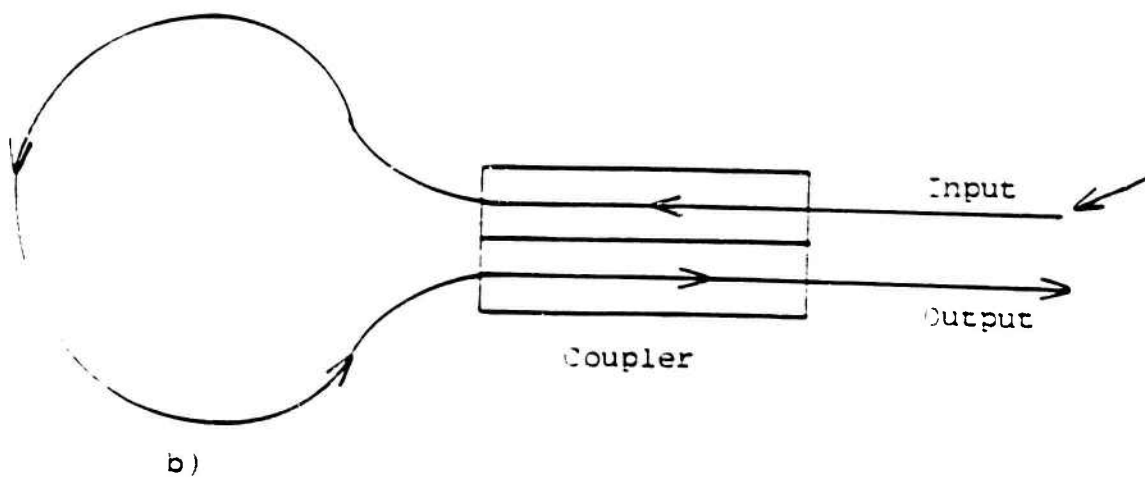
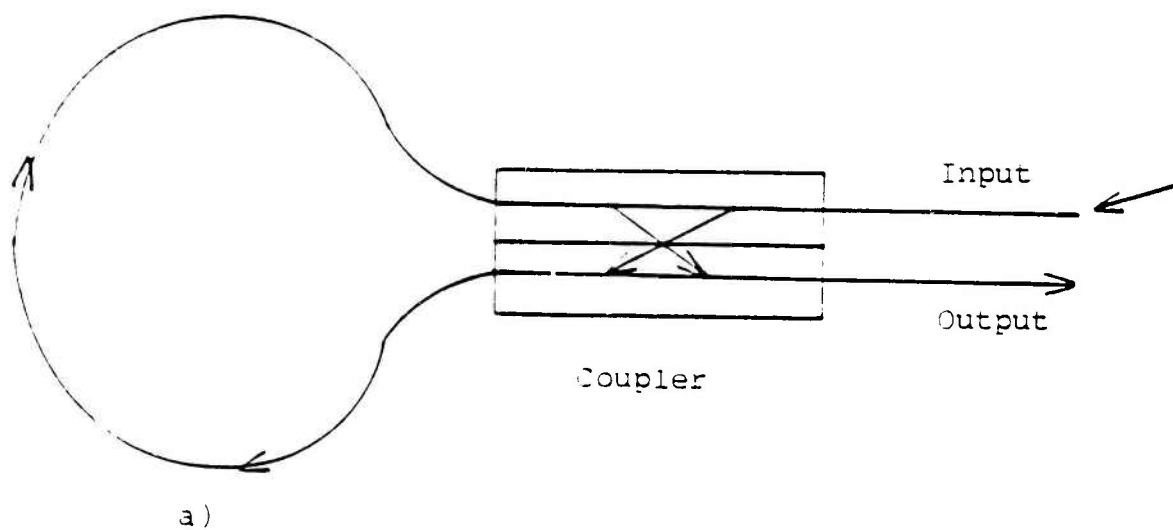


Fig. III-8. Optical paths in ring interferometer for detection at the non-reciprocal port. (a) clockwise path, (b) counter-clockwise path.

nonreciprocal port at rest.

In principle, the splitter/combiner coupler is aligned by positioning the two fibers (Fig. III-7) to null the scope trace. In general, this can not be done due to birefringence and modal coupling of the two polarization modes in the optical fiber. This results in a portion of the power in the input polarization to be coupled into the orthogonal polarization state. The counterpropagating waves, which exit at the nonreciprocal port in the orthogonal polarization state, have an additional phase shift ϕ due to the fiber birefringence. Eq. III-5 becomes:

$$P_{\text{detected}} = P_{\parallel}(1 - 2\delta)^2 + P_{\perp}[\delta^2 + (1 - \delta)^2 - 2\delta(1 - \delta)\cos\phi] \quad (\text{III} - 6)$$

where P_{\parallel} and P_{\perp} are the powers of the lightwaves exiting at the nonreciprocal port in the same and orthogonal polarization states respectively as the input. When $\delta \rightarrow 1/2$, the first term in the above equation goes to zero, while the second term goes to $P_{\perp}(1 - \cos\phi)/2$. The detected power is not zero at $\delta = 1/2$. In practice, the splitter/combiner coupler is aligned by positioning the fibers until the oscilloscope trace (Fig. III-7) is minimized.

After the oscilloscope trace (Fig. III-7) has been minimized, it is nulled by adjusting the loop and input polarization controllers (Fig. III-5). The input polarization controller affects all pulses to a degree. The first pulse, which does not enter the sensing loop, is solely controlled by the input polarization controller. The loop polarization controller partially controls the recirculating pulses.

4. Input Polarization Controller Alignment

The input polarization controller is aligned by rotating the plane of the controller loops until the first pulse is nulled. In general, the succeeding pulses are not nulled. The state of polarization of the first pulse when it returns to the

splitter/combiner coupler (Fig. III-5) is now the same as that of the input pulse which leaves the output ports (Fig. III-5) of the splitter/combiner coupler. The state of polarization at the loop I/O coupler is arbitrary in general. The succeeding pulses, which have propagated around the sensing loop, are not nulled because their state of polarization does not equal that of the input pulse at the loop I/O coupler.

5. Loop Polarization Controller Alignment

The loop polarization controller is aligned by rotating the plane of the controller loops until the recirculation pulses (i.e. second and succeeding pulses) are nulled. The state of polarization of the recirculating pulse pair and the state of polarization of the input pulse pair are equal at the loop I/O coupler.

After this is completed, the oscilloscope trace is a straight line. No pulses are visible and the re-entrant rotation sensor is aligned.

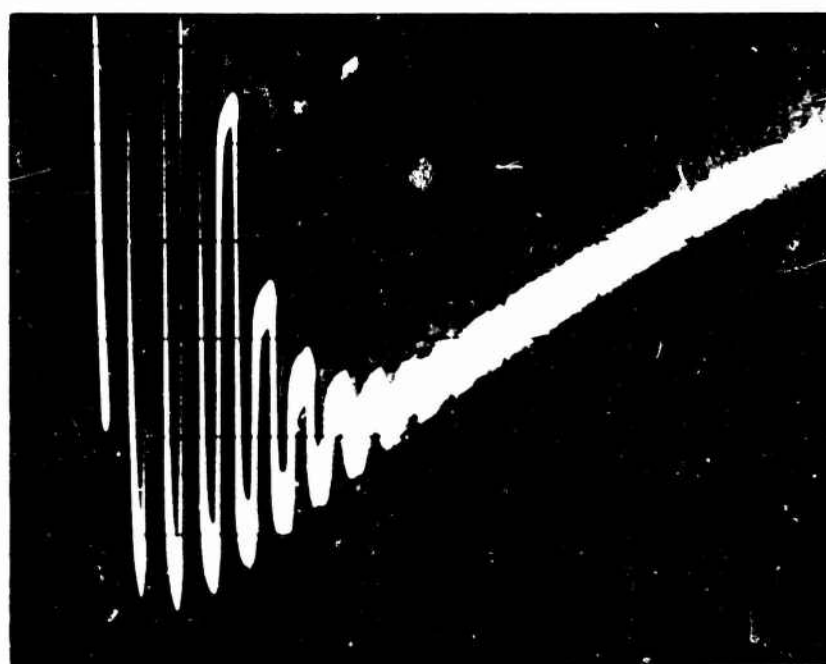
E. Typical Rotation Experiments

Figure III-9 (a), (b) is an oscilloscope photograph of the output pulse train when only the loop coupler is aligned and the splitter/combiner is misaligned. In this instance, there is a unidirectional flow of optical power around the sensing loop. The pulse train is not sensitive to rotation. The pictured pulse train is due to 15 recirculations of a single optical pulse. The sloping baseline is due to saturation of the detector.

Figure III-10 shows the output pulse train for various rotation rates when the sensor is completely aligned. No pulses are visible at rest (III-10) because the splitter/combiner coupler introduces a 180 degree phase shift between the counterpropagating pulses. The rotation rates of the succeeding pictures are chosen to show one (III-10), two (III-10), and three (III-10) cycles of the sinusoidal wave, i.e. $\sin\{\Delta\phi(t)\}$ which measures the continually increasing phase shift ($\Delta\phi(t)$).

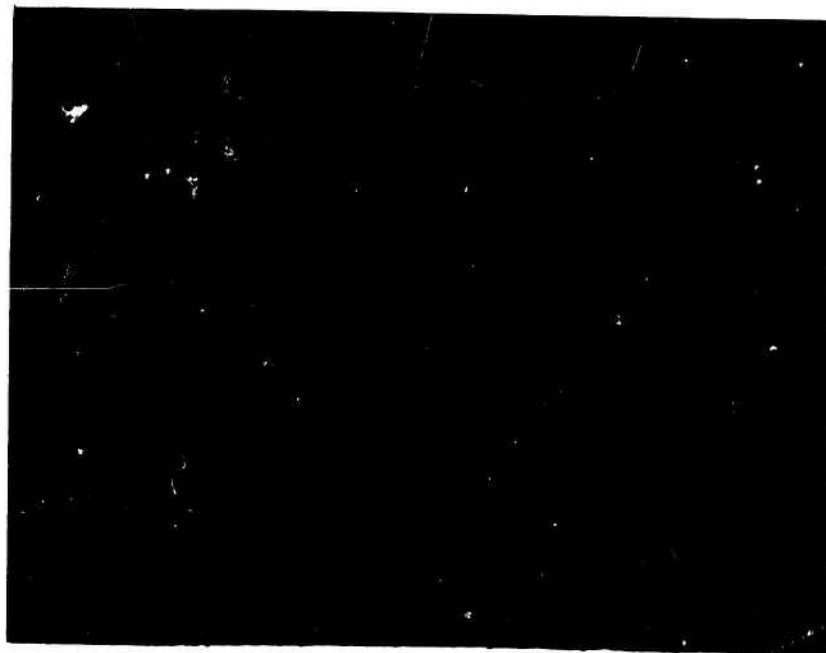


(a)

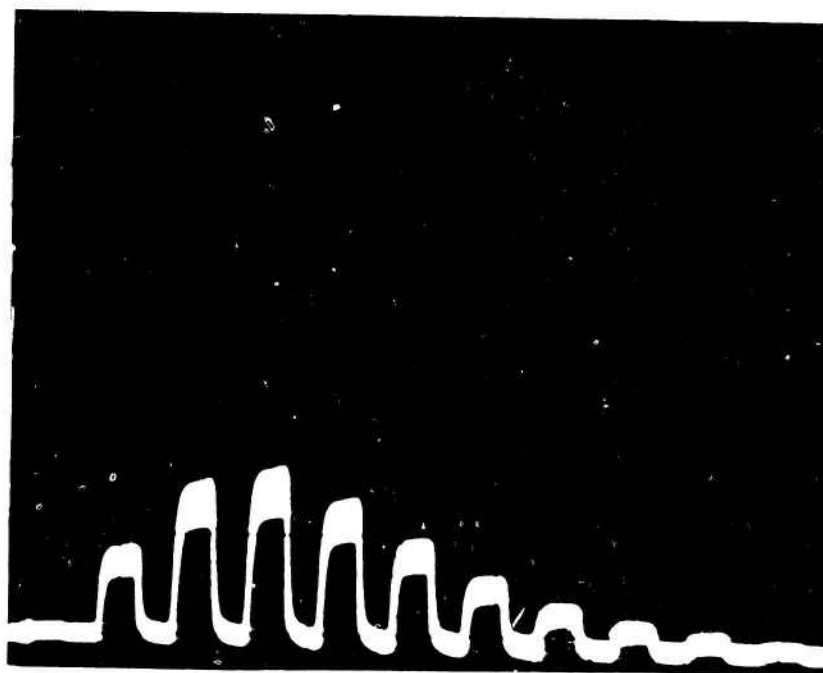


(b)

FIGURE III-9

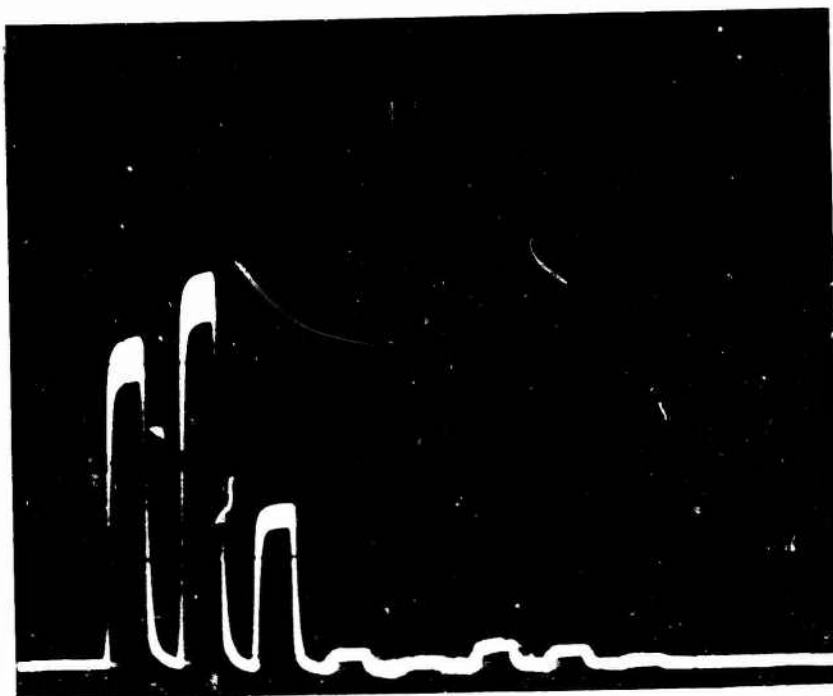


(a)



(b)

FIGURE III-10



(c)



(d)

FIGURE III-10

IV. POLARIZATION ANALYSIS OF RE-ENTRANT FIBER OPTIC ROTATION SENSORS

Previous experiments had indicated that it was necessary to maintain a single mode and single polarization of the wave in fiber gyros for error free operation. Detailed analysis indicates that a very advantageous alternative is to actually and purposefully use completely unpolarized light (i.e. light which has polarization components of equal intensity, but which are completely uncorrelated). If the intensity balance can be maintained through the system, it becomes completely insensitive to polarization conversion, and the measuring system becomes much less sensitive to laser fluctuation and drift and environmental changes. There results a possibility of a considerable improvement in sensitivity.

Unpolarized light should not be confused with "depolarized" coherent light or with circularly polarized light in which the orthogonal components are correlated. The sources of the two polarizations must have a large degree of independence not found in existing lasers. Furthermore it is required that the orthogonality, but not polarization of the two components must be maintained throughout the fiber loop.³

The theory in Section B involving a Jones matrix analysis using coherence matrices examines the various polarization modes that can be used in re-entrant fiber optic rotation sensors. Polarized unpolarized and partially polarized input light, with various locations for polarizers, are all considered in finding expressions for how accurately the measured signal provides the rotational phase shift. This analysis shows that for a polarized input into the re-entrant fiber optic rotation sensor the rotation error is reduced if some form of polarization control or polarization maintaining fiber is used. For an unpolarized input it is found that there are operating points where the detected signal is insensitive to environmental changes. In order to achieve high rotation sensitivity the signal must remain highly unpolarized and the biased operating points must be stably maintained.

The effects of polarization on the output of a re-entrant, pulsed fiber optic rotation sensor will be modeled by a Jones matrix which will be a function of the number of recirculations of the light waves. The input light wave will again be described by its coherence matrix. Figure IV-1 shows the three configurations of re-entrant, pulsed fiber optic rotation sensors which will be examined for polarized, unpolarized and partially polarized input light. The configurations differ by the placement of polarizers. In Fig. IV-1, a nonreciprocal phase bias element is added between the splitter/combiner coupler and the loop I/O coupler to obtain output signals as shown in Fig. IV-2. The mechanics of the optical pulse generation are neglected and the optical fibers and the couplers are assumed to be lossless.

The splitter/combiner coupler is assumed to be 50-50. Its Jones matrices for propagation across (T_{sc}) and along (R_{sc}) the couplers are given in Eqs. IV-1a&b, respectively.

$$\begin{aligned} a. & \begin{pmatrix} 0.5 \exp(j\pi/4) & 0 \\ 0 & 0.5 \exp(j\pi/4) \end{pmatrix} \\ b. & \begin{pmatrix} 0.5 \exp(-j\pi/4) & 0 \\ 0 & 0.5 \exp(-j\pi/4) \end{pmatrix} \end{aligned} \quad (IV-1)$$

$$\begin{aligned} a. & R_{I0} = \begin{pmatrix} \sqrt{1-\delta} \exp(-j\pi/4) & 0 \\ 0 & \sqrt{1-\delta} \exp(-j\pi/4) \end{pmatrix} \\ b. & T_{I0} = \begin{pmatrix} \sqrt{\delta} \exp(j\pi/4) & 0 \\ 0 & \sqrt{\delta} \exp(j\pi/4) \end{pmatrix} \end{aligned} \quad (IV-2)$$

The matrices describing propagation once around the optical fibers are given in Eqs. IV-3a and b.

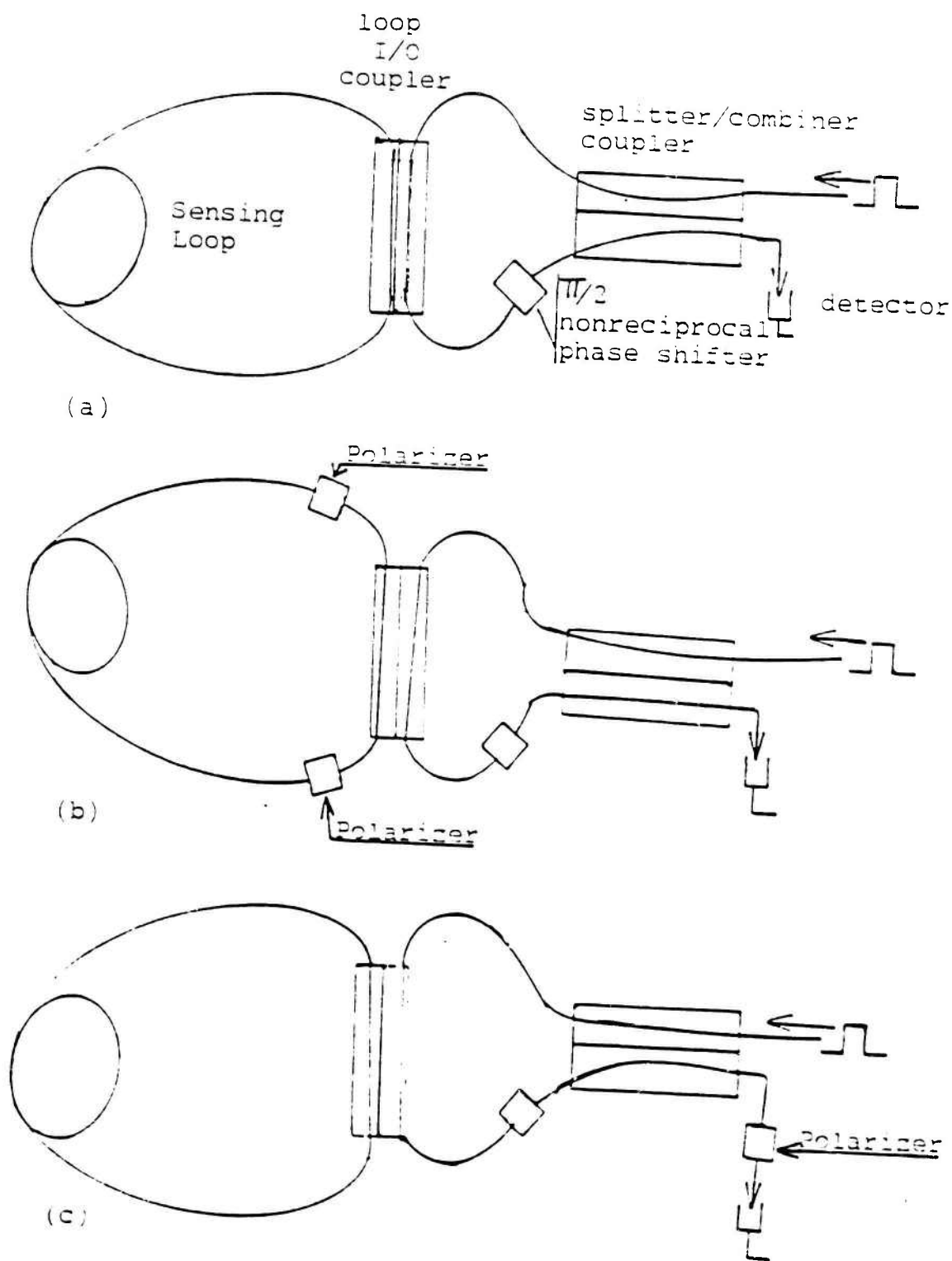


Fig. IV-1. Three configurations of passive re-entrant rotation sensors whose performance is analyzed for birefringent optical fiber sensing loops. (a) no polarizer; (b) polarizers in sensing loop; (c) polarizer exterior to sensing loop.

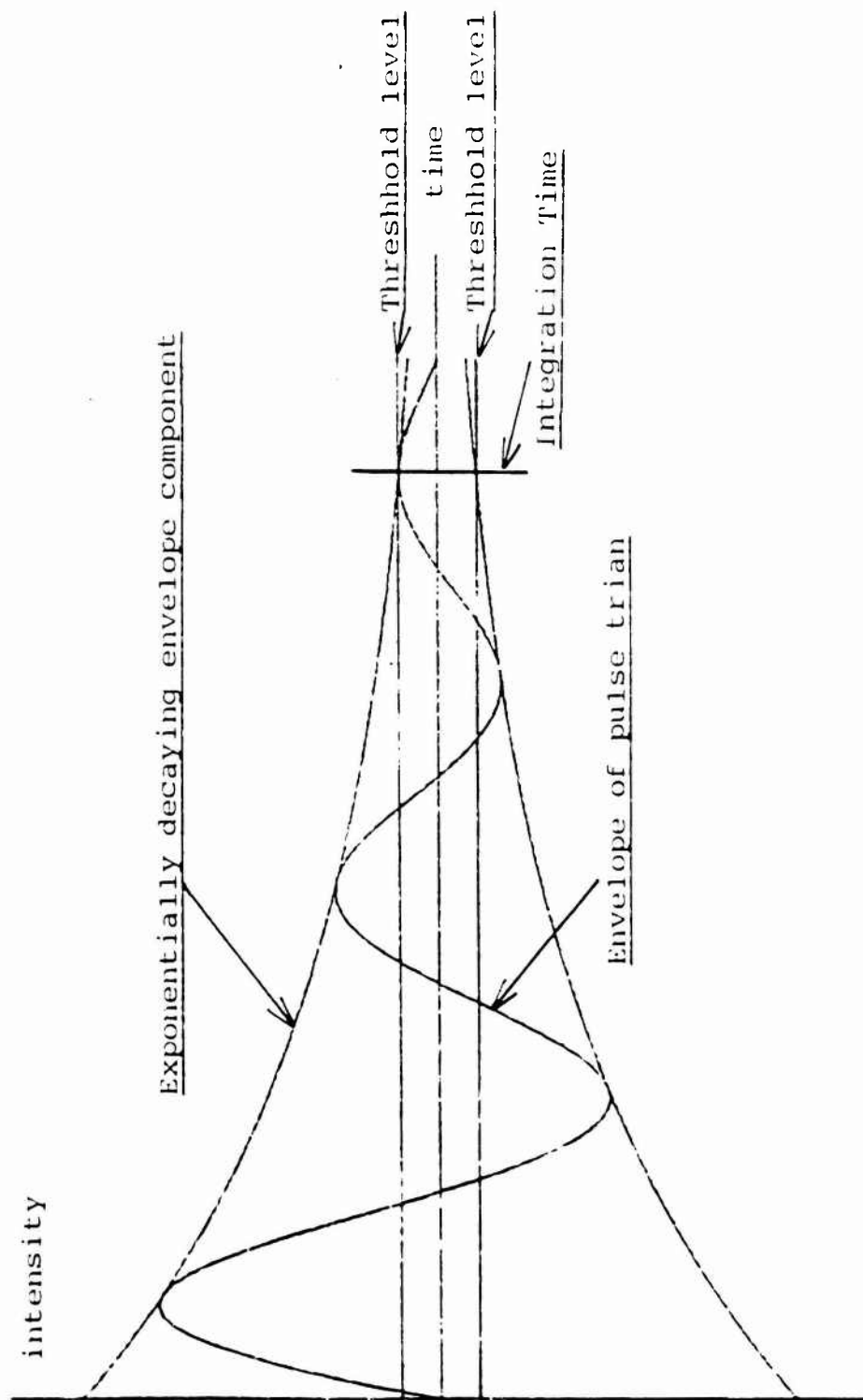


Fig. IV-2. Envelope of pulse train vs time. Also shown is the decaying envelope component and the threshold level. The envelope phase error is assumed to increase rapidly if the envelope phase is measured beyond the integration time (i.e., when the decaying envelope component is less than the threshold level).

$$\begin{aligned}
a. \quad S_{12} &= \exp(j\phi_s/2 + j\bar{\phi}(L)) \begin{pmatrix} \cos \theta \exp \frac{j\xi(L)}{2} & \sin \theta \exp \frac{-j\phi(L)}{2} \\ -\sin \theta \exp \frac{j\phi(L)}{2} & \cos \theta \exp \frac{-j\xi(L)}{2} \end{pmatrix} \\
b. \quad S_{21} &= \exp(-j\phi_s/2 + j\bar{\phi}(L)) \begin{pmatrix} \cos \theta \exp \frac{j\xi(L)}{2} & -\sin \theta \exp \frac{j\phi(L)}{2} \\ \sin \theta \exp \frac{-j\phi(L)}{2} & \cos \theta \exp \frac{-j\xi(L)}{2} \end{pmatrix}
\end{aligned} \tag{IV-3}$$

where ϕ_s is the Sagnac phase shift, θ describes the rotation of the input state of polarization by the fiber, $\bar{\phi}(L)$ is an average phase shift which depends on fiber length with $\xi(L)$ and $\phi(L)$ being phase shifts which depend on the birefringence and number of scattering centers in the fiber. The polarizers, which are considered ideal, are described by their Jones matrix, P , in Eq. IV-4.

$$P = \begin{pmatrix} \cos^2 a & \sin a \cos a \\ \sin a \cos a & \sin^2 a \end{pmatrix} \tag{IV-4}$$

where the angle a is between the polarizer and the x -axis. Using these matrices, the Jones matrices for the K^{th} recirculation for the fiber optic rotation sensors depicted in Fig. IV-3 are

$$a. \quad M_K^a = R_{SC} B_+ T_{IO} (S_{12} R_{IO})^{K-1} S_{12} T_{IO} R_{SC} + T_{SC} T_{IO} (S_{21} R_{IO})^{K-1} S_{21} T_{IO} B_- T_{SC}$$

$$\begin{aligned}
b. \quad M_K^b &= R_{SC} B_+ T_{IO} (P S_{12} P R_{IO})^{K-1} P S_{12} P T_{IO} R_{SC} \\
&\quad + T_{SC} T_{IO} (P S_{21} P R_{IO})^{K-1} P S_{21} P T_{IO} B_- T_{SC}
\end{aligned} \tag{IV-5}$$

$$c. \quad M_K^c = P [R_{SC} B_+ T_{IO} (S_{12} R_{IO})^{K-1} S_{12} T_{IO} R_{SC} + T_{SC} T_{IO} (S_{21} R_{IO})^{K-1} S_{21} T_{IO} B_- T_{SC}]$$

In the above equations, the matrices B_+ and B_- describe the effect of the non-reciprocal phase bias element. They are given in the x and y linear polarization basis as

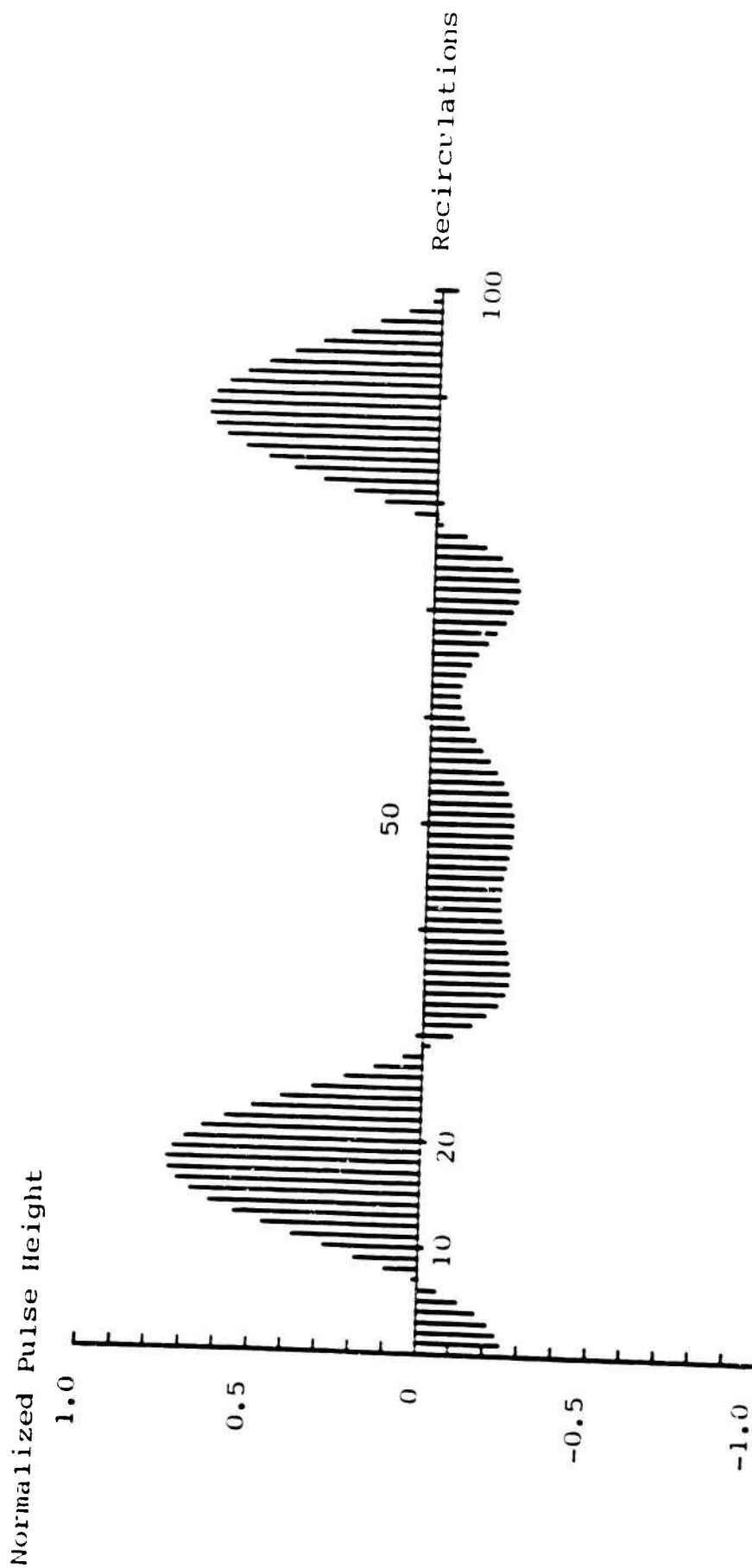


Fig. IV-3a. Normalized pulse height vs recirculations for a 9J degree phase biased re-entrant rotation sensor operated in the cross-polarized mode with external polarizers. The birefringent parameters are: $\theta = 5$ degrees, $\xi = 0$ degrees, and $\phi = 10$ degrees. The DC level has been suppressed.

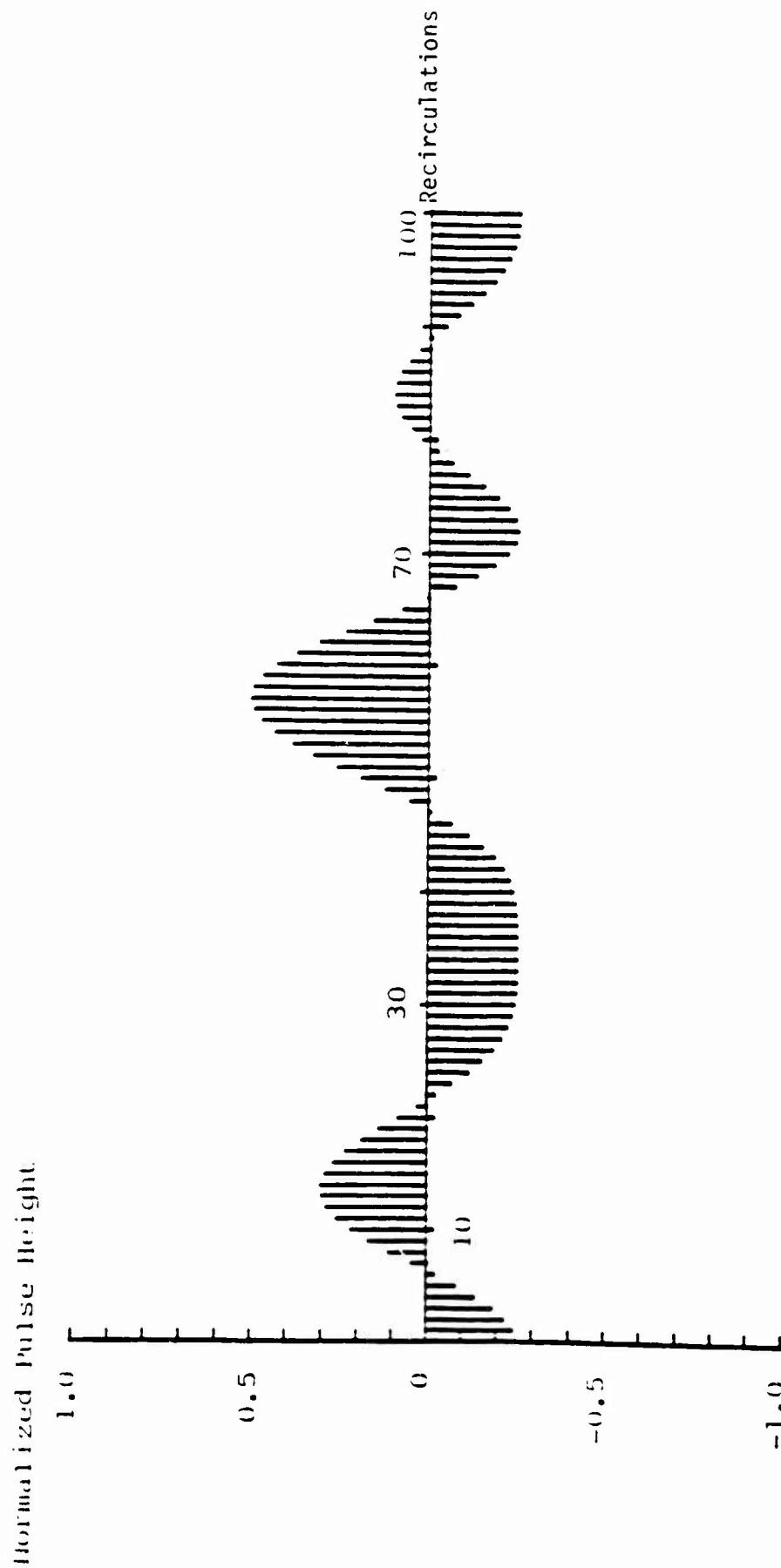


Fig. IV-3b. Normalized pulse height vs recirculations for a 90 degree phase biased re-entrant rotation sensor operated in the cross-polarized mode with external polarizers. The birefringent parameters are: $\theta = 5$ degrees, $\xi = 0$ degrees, and $\phi = 90$ degrees. The DC level has been suppressed.

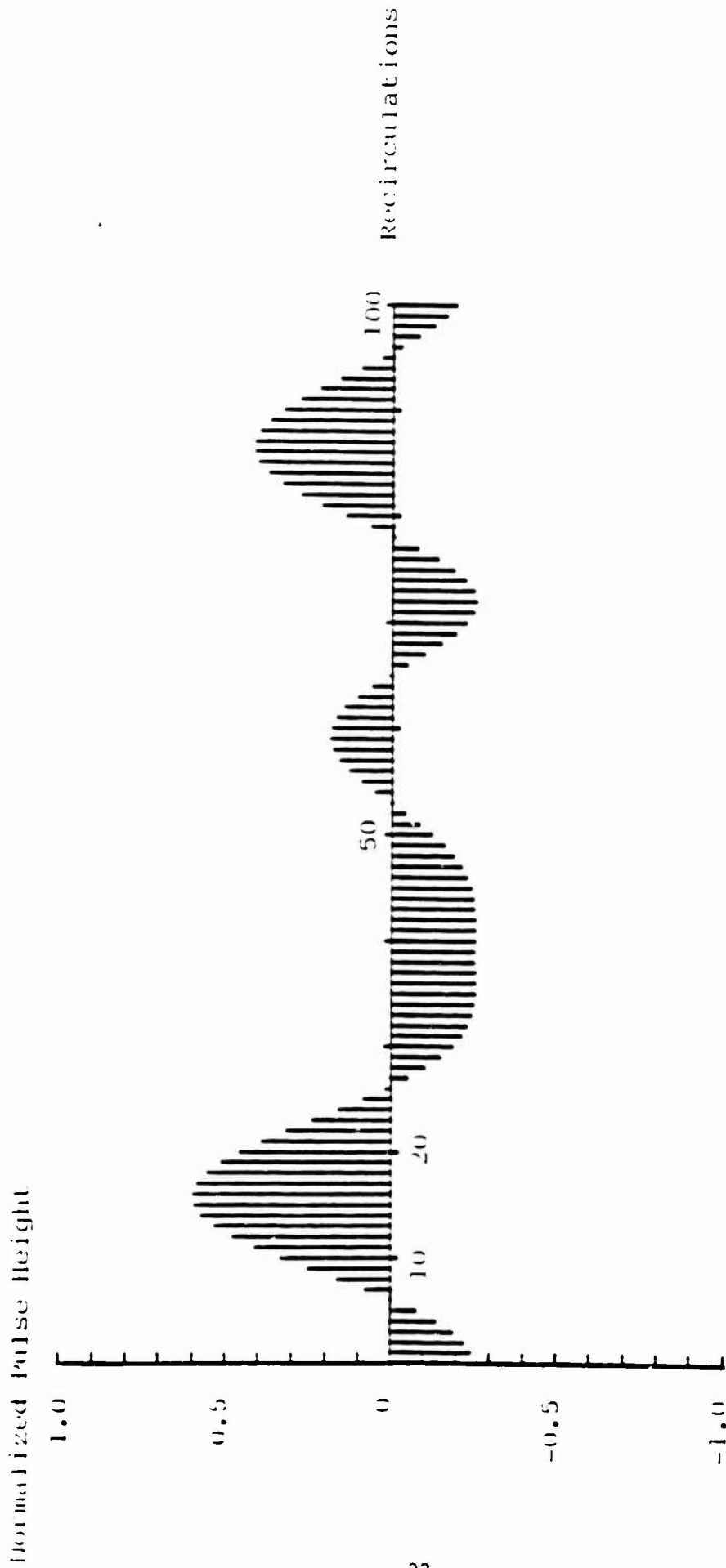


Fig. IV-3c. Normalized pulse height vs recirculations for a 90 degree phase biased re-entrant rotation sensor operated in the cross-polarized mode with external polarizers. The birefringent parameters are: $\theta = 5$ degrees, $\zeta = 0$ degrees, and $\phi = 45$ degrees. The DC level has been suppressed.

$$B_{\pm} = \begin{pmatrix} \exp(\pm j\pi/4) & 0 \\ 0 & \exp(\pm j\pi/4) \end{pmatrix} \quad (IV-6)$$

The coherence matrix of the output for the K^{th} recirculation is computed from the coherence matrix of the input and the Jones matrices given in Eq. IV-5 by the use of Eq. IV-7.

$$\begin{aligned} a. \quad I &= Tr(J) \\ b. \quad J_{pq} &= J_{pq}^* \end{aligned} \quad (IV-7)$$

where J is the coherence matrix and I the light intensity. The intensity of the output for the K^{th} recirculation is equal to the trace of the coherence matrix of the output for the K^{th} circulation.

It is observed that the matrices describing the couplers and the phase bias element are of the form of a scalar times the identity matrix. Such matrices commute with all matrices. It is also observed that the matrix products $PS_{12}P$ and $PS_{21}P$ in Eq. IV-5b have only one nonzero diagonal element. The only matrix products which are difficult to evaluate are S_{12}^K and S_{21}^K . These matrix products are evaluated by finding unitary matrices D_{12} and D_{21} which diagonalize S_{12} and S_{21} respectively. These matrix products are:

$$\begin{aligned} a. \quad S_{12}^K &= D_{12} \bigwedge_{12}^K D_{12}^* \\ b. \quad S_{21}^K &= D_{21} \bigwedge_{21}^K D_{21}^* \end{aligned} \quad (IV-8)$$

where \bigwedge is a diagonal matrix with the eigenvalues of S_{ki} as the diagonal elements. The Jones matrices, M_K , which describe the three configurations of re-entrant, pulsed fiber optic rotation sensors can be rewritten as

$$a. \quad M_K^q = 0.5\delta(1-\delta)^{(K-1)/2} \exp(-j(K-1)\pi/4) \exp(jk\phi)$$

$$\begin{pmatrix} 2A' \cos(K\phi_s/2 + \pi/4) & E \exp[j(K\phi_s/2 + \pi/4)] + F \exp[-j(K\phi_s/2 + \pi/4)] \\ F \exp[j(K\phi_s/2 + \pi/4)] E \exp[j(K\phi_s/2 + \pi/4)] & 2B' \cos(K\phi_s/2 + \pi/4) \end{pmatrix} \quad (IV-9)$$

$$b. \quad M_K^b = 0.5\delta(1-\delta)^{(K-1)/2} \exp(-j(K-1)\pi/4) \exp(jk\phi)$$

$$\begin{pmatrix} 2 \cos^K \theta \cos(K\phi_s/2 + \pi/4) \exp(jk\xi/2) & 0 \\ 0 & 0 \end{pmatrix}$$

$$c. \quad M_K^{(\sigma)} = P M_K^{(a)}$$

where in Eq. IV-9a the parameters A' , B' , E and F are defined as

$$\begin{aligned} a. \quad A' &= |A|^2 \exp(jK\eta)/N_+ + |A|^2 \exp(-jK\eta)/N_- \\ b. \quad B' &= (B-C)^2 \exp(jK\eta)/N_+ + (B+C)^2 \exp(-jK\eta)/N_- \\ c. \quad E &= -jA^*(B-C) \exp(jK\eta)/N_+ - jA^*(B+C) \exp(-jK\eta)/N_- \\ d. \quad F &= jA^*(B-C) \exp(jK\eta)/N_+ + jA^*(B+C) \exp(-jK\eta)/N_- \end{aligned} \quad (IV-10)$$

The parameters A , B , C , N_+ , N_- , η are in turn defined as:

$$\begin{aligned} a. \quad A &= -\sin \theta e^{+j\phi/2} \\ b. \quad B &= \cos \theta \sin \xi/2 \\ c. \quad C &= \sqrt{1 - \cos^2 \theta \cos^2 \xi/2} \\ d. \quad N_{\pm} &= 1 + \sin^2 \theta - \cos^2 \theta \cos \xi \mp 2 \cos \theta \sin \xi/2 \sqrt{1 - \cos^2 \theta \cos^2 \xi/2} \\ e. \quad \eta &= \cos^{-1}[\cos \theta \cos \xi/2] \end{aligned} \quad (IV-11)$$

where θ , ϕ and ξ are the parameters which characterize the birefringence of the optical fibers as before. These parameters are environmentally sensitive.

1. Co-Polarized With External Polarizer

In this configuration and mode of operation the input light is linearly polarized along the x -axis. The polarizer is exterior to the sensing loop (see Fig. IV-1c). The polarizer is oriented to pass the x -linear polarization. The intensity of the output pulse for the K^{th} recirculation, $I_K^{(x)}$ is:

$$I_K^{(x)} = 0.5\delta^2(1-\delta)^{(K-1)}[1 - \sin K\phi_s]|A'|^2 \quad (IV-12)$$

where A' is defined by Eqs. IV-19 and IV-11. The factor $|A'|^2$ contains all the environmentally sensitive birefringence parameters. The factor, $|A'|^2$, in Eq. IV-12 is of the form of a constant plus a constant times a sinusoid. The frequency of this sinusoid is dependent on the birefringence of the fiber. Let a normalized frequency \bar{v} be defined as the product of the frequency and the loop transit time τ_t

$$\bar{v} = v\tau_t \quad (IV-13)$$

The normalized frequency due to birefringence, \bar{v}_B , and the normalized frequency due to rotation, \bar{v}_R , are

$$\begin{aligned} a. \quad \bar{v}_B &= \cos^{-1}(\cos \theta \cos \tau/2)/\pi \\ b. \quad \bar{v}_R &= \phi_s/2\pi \end{aligned} \quad (IV-14)$$

where ϕ_s is the Sagnac shift for one transit of the sensing loop. Using these definitions of the normalized frequencies and the definition of A' given in Eq. IV-10a, the detected intensity for the K^{th} recirculation is rewritten as:

$$\begin{aligned} I_K^{(x)} &= 0.5\delta^2(1-\delta)^{(K-1)}|A|^4[(1/N_+^2 + 1/N_-^2) - (1/N_+^2 + 1/N_-^2)\sin 2\pi K\bar{v}_R \\ &\quad + (2\cos 2\pi K\bar{v}_B)/(N_+N_-) - (2\sin 2\pi K(\bar{v}_R + \bar{v}_B))/(N_+N_-) \\ &\quad - (2\sin 2\pi K(\bar{v}_R - \bar{v}_B))/(N_+N_-)] \end{aligned} \quad (IV-15)$$

To better visualize the effect of birefringence on the performance of a re-entrant, pulsed fiber optic rotation sensor, the effect of the decaying envelope due to the sampling of the light waves each transit, is normalized by defining a normalized detected intensity for the K^{th} recirculation, \bar{I}_K , as

$$\bar{I}_K = I_K / \epsilon^2 (1 - \delta)^{(K-1)} \quad (IV - 16)$$

The DC level (i.e. the first term in Eq. IV - 15) is suppressed.

The normalized intensity \bar{I}_K is the sum of four sinusoidally terms. The amplitude of the pure rotation term is different from the amplitudes of the birefringence terms. The ideal output occurs when only the amplitude of the pure rotation or ν_R frequency term is nonzero. The other terms can introduce additional zero crossings in the pulse train which result in errors in the measured rotation rate. Fig. IV-4 shows curves of the absolute value of the amplitude of the ν_R frequency term, A_r , versus the state of polarization rotation parameter, θ . The curves are described by the linear birefringence parameter, ξ . Figure IV-5 shows curves of the absolute value of the amplitude of the birefringence terms, A_B , within a factor of two. For rotations of the state of polarization near 90 degrees, the ratio of amplitudes of the pure rotation and the birefringence terms is about 2. This ratio should be made large possible in practice, by parameter near 180 degrees as seen in Figs. IV-6 and IV-7. Figure IV-6 is a plot of $\bar{I}_K^{(r)}$ versus K for $\xi = 0$ and various values of θ while Fig. IV-7 is a plot of $\bar{I}_K^{(r)}$ versus K for $\theta = 5$ degrees and various values of ξ . The DC level has been suppressed in Figs. IV-6 and IV-7.

In Figure IV-6a, the undistorted or ideal pulse train is shown for normalized rotation frequency of 3/200, which results in exactly 3 half cycles in 100 recirculations. In this figure, the pulses start at zero and have three additional zero crossings. Increasing the rotation parameter, while the linear birefringence is zero, results in increasing distortion of the pulse train (Fig. IV-6). The pulse trains no longer start

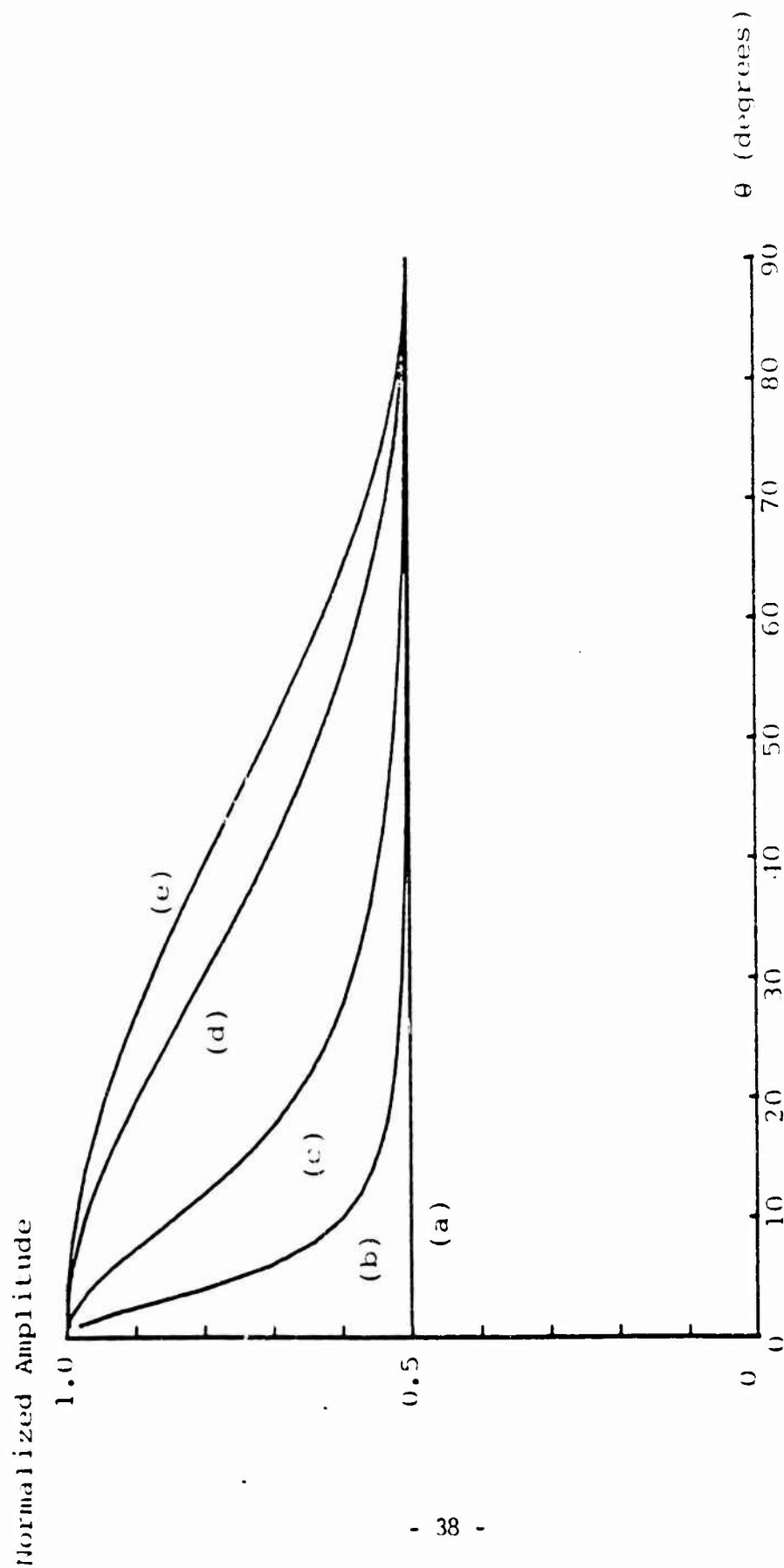


Fig. IV-4. Amplitude of \bar{V}_R term vs the state of polarization rotation parameter, θ , for a re-entrant rotation sensor operated in the copolarized mode with external polarizers. The curves are described by the linear birefringence parameter, ξ : (a) 0 degrees, (b) 10 degrees, (c) 30 degrees, (d) 90 degrees, and (e) 180 degrees.

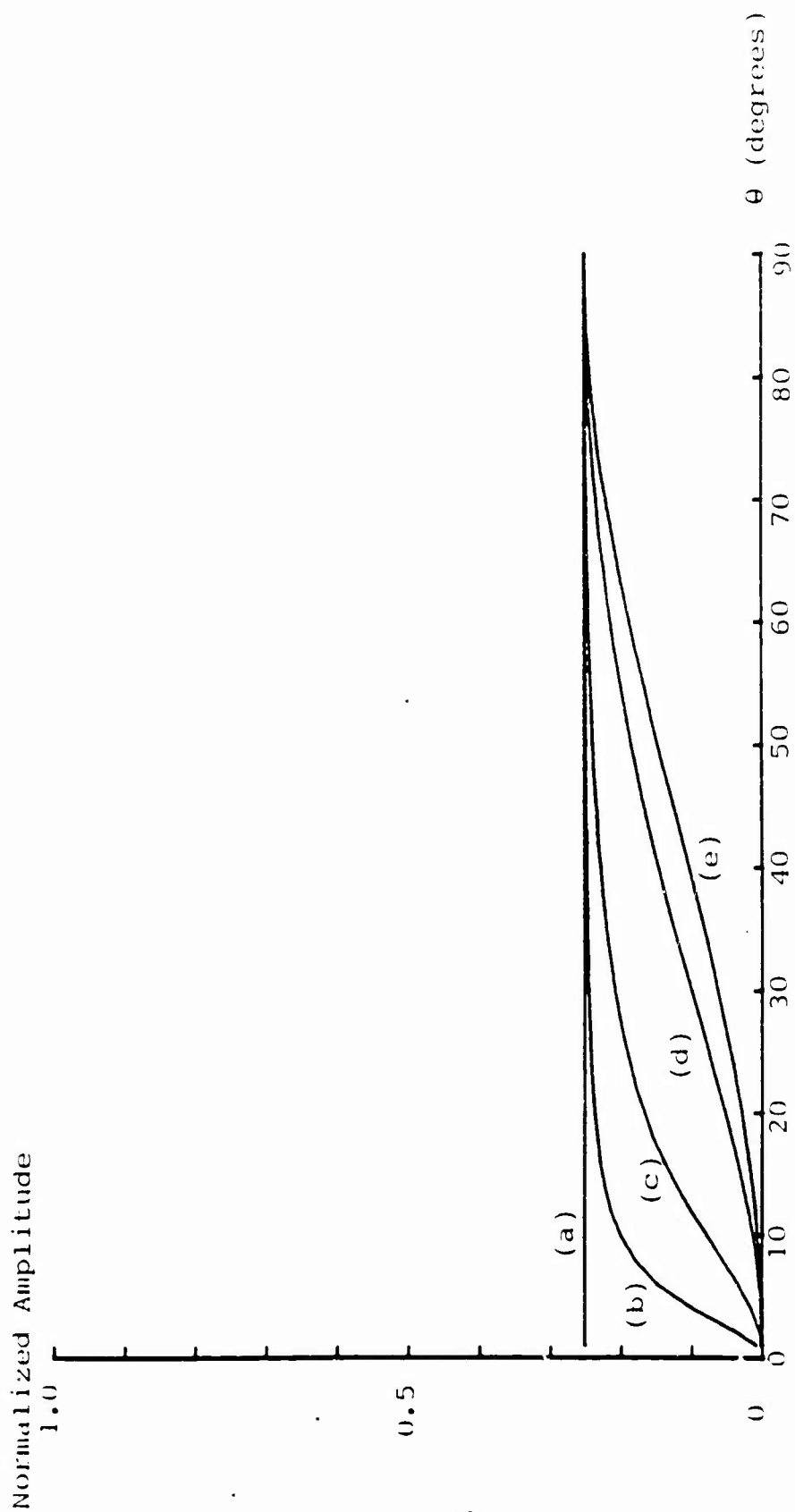


Fig. IV-5. Amplitude of birefringent terms (i.e., terms at normalized frequencies of $\bar{\nu}_B$, $\bar{\nu}_R - \bar{\nu}_B$, $\bar{\nu}_R + \bar{\nu}_B$ vs the state of polarization parameter, θ , for a re-entrant rotation sensor operated in the copolarized mode with external polarizers. The curves are described by the linear birefringence parameter, ξ : (a) 0 degrees, (b) 10 degrees, (c) 30 degrees, (d) 90 degrees, and (e) 180 degrees.

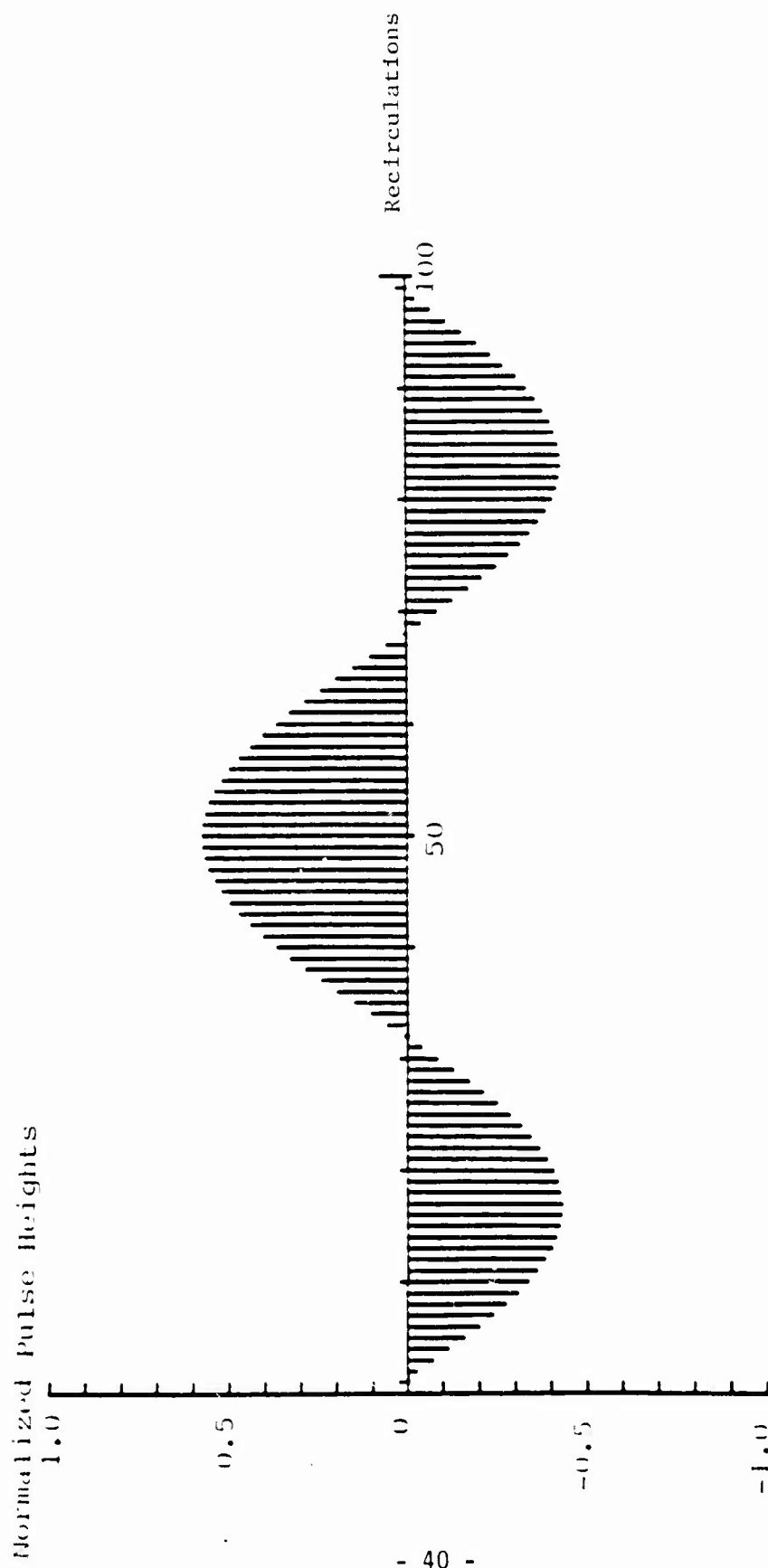


Fig. IV-6a. Normalized pulse heights vs recirculations for a 90 degree phase biased, re-entrant rotation sensor operated in the copolarized mode with external polarizers. The birefringent parameters θ , ϕ , and ζ are equal to zero. The DC level has been suppressed.

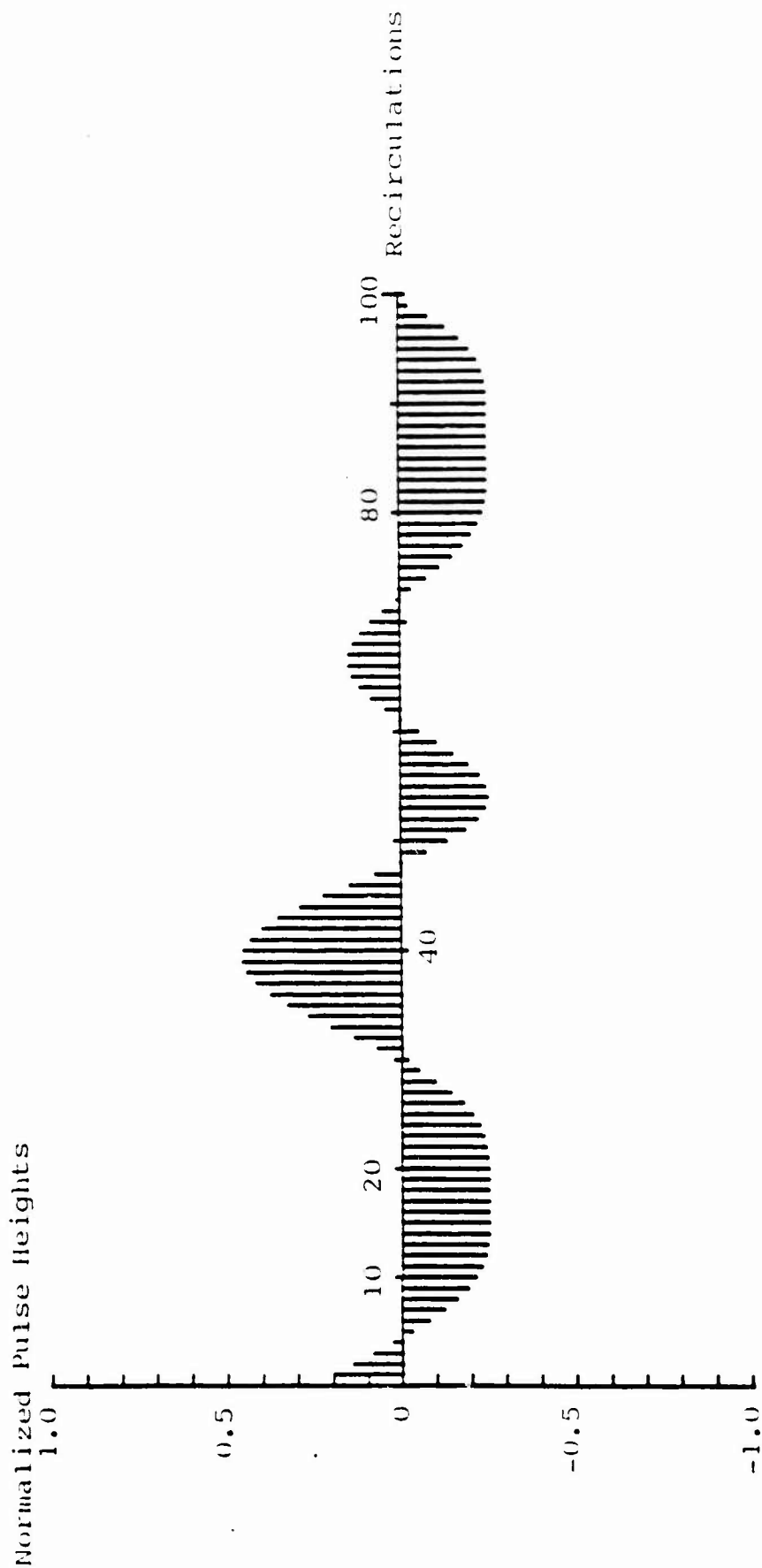


Fig. IV-6b. Normalized pulse heights vs recirculations for a 90 degree phase biased re-entrant rotation sensor operated in the copolarized mode with external polarizers. The birefringent parameters are: $\theta = 5$ degrees, $\phi = \xi = 0$ degrees. The DC level has been suppressed.

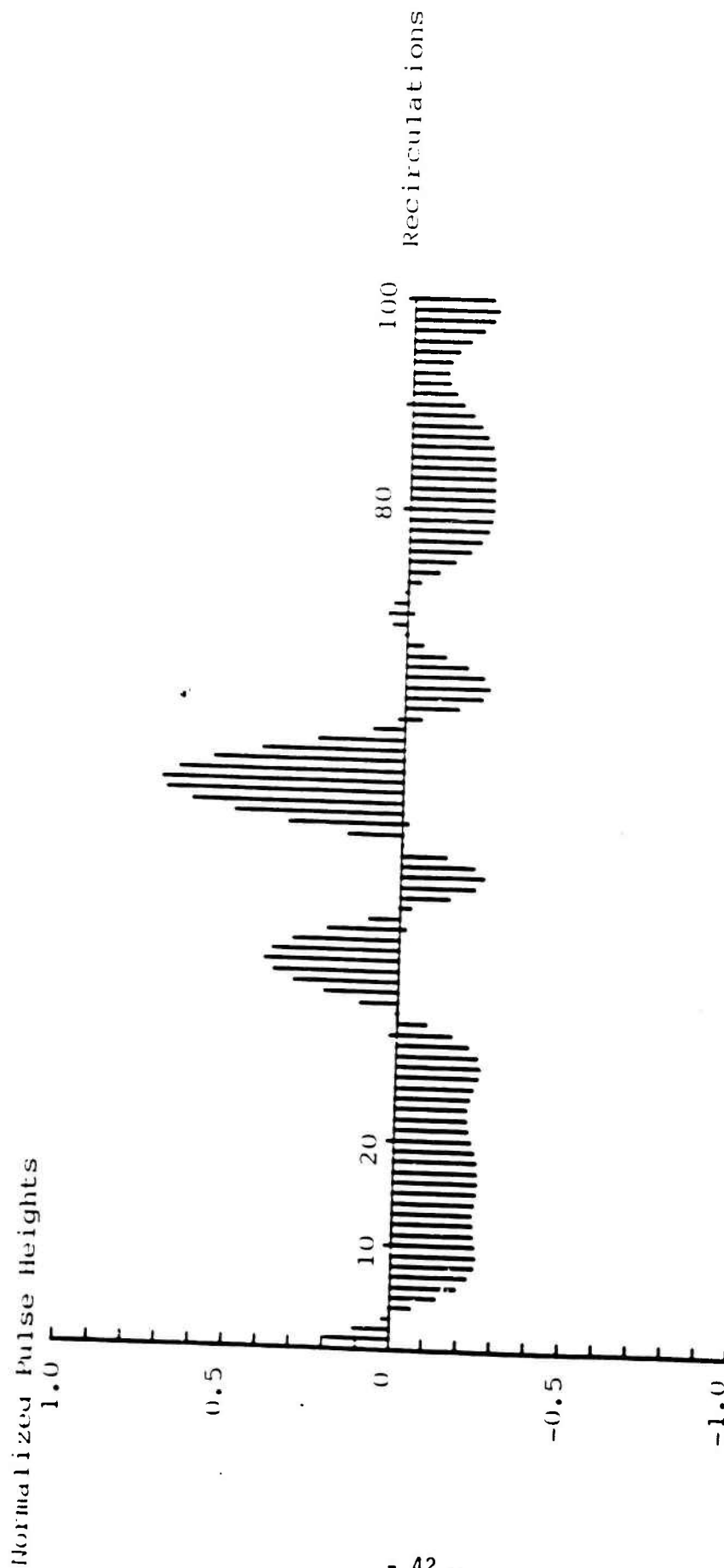


Fig. IV-6c. Normalized pulse heights vs recirculations for a 90 degree phase biased re-entrant rotation sensor operated in the copolarized mode with external polarizers. The birefringent parameters are : $\theta = 10$ degrees, $\phi = \xi = 0$ degrees. The DC level has been suppressed.

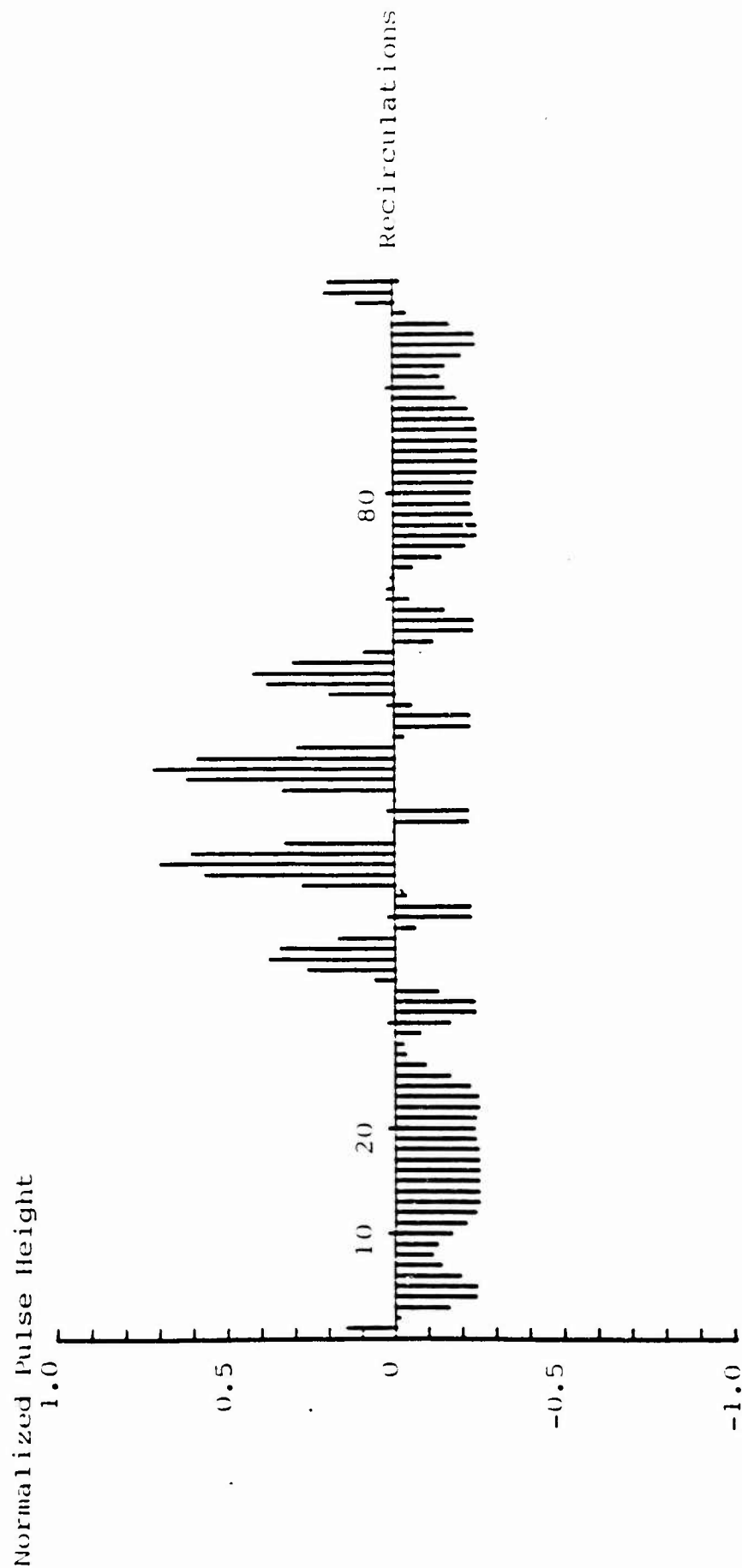


Fig. IV-6d. Normalized pulse heights vs recirculations for a 90 degree phase biased re-entrant rotation sensor operated in the copolarized mode with external polarizers. The birefringent parameters are: $\theta = 20$ degrees, $\phi = \xi = 0$ degrees. The DC level has been suppressed.

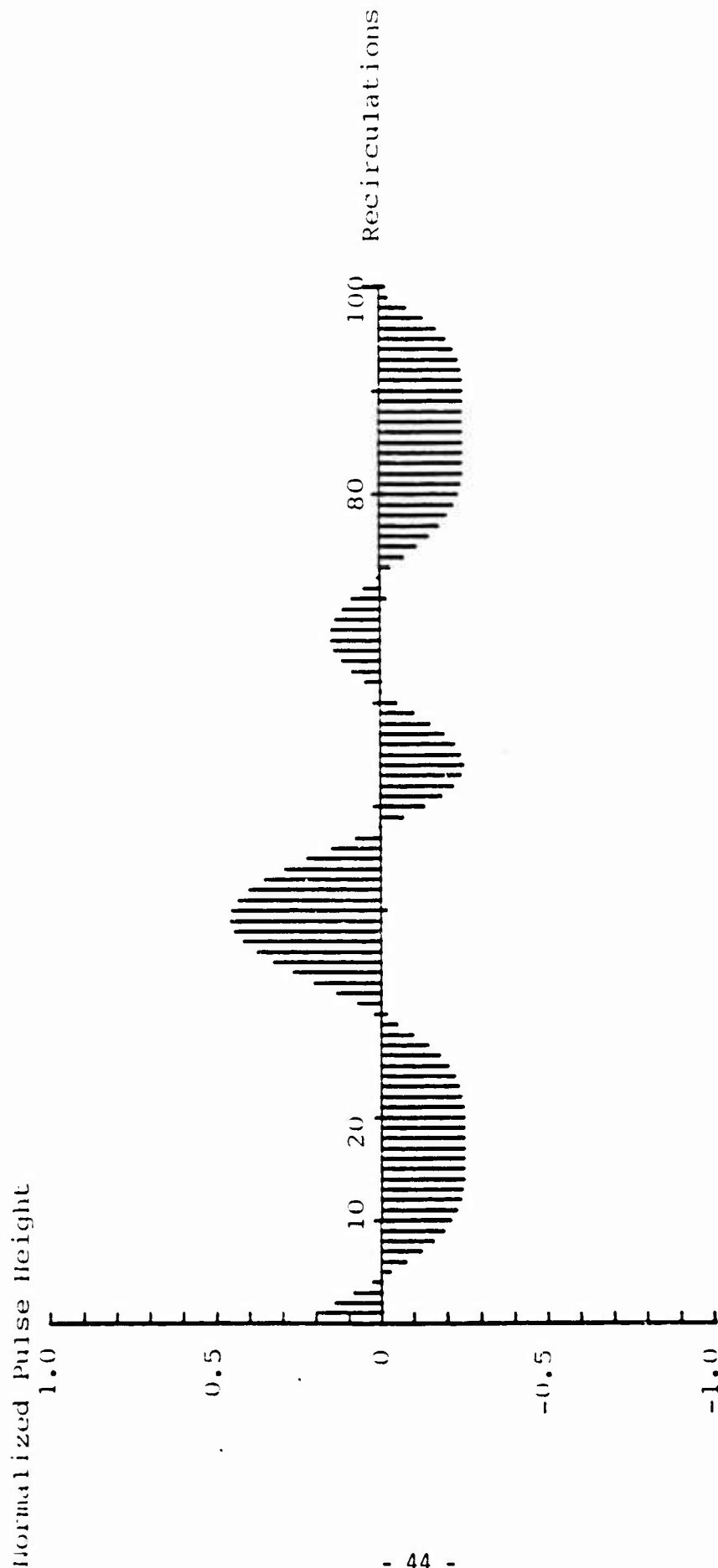


Fig. IV-7a. Normalized pulse height vs recirculations for a 90 degree phase biased re-entrant rotation sensor operated in the copolarized mode with external polarizers. The birefringent parameters are: $\theta = 5$ degrees, $\xi = 0$ degrees, and $\phi = 0$ degrees. The DC level has been suppressed.

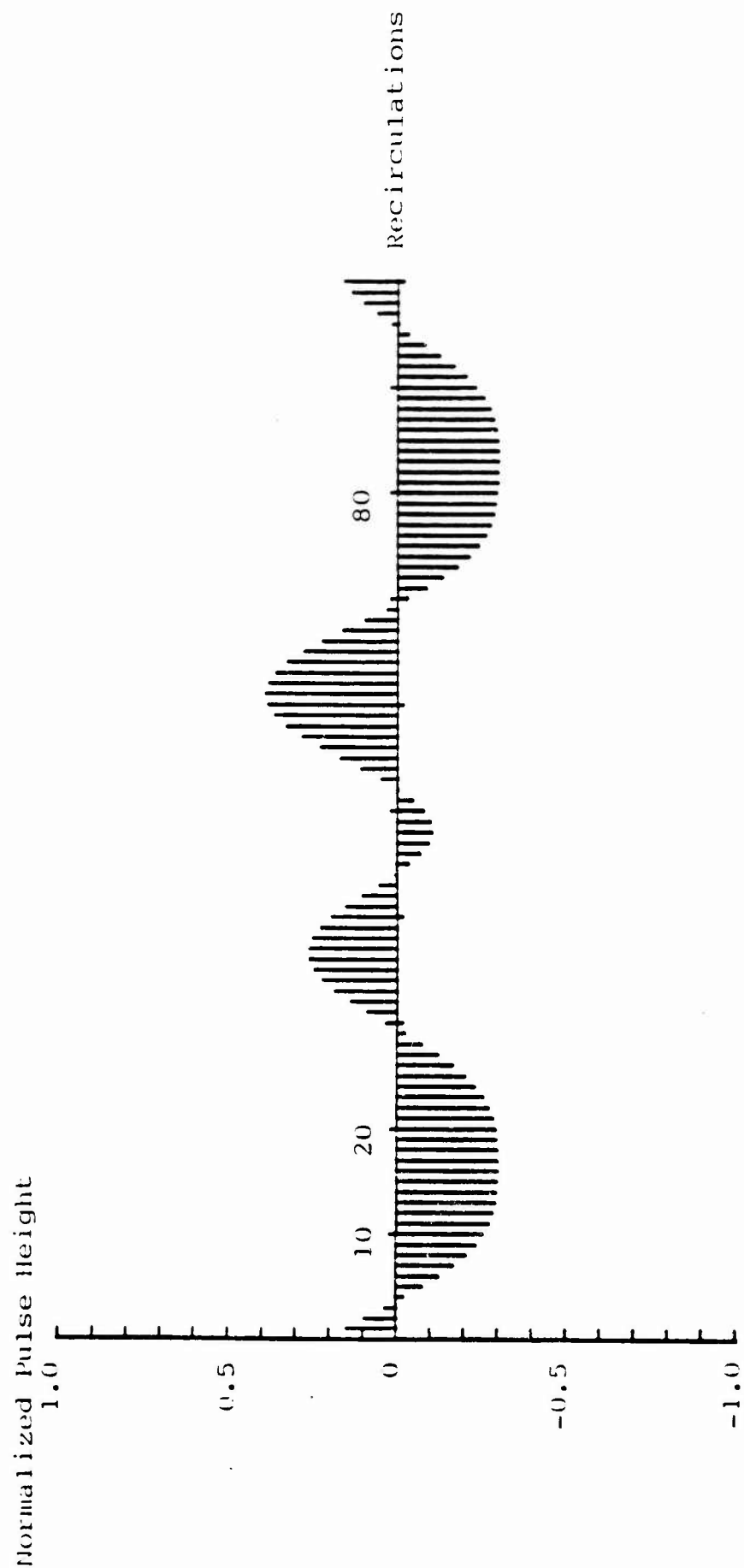


Fig. IV-7b. Normalized pulse height vs recirculations for a 90 degree phase biased re-entrant rotation sensor operated in the copolarized mode with external polarizers. The birefringent parameters are: $\theta = 5$ degrees, $\xi = 5$ degrees, and $\phi = 0$ degrees. The DC level has been suppressed.

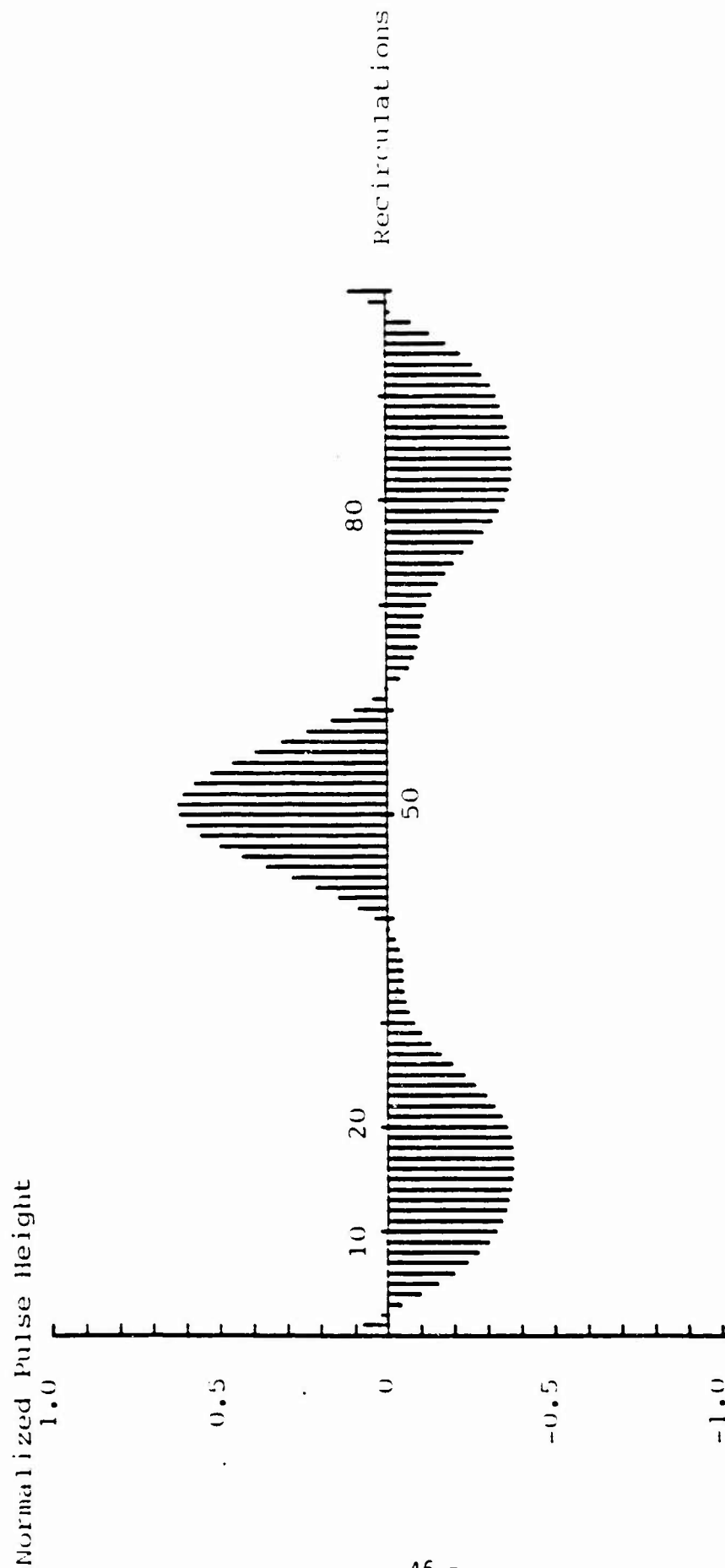


Fig. IV-7c. Normalized pulse height vs recirculations for a 90 degree phase biased re-entrant rotation sensor operated on the copolarized mode with external polarizers. The birefringent parameters are: $\theta = 5$ degrees, $\xi = 10$ degrees, and $\phi = 0$ degrees. The DC level has been suppressed.

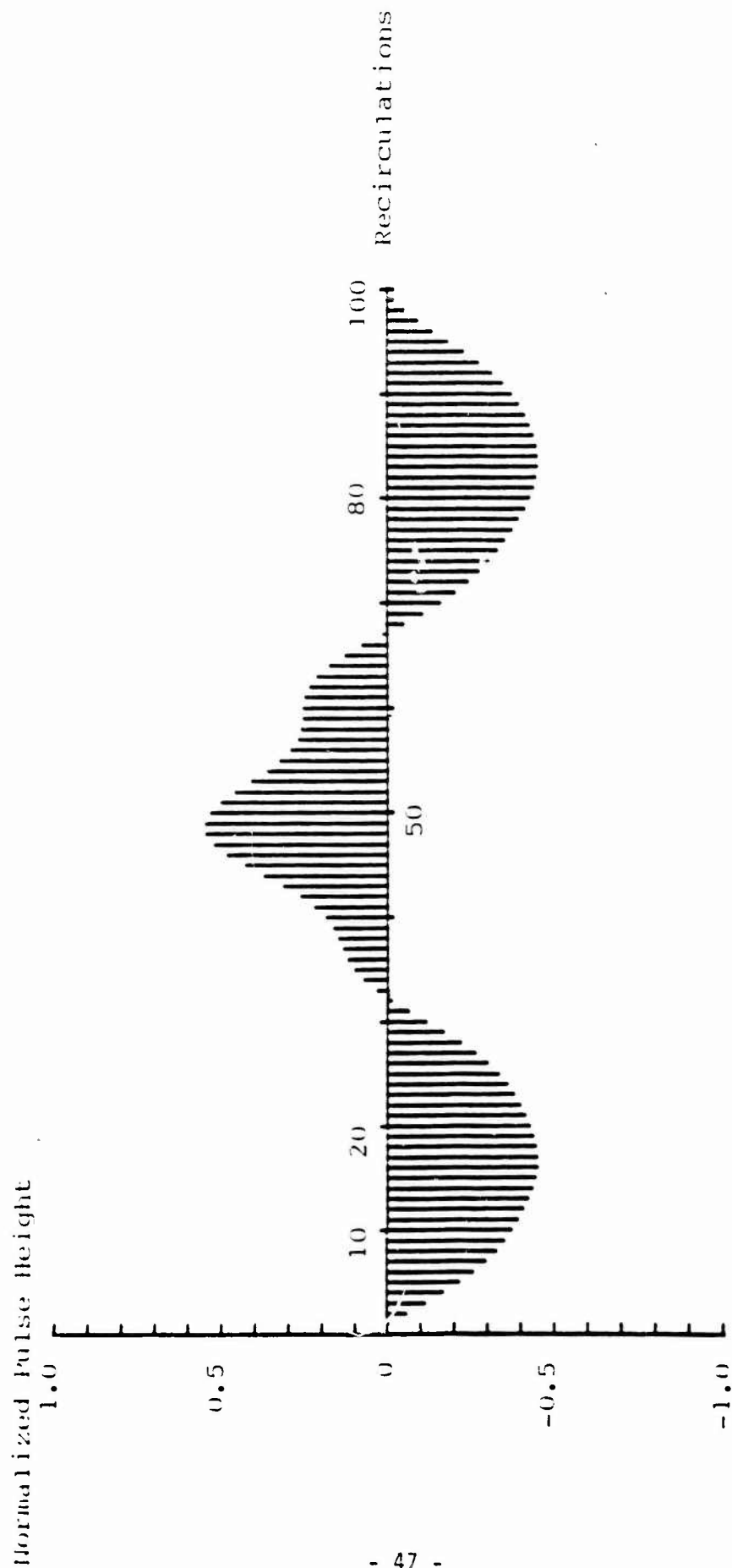


Fig. IV-7d. Normalized pulse height vs recirculations for a 90 degree phase biased re-entrant rotation sensor operated in the copolarized mode with external polarizers. The birefringent parameters are: $\theta = 5$ degrees, $\xi = 20$ degrees, and $\phi = 0$ degrees. The DC level has been suppressed.

at zero and additional zero crossings occur. In Fig. IV-6b, three additional zero crossings are present, while in Fig. IV-6d nine new zero crossings can be found. Increasing the linear birefringence parameter while the rotation parameter is small (Fig. IV-7) results in decreased distortion. In Fig. IV-7d, the pulse train appears undistorted to the eye. These results imply the fiber used in the sensing loop should be polarization preserving.

2. Cross Polarized With External Polarizer

In this configuration and mode of operation, the input light is linearly polarized along the x -axis. The polarizer is exterior to the sensing loop and is oriented to pass the y -linear polarization.

Using Eq. IV-9c to describe the re-entrant, pulsed fiber optic rotation sensor with P representing the polarizer oriented to pass the y -linear polarization, the detected normalized intensity $I_K^{(y)}$ for the K^{th} recirculation is:

$$I_K^{(y)} = 0.5[1 + \sin(2\pi K \bar{v}_R + \phi)]|F|^2 \quad (IV-17)$$

where ϕ is the reciprocal birefringent dependent phase shift and F is defined in Eq. IV-10d. $|F|^2$ has the form a constant plus a constant times a sinusoid. The frequency of this sinusoid is due to the birefringence of the optical fiber and is given in Eq. IV-14b. The normalized intensity again contains frequencies \bar{v}_R , \bar{v}_B , $\bar{v}_r + \bar{v}_B$, $\bar{v}_R - \bar{v}_B$. Equation IV-17 can be rewritten as:

$$\begin{aligned} I_K^{(y)} = & 0.5|A|^2((B-C)/N_+)^2 + ((B+C)/N_-)^2 + \left[((B-C)/N_+)^2 \right. \\ & \left. + ((B+C)/N_-)^2 \right] \sin(2\pi K \bar{v}_R + \phi) + [2(B^2 - C^2)/(N_+ N_-)] \cos 2\pi K \bar{v}_B \\ & + [(B^2 - C^2)/(N_+ N_-)] [\sin(2\pi K(\bar{v}_R + \bar{v}_B) + \phi) + \sin(2\pi K(\bar{v}_R - \bar{v}_B) + \phi)] \end{aligned} \quad (IV-18)$$

The quantities A , B , C , N_+ and N_- have been defined before. The amplitude of

the pure rotation term is different from the amplitudes of the birefringent terms. The phase of the rotation terms with respect to the pure birefringent term is θ , the reciprocal birefringent dependent phase shift.

Figures IV-3 and IV-9 show the amplitudes of the pure rotation, A_R , and birefringent, A_B , terms respectively versus the rotation parameter θ . The curves are described by the linear birefringence parameter ξ . As θ goes to 90 degrees the ratio A_R/A_B goes to minus two. Both amplitudes go to zero as θ goes to zero. The ratio A_R/A_B is approximately constant at a nonzero value. The pure rotation term can never be made dominant.

In Figs. IV-10, pulse trains are plotted for $\theta = \xi = 0$, and various values of θ . If θ is zero then there is no pulse train because the x -linear polarization at the input is never rotated into the y -linear polarization at the output. The pulse trains become more and more distorted as θ increases but the amplitudes are constant. In these figures and all succeeding figures the DC level (i.e. the first term in the brackets in Eq. IV-18) is subtracted out before the normalized intensity is plotted for a pulse train. In Figs. IV-11, the pulse trains are shown for $\theta = 5$ degrees, $\phi = 0$ and various values of ξ . As the linear birefringence parameter ξ increases the amplitude of the pulses is decreased and the distortion of the pulse train is increased. For θ around zero degrees and for ξ going to 180 degrees the normalized intensity goes to zero. In Figs. IV-12, $\theta = 5$ degrees, $\xi = 0$ degrees and ϕ is as shown. The pulse trains are increasingly distorted as the reciprocal birefringent phase shift parameter, ϕ , is increased. This configuration and mode of operation is not suitable for use as a rotation sensor.

3. No Polarizer

This configuration is shown in Fig. IV-1a and is modeled by the Jones matrix in Eq. IV-9a. The input light is linearly polarized along the x -axis. The normalized

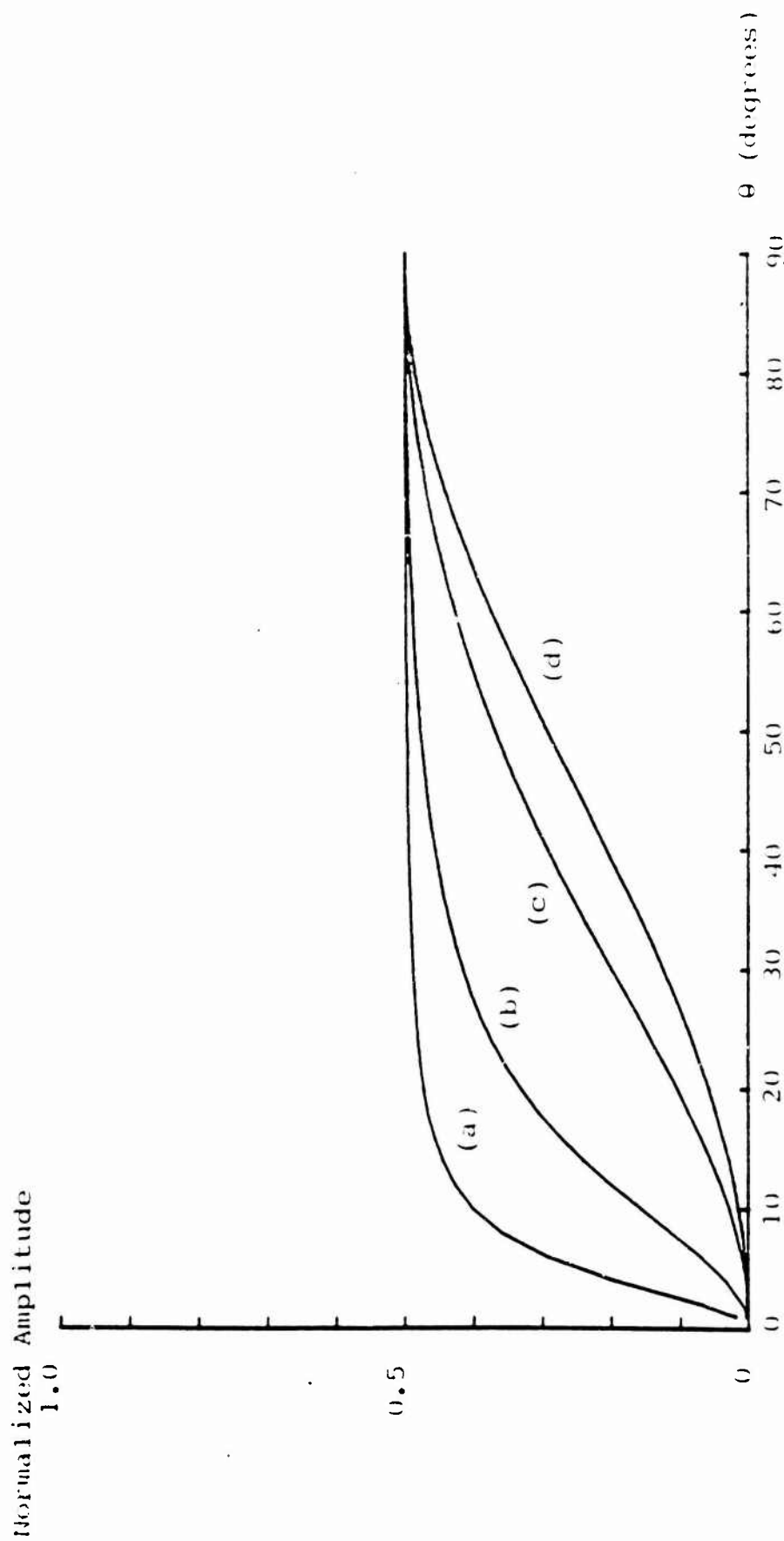


Fig. IV-8. Amplitude of \bar{V}_p terms vs the state of polarization parameter, θ , for a re-entrant rotation sensor operated in the cross-polarized mode with external polarizers. The curves are described by the linear birefringence parameters, ξ : (a) 10 degrees, (b) 30 degrees, (c) 90 degrees, and (d) 180 degrees.

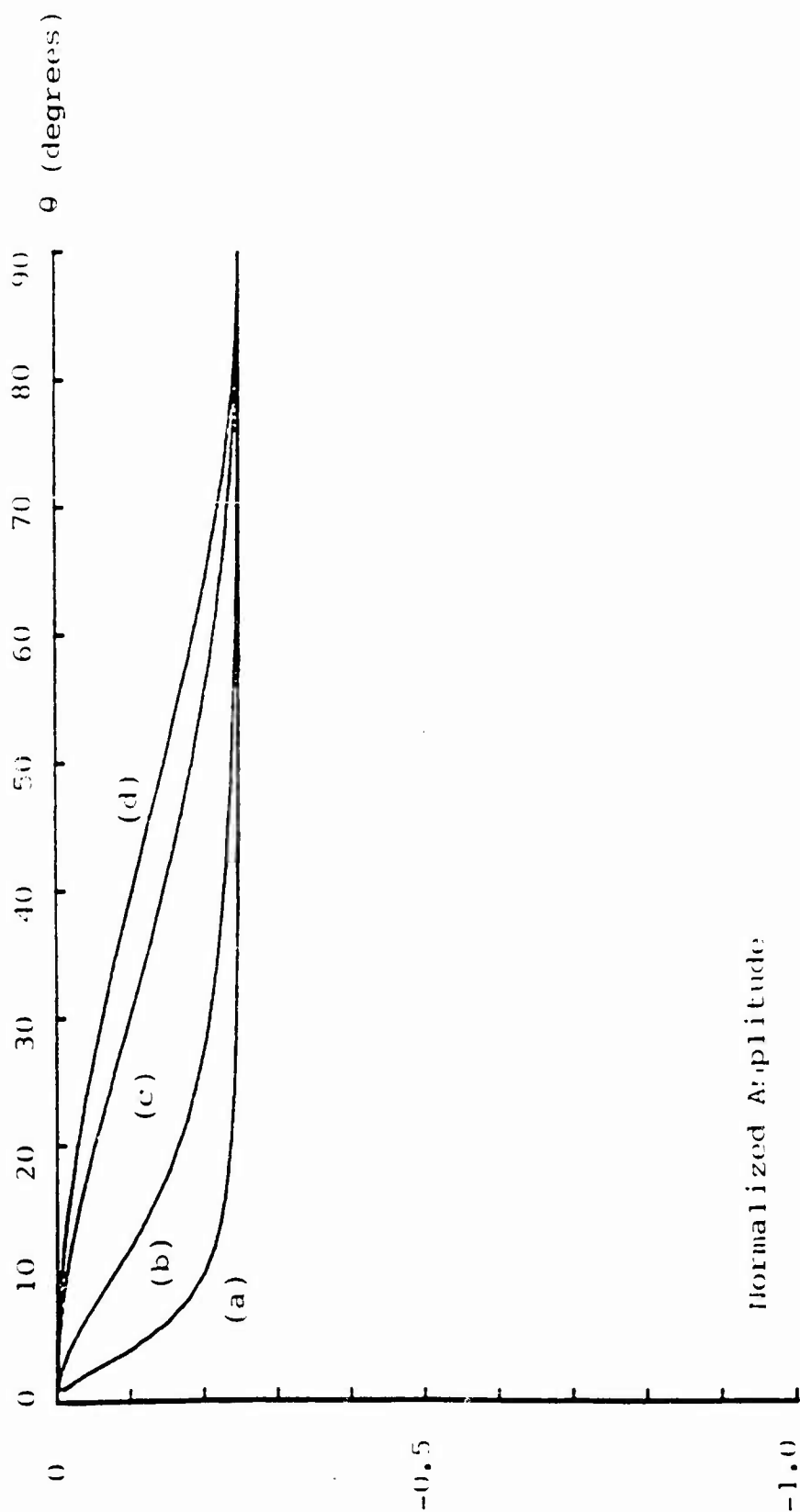


Fig. IV-9. Amplitude of birefringent terms (i.e., terms at normalized frequencies of \bar{V}_B , $\bar{V}_R - \bar{V}_B$, $\bar{V}_R + \bar{V}_B$) vs the state of polarization rotation parameter, θ , for a re-entrant rotation sensor operated in the cross-polarized mode with external polarizers. The curves are described by the linear birefringence parameters, ξ : (a) 10 degrees, (b) 30 degrees, (c) 90 degrees, and (d) 180 degrees.

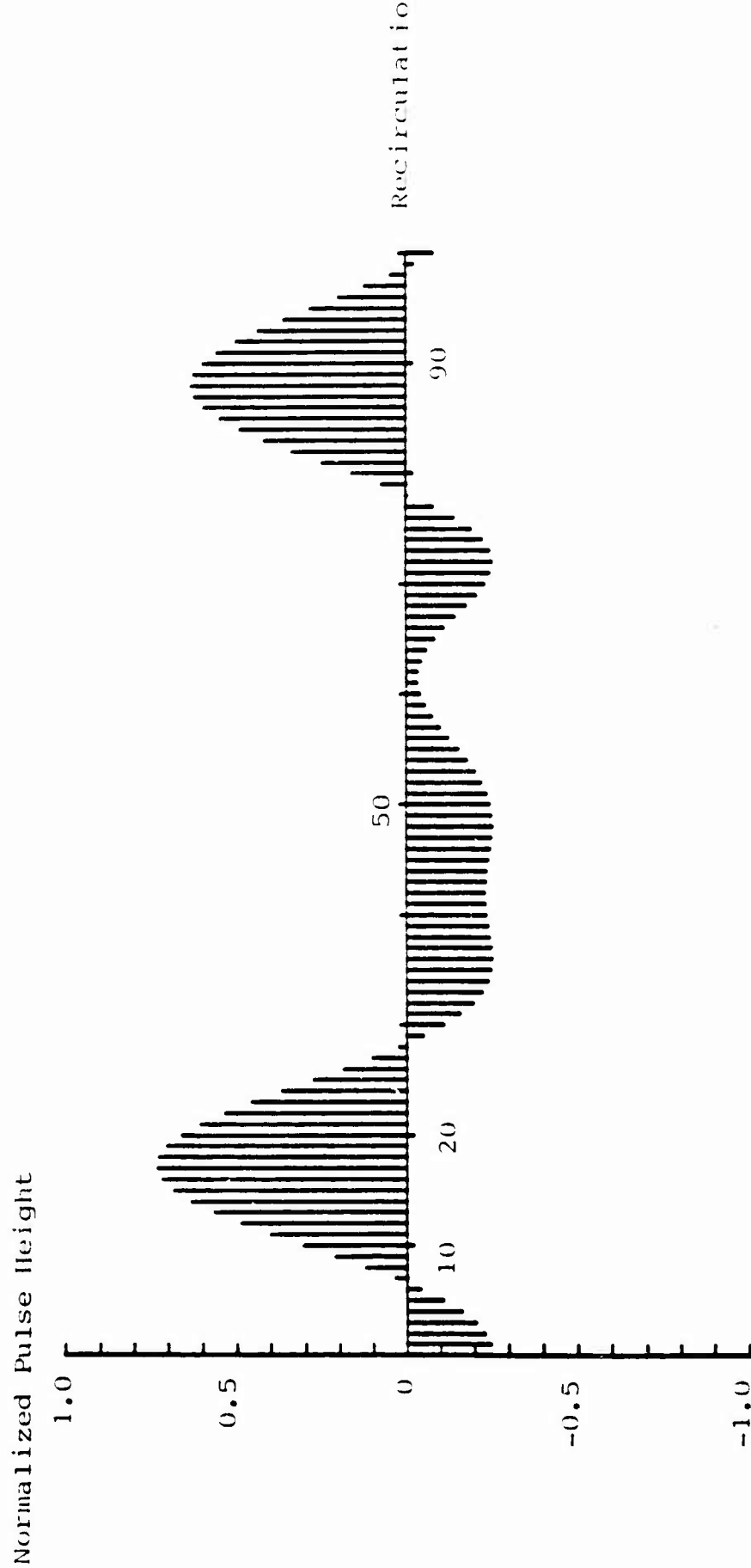


Fig. IV-10a. Normalized pulse height vs recirculations for a 90 degree phase biased re-entrant rotation sensor operated in the cross-polarized mode with external polarizers. The birefringent parameters are: $\theta = 5$ degrees, $\xi = 0$ degrees, and $\phi = 0$ degrees. The DC level has been suppressed.

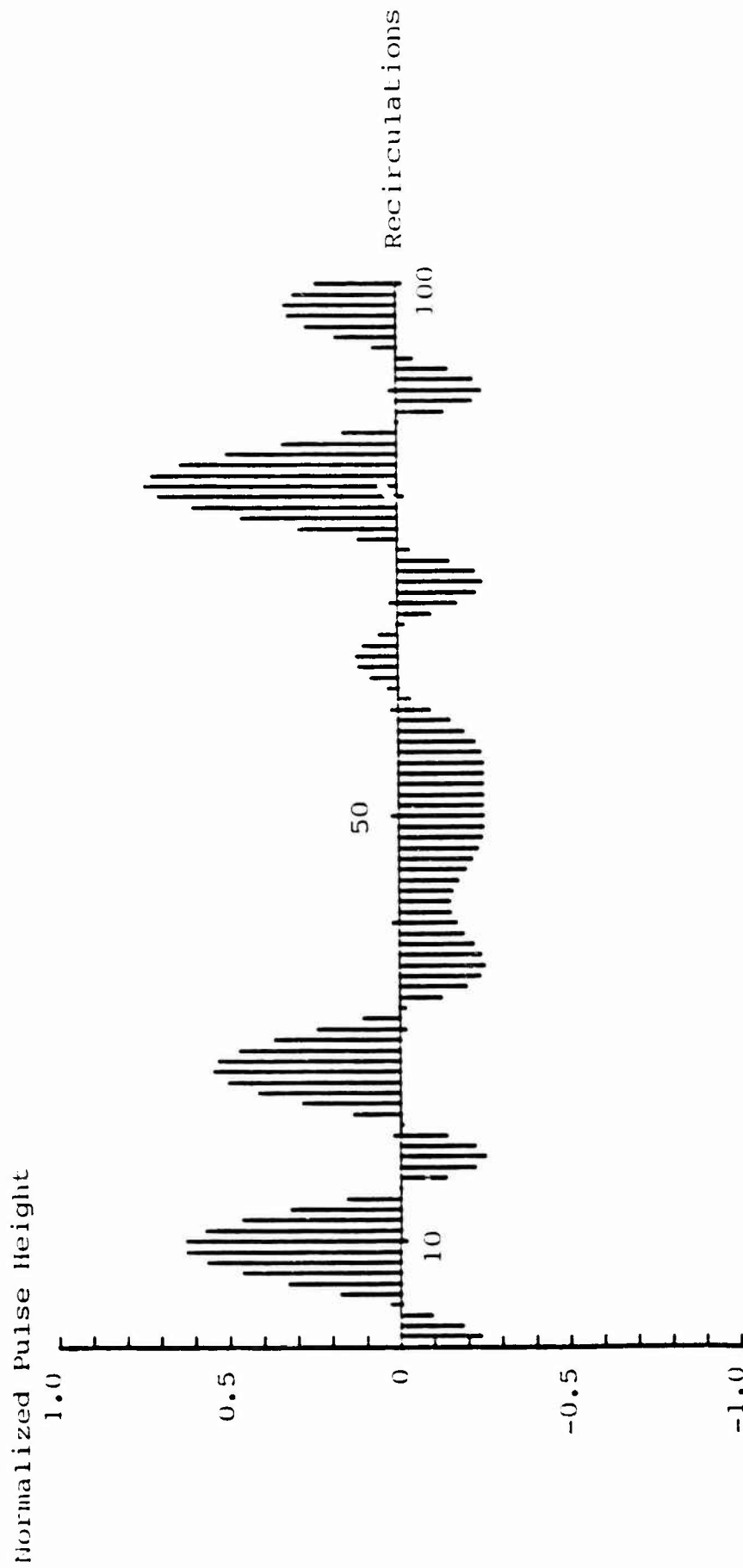


Fig. IV-10b. Normalized pulse height vs recirculations for a 90 degree phase biased re-entrant rotation sensor operated in the cross-polarized mode with external polarizers. The birefringent parameters are: $\theta = 10$ degrees, $\xi = 0$ degrees, and $\phi = 0$ degrees. The DC level has been suppressed.

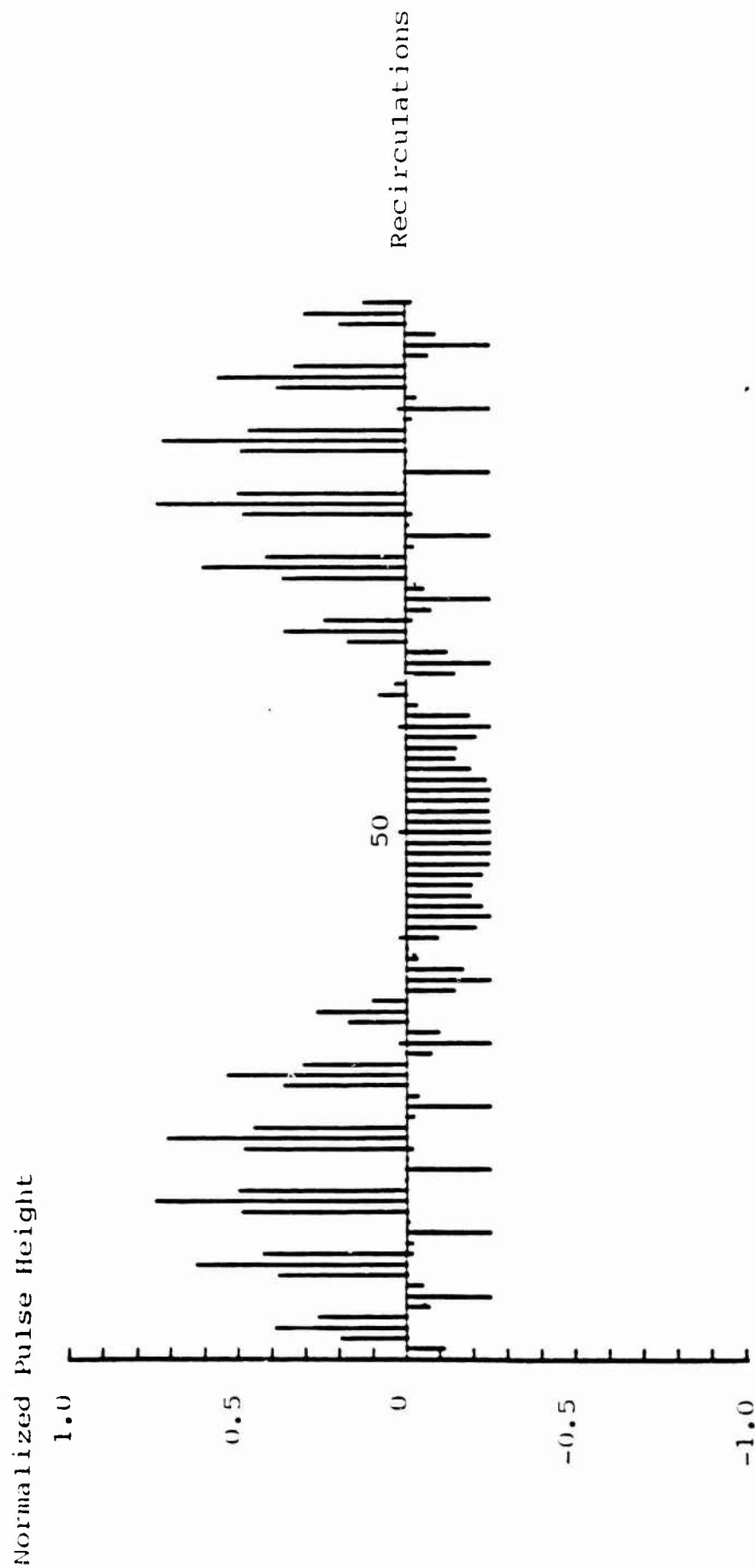


Fig. IV-10c. Normalized pulse height vs recirculations for a 90 degree phase biased re-entrant rotation sensor operated in the cross-polarized mode with external polarizers. The birefringent parameters are: $\theta = 30$ degrees, $\xi = 0$ degrees, and $\phi = 0$ degrees. The DC level has been suppressed.

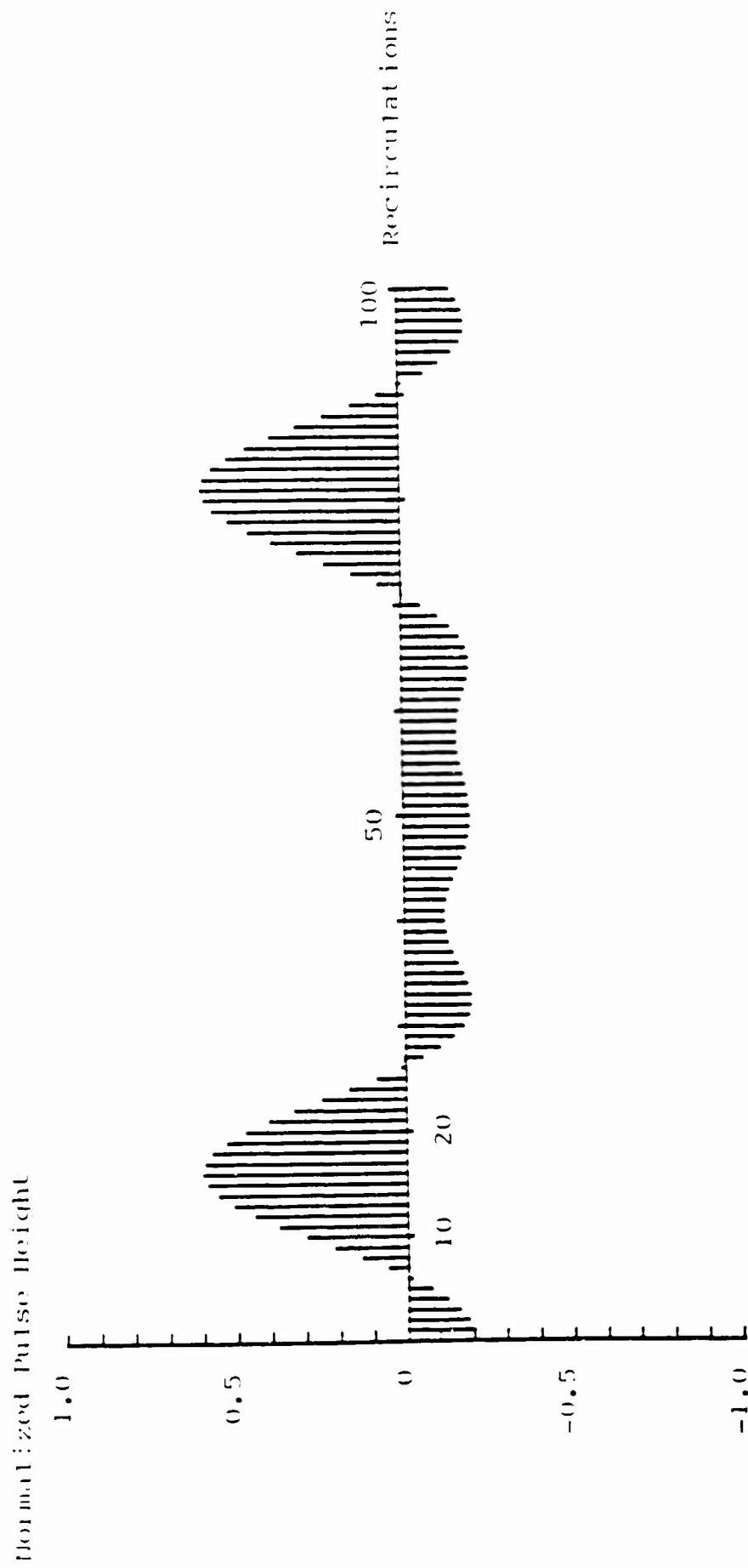


Fig. IV-11a. Normalized pulse height vs recirculations for a 90 degree phase biased re-entrant rotation sensor operated in the cross-polarized mode with external polarizers. The birefringent parameters are: $\theta = 5$ degrees, $\xi = 5$ degrees, and $\phi = 0$ degrees. The DC level has been suppressed.

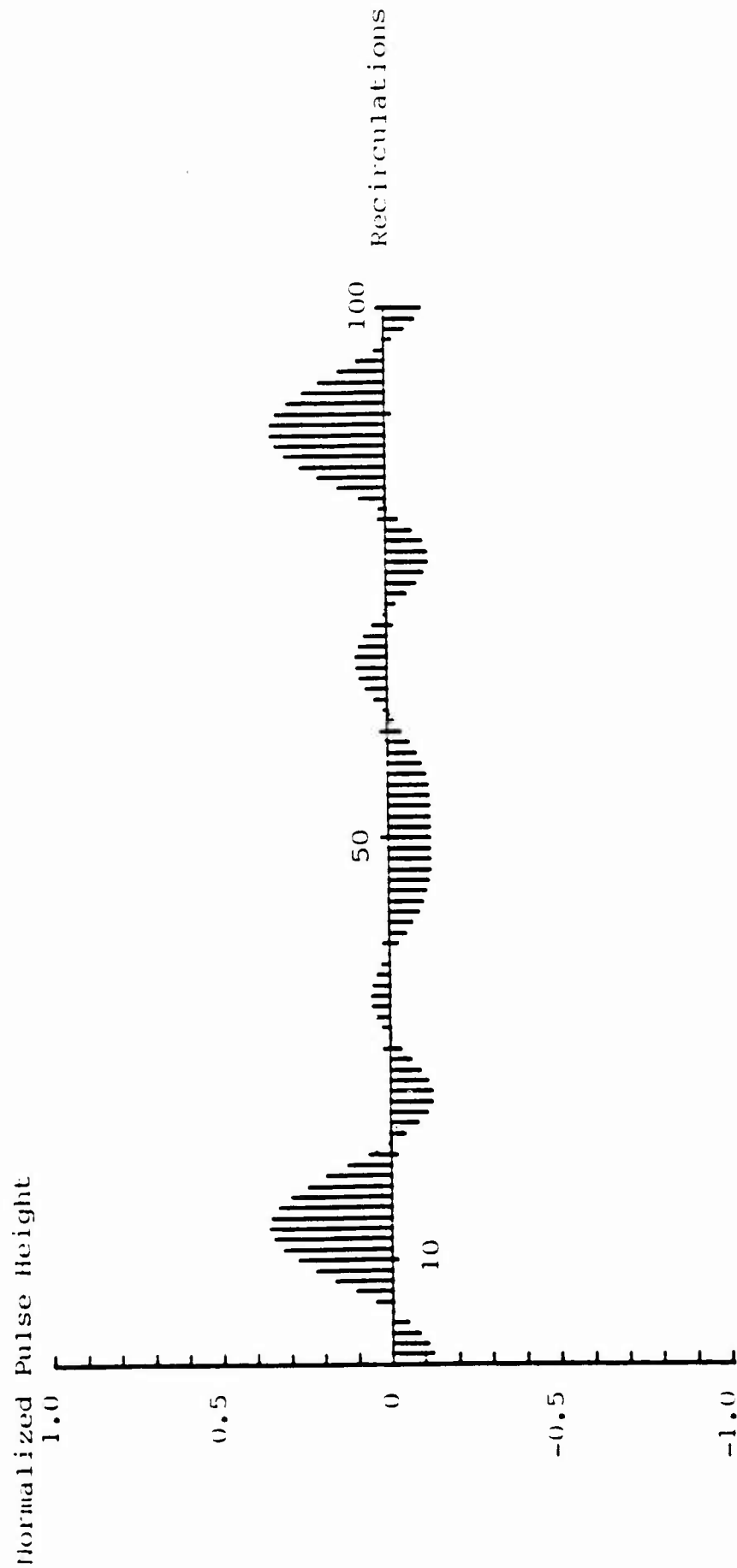


Fig. IV-11b. Normalized pulse height vs recirculations for a 90 degree phase biased re-entrant rotation sensor operated in the cross-polarized mode with external polarizers. The birefringent parameters are: $\theta = 5$ degrees, $\xi = 10$ degrees, and $\phi = 0$ degrees. The DC level has been suppressed.

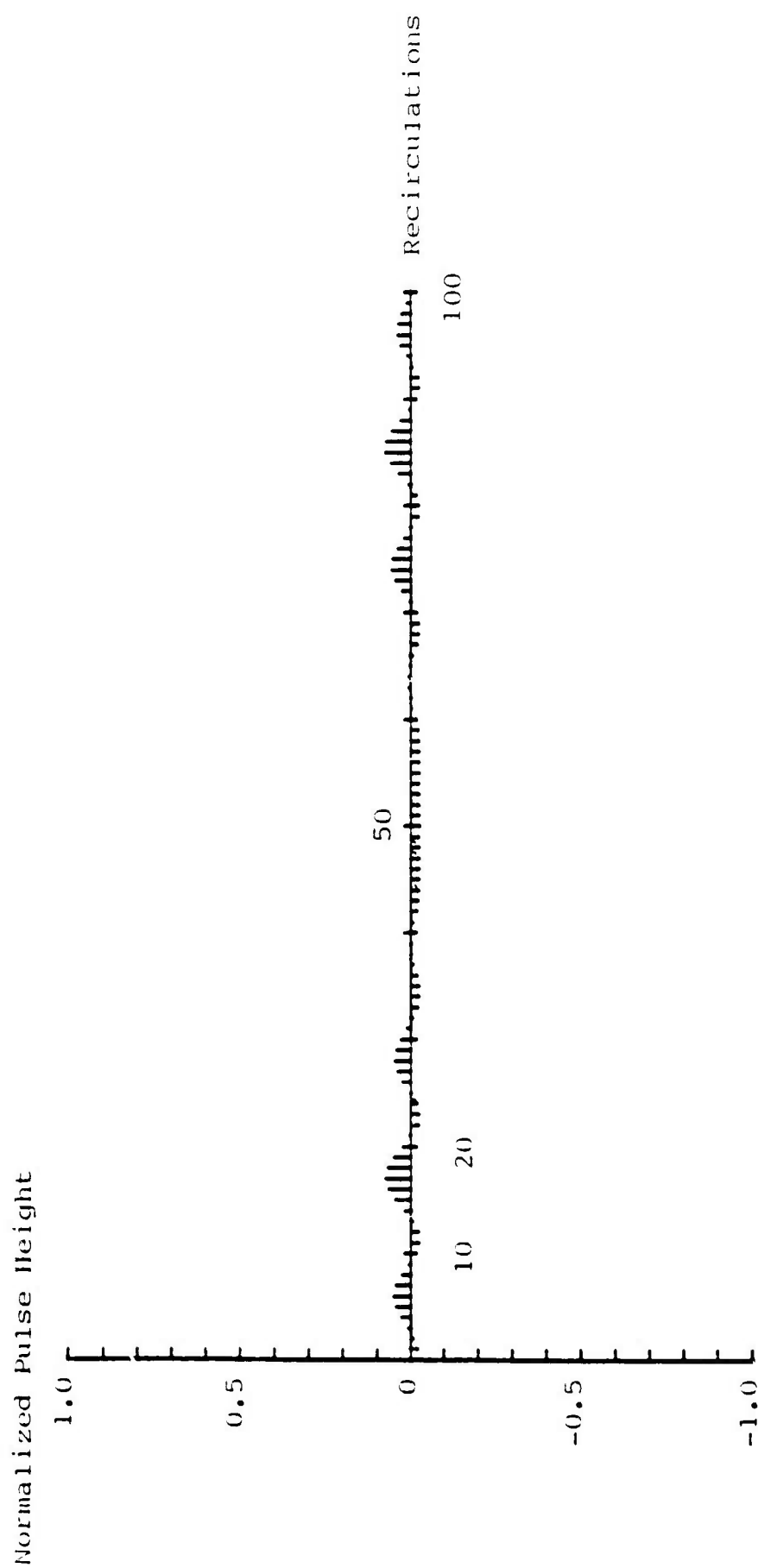


Fig. IV-11c. Normalized pulse height vs recirculations for a 90 degree phase biased re-entrant rotation sensor operated in the cross-polarized mode with external polarizers. The birefringent parameters are: $\theta = 5$ degrees, $\xi = 30$ degrees, and $\phi = 0$ degrees. The DC level has been suppressed.

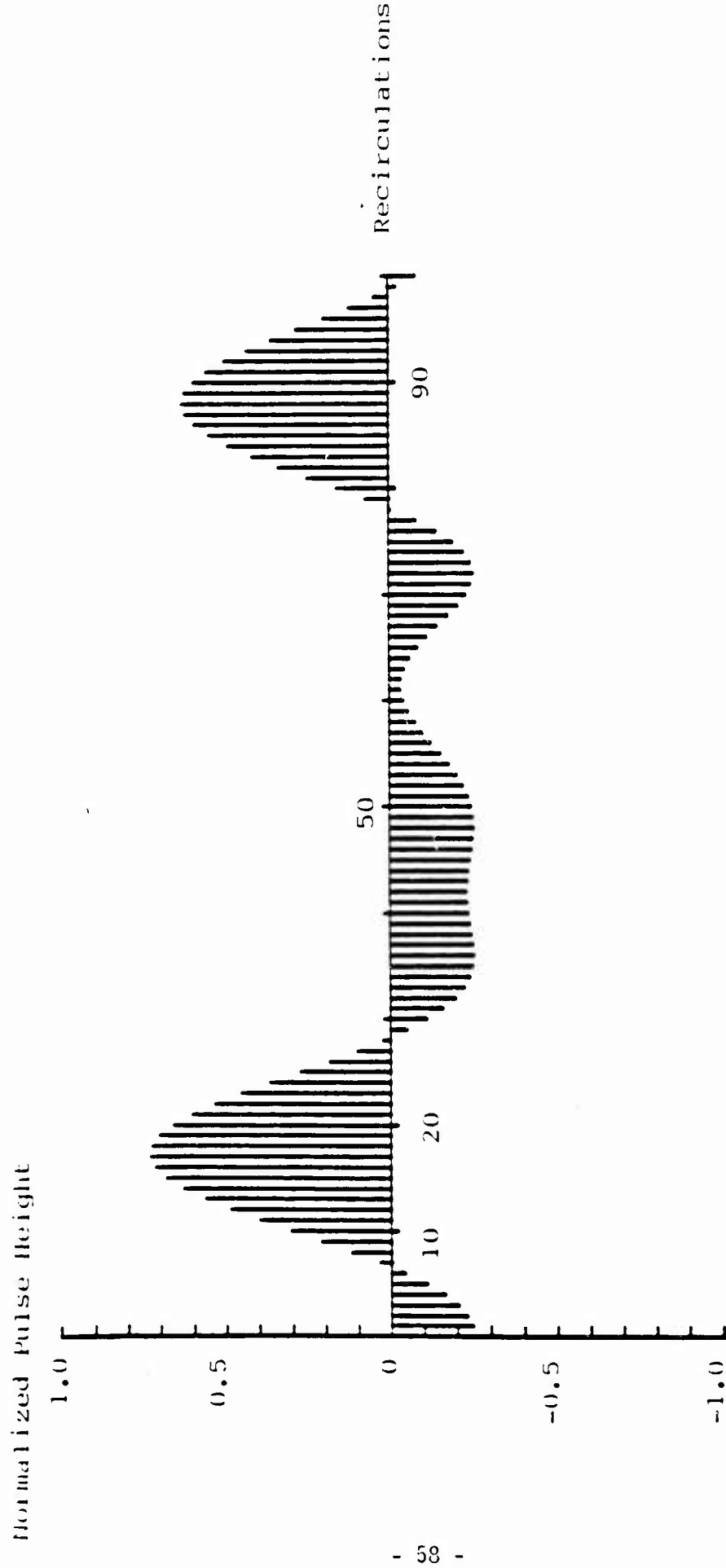


Fig. IV-12a. Normalized pulse height vs recirculations for a 90 degree phase biased re-entrant rotation sensor operated in the cross-polarized mode with external polarizers. The birefringent parameters are: $\theta = 5$ degrees, $\xi = 0$ degrees, and $\phi = 10$ degrees. The DC level has been suppressed.

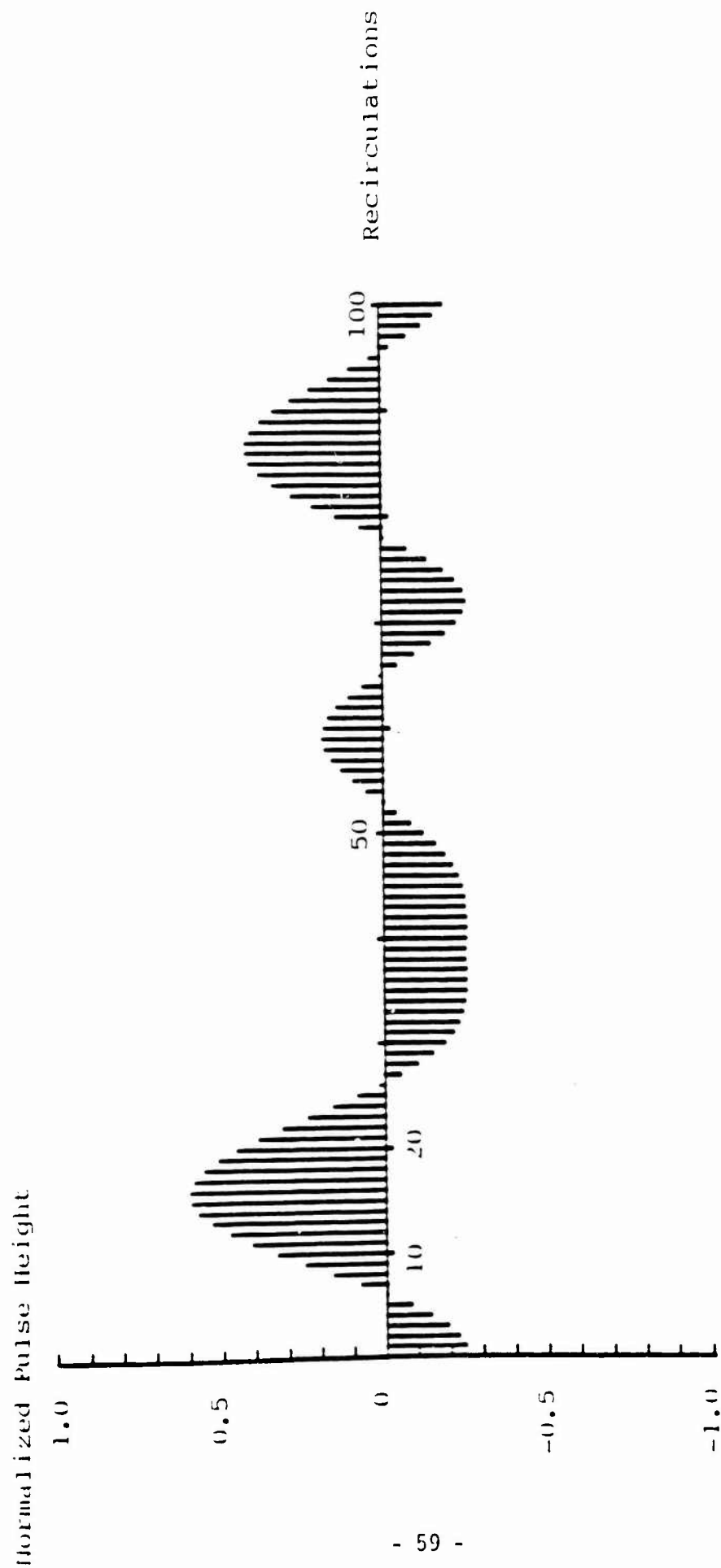


Fig. IV-12b. Normalized pulse height vs recirculations for a 90 degree phase biased re-entrant rotation sensor operated in the cross-polarized mode with external polarizers. The birchfringent parameters are: $\theta = 5$ degrees, $\xi = 0$ degrees, and $\phi = 45$ degrees. The DC level has been suppressed.

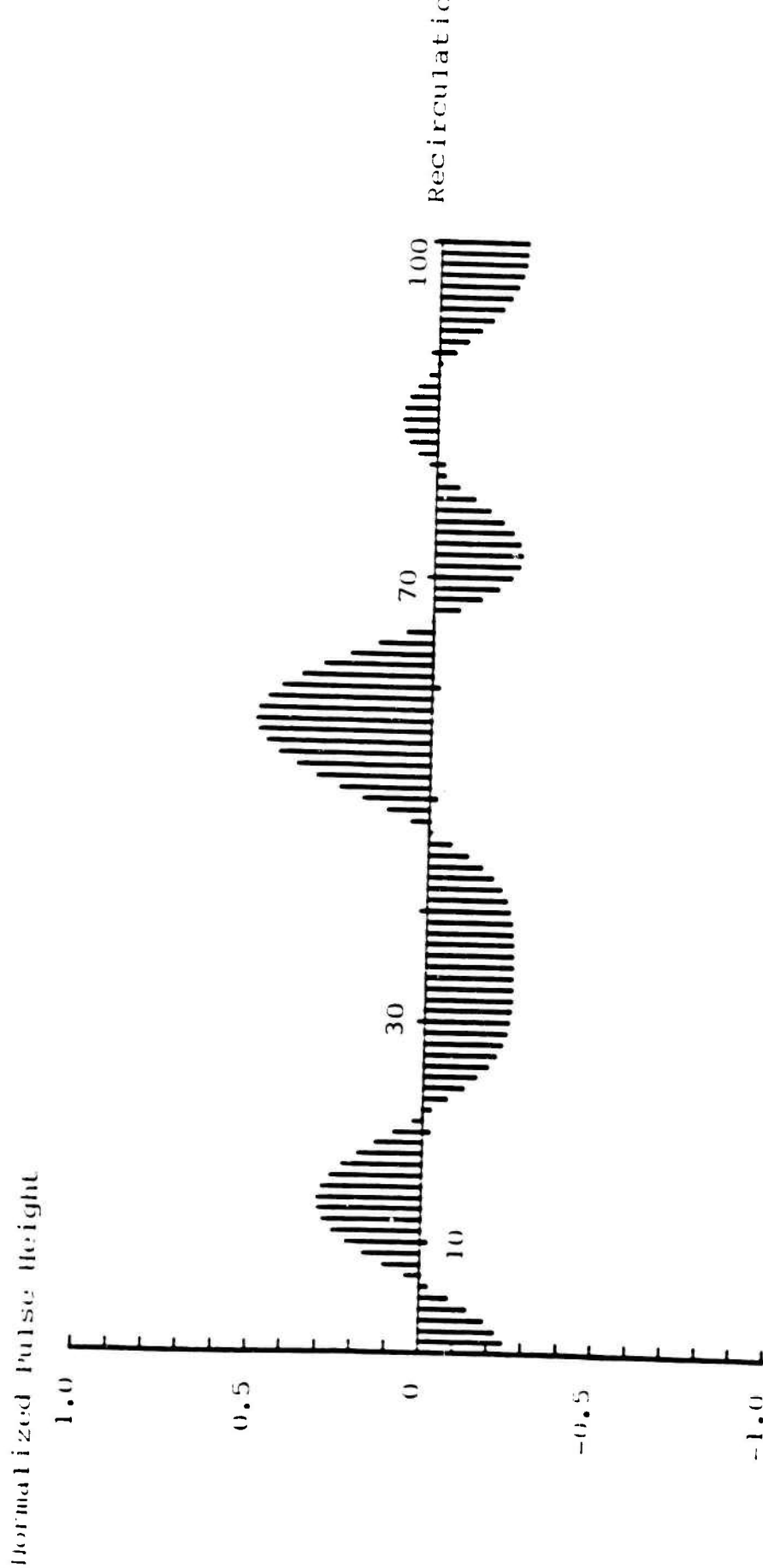


Fig. IV-12c. Normalized pulse height vs recirculations for a 90 degree phase biased re-entrant rotation sensor operated in the cross-polarized mode with external polarizers. The birefringent parameters are: $\theta = 5$ degrees, $\xi = 0$ degrees, and $\phi = 90$ degrees. The DC level has been suppressed.

intensity for this configuration is the sum of the copolarized and crosspolarized configurations. The normalized intensity, \bar{I}_K is the sum of Eqs. IV-15 and IV-18.

$$\bar{I}_K = \bar{I}_K^{(x)} + \bar{I}_K^{(y)} \quad (IV-19)$$

\bar{I}_K approaches the ideal response when θ is around zero and is around 180 degrees because $\bar{I}_K^{(y)}$ goes to zero and $\bar{I}_K^{(x)}$ goes to the ideal response. Figures IV-13a and b, show the pulse trains for small θ and for ξ equal to zero. The pulse trains are highly distorted. In Figs. IV-14a and b, the pulse trains are shown for the same value of θ as in Fig. IV-13, but the linear birefringence, ξ , increases. For $\xi = 10$ (Fig. IV-14a), the pulse train is less distorted. For $\xi = 90$ (Fig. IV-14b), the pulse train appears to be ideal. Figures IV-15a and b, show the pulse train for a reciprocal birefringent dependent phase shift (ϕ) of 90 degrees and a low value of θ . A large amount of linear birefringence removes the distortion of the pulse train (Fig. IV-15b).

It can be concluded from the three configurations examined that some form of polarization control or polarization maintaining fiber is necessary for a re-entrant, pulsed fiber optic rotation sensor to avoid distortion of the pulse train which leads to errors in the measured rotation rate. Major distortions of the pulse train can be caused by small, and linear birefringence parameter, ξ .

4. Copolarized With Internal Polarizer

If the polarizers are placed inside the optical fiber sensing loop the spurious zero crossings are eliminated. An additional loss factor appears which depends on the rotation parameter θ . The loss of the sensing loop is environmentally sensitive. This configuration of a re-entrant, pulsed fiber optic rotation sensor is shown in Fig. IV-1b. The polarizers are oriented to pass the input polarization. The Jones matrix describing this configuration is given in Eq. IV-9b. If the input is linearly

Normalized Pulse Height

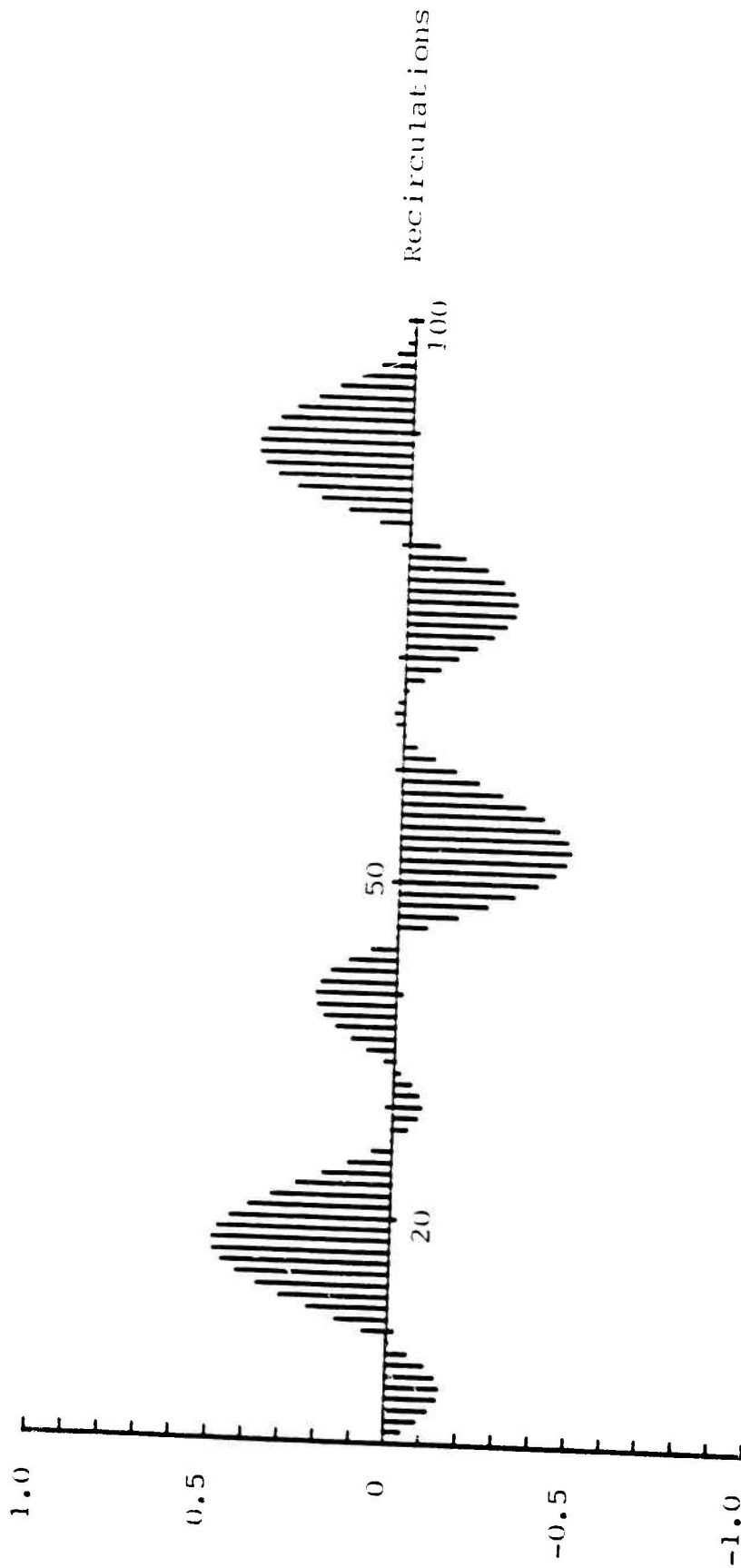


Fig. IV-13a. Normalized pulse height vs recirculations for a 90 degree phase biased re-entrant rotation sensor operated in the no polarizer mode. The birefringent parameters are: $\theta = 5$ degrees, $\xi = 0$ degrees. The DC level has been suppressed.

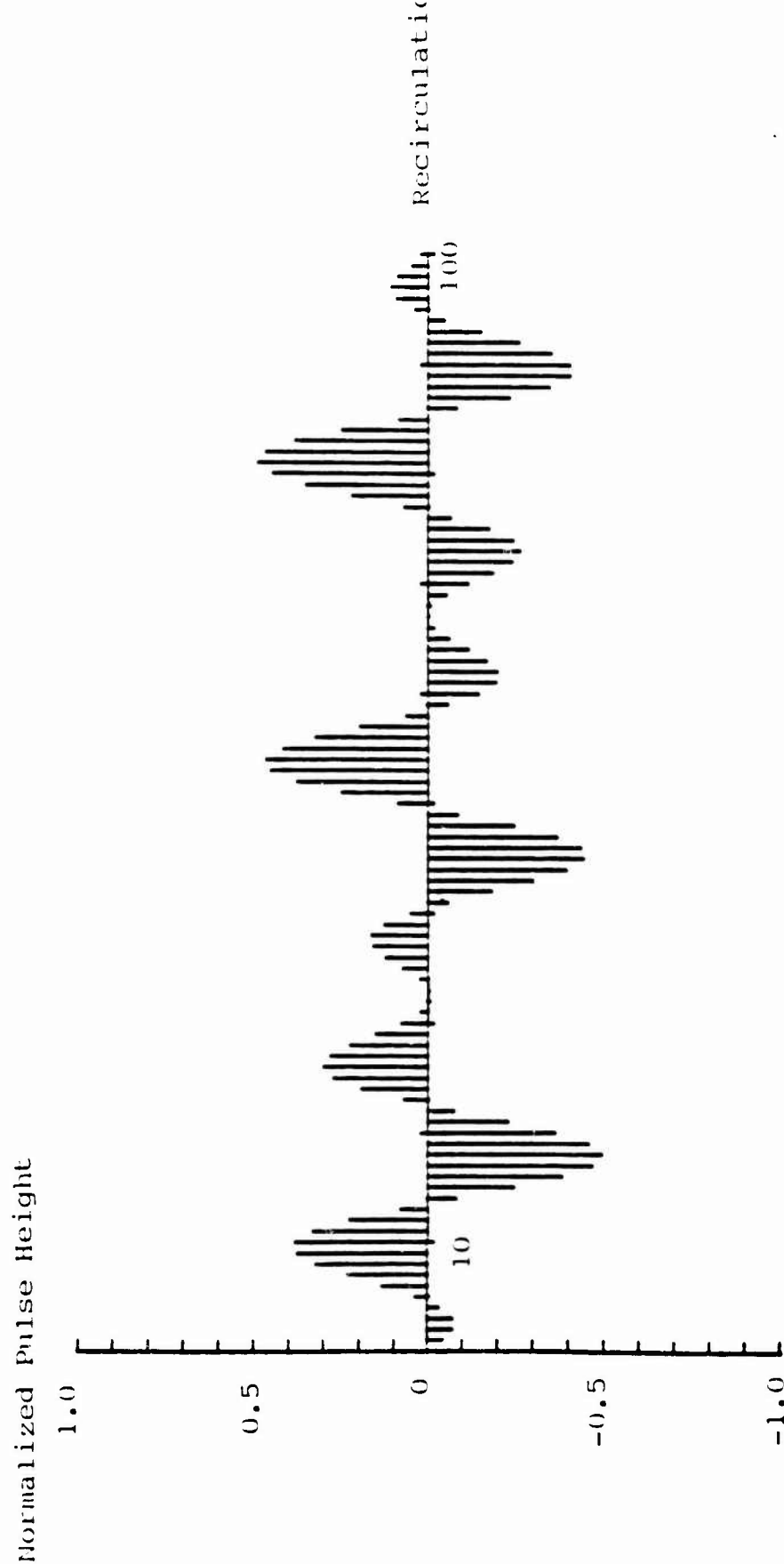


Fig. IV-13b. Normalized pulse height vs recirculations for a 90 degree phase biased re-entrant rotation sensor operated in the no polarizer mode. The birefringent parameters are: $\theta = 10$ degrees, $\xi = 0$ degrees. The DC level has been suppressed.

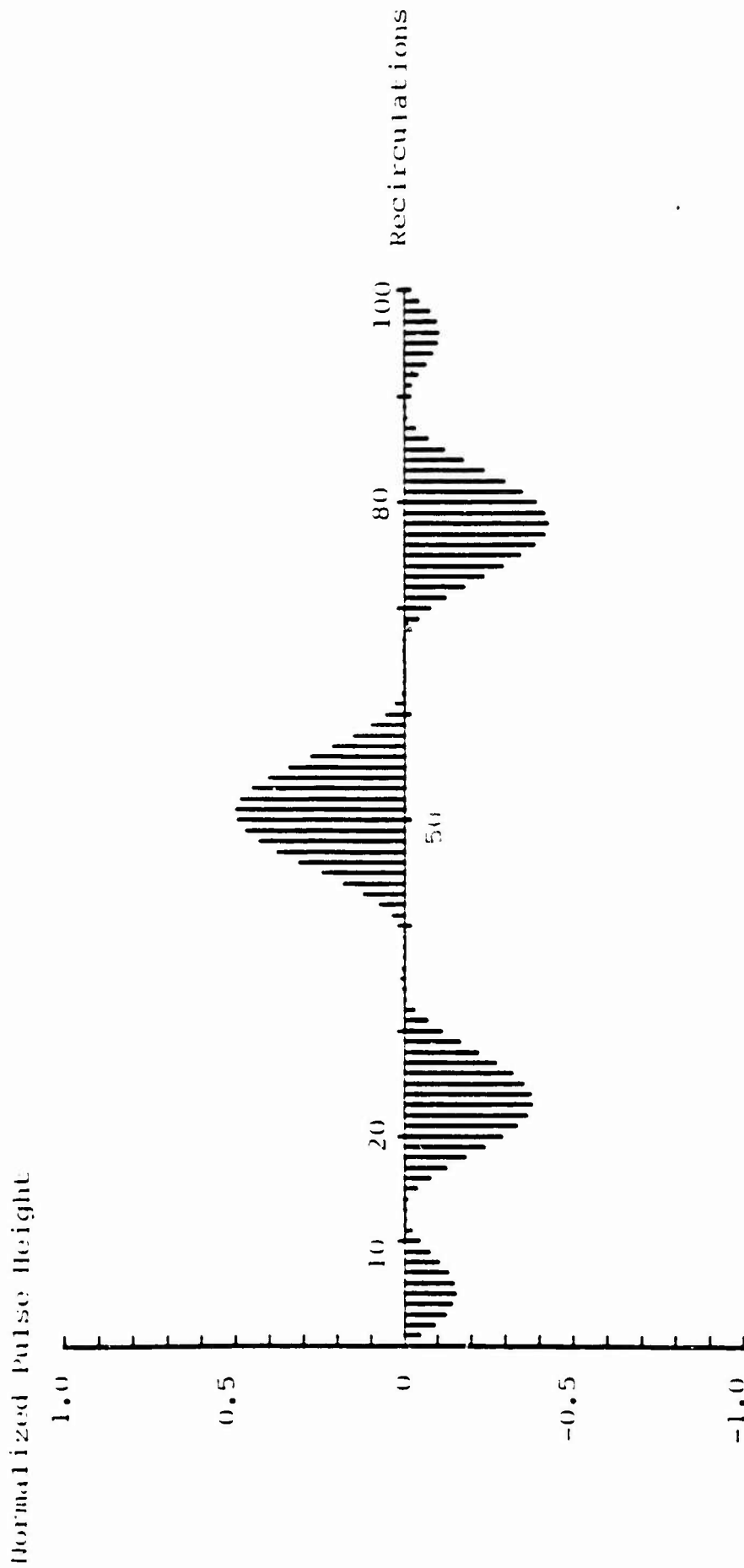


Fig. IV-14a. Normalized pulse height vs recirculations for a 90 degree phase biased re-entrant rotation sensor operated in the no polarizer mode. The birefringent parameters are: $\theta = 5$ degrees, $\xi = 10$ degrees, and $\phi = 0$ degrees. The DC level has been suppressed.

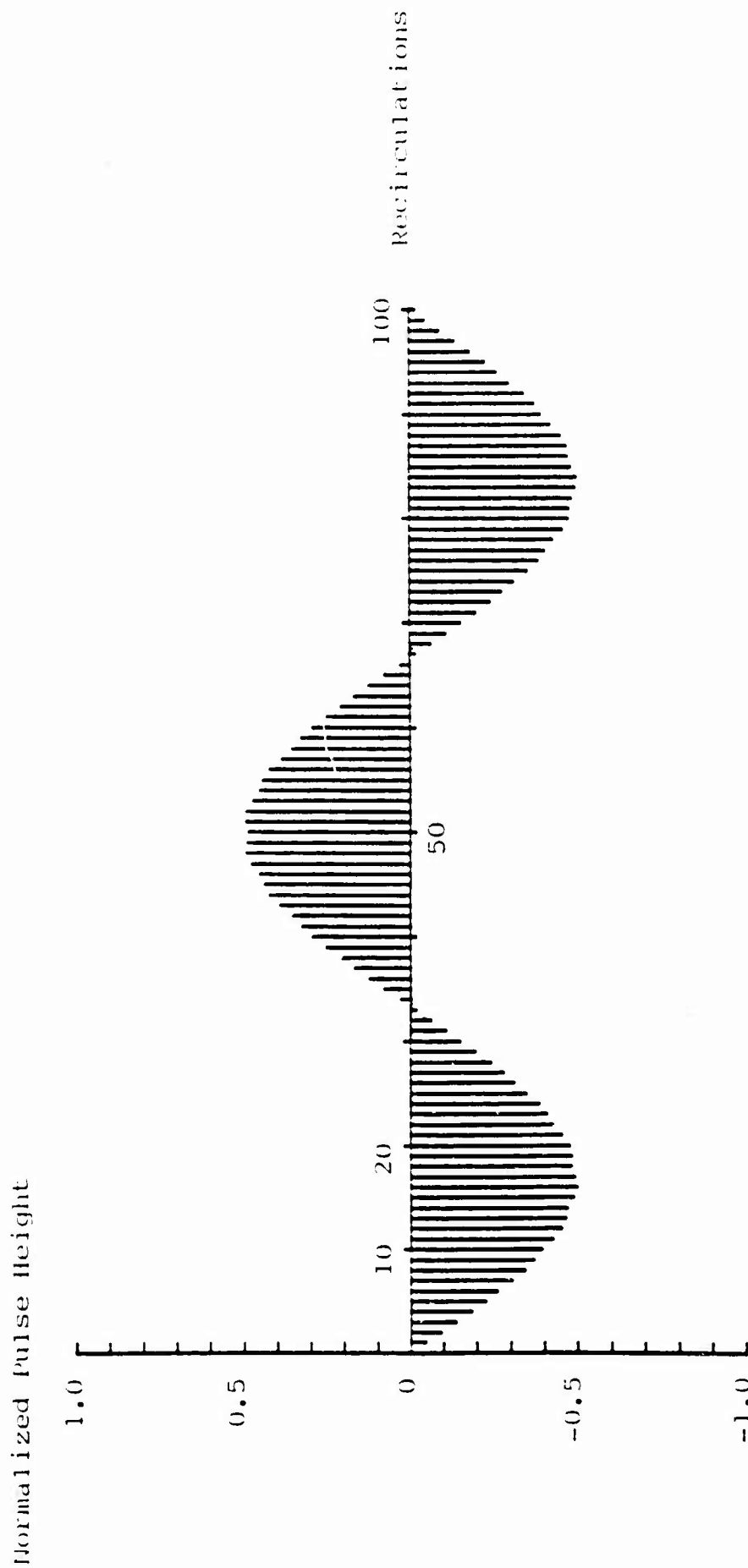


Fig. IV-14b. Normalized pulse height vs recirculations for a 90 degree phase biased re-entrant rotation sensor operated in the 10 polarizer mode. The birefringent parameters are: $\theta = 5$ degrees, $\phi = 90$ degrees, and $\delta = 0$ degrees. The DC level has been suppressed.

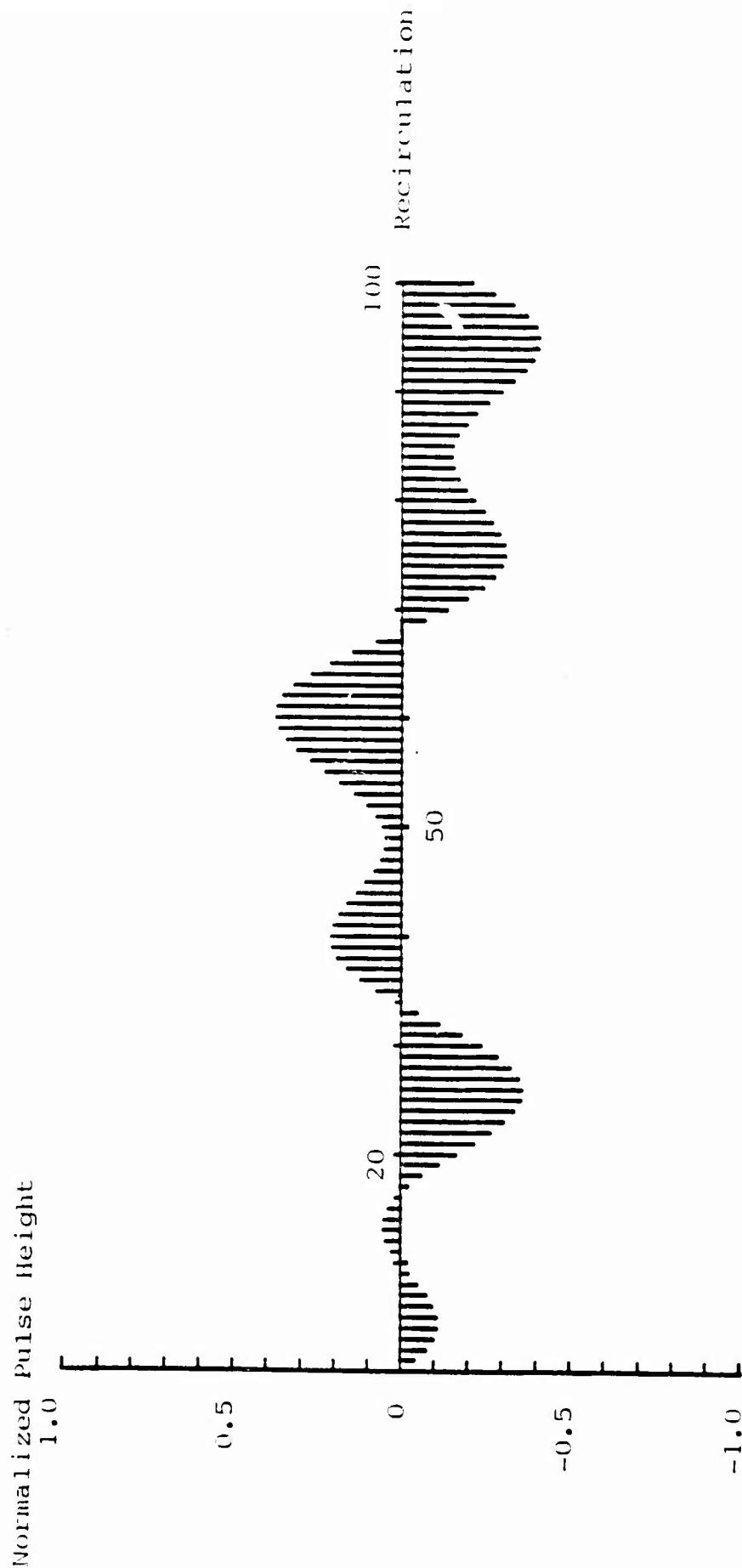


Fig. IV-15a. Normalized pulse height vs recirculations for a 90 degree phase biased re-entrant rotation sensor operated in the no polarizer mode. The birefringent parameters are: $\theta = 5$ degrees, $\xi = 0$ degrees, and $\phi = 90$ degrees. The DC level has been suppressed.

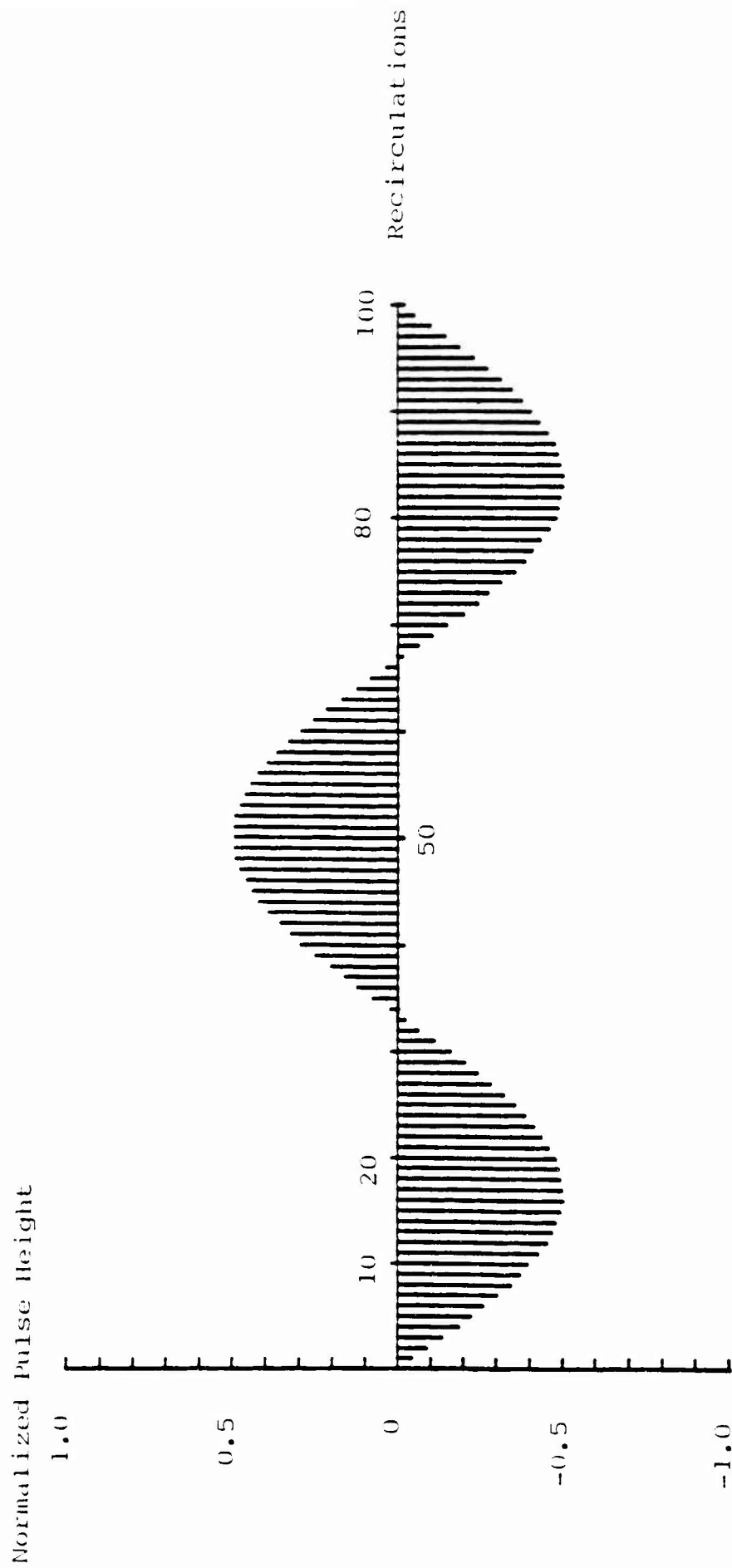


Fig. IV-15b. Normalized pulse height vs recirculations for a 90 degree phase biased re-entrant rotation sensor operated in the no polarizer mode. The birefringent parameters are: $\theta = 5$ degrees, $\xi = 90$ degrees, and $\phi = 90$ degrees. The DC level has been suppressed.

polarized along the x -axis the normalized detected intensity is:

$$\bar{I}_K = 0.5 \cos^2 \theta (1 - \sin 2\pi K \bar{v}_R) \quad (IV - 20)$$

The frequency of the sinusoid which modulates the amplitude of the pulse train is unaffected by the fiber birefringence. The amplitude of the pulses will decay as the number of recirculation increases because of the $\cos^2 \theta$ factor. In Fig. IV-16, the envelope of the pulse train is plotted for zero rotation rate. The curves are parameterized by the rotation parameter, θ . These curves show that θ must be in the range of $[0.5]$ degrees, for the normalized amplitude of the 100^{th} recirculation is more than 55 dB down from the input pulse level. The maximum value of θ for which the last recirculation is within 3dB of the input pulse level depends on the number of recirculations. For 1000 recirculations, θ must be less than 1.5 degrees. Polarization control or polarization maintaining fiber is required for use of this configuration as a practical rotation sensor.

5. Unpolarized

In this configuration and mode of operation the input light is unpolarized. The rotation sensor configuration is shown in Fig. IV-1a. The normalized detected intensity of the K^{th} recirculation is:

$$\begin{aligned} \bar{I}_K^{(u)} = & 0.5 - 0.5 \left[1 - 2|A|^2 \left[\left((B - C)/N_+ \right)^2 \right. \right. \\ & \left. \left. + \left((B + C)/N_- \right)^2 \right] \cos^2(\phi/2) \right] \sin 2\pi K \bar{v}_R \\ & + [|A|^2 (B^2 - C^2)/(N_+ N_-)] \cos^2(\phi/2) \\ & \times [\sin 2\pi K (\bar{v}_R + \bar{v}_B) + \sin 2\pi K (\bar{v}_R - \bar{v}_B)] \end{aligned} \quad (IV - 21)$$

where all the quantities have been defined previously. The DC level is independent of the parameters θ and ϕ . For polarized input light the DC level depended on these parameters. Three normalized frequencies, \bar{v}_R , $\bar{v}_R + \bar{v}_B$ and $\bar{v}_R - \bar{v}_B$ are present for

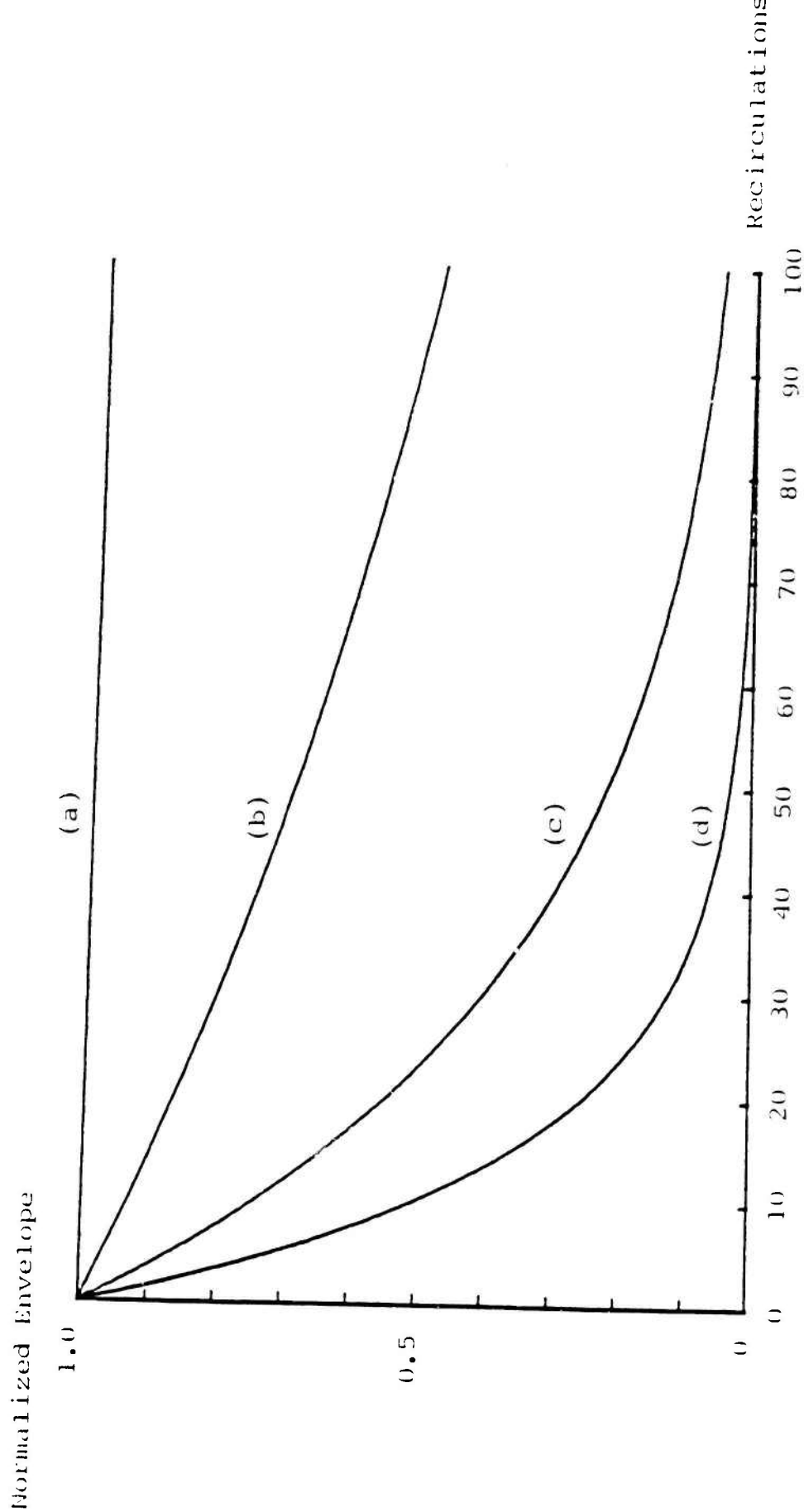


Fig. IV-16. Normalized envelope of pulses vs recirculations for a re-entrant rotation sensor operated in the co-polarized mode with internal polarizers. The curves are described by the state of polarization rotation parameter, θ : (a) 1 degree, (b) 5 degrees, (c) 10 degrees, and (d) 15 degrees.

unpolarized input light. For polarized input light, four normalized frequencies were present.

If the birefringent dependent phase shift parameter, ϕ , equals 180 degrees, then the sum and difference frequencies are not present in the normalized intensity which is then independent of the rotation parameter θ , and the linear birefringence parameter ξ . The environmental sensitivity of the fiber can be reduced by placing a controllable, reciprocal birefringent dependent phase shifter in the optical fiber sensing loop. The spectrum of the normalized pulse trains will have three frequency components. Adjust the reciprocal birefringent dependent phase shifter so that only the central frequency component is nonzero. The reciprocal birefringent dependent phase shift around the loop will be 180 degrees. The detected intensity will be environmentally insensitive. Feedback is required to maintain the reciprocal birefringent dependent phase shift at 180 degrees.

In Figs. IV-17, IV-18 and IV-19, the normalized detected intensity less the DC level is plotted versus the number of recirculations, in each figure, one of the three parameters, θ , ξ or ϕ is varied while the other two remain constant. In Fig. IV-17, θ is varied, in Fig. IV-18 ξ is varied, and in Fig. IV-19 ϕ is varied. The undistorted pulse train is shown in Fig. IV-17a. The normalized rotation frequency, $\bar{\nu}_R$, is 3/200. As the rotation parameter θ increases, extra zero crossings are introduced (Figs. IV-17b, c, d). These extra zero crossings result in errors in the measured rotation rate and the angle turned through. To avoid these spurious zero crossings, θ must be restricted to the range $[0, \theta_{\max}]$. Given the parameters of Figs. IV-17, θ_{\max} is less than 1 degree. It will be seen that θ_m is independent of the number of recirculations. In Fig. IV-18a, the pulse train is shown for $\theta = 5$ degrees, $\phi = \xi = 0$. This figure is identical to Fig. IV-17c. As the linear birefringence parameter increases (Fig. IV-18b, c, d), the extra zero crossings disappear. In Fig. IV-18d, when the birefringence parameter, ξ , equals 90 degrees, the pulse train distortion is quite small. This occurs

only when the rotation parameter is small. In Fig. IV-19a, the pulse train is shown for $\theta = \xi = 5$ degrees. As the reciprocal birefringent dependent phase shift, ϕ , increases (Figs. IV-19b, c, d) the extra zero crossing disappear and the distortion decreases. For $\phi = 180$ degrees, no distortion is present, regardless of the values of θ and ξ .

6. Partially Polarized

Most light sources produce partially polarized light and most optical components exhibit some degree of polarization selectivity, hence the operation of a re-entrant, pulsed fiber optic rotation sensor using partially polarized input light is examined. A partially polarized light wave can be expressed as the sum on an intensity basis of a polarized and an unpolarized light wave. The polarized light wave is assumed to have x -linear polarization. The normalized detected intensity for partially polarized input light is the weighted sum of the normalized detected intensities for the unpolarized (Eq. IV - 21) and the nonpolarizer (Eq. IV - 19) configurations. The weighting factors depend on the degree of polarization, P . The normalized detected intensity for K^{th} recirculation, $\bar{I}_K^{(p)}$ is:

$$\bar{I}_K^{(p)} = P(\bar{I}_K^{(x)} + \bar{I}_K^{(y)}) + (1 - P)\bar{I}_K^{(u)} \quad (IV - 22)$$

where $\bar{I}_K^{(x)}$, $\bar{I}_K^{(y)}$ and $\bar{I}_K^{(u)}$ are given in Eqs. IV - 15, IV - 18 and IV - 21 respectively. The intensity $\bar{I}_K^{(p)}$ contains normalized frequency components of \bar{v}_R , \bar{v}_B , $\bar{v}_R - \bar{v}_B$ and $\bar{v}_R + \bar{v}_B$. The normalized detected intensity $\bar{I}_K^{(p)}$ approaches the ideal response for the rotation parameter, θ , being small and the linear birefringence parameter near 180 degrees, regardless of the degree of the polarization P . It can be concluded that for no polarizers in a re-entrant system, the detected intensity approaches the ideal response for θ small and ξ near 180 degrees regardless of input state and degree of polarization.

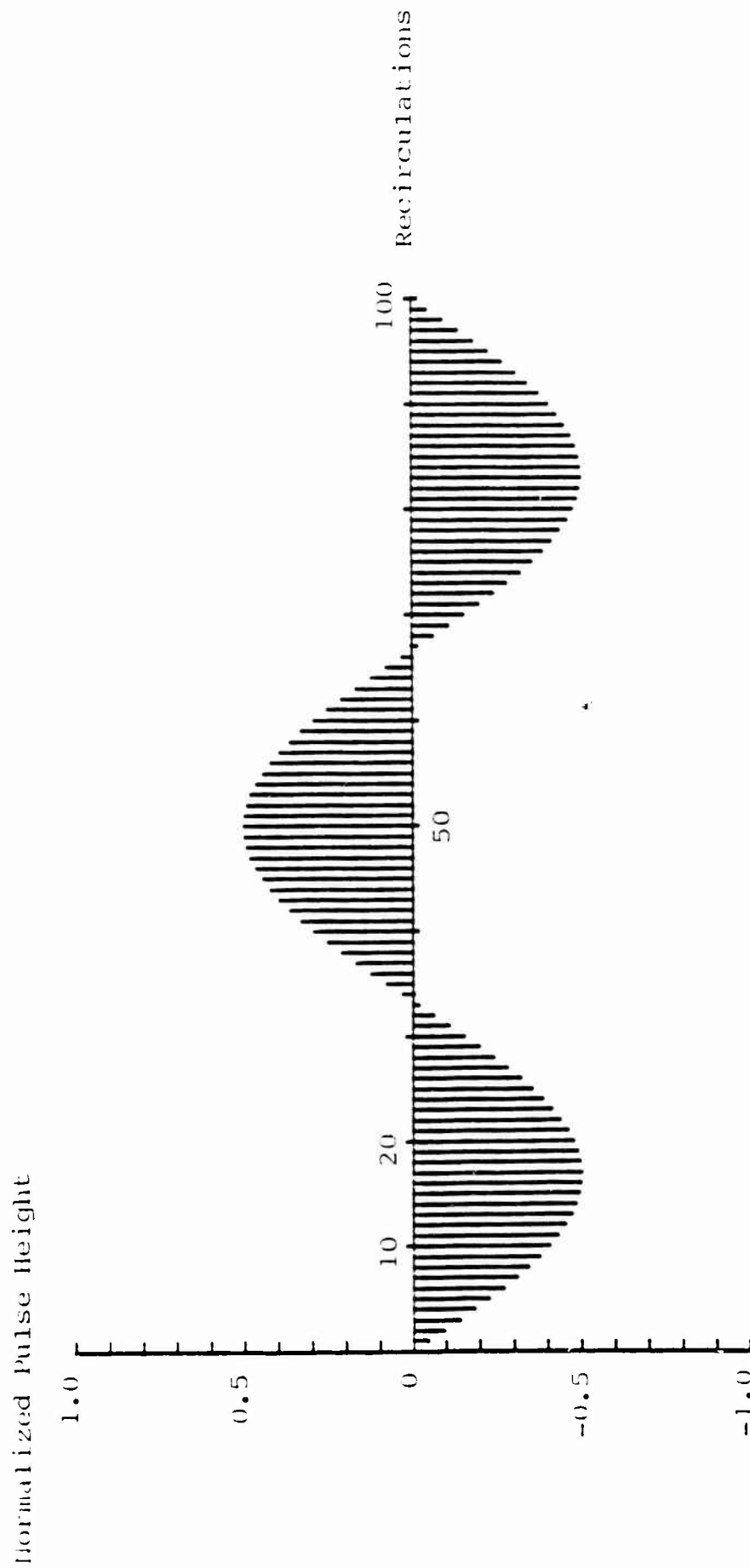


Fig. IV-17a. Normalized pulse height vs recirculations for a 90 degree phase biased re-entrant rotation sensor operated in the unpolarized mode. The birefringent parameters are: $\theta = \xi = \emptyset = 0$ degrees. The DC level has been suppressed.

Normalized Pulse Height

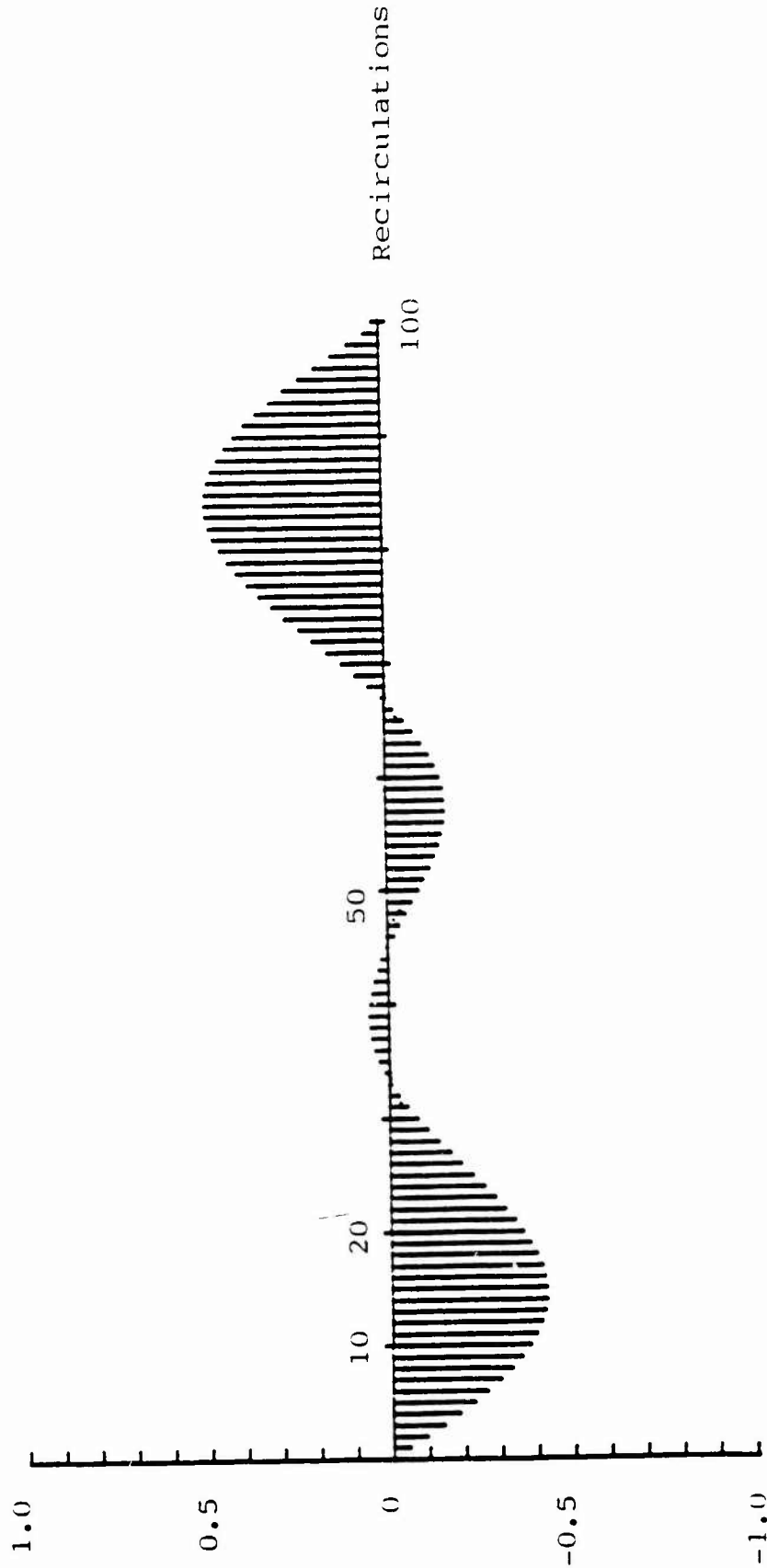


Fig. IV-17b. Normalized pulse height vs recirculations for a 90 degree phase biased re-entrant rotation sensor operation in the unpolarized mode. The birefringent parameters are: $\theta = 1$ degree, $\xi = 0$ degrees. The DC level has been suppressed.

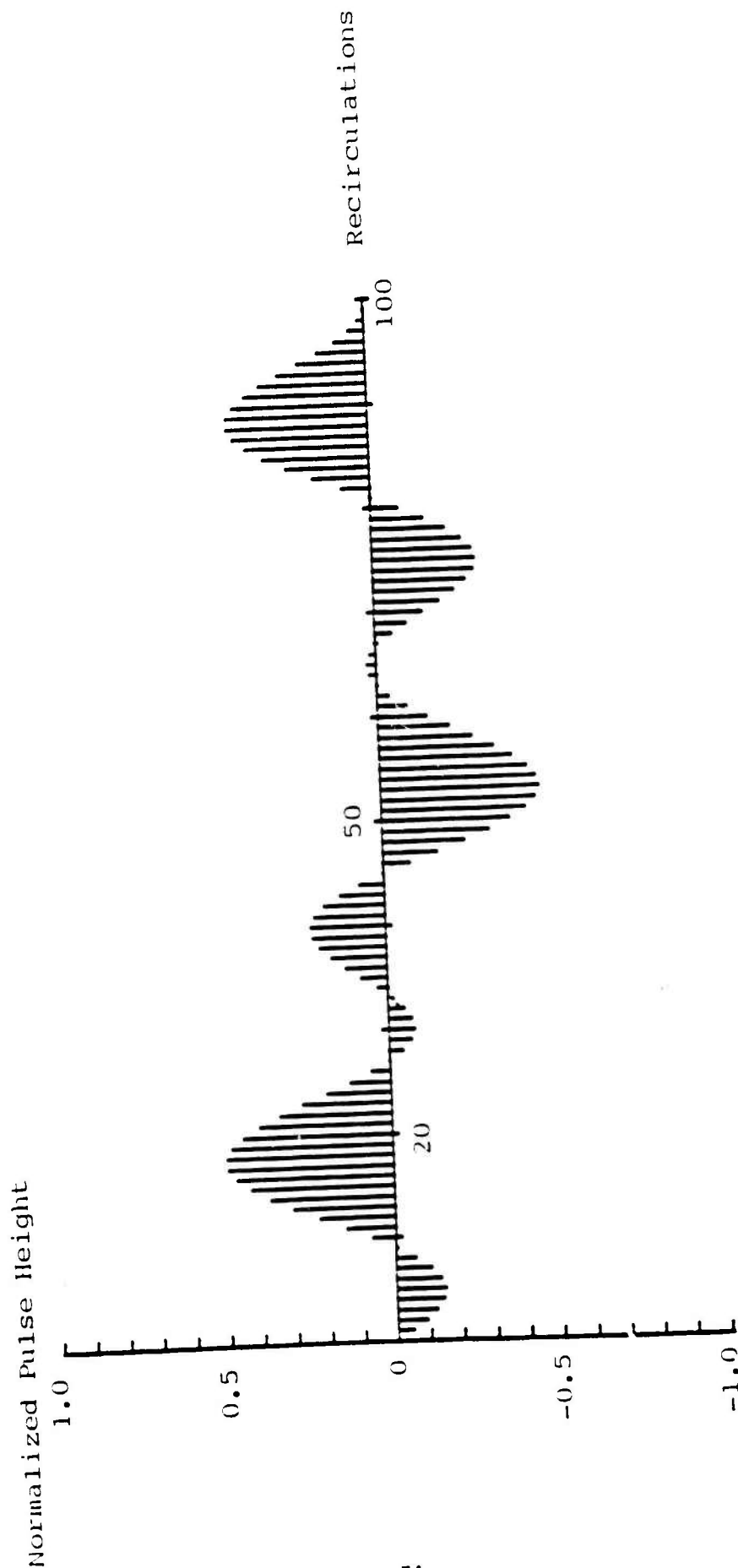


Fig. IV-17c. Normalized pulse height vs recirculations for a 90 degree phase biased re-entrant rotation sensor operated in the unpolarized mode. The birefringent parameters are: $\theta = 5$ degrees, $\xi = 0$ degrees. The DC level has been suppressed.

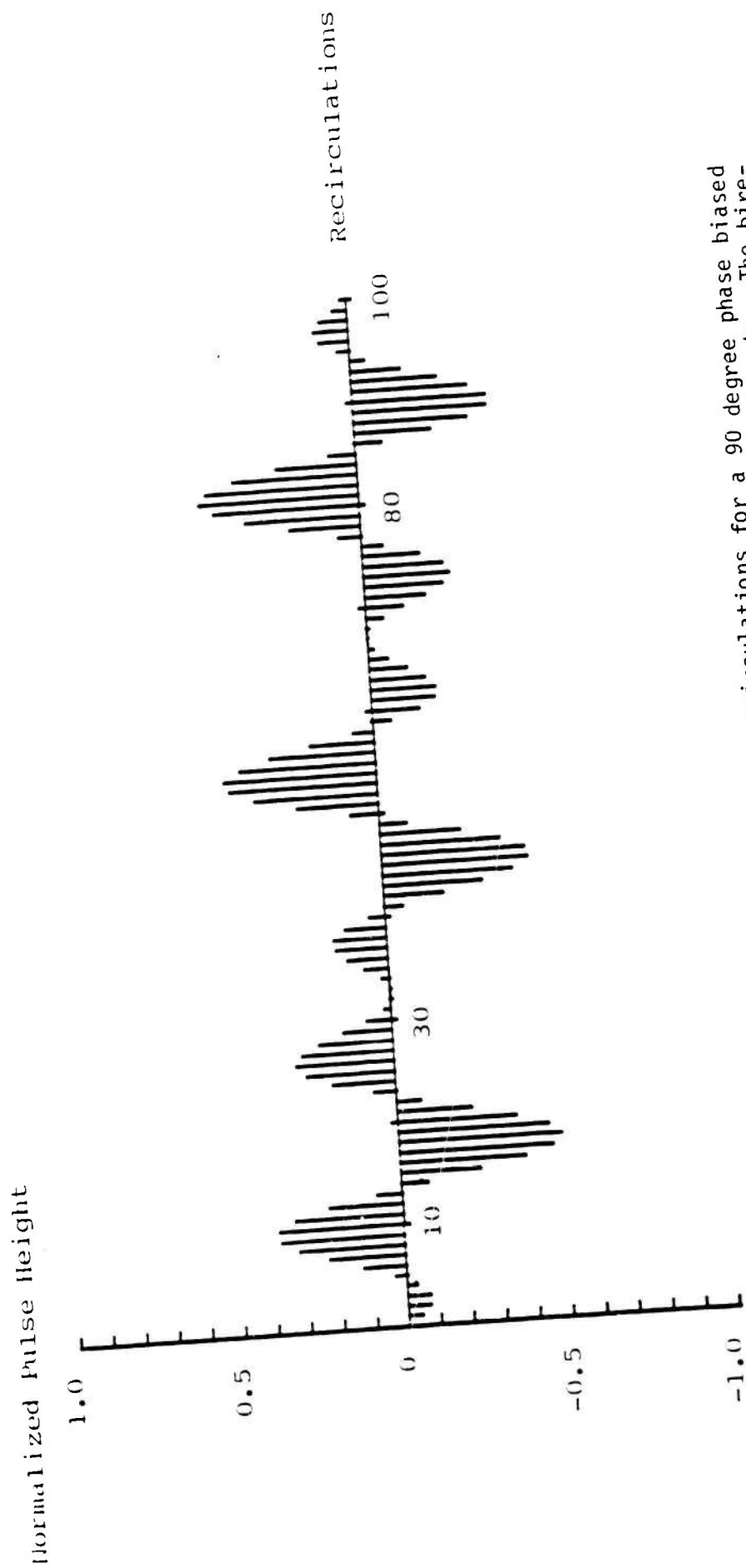


Fig. IV-17d. Normalized pulse heights vs recirculations for a 90 degree phase biased re-entrant rotation sensor operated in the unpolarized mode. The birefringent parameters are: $\theta = 10$ degrees, $\epsilon = 0$ degrees. The DC level has been suppressed.

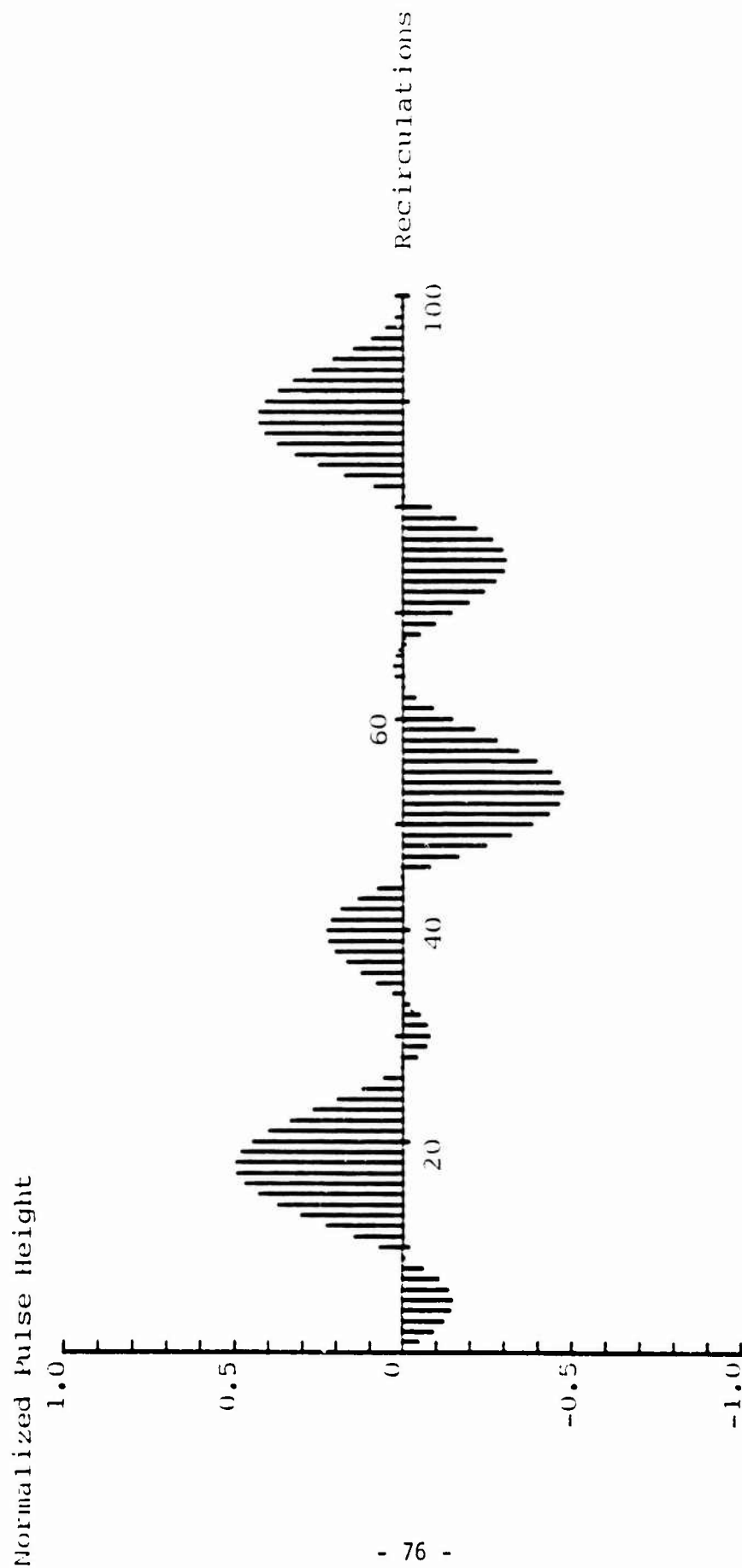


Fig. IV-18a. Normalized pulse height vs recirculations for a 90 degree phase biased re-entrant rotation sensor operated in the unpolarized mode. The birefringent parameters are: $\theta = 5$ degrees, $\xi = 0$ degrees. The DC level has been suppressed.

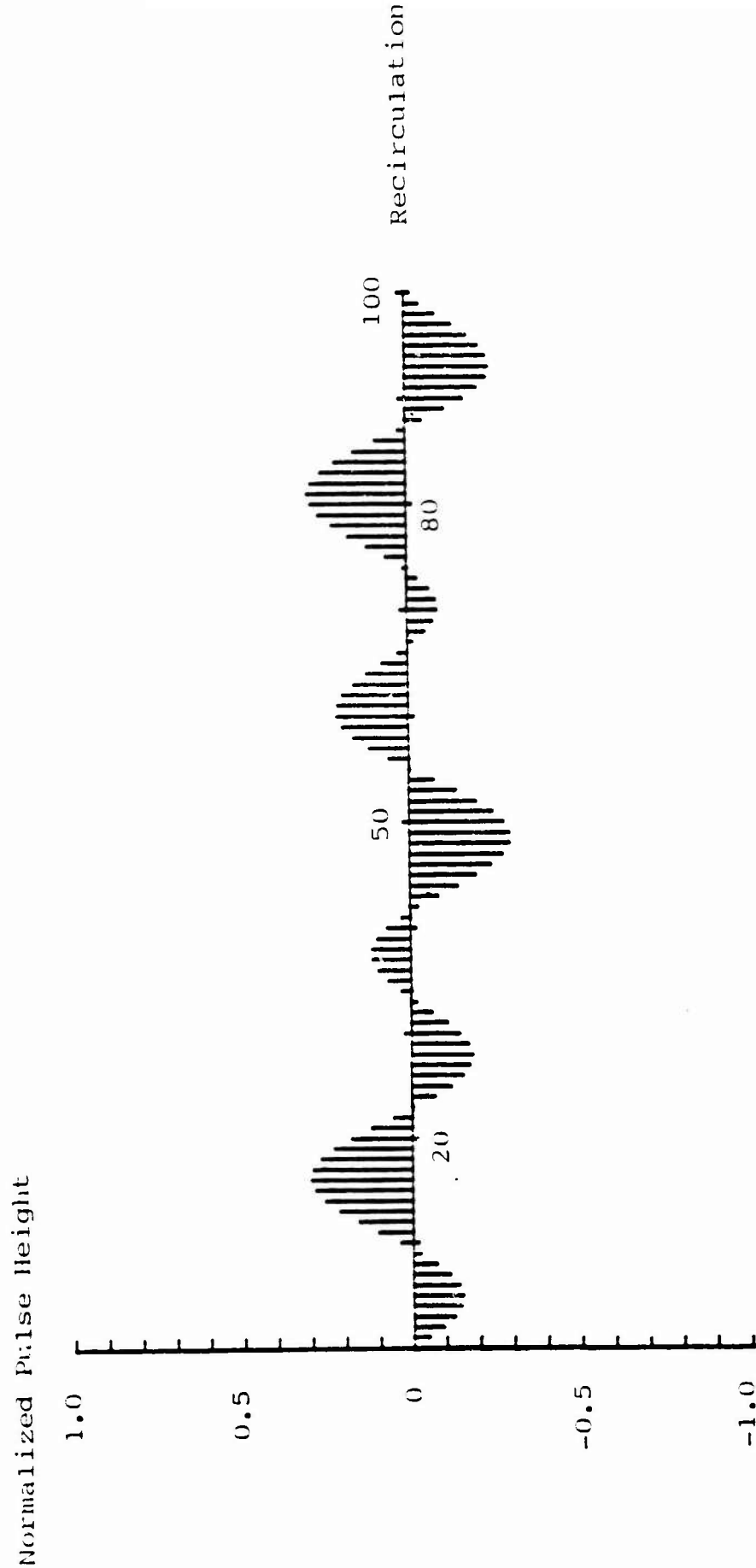


Fig. IV-18b. Normalized pulse height vs recirculations for a 90 degree phase biased re-entrant rotation sensor operated in the unpolarized mode. The birefringent parameters are: $\theta = 5$ degrees, $\xi = 5$ degrees, and $\phi = 0$ degrees. The DC level has been suppressed.

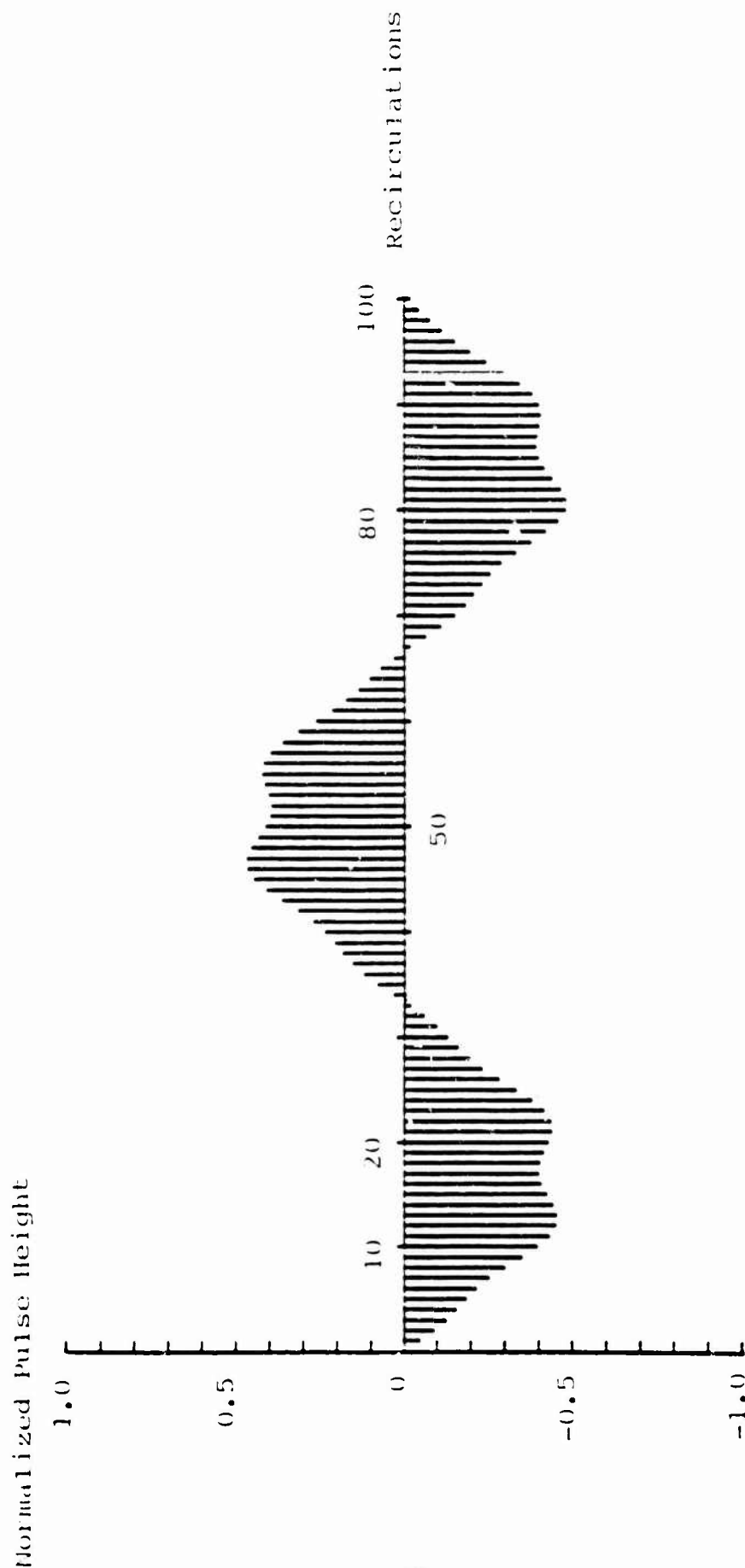


Fig. IV-18c. Normalized pulse height vs recirculations for a 90 degree phase biased re-entrant rotation sensor operated in the unpolarized mode. The birefringent parameters are: $\theta = 5$ degrees, $\delta = 36$ degrees, and $\phi = 0$ degrees. The DC level has been suppressed.

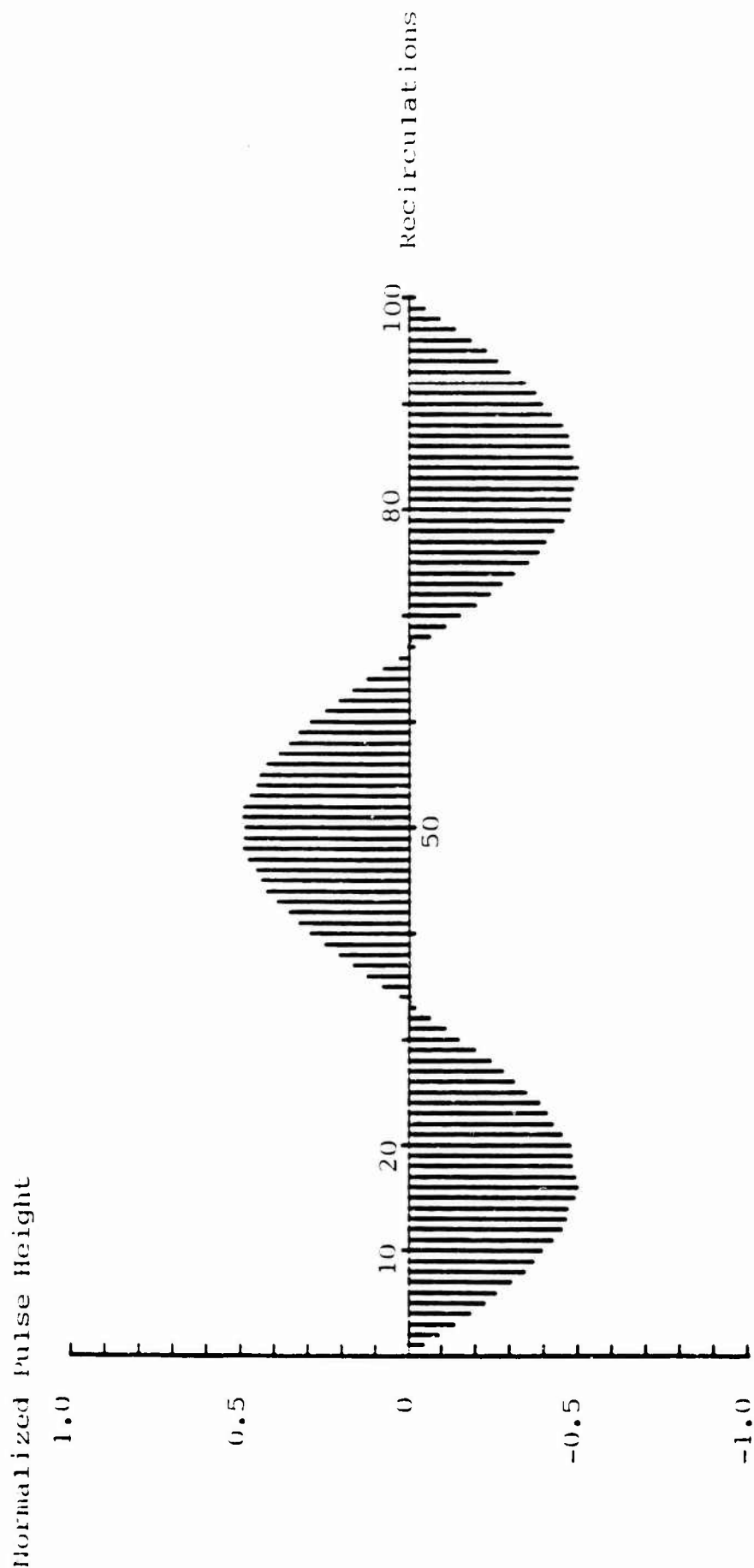


Fig. IV-18d. Normalized pulse height vs recirculations for a 90 degree phase biased re-entrant rotation sensor operated in the unpolarized mode. The birefringent parameters are: $\theta = 5$ degrees, $\xi = 90$ degrees, and $\phi = 0$ degrees. The DC level has been suppressed.

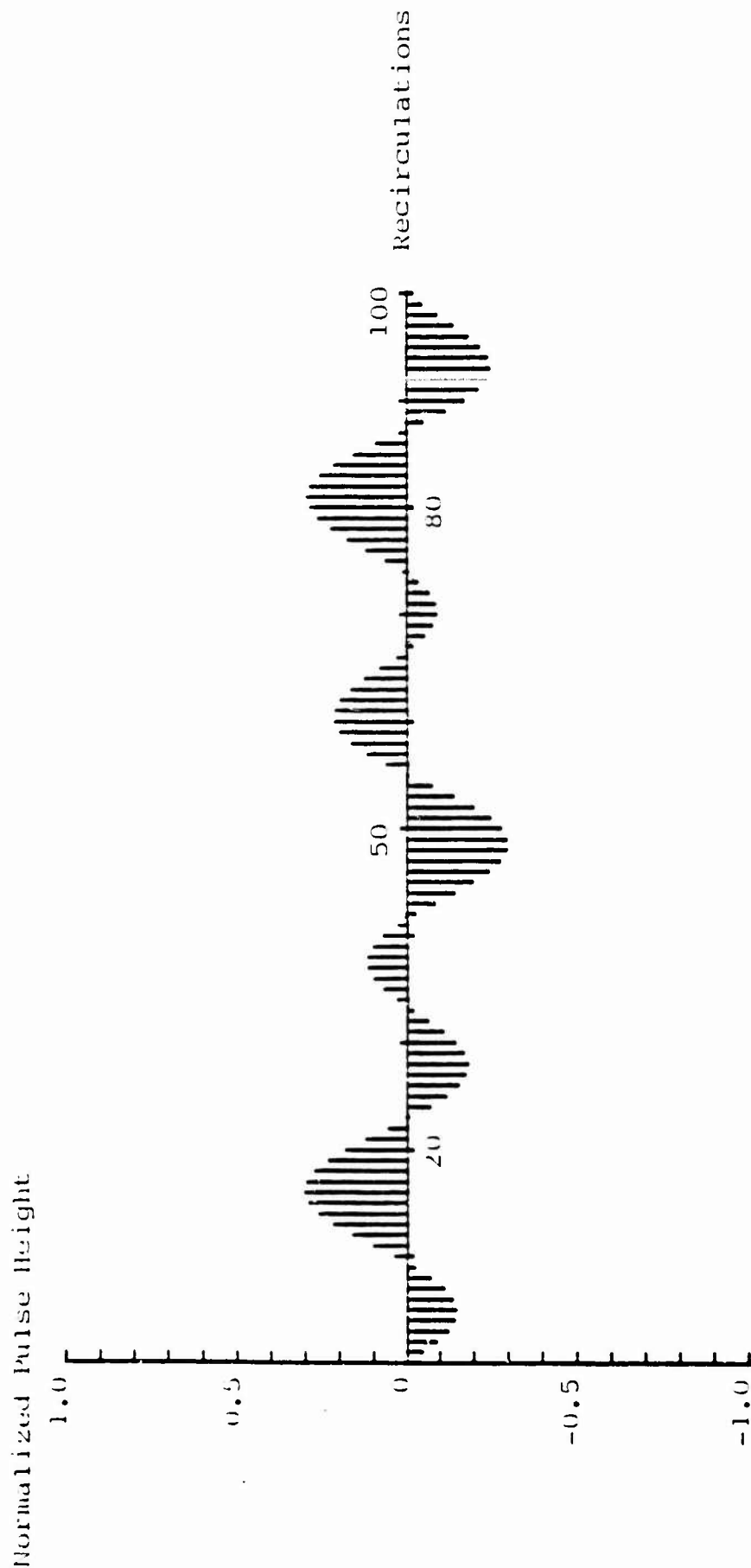


Fig. IV-19a. Normalized pulse height vs recirculations for a 90 degree phase biased re-entrant rotation sensor operated in the unpolarized mode. The birefringent parameters are: $\theta = 5$ degrees, $\xi = 5$ degrees, and $\phi = 0$ degrees. The DC level has been suppressed.

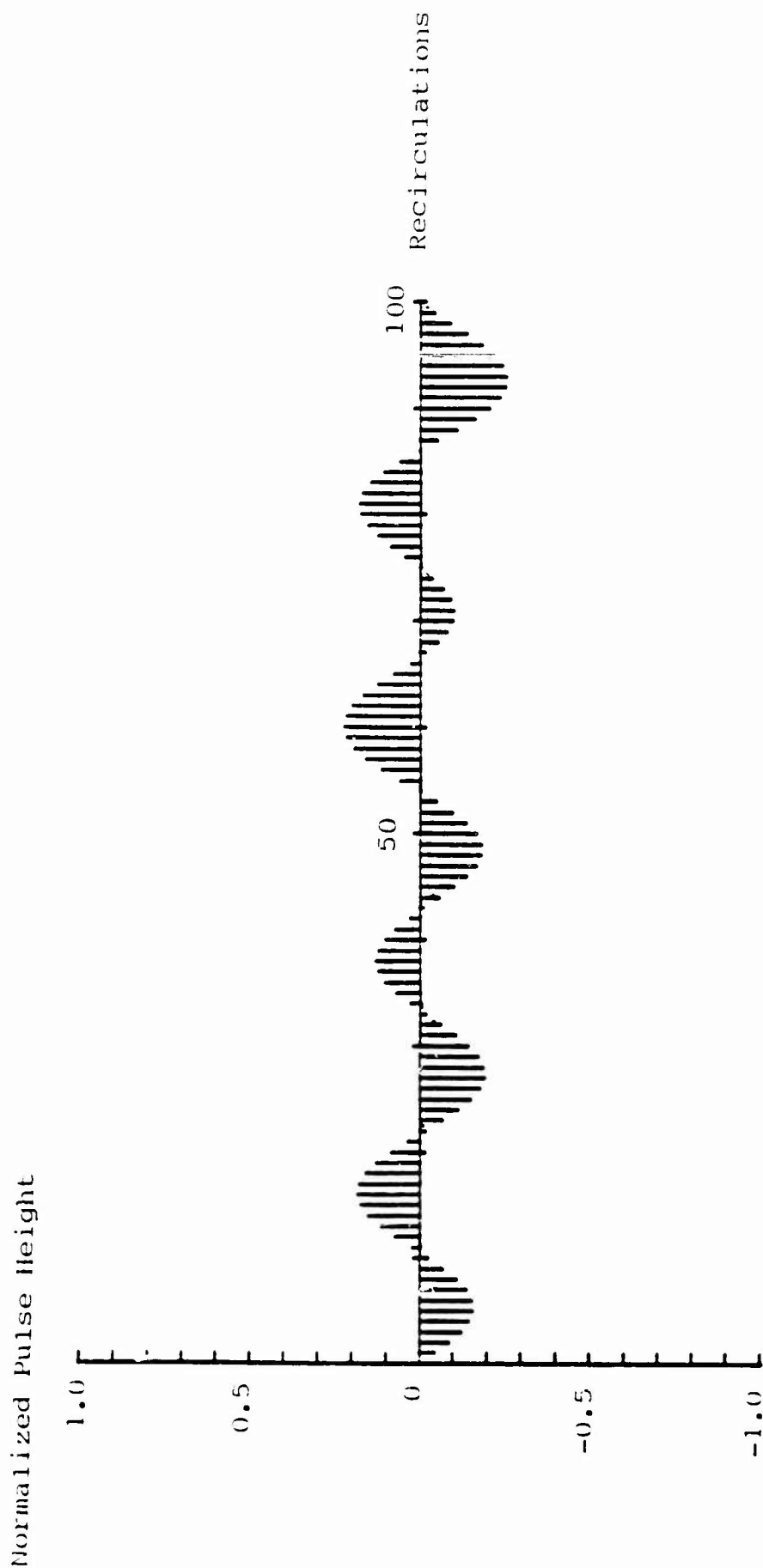


Fig. IV-19b. Normalized pulse height vs recirculations for a 90 degree phase biased re-entrant rotation sensor operated in the unpolarized mode. The birefringent parameters are: $\theta = 5$ degrees, $\xi = 5$ degrees, and $\phi = 45$ degrees. The DC level has been suppressed.

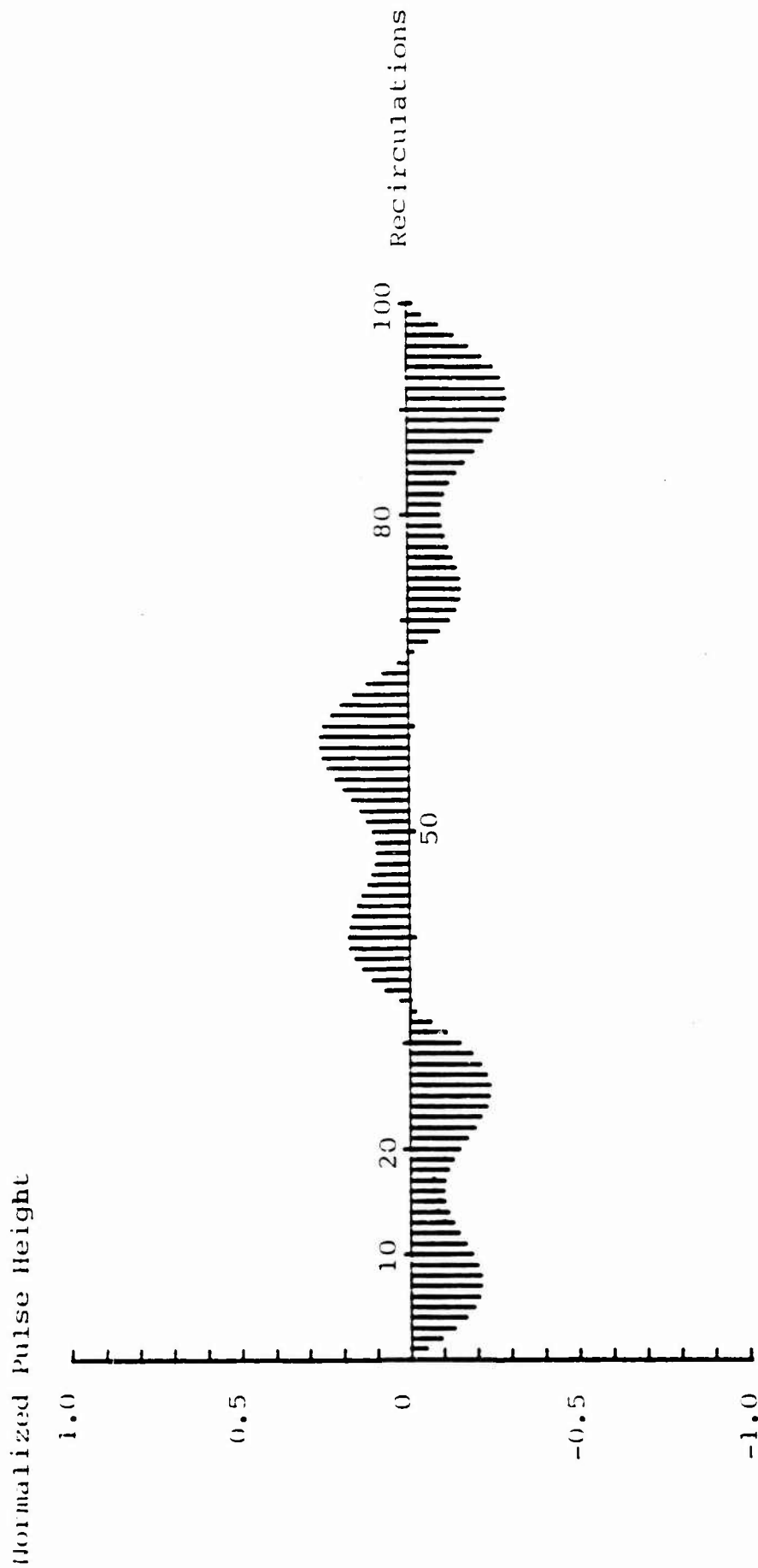


Fig. IV-19c. Normalized pulse height vs recirculations for a 90 degree phase biased re-entrant rotation sensor operated in the unpolarized mode. The birefringent parameters are: $\theta = 5$ degrees, $\xi = 5$ degrees, and $\varnothing = 90$ degrees. The DC level has been suppressed.

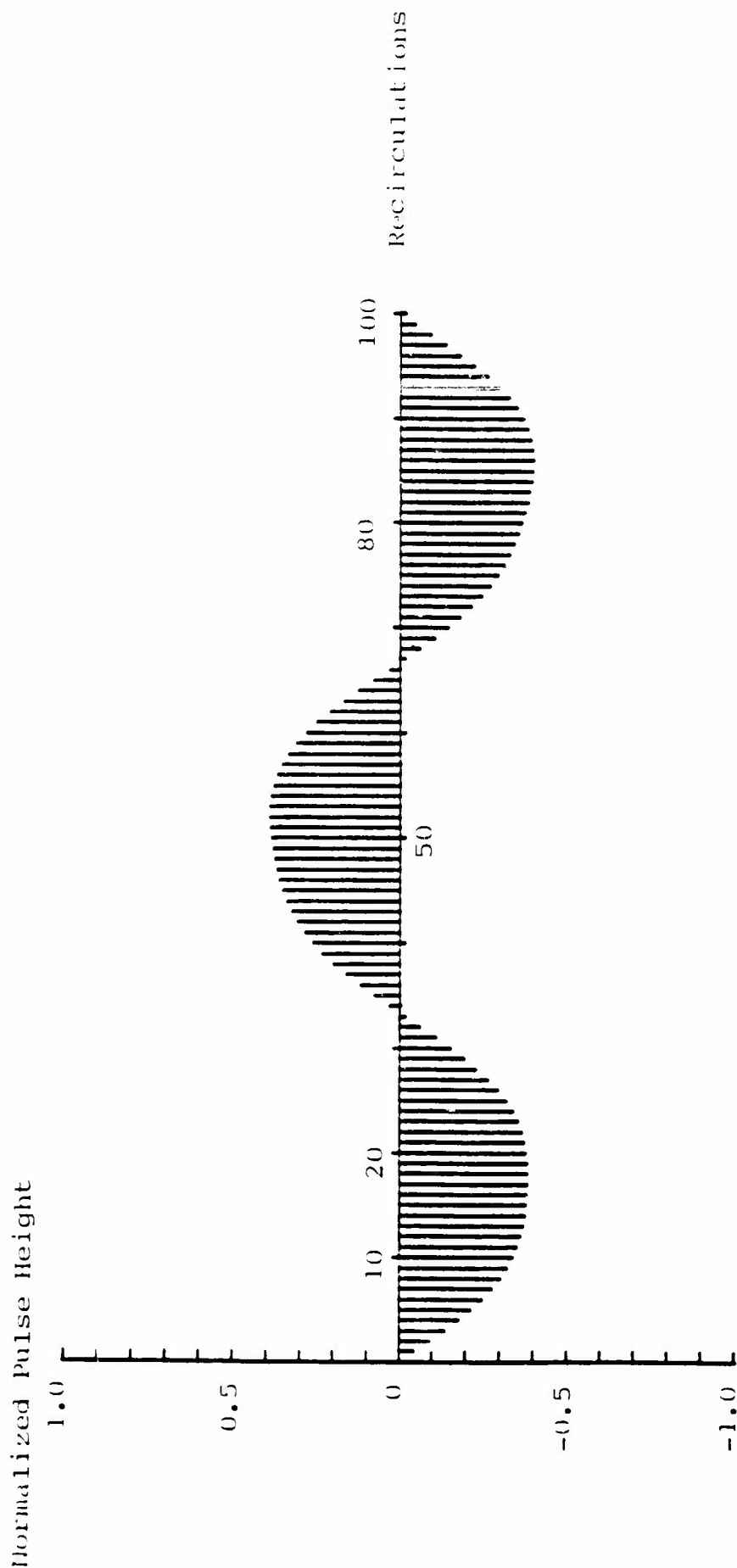


Fig. IV-19d. Normalized pulse height vs recirculations for a 90 degree phase biased re-entrant rotation sensor operated in the unpolarized mode. The birefringent parameters are: $\theta = 5$ degrees, $\xi = 5$ degrees, and $\phi = 135$ degrees. The DC level has been suppressed.

Assume instead that the reciprocal birefringent constant at 180 degrees. The unpolarized part of the response, $\bar{I}_K^{(u)}$ in Eq. IV - 22 have normalized amplitudes which are less than the maximum degree of polarization in general. The ideal response which is the term at a frequency of $\bar{\nu}_R$ is sinusoidal, thus the value of the pure rotational term can be vanishingly small at those K , hence extra zero crossings can be introduced regardless of how small P is.

If a threshold of detection is used this problem can be eliminated. If the absolute value of the amplitude of a particular recirculation is less than the threshold value, then this recirculation is not used in the measurement of the phase of the envelope of the pulse train. If the threshold level is T , the degree of polarization, P , must be less than T to avoid counting extra zero crossing if there is no noise. If there is noise and/or the reciprocal birefringent dependent phase shift, ϕ , is not 180 degrees, the threshold level must be increased to avoid detection of the extra zero crossings. The threshold level can not be increased without reducing the number of recirculations drastically. The reciprocal birefringent dependent phase shift, ϕ , must be kept at 180 degrees with high accuracy, the degree of polarization of the light source must be small, and the polarization sensitivity of the components must also be small, in order to achieve a rotation sensor with high sensitivity.

V. PROPAGATION OF NOISE IN PASSIVE RE-ENTRANT PULSED FIBER OPTIC ROTATION SENSORS

The key difference between single pass and re-entrant systems in the propagation of noise is due to the rotation rate being obtained by N measurements in the re-entrant system versus one measurement in the single pass system. Because of this difference, the error analysis for single pass systems does not apply to re-entrant systems. A new result describing the contribution of each noise source to rotation rate error must be derived.

The propagation of noise in a re-entrant system is strongly effected by the detec-

tion scheme used. This scheme determines the relationship between the observed pulse heights of N recirculations and the rotation rate. Two detection schemes will be analyzed here. One of these is called the least square error method.⁵ It is difficult to implement in practice, because of the large amount of calculation required. The propagation of noise is easy to calculate for this detection scheme. The other scheme is called the cycle counting method. It is easy to implement, but it is quite difficult to calculate the propagation of noise for this detection scheme. A computer is required for the evaluation of the rotation rate error for this scheme.

The least square error method will be covered first. From the output of a re-entrant rotation sensor, one obtains pulse heights, f_K , at times t_K . The pulse heights, f , are related to the rotation rate, Ω , as

$$f = f(\Omega, X_i, t_K) \quad (V-1)$$

where X_i are the instantaneous values of the noise parameters.

The square error, E^2 , between the observed and calculated pulse heights is defined as

$$E^2 = \sum_{K=1}^N (f_K - f(\Omega_m, X_i, t_K))^2 \quad (V-2)$$

The measured rotation rate, Ω_m , is that which minimizes the square error. Let f_K , the measured pulse height, be expressed as

$$f_K = f(\Omega_a, X_i + \Delta X_i, t_K) \quad (V-3)$$

where Ω_a is the actual rotation rate, X_i is the mean value of the noise parameter X_i , and ΔX_i is the instantaneous deviation of X_i from its mean. Let the measured rotation rate be expressed as

$$\Omega_m = \Omega_a + \Delta\Omega \quad (V-4)$$

where $\Delta\Omega$ is the deviation of the measured from the actual rotation rate.

Equation V-2 can be rewritten as

$$E^2 = \sum_{K=1}^N [f(\Omega_a, \bar{\mathbf{X}}_i + \Delta\mathbf{X}_i, t_K) - f(\Omega_a + \Delta\Omega, \mathbf{X}_i, t_K)]^2 \quad (V-5)$$

Each pulse height, f , in the above equation is expanded in a Taylor series to first order about the point $(\Omega_a, \bar{\mathbf{X}}_i)$. The result is

$$E^2 = \sum_{K=1}^N \left(\sum_{i=1}^M \frac{\partial f_K}{\partial X_i} \Delta X_i - \frac{\partial f_K}{\partial \Omega} \Delta\Omega \right)^2 \quad (V-6)$$

where the partial derivatives $\frac{\partial f_K}{\partial X_i}$ and $\frac{\partial f_K}{\partial \Omega}$ are evaluated at $(\Omega_a, \bar{\mathbf{X}}_i, t_K)$. The instantaneous rotation rate error $\Delta\Omega$, is that which minimizes E^2 , the other quantities are all known. Differentiating E^2 with respect to $\Delta\Omega$, setting it equal to zero, and solving for $\Delta\Omega$ yields

$$\Delta\Omega = \frac{\sum_{K=1}^N \sum_{i=1}^M \frac{\partial f_K}{\partial \Omega} \frac{\partial f_K}{\partial X_i} \Delta X_i}{\sum_{K=1}^N \left(\frac{\partial f_K}{\partial \Omega} \right)^2} \quad (V-7)$$

The mean square rotation rate error is obtained by squaring equation V-7 and taking the average value. The mean square rotation rate error, σ_{Ω}^2 , is (assuming ΔX_i are independent)

$$\Delta_{\Omega}^2 = \frac{\sum_{i=1}^M \sum_{K=1}^N \frac{\partial f_K}{\partial \Omega} \frac{\partial f_K}{\partial X_i} \frac{\partial f_K}{\partial X_i} \frac{\partial f_K}{\partial \Omega} \sigma_{X_i}^2}{\left(\sum_{K=1}^N \left(\frac{\partial f_K}{\partial \Omega} \right)^2 \right)^2} \quad (V-8)$$

where $\sigma_{X_i}^2$ is the mean square value of ΔX_i and the other quantities have been defined previously. To calculate σ_{Ω}^2 , requires $\sigma_{X_i}^2$ and $f(\Omega, X_i, t)$ be known.

To use the cycle counting method of detection requires that the signal be passed through a high pass filter to remove the DC level. The filtered signal can have equal excursions in the + and - directions. The number of half cycles of the envelope of the pulses is determined by counting the number of zero-crossings. A zero-crossing occurs when two adjacent pulses have opposite signs. Once the number of zero-crossings is known, the frequency of the envelope can be determined and thus the rotation rate by using Eq. V - 9.

$$F = \frac{D\Omega}{n\lambda} \quad (V - 9)$$

where F is the envelope frequency, D the loop diameter, Ω the angular velocity, n the refractive index and λ the optical wavelength.

The measured filtered pulse height, f'_k , has two parts. One part is due to the rotation rate, and the other is due to noise. This can be expressed as

$$f'_k = \bar{f}'_k + \Delta f'_k \quad (V - 10)$$

where \bar{f}'_k is the mean value of f'_k and represents the signal, and $\Delta f'_k$ is the instantaneous difference between the measured pulse height f'_k and the mean pulse height \bar{f}'_k . $\Delta f'_k$ is due to noise.

To calculate the mean square rotation rate error requires that the probability be calculated for observing 0, 1, 2, 3, ..., $N - 1$ zero-crossings due to noise from the ideal waveform which will have K zero-crossings due to rotation. Due to noise, one or more of the pulses can change sign giving fewer or greater number of zeros. Let $P_{ZC}(K)$ be the probability of observing exactly K zero-crossings. The mean square frequency error, σ_F^2 , is

$$\frac{\sigma_F^2}{F_0^2} = \sum_{L=0}^{N-1} P_{ZC}(L)L^2 - \left(\sum_{L=0}^{N-1} P_{ZC}(L)L \right)^2 \quad (V - 11)$$

where F_0 is the lowest frequency measurable. Using Eq. V-12 allows the calculation of the rotation rate error, σ_Ω .

$$\sigma_n = \left(\frac{nP\lambda}{4A} \right) \sigma_F \quad (V-12)$$

where A is the area enclosed by the sensing loop and P is the perimeter of the area.

The problem is reduced to finding the probabilities $P_{ZC}(K)$ which depend on the ideal waveform (i.e. actual rotation rate) and on the probability of observing a $\Delta f'_k$. The probability density function $P_{\Delta f'_k}(\Delta f'_k)$ is obtained by the following reasoning.

The measured pulse heights can be written as

$$f'_k = f'_k(\Omega_s, \mathbf{X}_i + \Delta \mathbf{X}_i) \quad (V-13)$$

where all parameters are as before. Expanding this function in a Taylor series to first order about the point (Ω_s, \mathbf{X}_i) results in

$$f'_k = f'_k(\Omega_s, \mathbf{X}_i) + \sum_{i=1}^M \frac{\partial f'_k}{\partial X_i} \Delta X_i \quad (V-14)$$

Comparing Eqs. V-14 and V-10 gives $\Delta f'_k$ as

$$\Delta f'_k = \sum_{i=1}^M \frac{\partial f'_k}{\partial X_i} \Delta X_i \quad (V-15)$$

The characteristic function⁶ $M_{\Delta f'_k}(w)$ is given in terms of the characteristic function of ΔX_i as

$$M_{\Delta f'_k}(w) = \prod_{i=1}^M M_{\Delta X_i} \left(w \frac{\partial f'_k}{\partial X_i} \right) \quad (V-16)$$

where the characteristic function is the Fourier transform of the probability density function P , $\partial f'_k / \partial X_i$ is evaluated at (Ω_s, \mathbf{X}_i) and the ΔX_i have been assumed in-

dependent as previously. By inverse Fourier transforming $M_{\Delta f'_K}(w)$ the probability density function $P_{\Delta f'_K}(\Delta f'_K)$ is obtained.

For analysis purposes, the probability density functions of ΔX_i are assumed Gaussian with standard deviation σ_{X_i} and zero mean. In this case, the probability density function, $P_{\Delta f'_K}(\Delta f'_K)$ is also Gaussian with zero mean and a standard deviation, $\sigma_{\Delta f'_K}$, given as

$$\sigma_{\Delta f'_K}^2 = \sum_{i=1}^M \left(\frac{\partial f'_K}{\partial X_i} \right)^2 \sigma_{X_i}^2 \quad (V-17)$$

The probability density function is written as

$$P_{\Delta f'_K}(\Delta f'_K) = (2\pi\sigma_{\Delta f'_K})^{-1} \exp[-(\Delta f'_K/\sigma_{\Delta f'_K})^2/2] \quad (V-18)$$

In calculating the probability density function $P_z(k)$, the probabilities of observing and not observing a change in the sign of K^{th} pulse which has amplitude $f(\Omega_a, X_i, t_k)$ must be known. These probabilities are

$$\begin{aligned} a. \quad P_{nec}^{(f'_k)} &= \int_{-\infty}^{|f'_k|} P_{\Delta f'_K}(\Delta f'_K) d(\Delta f'_K) \\ b. \quad P_{ec}^{(f'_k)} &= 1 - P_{nec}^{(f'_k)} \end{aligned} \quad (V-19)$$

where $P_{nec}^{(f'_k)}$ and $P_{ec}^{(f'_k)}$ are the probabilities for not observing and observing a sign change in the K^{th} circulation.

Let $S(J)$ be the set of all possible ways of getting exactly J zero-crossings from N recirculations. Let $S(J)_i$ be the i^{th} element of this set. The probability P of observing this element given ideal pulse heights $f'_k(\Omega_a, X_i)$ can be expressed in terms of $P_{nec}^{(f'_k)}$ and $P_{ec}^{(f'_k)}$ as

$$P(J)_i = \prod_{\text{same}} P_{nec}^{(f'_k)} \prod_{\text{opposite}} P_{ec}^{(f'_k)} \quad (V-20)$$

where Π_{same} is the product over the pulses in $S(J)_i$ which have the same sign as the corresponding pulses in $f'_k(\Omega_a, \mathbf{X}_i)$ and $\Pi_{opposite}$ is the product over the pulses in $S(J)_i$ which have opposite signs compared to the corresponding pulses in $f'_k(\Omega_a, \mathbf{X}_i)$. The probability of observing exactly J zero-crossings, $P(J)$, is the sum of $P(J)_i$ over all elements of the sets $S(J)$.

For N recirculations, the number of zero-crossings is between 0 and $N - 1$. There are also 2^N different ways of arranging the signs of N recirculations. A particular arrangement is represented by a sequence of N elements, where each element can be 1 or -1. The 1's and -1's refer to positive and negative pulse heights respectively. Calculating the probabilities $P(J)$ for N large is extremely difficult.

A computer is used to calculate the probabilities of $P(J)$. The input into the computer program are the function $f'(\Omega, \mathbf{X}_i, t_k)$, the number of recirculations, the rotation rate and the standard deviations of noise parameters. The computer calculates the probability of observing each of the 2^N arrangement of the signs of N recirculations given $f'(\Omega, \mathbf{X}_i, t_k)$. It also determines the number of zero-crossings for each arrangement. From this it computes the probabilities of observing exactly J zeroes, $P_{ZC}(J)$. The normalized mean square frequency error $(\sigma_f/F_0)^2$ is then calculated using Eq. V - 11. For ten recirculations there are 1024 arrangements, while for 20 recirculations there are 1,048,576 arrangements. Even the computer can not handle more than about 20 recirculations due to the extensive computation time.

The computer was used to analyze the performance of a phase biased, non-birefringent re-entrant rotation sensor in the presence of noise. The noise sources which were used are source power noise, source frequency noise, input coupling noise, coherent backscattering noise, shot noise, thermal noise, amplifier noise, and phase biased noise. Birefringent noise, $1/f$ noise, and nonreciprocal noise sources were not included. The mean values and standard deviations of these noise parameters are

shown in Fig. V-1.

The other parameters of the rotation sensor are given in Fig. V-2. The schematic of the rotation sensor is shown in Fig. V-3. The equation which described the detected signal is

$$V_{det} = Z \left[(e\eta_{eff}/h\nu) [-\eta P_{out}(1-\delta)^2 \delta^{K-1} \exp(-\alpha K L) \cos(K\phi_s - \pi/2) - \eta P_{out}(1-\delta)^2 \delta^{K-1} \exp(-\alpha K L) \sqrt{2B_s \alpha L_{coh}} \sin(K\phi_s/2) X_s] + I_{shot} + \sqrt{F} I_{thermal} \right] \quad (V-21)$$

where ϕ_s is

$$\phi_s = 4\pi LR\Omega v/c^2 \quad (V-22)$$

where all the quantities are defined in Figs. V-1 and V-2.

The program was run three times to examine the behavior of the re-entrant rotation sensor for six, seven and eight recirculations. Figures V-4a, b and c are plots of actual zero-crossings versus rotation rate in the absence of noise. These plots resemble "staircases." The jumps between zero-crossings are actually discontinuous. The slope is due to the finite horizontal resolution of the computer program (i.e. the rotation rate increment is 10^{-2} rad/sec).

Figures V-5a, b and c are plots of the mean number of zero-crossings versus rotation rate for six, seven and eight recirculations with noise present. A noninteger number of zero-crossings is to be interpreted in a probabilistic sense. The general form of these plots is that of a rounded staircase (i.e. the transitions between zero-crossings are sloped). The degree of roundness increases with increasing number of recirculations. Near zero rotation rate, the mean value of the zero-crossings increases rapidly.

Noisy Parameter	Physical Variable	Mean Value	Standard Deviation
X_1	ν	3×10^{-4} Hz	10^2 Hz
X_2	P_{out}	10 mW	1 mW
X_4	η	25%	0.25%
X_9	$\lambda_{Effective}$ Backscatter	0 rad	K
X_9	i_{shot}	0 Amp	eqn 173a
X_{10}	$i_{Thermal}$	0 Amp	eqn 173b
X_{12}	λ_{Bias}	$\pi/2$ rad	$\pi/100$ rad

Fig. V-1. Table of means and standard deviations of noisy parameters used in the numeric evaluation of the noise in re-entrant rotation sensors using cycle counting detection algorithm.

Parameter	Physical Meaning	Value
L	Fiber Length	330 m
R	Loop Radius	7.6 cm
B	Bandwidth	20 MHz
F	Amp Noise Figure	1 dB
α	Fiber Attenuation	1.8 dB/Km
L_{coh}	Coherence Length	7.5 cm
δ	Loop Coupling Ratio	70%
Z	Transimpedance	20,000 V/A
K	Recirculation Number	1 to 8
Ω	Rotation Rate	0 to 1 rad/s
T	Temperature	300 K
r_s	Photodiode Series Res.	50 Ohms
η_{eff}	Quantum Eff.	50%

Fig. V-2. Table of values of the system parameters used in the numeric evaluation of the noise in re-entrant rotation sensors using cycle counting detection algorithm.

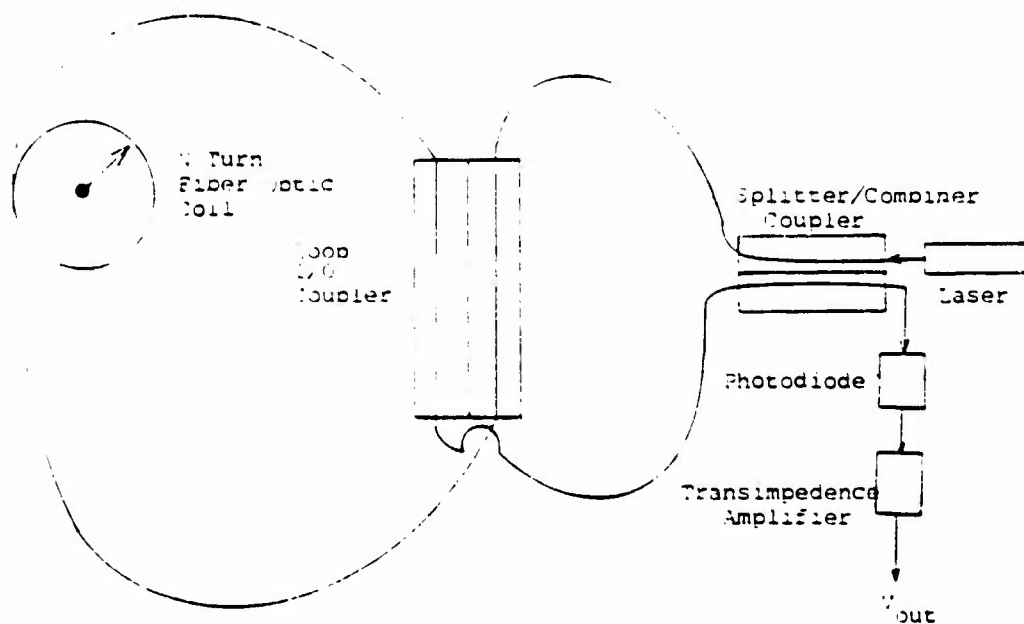


Fig. V-3. Schematic of the re-entrant rotation sensor using a cycle counting detection algorithm whose response was numerically evaluated in the presence of noise.

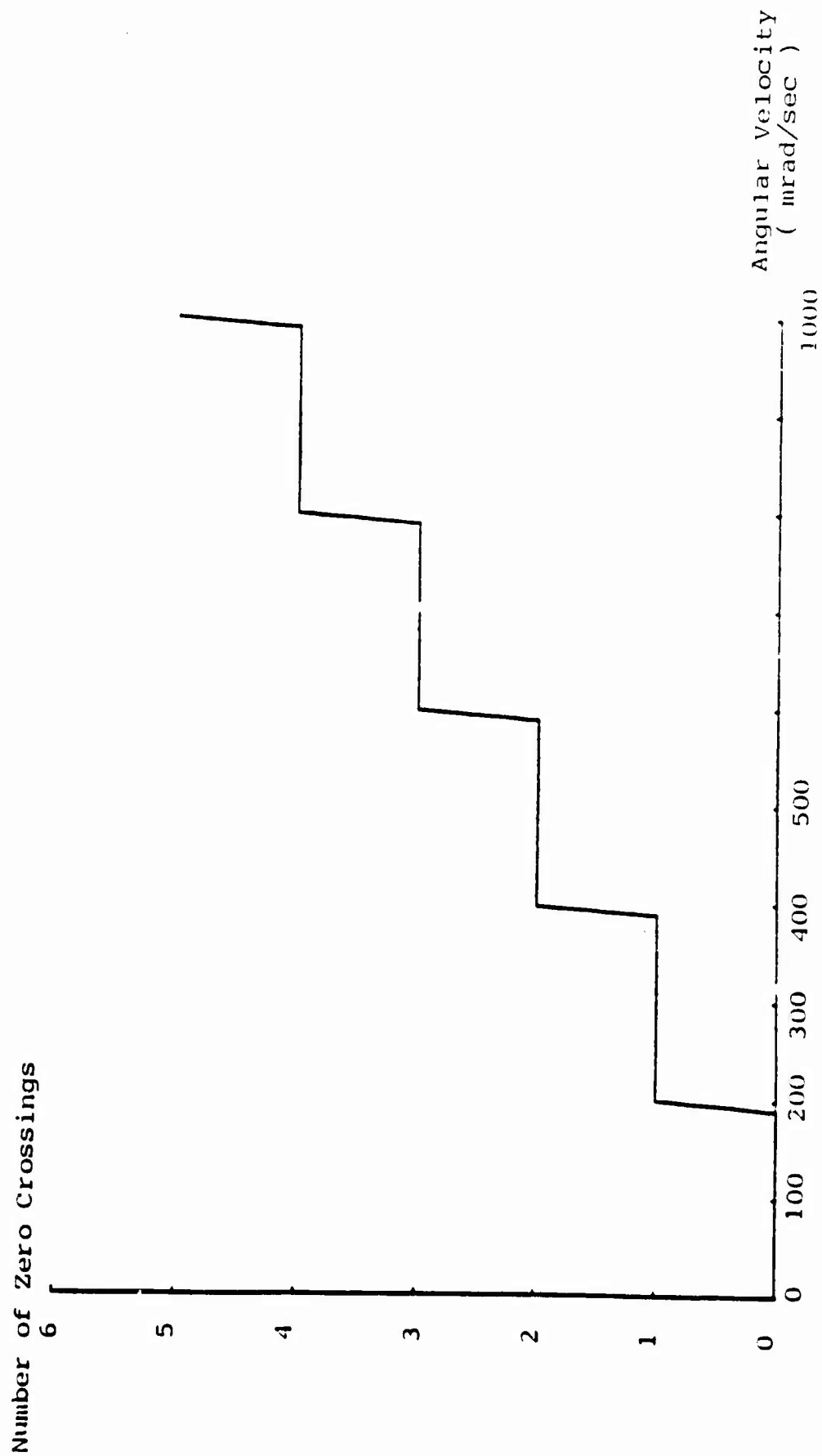


Fig. V-4a. Number of zero crossings vs rotation rate for noiseless re-entrant rotation sensor using cycle counting. Six recirculations are used.

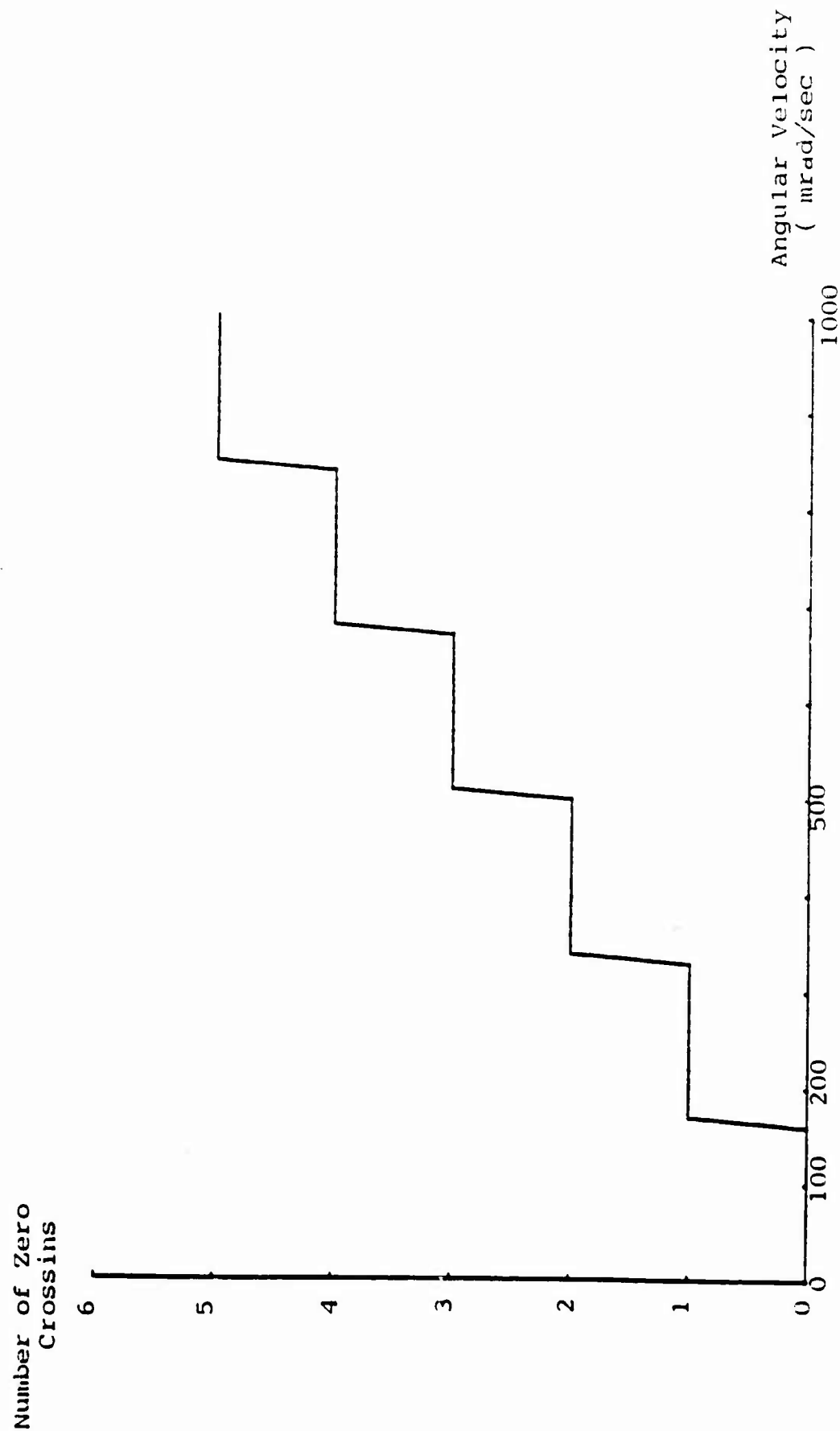


Fig. V-4b. Number of zero crossings vs rotation rate for noiseless re-entrant rotation sensor using cycle counting. Seven recirculations are used.

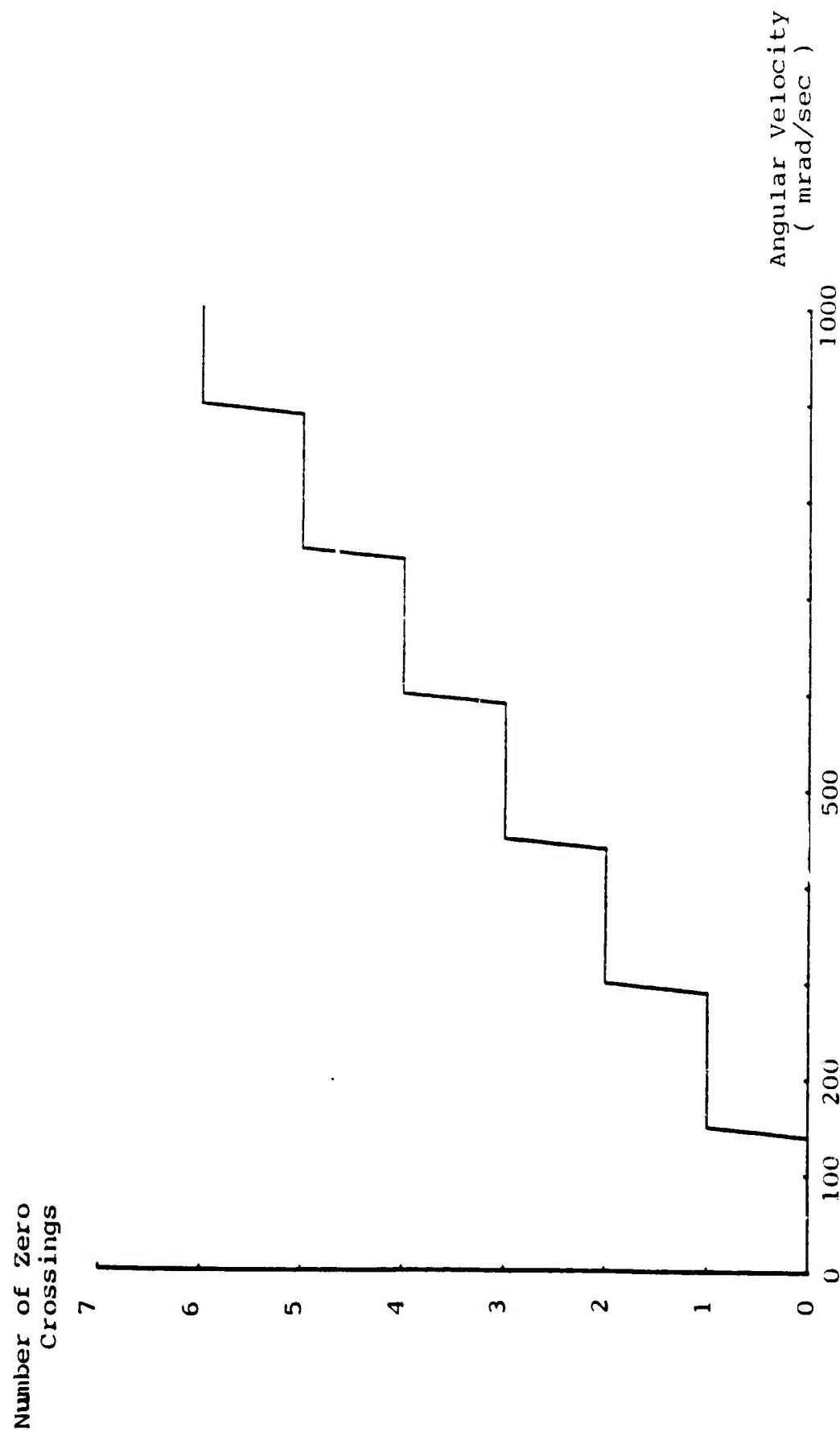


Fig. V-4c. Number of zero crossings vs rotation rate for noiseless re-entrant rotation sensor using cycle counting. Eight recirculations are used.

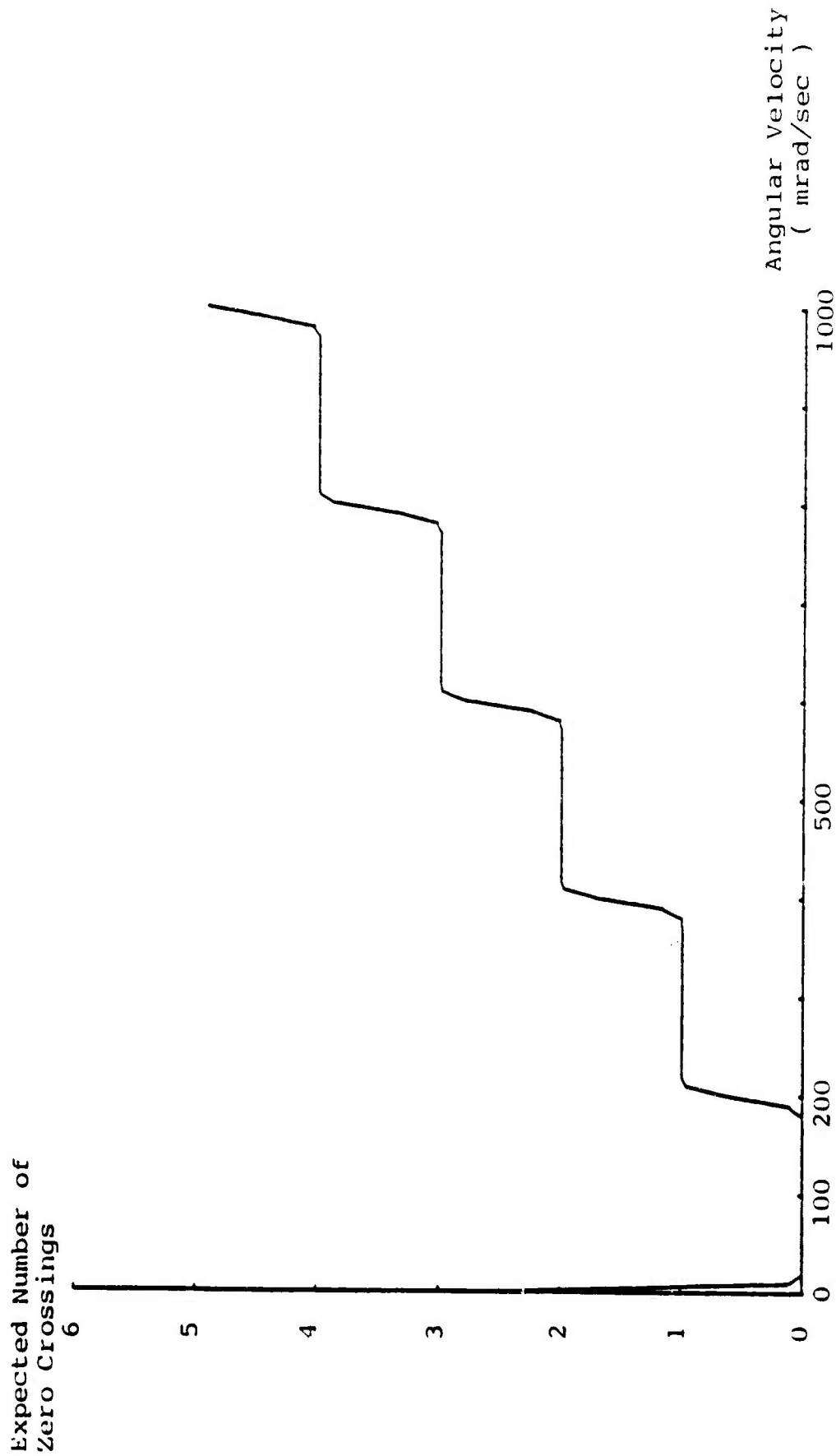


Fig. V-5a. Expected number of zero crossings vs rotation rate for a noisy re-entrant rotation sensor using cycle counting. Six recirculations are used.

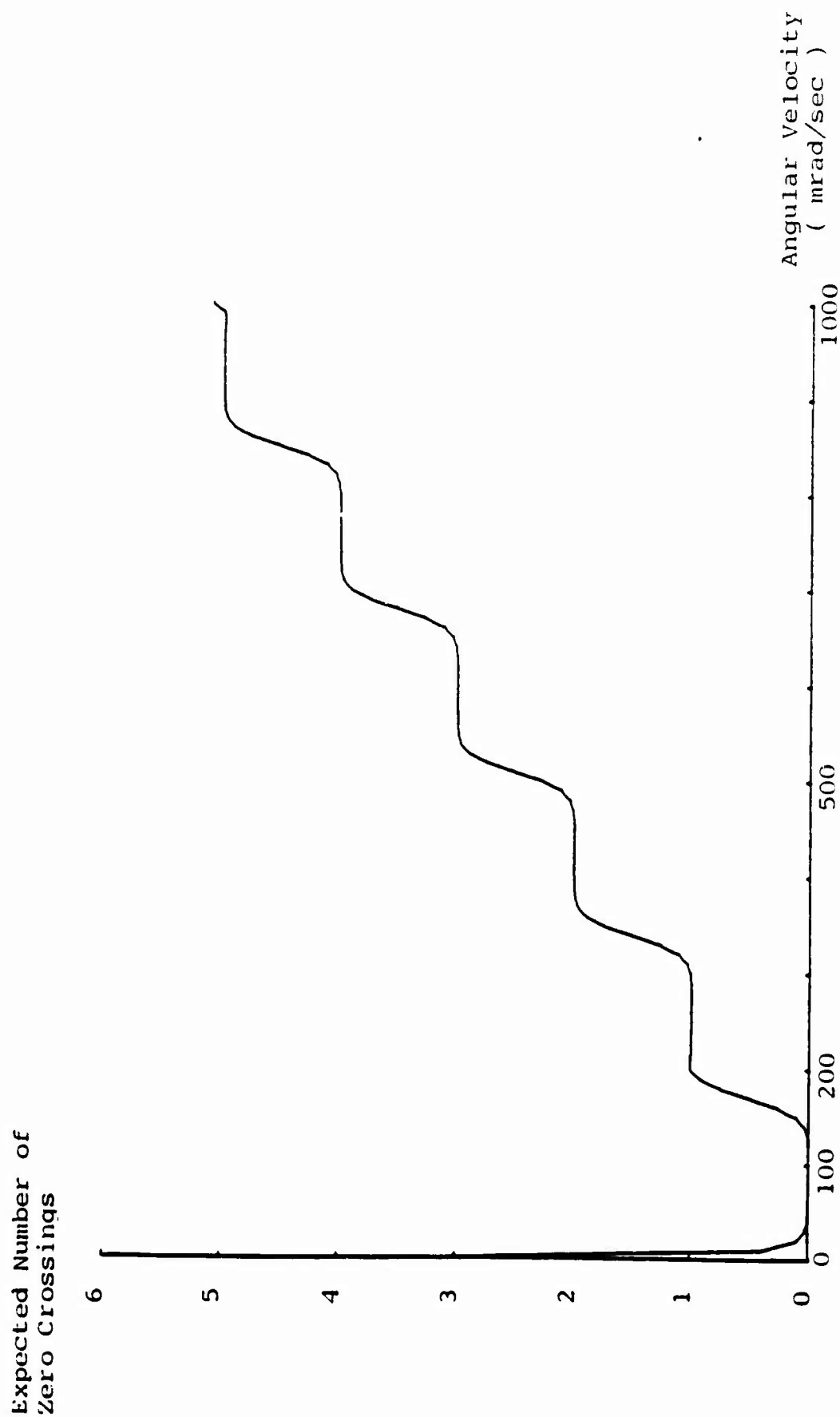


Fig. V-5b. Expected number of zero crossings vs rotation rate for a noisy re-entrant rotation sensor using cycle counting. Seven recirculations are used.

Expected Number of
Zero Crossings

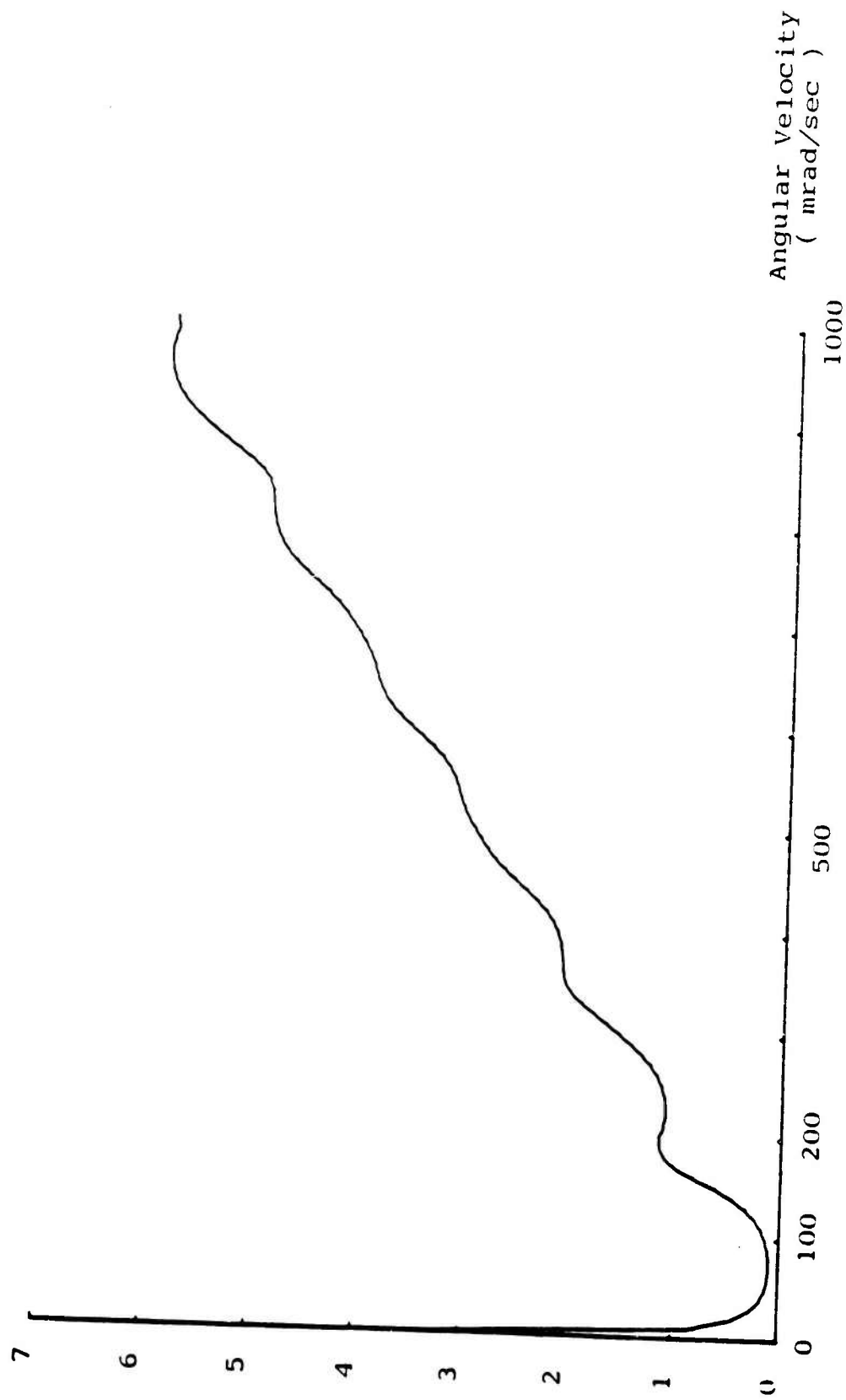


Fig. V-5c. Expected number of zero crossings vs rotation rate for a noisy re-entrant rotation sensor using cycle counting. Eight recirculations are used.

These observations are explained as follows. When a transition is made between zero-crossings, the last recirculation is very small in absolute value. The noise which is present now easily causes sign reversals of the last recirculation. This uncertainty in the sign of the last pulse results in the roundness of the transition between zero-crossings.

When this rotation sensor is rotating at low angular velocity, the pulses are all near zero. The noise again causes sign reversals of the pulses easily. This uncertainty of the signs of the pulses results in a large mean value of the zero-crossings at low rotation rates.

Both of these effects are more severe for more recirculations, because there are more pulses which can be in error. Using too many recirculations in the measurement of the rotation rate leads to error. Figures V-6a, b and c are plots of the standard deviation of the zero-crossings versus rotation rate. The standard deviation is a measure of the rotation rate error caused by the noise. This error is in addition to the one part in N error associated with counting N cycles. In these figures, the errors are seen to be largest at the transition between zero-crossings and low rotation rates. As more recirculations are used in the measurement, the overall error increases. The reasons for these are the same as for the rounding of the mean zero-crossing plots (Figs. V-5a, b and c). A threshold of detection or better signal processing can reduce the error at low rotation rates and at zero-crossing transitions. At present, one zero-crossing is counted when two adjacent pulses have opposite signs. The pulses on either side of these oppositely signed pulses could also be examined. Then by use of an appropriate algorithm, it could be determined that the pulse trains in Fig. V-7 have only one real zero-crossing. The dynamic range is reduced in this scheme (i.e. the maximum detectable rotation rate is decreased). Perhaps an adaptive algorithm could reduce the errors without reducing the dynamic range too much.

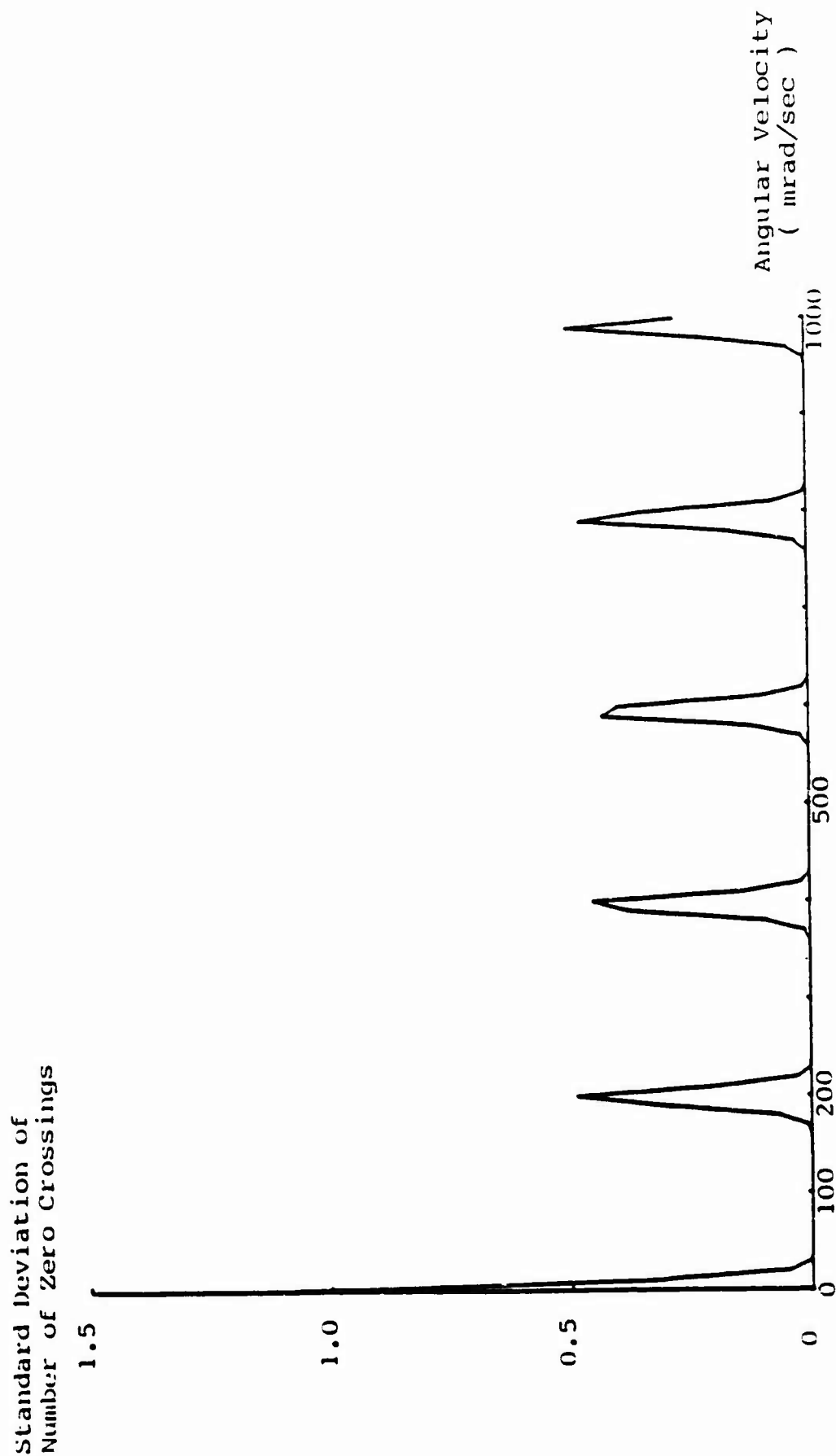


Fig. V-6a. Standard deviation of number of zero crossings for a noisy re-entrant rotation sensor using cycle counting. Six recirculations are used.

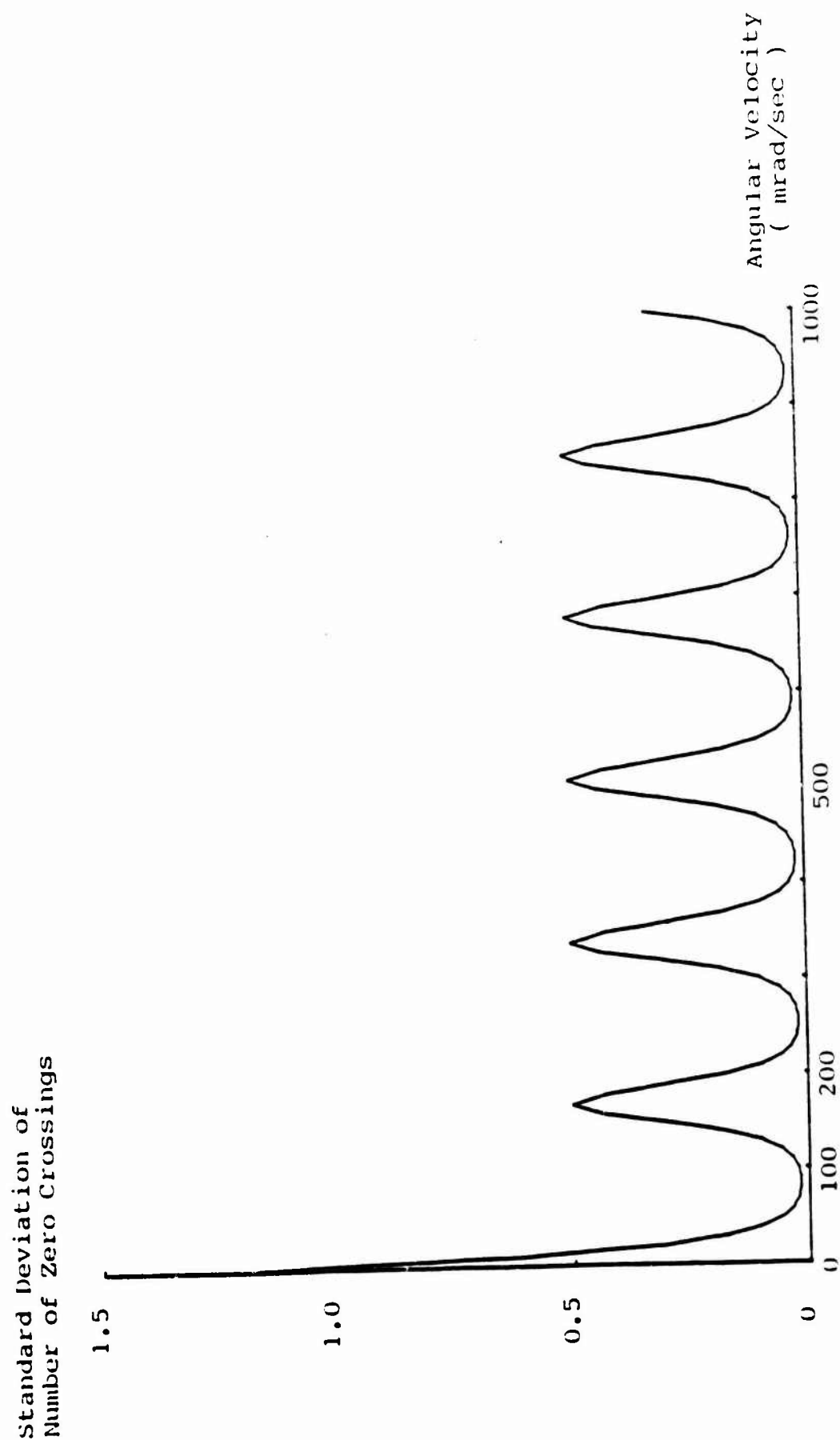


Fig. V-6b. Standard deviation of number of zero crossings vs rotation rate for a re-entrant rotation sensor using cycle counting. Seven recirculations are used.

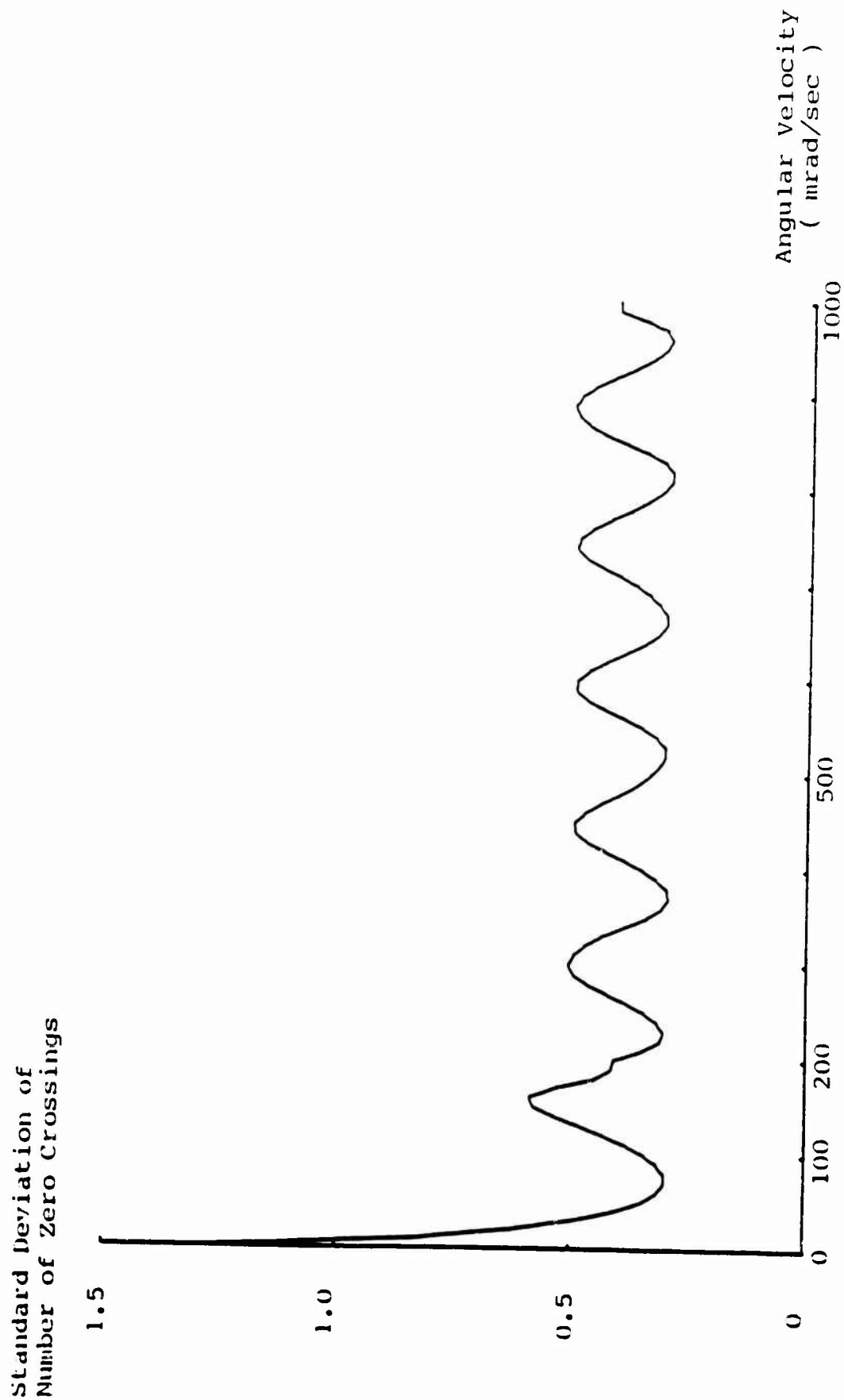
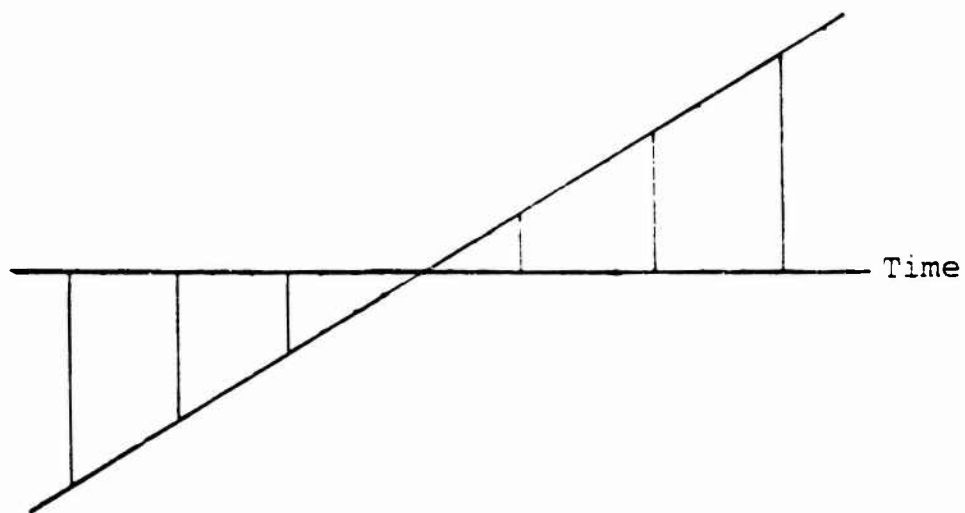
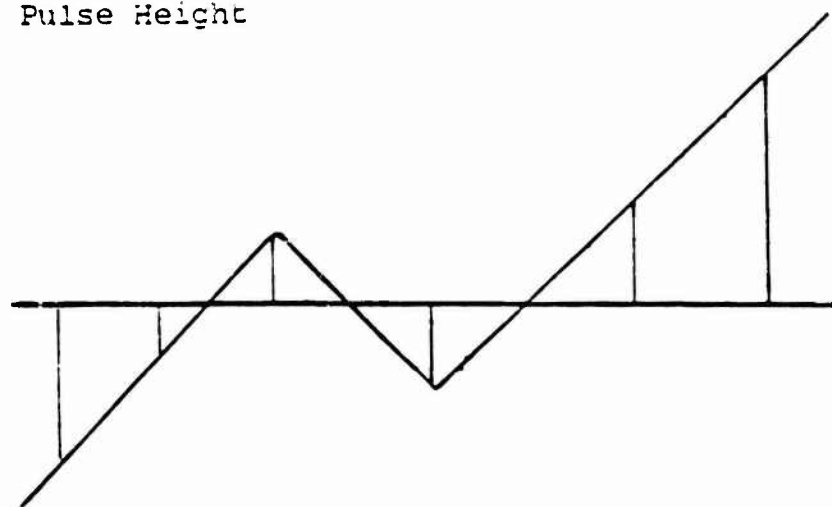


Fig. V-6c. Standard deviation of number of zero crossings vs rotation rate for a noisy re-entrant rotation sensor using cycle counting. Eight recirculations are used.



a)

Pulse Height



b)

Fig. V-7. Pulse heights vs time for a re-entrant rotation sensor: (a) noiseless, (b) noisy. Rotation rates are identical.

The next section deals with active re-entrant rotation sensors which have an optical amplifier in the sensing loop to compensate for loss. A new noise source is present, namely optical amplifier noise. The behavior of this system in the presence of noise is examined from the viewpoint of maintaining the signal to noise ratio above a specific value for as long as possible. In all rotation sensors, the error increases rapidly if too many recirculations are used.

VI. AMPLIFIER AND INCOHERENT RAYLEIGH BACKSCATTERING NOISE IN ACTIVE RE-ENTRANT ROTATION SENSORS

1. Amplifier Noise

The method for increasing the integration time which is being developed involves placing a bidirectional optical amplifier inside the optical fiber sensing loop. The gain of the amplifier is used to compensate for the loss in the sensing loop. This rotation sensor is termed an active, re-entrant pulsed fiber optic rotation sensor. A schematic of this rotation sensor is shown in Fig. VI-1. The differences between this system and the re-entrant system shown in Fig. VI-2 are the bidirectional amplifier and the reciprocity coupler. The reciprocity coupler assures that the counterpropagating waves travel the same optical path through the system. The amplifier reduces the loss in the loop and also adds noise to the system. In all other aspects the active re-entrant fiber optic rotation sensor is identical to the passive re-entrant fiber optic rotation system discussed previously.

Figure VI-3 shows the pulse train observed by the detector as a function of time. The pulse trains have a very gradual decay because the round trip loss is low. The noise which the amplifier introduces and amplifies in the loop serves to destroy the coherence between the counterpropagating pulses. This results in the depth of modulation of the envelope of the pulse train going to zero. When the depth of modulation falls below some value, the error in the measurement of the phase of

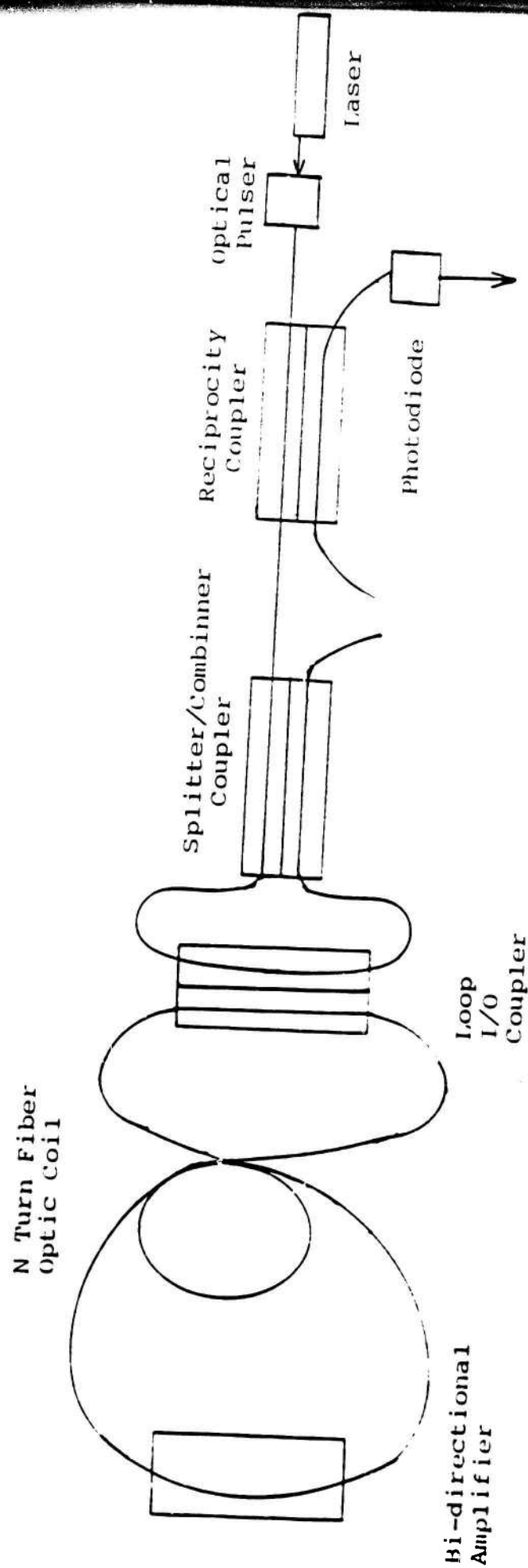


Fig. VI-1. Schematic of a reciprocal active re-entrant rotation sensor.

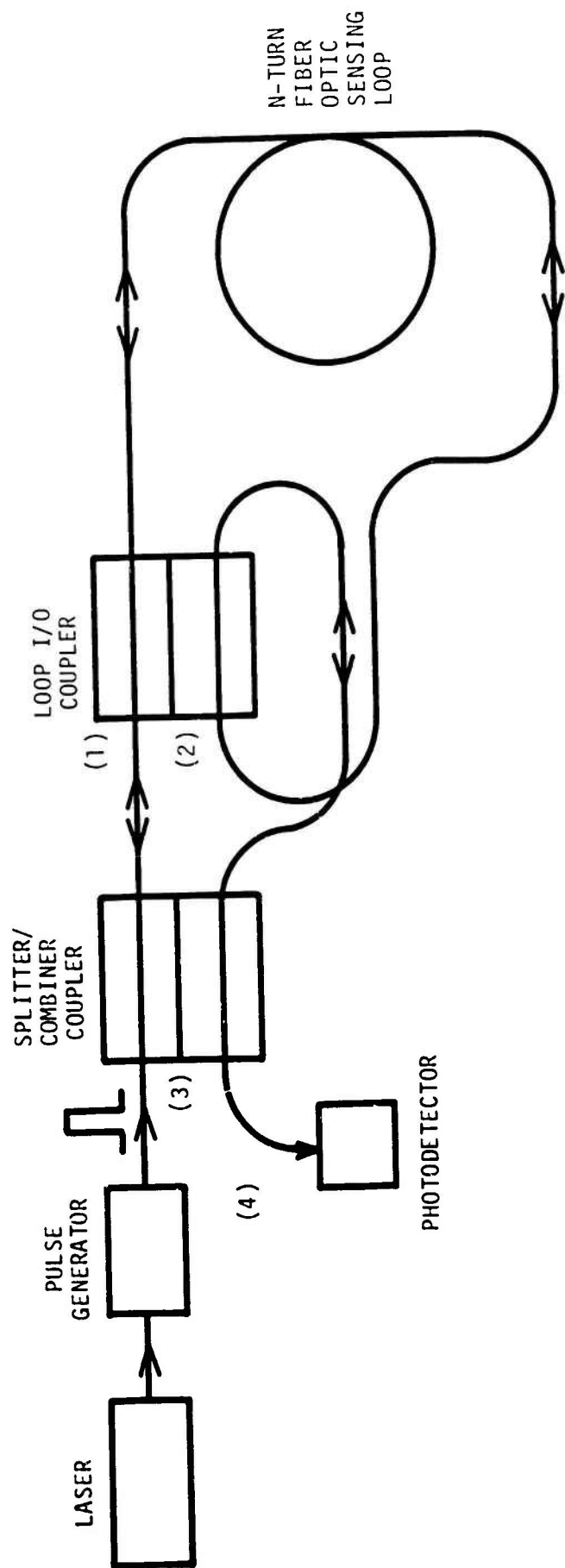


Fig. VI-2. Schematic of a basic passive re-entrant fiber optic rotation sensor. This rotation sensor is not completely reciprocal.



Fig. VI-3. Pulse intensity vs time for an active re-entrant rotation sensor. The loss of contrast of the pulse envelope is due to noise buildup caused by the bi-directional amplifier.

the envelope begins to increase rapidly and therefore sensitivity to rotation rate and angle decreases rapidly.

It will be first determined how the signal to noise ratio in the fiber optic sensing loop decreases due to amplifier noise. Other sources of noise will temporarily be neglected. The amplifier is assumed to have a noise input power of N_o . There can also be other noise (N_{other}) in the loop. The noise at the output of the amplifier is given as

$$N_{out} = (N_{other} + N_o) \exp(g) \quad (VI-1)$$

where $\exp(g) = G$ is the gain of the amplifier. Expressing the amplifier gain in this form will be convenient later.

The amplifier must be so placed in the loop, that the counterpropagating waves transit the amplifier simultaneously to avoid nonreciprocal effects. Thus in Fig. VI-4, the amplifier is placed at the midpoint of the sensing loop opposite the loop I/O coupler. The noise power grows as the number of recirculations increases. The noise power (N_K) for the K^{th} recirculation is given as:

$$N_K = N_o \delta \exp(\Delta + \alpha L/2) [\exp(Kx) - 1] / [1 - \exp(-x)] \quad (VI-2)$$

In this equation, δ is the coupling ratio of the loop I/O coupler, α is the loss per unit length of the fiber and L is the length of fiber. The quantities $\exp(\Delta)$ and x are defined as follows:

$$\begin{aligned} a. \quad & \exp(-\Delta) = 1 - \delta \\ b. \quad & x = g - \alpha L - \Delta \end{aligned} \quad (VI-3)$$

Equation VI-2 is derived by using Eq. VI-1. The other noise in the loop is assumed zero for the first recirculation in Eq. VI-2. The noise at the amplifier

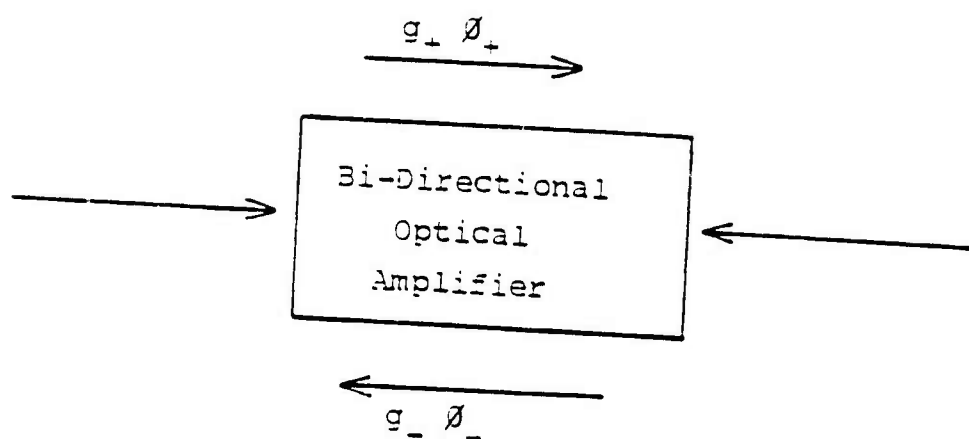


Fig. VI-4. Schematic of a nonreciprocal amplifier, g and \varnothing are the field gain coefficient and the phase shift of the amplifier.

output is propagated around the loop and becomes the other noise for the second recirculation. By continuing this procedure, a geometric series is obtained for N_K . Equation VI-2 is the sum of this geometric series.

The noise power incident on the detector for the K^{th} recirculation is given as

$$N_{amp}^{det}(K) = N(K)\gamma \quad (VI-4)$$

where γ is the loss between the loop I/O coupler and the detector.

The optical power, P_K , of the K^{th} recirculation of the signal in one direction at the output port of the loop I/O coupler is given as

$$P_K = P_o \delta^2 \exp(Kx) \exp(\Delta) \quad (VI-5)$$

where P_o is the power incident at one input port of the loop I/O coupler and δ and x are as before. The signal power detected at the detector is given as

$$P^{det}(K) = P_o \gamma \delta^2 \exp(Kx) (1 + \cos \phi_s) \exp(\Delta) \quad (VI-6)$$

ϕ_s is the Sagnac phase shift. In this equation all birefringence effects are neglected. It can be seen that the detected signal power of the K^{th} recirculation can have any value between zero and some maximum value P_K^{max} depending on the rotation rate. Significant errors in the measurement of the envelope phase will only begin to occur when the maximum detected signal power for K^{th} recirculation begins to approach the detected noise power of the K^{th} recirculation.

The detected signal to noise ratio can now be written as

$$(S/N)_{K,det} = (P_K^{max}/N_K)_{det} = \delta(P_o/N_o) \exp(-\alpha L/2) [1 - \exp(-x)] / [1 - \exp(-Kx)] \quad (VI-7)$$

where all the quantities have been defined previously. It is now desired to make the signal to noise ratio for the K^{th} recirculation as large as possible. This condition will give the maximum number of recirculations for a given signal to noise ratio. The parameter which is adjusted is the gain of the amplifier. The partial derivative with respect to g is taken of Eq. VI-7 and is set equal to zero. The result of this operation is

$$g = \alpha L + \Delta \quad (VI-8)$$

In physical terms this means that the gain of the amplifier equals the round trip loss of the loop. In practice, the gain of the amplifier will be slightly less than the round trip loss so as to avoid oscillation of the loop.

Evaluating Eq. VI-7 for the gain in Eq. VI-8 results in the number of recirculations for a given S/N ratio as

$$K = \delta(P_o/N_o) \exp(-\alpha L/2)/(S/N) \quad (VI-9)$$

In the re-entrant rotation sensor, it is the integration time and not the number of recirculations which is important. The integration time is given as

$$T_{int} = K T_o \quad (VI-10)$$

where T_o is the loop transit time. The loop transit time is

$$T_o = nL/c \quad (VI-11)$$

where L is the length of the fiber which forms the sensing loop, n is the index of refraction of the fiber and c is the in vacuo velocity of the light. Combining Eqs. VI-9, VI-10 and VI-11 results in the integration time

$$T_{int} = (\delta n/c)(P_o/N_o)L \exp(-\alpha L/2)/(S/N) \quad (VI-12)$$

This integration time can be maximized by adjusting the length of the fiber which forms the sensing loop. The fiber length which maximizes the integration time is given as

$$L = 2/\alpha \quad (VI-13)$$

The maximum integration time is given as

$$T_{int} = 4\delta n(P_o/N_o)/[\alpha c(S/N)e] \quad (VI-14)$$

The equivalent noise input power, N_o , can be written as

$$N_o = Fh\nu\Delta\nu \quad (VI-15)$$

where the F is the amplifier noise figure, h is Planck's constant, ν is the optical frequency and $\Delta\nu$ is the amplifier bandwidth. Assume the amplifier is formed from Nd:YAG, let the noise figure, F , equal 10, the optical frequency is about 300 THz for a wavelength of 1.06 μm , and the bandwidth is about 2 GHz. The equivalent noise input power is about 4 nW.

In evaluating Eq. VI-14, for the maximum integration time the following values are assumed for the other parameters

- a. $P_o = 100\text{mW}$
 - b. $S/N = 10$
 - c. $\delta = 0.01$
 - d. $\alpha = 1.8\text{dB/km}$
 - e. $n = 1.45$
- (VI-16)

These values are typical of the all fiber, passive re-entrant rotation sensor discussed previously. The maximum integration time is 0.21 seconds. This integration time

corresponds to minimum detectable rotation rate of 6.8 deg/hr for a rotation sensor of 10 cm diameter. This is not a too impressive rotation rate. Mechanical and laser gyroscopes can sense rotation rates of 10^{-2} to 10^{-3} deg/hr. How can the performance of the active re-entrant rotation sensor be improved?

Increasing the loop I/O coupler coupling ratio, δ from 1% to 10%, the minimum detectable rotation rate is improved to 6.8×10^{-1} deg/hr. This requires that the amplifier have ten times as much gain. The diameter of the sensing loop can also be increased. The minimum detectable rotation rate for sensing loop diameters of 1 and 10 meters is 6.8×10^{-2} deg/hr and 6.8×10^{-3} deg/hr. Finally, the required bandwidth of the amplifier can be decreased by using long pulses (e.g. pulsewidth equals half of the loop transit time). By using Eq. VI-13 to calculate the optimal length of the fiber, the pulse width which equals half the loop transit time is 6 μ s. This corresponds approximately to a bandwidth of about 170 KHz. The minimum detectable rotation rate can be as low as 5.8×10^{-6} deg/hr for a sensing loop diameter of 1 meter with a 10% loop I/O coupler coupling ratio. This is an impressive rotation rate. These results are summarized in Fig. VI-5.

2. Noise Due to Incoherent Backscattering

It is recognized today,⁷ that backscattered radiation which is superimposed on the optical signal waves can be the limiting factor in rotation sensor performance. The source of this backscattered radiation is Rayleigh scattering from the optical signal waves which is trapped by the fiber. The backscattered optical power can be expressed in the following form:

$$P = B\alpha P_o L_{int} \quad (VI-17)$$

where α is the fiber attenuation due to Rayleigh scattering, B is the trapping factor (i.e. fraction power trapped by the fiber in the backwards direction), L_{int} is the

δ (%)	Loop Diam. D (m)	Amplifier $\Delta\nu$	T_{int} (s)	Ω_{min} (deg/hr)
1	0.1	2 GHz	1.6	9.3×10^{-1}
10	0.1	2 GHz	16	9.3×10^{-2}
10	1	2 GHz	16	9.3×10^{-3}
10	10	2 GHz	16	9.3×10^{-4}
10	1	170 KHz	1.88×10^5	7.0×10^{-7}

Fig. VI-5. Minimum detectable rotation rate for various loop I/O coupling ratios, loop diameters, and amplifier bandwidths. Noise consists solely of amplifier noise.

length over which the backscattering occurs and P_o is the power of the forward wave. Eq. VI-17 is valid only if $\alpha L_{int} \ll 1$.

It will be assumed in the treatment which follows that the backscattered optical wave is not coherent with the forward optical wave (i.e. signal). It has been shown for single pass, CW fiber optic gyroscope⁸ that there is a small amount of coherence between the forward and backward waves. This residual coherence results in the backwards scattered wave having a larger effective noise power. Work is being done to reduce the coherence between the forward and backscattered waves. The ultimate lower noise limit caused by backscattered light waves occurs when they are not coherent with the forward light waves. The integration time calculated in this case will be an upper bound on the integration times achievable in practice.

In the re-entrant type of rotation sensor, there are two pulses which counterpropagate many times around the closed optical fiber sensing loop. A particular point on one of the optical pulses will pick up effective backscattered optical power only when it is overlapped by the other optical pulse. In the present case, the interaction length (L_{int}) in Eq. VI-17 is the pulse length. Each pulse generates backscattered waves at each point along the loop, but it is only the backscattered waves which are generated when the two pulses are coincident that arrive at the photodetector at the same time as the two pulses. The pulses overlap each other at two points in the sensing loop: at the beginning of the loop (i.e. at the loop I/O coupler) and at the midpoint of the loop (i.e. at the amplifier).

The build up of effective backscattered power will be treated as follows. Each time the pulses overlap, backscattered power as given by Eq. VI-17 is generated in each direction. This newly generated backscattered power is assumed to add incoherently to the backscattered power generated during previous pulse coincidences. This assumption allows for the slowest growth of the backscattered power and consequently, the longest integration time. In practice, there will be some degree of

coherence between the backscattered waves and the integration time will be smaller. The total backscattered power is then propagated around the loop until the next pulse coincidence.

The effective backscattered power generated when the pulses coincide at the amplifier is slightly modified from that given in Eq. VI-17. It is assumed that the forward wave is then amplified. The backscattered power at the amplifier is given as

$$P_{e,amp} = B\alpha P_o L_{pulse} \exp(2g) \quad (VI-18)$$

where L_{pulse} is pulse length and e^g is the amplifier gain. This is a worst case limit which applies when the amplifier length is much less than the pulse length.

Initially, there is no backscattered power in the sensing loop. At some time, T_o , two pulses are simultaneously injected into the loop in opposite direction by the loop I/O coupler. The backscattered power produced by the initial injection is less than that given by Eq. VI-17, since the two pulses are not really coincident. It is assumed, that this backscattered power is given by Eq. VI-17. This approximation is accurate to one part in K , where K is the number of recirculations. The backscattered noise power in one direction for the K^{th} recirculation can be written as:

$$N_e(K) = BP_o\alpha\delta^2 L_{pulse} \exp[K(g - \alpha L - \Delta)][K \exp(g) + K + 1] \quad (VI-19)$$

The above noise power is at one of the output ports of the loop I/O coupler. The total backscattered noise power reaching the detector is given in terms of $N_S(K)$.

$$N_S^{det}(K) = \gamma N_S(K) \quad (VI-20)$$

Combining Eqs. VI-2, VI-4, VI-6, VI-19, VI-20, the signal to noise ratio for the K^{th} recirculation is written as

$$\left(\frac{S}{N}\right)_K = \frac{P_o \delta}{\exp(\alpha L/2)[1 - \exp(-Kx)]/[1 - \exp(-x)] + \alpha \delta B P_o \exp(-\Delta)][K \exp(g) + K + 1]} \quad (\text{VI-21})$$

The maximum signal to noise ratio again occurs when the amplifier gain equals the roundtrip loop loss (i.e. $g = \alpha L + \Delta$). The signal to noise ratio now becomes:

$$\left(\frac{S}{N}\right)_K = \frac{P_o \delta}{N_o \exp(\alpha L/2)K + B P_o L_p K \alpha \delta \exp(-\Delta)[\exp(\alpha L + \Delta) + 1]} \quad (\text{VI-22})$$

where it has been assumed that $K[\exp(g) + 1] \gg 1$, for K large. The number of recirculations, K , for a given signal to noise ratio S/N can be written as

$$K = \frac{P_o \delta / (S/N)}{N_o \exp(\alpha L/2) + B P_o L_p \alpha \delta [\exp(\alpha L) + \exp(-\Delta)]} \quad (\text{VI-23})$$

The integration time can now be written as

$$T_{\text{int}} = \frac{\delta P_o L n / [c(S/N)]}{N_o \exp(\alpha L/2) + B P_o L_p \alpha \delta [\exp(\alpha L) + \exp(-\Delta)]} \quad (\text{VI-24})$$

The integration time must be maximized by proper choice of the loop length, L , and the pulse length, L_p .

Differentiating Eq. VI-24 with respect to L and setting it equal to zero, yields the following transcendental equation for L .

$$N_o \exp(\alpha L/2)(1 - \alpha L/2) + B P_o L_p \alpha \delta (1 - \alpha L) \exp(\alpha L) + B P_o L_p \alpha \delta \exp(-\Delta) = 0 \quad (\text{VI-25})$$

To solve this equation numerically, the pulse length, L_p , must be known.

The equivalent noise input power of the amplifier is given in Eq. VI-15. The bandwidth required for a particular pulse width can be approximately expressed as

$$\Delta\nu \simeq 1/\tau_p = c/nL_p \quad (VI-26)$$

The derivative of Eq. VI-24, with respect to the pulse length, L_p , is taken and set equal to zero. The optimum pulse length is

$$L_p = \sqrt{\frac{F h \nu c / n}{B P_a \alpha \delta [\exp(\alpha L) + \exp(-\Delta)]}} \quad (VI-27)$$

where F_a is the noise figure of the amplifier and B is the trapping factor for the backscattered radiation. The length of the fiber, L , must be known to solve for the pulse length.

No maximization of Eq VI-24 with respect to δ need be done. This is because Eq. VI-24 is monotonically increasing for $\delta \in [0, 1]$. The simultaneous numerical solution of Eq. VI-27 some value of L is assumed and the corresponding pulse length is calculated. This pulse length is then used in Eq. VI-25 and a new value of the length of the loop L is calculated. This new value of L is then substituted back into Eq. VI-25 and the above procedure is done again. The values of loop length and pulse length so obtained converge rapidly. After four iterations, L and L_p are known to one part in ten thousand.

This iterative procedure was carried out for loop I/O coupling ratios of 1 and 10 percent. The result for these calculations are summarized in Fig. VI-6. The diameter of the rotation sensor is assumed to be 10 cm as before to facilitate comparisons.

Comparisons of Figs. VI-5 and VI-6 show that the inclusion of backscattered optical radiation as an incoherent noise source decreases the sensitivity of the rotation sensor by at least an order of magnitude. If the backscattered optical radiation is treated as a coherent noise source then the sensitivity is decreased

δ	τ_p (nS)	$\Delta\nu$ (GHz)	L (Km)	T_{int} (mS)	Ω_{min} (deg/hr)
0.01	0.85	1.12	2.12	278	5.4
0.10	0.28	3.5	2.10	886	1.7

Fig. VI-6. Minimum detectable rotation rate as a function of the loop I/O coupling ratio for active re-entrant gyro with backscattering.

even more. The only way to reduce the effect of backscattering is to go to longer wavelengths, since Rayleigh scattering scales as the inverse of the fourth power of the length. Large diameters can also be used to increase rotation sensitivity.

VII. AMPLIFIER NONRECIPROCITY

It has been shown that amplifier noise and backscattering noise can be limiting factors on the performance of an active re-entrant fiber optic rotation sensor. There is another factor which could be a limiting factor on the performance: the nonreciprocity of the amplifier.

The power gain of the amplifier is represented $\exp(g)$ where g is the power gain coefficient. The complex field transfer coefficient of the amplifier can be represented as:

$$g_{field} = g/2 + j\phi \quad (VII-1)$$

where $g/2$ is the field gain coefficient and ϕ is the phase shift of the amplifier. A differential, complex field gain coefficient $\hat{\gamma}$ is defined by the following integral equation:

$$g_{field} = \int_0^L \hat{\gamma}(z, t) dz \quad (VII-2)$$

where L is the length of the amplifier and z is the coordinate along the amplifier axis. The differential field gain coefficient is a function of position and time. This differential gain coefficient can be viewed as a complex propagation constant. For the amplifier to be reciprocal requires that the differential gain coefficient, $\hat{\gamma}$, satisfy the same conditions as does the fiber propagation constant, β , for a reciprocal fiber. These conditions can be written as:

$$\begin{aligned} a. \quad \hat{\gamma}(z, t) &= \hat{\gamma}(L - z, t) \\ b. \quad \hat{\gamma}(z, t) &= \hat{\gamma}(z, \tau - t) \end{aligned} \quad (VII-3)$$

where L is the length of the amplifier and τ is the transit time of the amplifier. These equations are only valid if the counterpropagating waves are simultaneously incident at the ends of the fiber amplifier.

If the amplifier is nonreciprocal then the complex field transfer coefficient is not the same for each direction through the amplifier. Let g_{field}^+ and g_{field}^- be the transfer coefficients in the $+z$ and $-z$ directions respectively (Fig. VI-4). These transfer coefficients can differ in the field gain coefficient, the phase shift or both.

The effect of a difference in field gain coefficients is a reduction in visibility⁹ of the envelope of the detected pulse trains. The visibility of a particular recirculation is defined as:

$$V = \frac{I_{\max}^{(K)} - I_{\min}^{(K)}}{I_{\max}^{(K)} + I_{\min}^{(K)}} \quad (VII-4)$$

where $I_{\max}^{(K)}$ and $I_{\min}^{(K)}$ are the maximum and minimum intensities of the K^{th} recirculation. The visibility is one for the 0^{th} recirculation and decreases to zero as K goes to infinity. In terms of signal to noise ratio, the effect of unequal field gain coefficients is an additional attenuation of the signal power.

Let $g_+/2$ and $g_-/2$ be the field gain coefficients in the $+z$ and $-z$ directions. The magnitudes of the field for the K^{th} recirculation traveling in the $+z$ and $-z$ directions can be written as

$$\begin{aligned} a. \quad |E_+(K)| &= \sqrt{\delta} |E(o)| \exp[K(g_+ - \alpha L - \Delta)/2] \\ b. \quad |E_-(K)| &= \sqrt{\delta} |E(o)| \exp[K(g_- - \alpha L - \Delta)/2] \end{aligned} \quad (VII-5)$$

where $|E(o)|$ is the field magnitude at each input port of the loop I/O coupler at time $t = 0$. Optimum signal to noise ratio is still obtained if either g_+ or g_- equals the round trip loss. Let g_+ equal the round trip loop loss, but g_- is slightly less than the round trip loss ($\alpha L - \Delta$)

$$\begin{aligned} a. \quad g_+ - \alpha L - \Delta &= 0 \\ b. \quad g_- - \alpha L - \Delta &= -\epsilon \quad \epsilon > 0 \end{aligned} \quad (VII-6)$$

The fields for the K^{th} recirculation now become:

$$\begin{aligned} a. \quad |E_+(K)| &= |E(O)| \\ b. \quad |E_-(K)| &= |E(O)| \exp(-K\epsilon/2) \end{aligned} \quad (VII-7)$$

The detected signal power, P_{sig} , for the K^{th} recirculation is the difference between the maximum and minimum detected powers for the K^{th} recirculation.

$$P_{sig}(K) = P_{max}(K) - P_{min}(K) \quad (VII-8)$$

The maximum and minimum detected power can be written as

$$\begin{aligned} a. \quad P_{max}(K) &= 0.5\delta^2 P_o |1 + \exp(-\epsilon K/2)|^2 \\ b. \quad P_{min}(K) &= 0.5\delta^2 P_o |1 - \exp(-\epsilon K/2)|^2 \end{aligned} \quad (VII-9)$$

Substituting Eqs. VII-9 into Eq. VII-8, the detected signal power for the K^{th} recirculation becomes

$$P_{sig}(K) = 2\delta^2 P_o e(-\epsilon K) \quad (VII-10)$$

where P_o is the power at each input port of the loop I/O coupler at $t = 0$ (i.e. $P_o = |E(o)|^2$). The detected signal power now decreases with increasing number of recirculations. Previously, with a reciprocal amplifier, the signal power has been constant while only the noise power has increased.

The number of recirculations, K , obtained with a nonreciprocal amplifier which has a nonreciprocity in the power gain of ϵ is now given as:

$$K \exp(\epsilon K) = K_o \quad (VII-11)$$

where K_o is the number of recirculations if the amplifier is reciprocal (i.e. $\epsilon = 0$). From this equation, it is seen that a nonreciprocal amplifier reduces the number of recirculations for a given signal to noise ratio. This results in a lower sensitivity for the re-entrant rotation sensor which uses a nonreciprocal amplifier.

For numerical evaluation of the allowable nonreciprocity, ϵ , in the power gain of the amplifier, the following criteria will be used. The maximum allowable amplifier power gain nonreciprocity is that which reduces the number of recirculations to one half of the number of recirculations obtained with a reciprocal amplifier. In this case the rotation sensitivity is one half of the ideal rotation sensitivity. This power gain nonreciprocity which causes a 3 dB reduction in recirculations and rotation sensitivity satisfies the following equation:

$$(K_o/2) \exp[(K_o/2)\epsilon_{3dB}] = K_o \quad (VII-12)$$

This equation can be solved for ϵ_{3dB} . This nonreciprocity is given as

$$\epsilon_{3dB} = 2 \ln(2/K_o) \quad (VII-13)$$

The table in Fig. VII-1 shows ϵ_{3dB} for various numbers of recirculations, K_o .

In the tables in Fig. VI-5 and VI-6, the number of recirculations is between 10^4 and 10^6 . At this writing, no data is available for power gain nonreciprocity in bidirectional optical amplifiers. The tolerable nonreciprocities in Fig. VII-1 appear to be restrictive.

The field gain coefficients are now assumed to be equal. The phase shift ϕ of the amplifier is assumed to depend on the direction of propagation through the amplifier. The amplifier will now introduce a phase shift, ϕ_{amp} , between the counterpropagating electromagnetic waves which can be written as:

$$\phi_{amp} = \phi_+ - \phi_- \quad (VII-14)$$

K_o	ϵ_{3dB}
10^3	1.39×10^{-3}
10^4	1.39×10^{-4}
10^5	1.39×10^{-5}
10^6	1.39×10^{-6}
10^7	1.39×10^{-7}
10^8	1.39×10^{-8}

Fig. VII-1. Amplifier power gain non-reciprocity which results in a 3 dB reduction in recirculations and rotation sensitivity in a re-entrant rotation sensor vs the maximum number of recirculations.

where ϕ_+ and ϕ_- are the phase shifts through the amplifier in the + and - directions respectively. This amplifier induced nonreciprocal phase shift per pass is indistinguishable from the Sagnac phase shift per pass in general.

The nonreciprocal phase shift for the K^{th} recirculation, $\phi(K)$, is now given as

$$\phi(K) = K(\phi_S + \phi_{amp}) \quad (VII-15)$$

where ϕ_S and ϕ_{amp} are the Sagnac phase shift and the amplifier phase per pass respectively. The measured envelope frequency, F_m , associated with this phase dependence is

$$F_m = F_{rot} + F_{amp} \quad (VII-16)$$

where F_{rot} is the frequency due to rotation and F_{amp} is the frequency due to the phase nonreciprocity of the amplifier.

$$\begin{aligned} a. \quad F_{rot} &= \frac{4A\Omega}{nP\lambda} \\ b. \quad F_{amp} &= c\phi_{amp}/2mL \end{aligned} \quad (VII-17)$$

In the above equation, c is the velocity of light in free space, n the index of the guiding medium, Ω the angular velocity of the sensor, L the length of the loop, A its area and P its perimeter.

The measured envelope frequency, F_m , is related to the angular velocity by Eq. VII-17. The amplifier phase nonreciprocity introduces an error into the measurement of the angular velocity of the system. This error Ω_{error} , can be written as:

$$\Omega_{error} = \Omega_{meas} - \Omega_{act} = (\lambda c/8\pi)(1/NA)\phi_{amp} \quad (VII-18)$$

where Ω_{meas} and Ω_{act} are the measured and actual rotation rate respectively, λ and c are the free space values of the wave length and speed of light. A is the area

enclosed by the optical fiber sensing loop. N is the number of turns of optical fiber about this area and ϕ_{amp} is as before. If the optical fiber sensing loop is circular, then Eq. VII - 18 becomes:

$$\Omega_{error} = (\lambda c / 2\pi)(1/LD)\phi_{amp} \quad (VII - 19)$$

where L is the length of the optical fiber and D is the diameter of the sensing loop.

Assume that a fiber length 2.1 Km is wound about a cylindrical form of 10 cm diameter to form an active re-entrant rotation sensor. The minimum detectable rotation rates for this rotation sensor are shown in Fig. VI-6, where the backscattered power is incoherent with the signal power. The amplifier phase nonreciprocity will be calculated which gives an angular velocity error just equal to the minimum detectable rotation rate for each entry in Fig. VI-6. These results are summarized in Fig. VII-1.

Again, no information exists for phase nonreciprocity in bidirectional optical amplifiers. The quantities specified in Fig. VII-2 appear to be restrictive. If the diameter of the sensing loop is increased to achieve a lower minimum detectable rotation rate, the amplifier phase nonreciprocity remains constant. This occurs because the minimum detectable rotation rate and the rotation rate error are both inversely proportional to the diameter of the sensing loop. If the length of the optical fiber sensing loop is increased by using a fiber with a lower attenuation, the behavior of the allowable amplifier phase nonreciprocity is not easily determined. This arises because the rotation rate error is inversely proportional to the fiber length, but the minimum detectable rotation rate has a nonlinear dependence on the fiber length through Eqs. VI - 25 and VI - 27. If the minimum detectable rotation rate is decreased by changing the loop I/O coupler coupling ratio, then the allowable amplifier phase nonreciprocity also decreases. Work needs to be done on bidirectional optical amplifiers.

$\Omega_{\text{error}}(\text{deg/hr})$	$\phi_{\text{amp}}(\text{rad/pass})$
5.4	1.15×10^{-4}
1.7	3.63×10^{-5}

Fig. VII-2. Amplifier phase non-reciprocity for various measured errors in the angular velocity for active re-entrant rotation sensor.

VIII. MULTIMODE FIBER GYROS

Another task under the contract during the reporting period has resulted in a proposal for a new form of single pass cw gyro using multimode fiber. A generalization of the analysis reveals that using many modes in a multimode fiber carries the advantage much further, but again complete independence and maintenance of mode intensity and orthogonality (but not mode integrity) is required.¹⁰ The multimode gyro is considered to be potentially very important because, in addition to allowing the use of multimode fiber which eases coupling problems, it eliminates the need for a polarizer. This is a major consideration because of the strict requirements imposed on the polarizer by the very small optical phase shifts which must be sensed by the gyro measuring small rotation rates involved in inertial navigation.

Earlier under the AFOSR program¹ we developed an analysis which extended the conditions of operation of single pass cw fiber gyros using single mode fiber by lifting the requirement that the degree of polarization be unity, i.e. that the state of polarization be constant in time. This allowed the calculation of the response of the gyro for an arbitrary state of polarization of the input light and for arbitrary birefringence in the fiber. This work showed that the gyro could be operated with completely unpolarized light, thus eliminating the polarizer, and that this type of operation would allow the full sensitivity of the system to small rotation rates to be retained.

During the reporting period we continued this analytical work, extending it to the case of prospective gyros in which the single mode fiber would be replaced by general multimode fiber.

In the analysis of the multimode systems we have been able to show that an essential property, referred to as reciprocity, is retained. In the conventional fiber gyro using single mode fiber and polarized light, reciprocity, which is necessary for high gyro sensitivity, requires the use of a polarizer with requirements on the

discrimination ratio which can be as high as 100 dB.

We can perhaps clarify this further as follows. It is first helpful to consider the nature of the output response of single pass gyros. In these systems the detector current is a periodic function of the rotation rate being measured. As a result, the system must be biased so that the current at zero rotation rate occurs halfway between a maximum and minimum of this periodic function where the response to a small increment of rotation is maximum and linear. Without bias this operating point occurs at a maximum of the detector current where the response is minimum and nonlinear. This requires the introduction of a quadrature phase relationship between the two optical waves, clockwise and counterclockwise, which propagate around the fiber sensing loop.

A properly biased gyro, with reciprocity, has the property that, **at the bias point**, the output current is independent of changes in the propagation constants of the fiber in the sensing loop, such as are produced by environmental effects acting on the fiber. Our work showed that this property is possessed intrinsically by the proposed multimode system, free of polarizers when it is properly excited.

A schematic diagram of the proposed multimode gyro is shown in Fig. VIII-1. The couplers could be bulk beam splitters, but fiber directional couplers would be preferable. The differences between this circuit and that of the conventional fiber gyro are in the multimode specifications of the source and sensing loop, and the absence of a polarizer which in the conventional case is located in series with the path between the two couplers.

Details of this system are given in the Appendix.

The concept of reciprocal gyros was introduced under the AFOSR program, including the need for polarizers in gyros using polarized light.¹¹ This was followed by introduction of the concept of sensitivity limitations in gyros due to Rayleigh scattering in the fiber, and the primary approach of source spectrum broadening

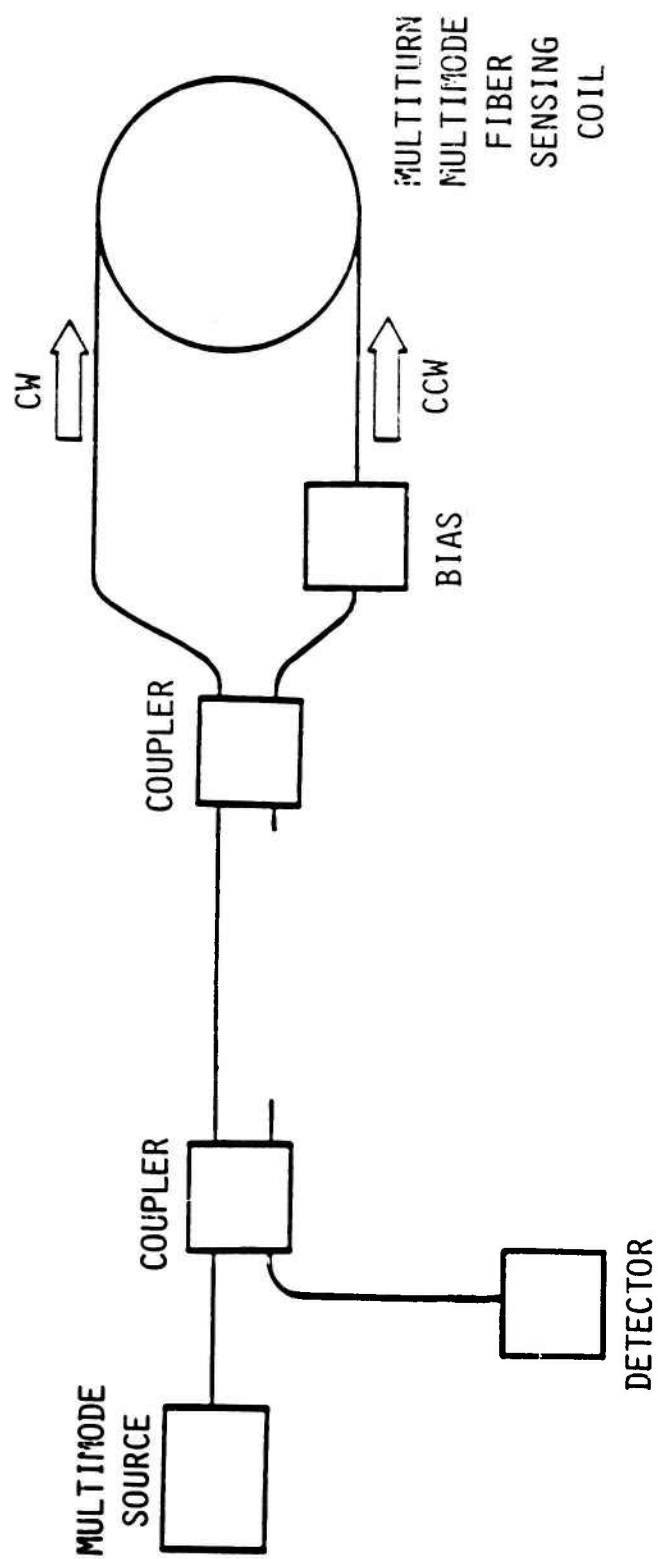


Fig. VIII-1. Multimode fiber gyro schematic.

to reduce the effects.¹² These are two of the key considerations which have led to the realization of single pass fiber gyros whose threshold sensitivity and drift are consistent with requirements of long term navigation. Another of the key factors has been control of the nonlinear optical Kerr effect, which was developed in this laboratory under another program. These procedures have become rather standard in the fiber gyro art. The newer proposals for single pass gyros, namely unpolarized single pass systems, and multimode systems, arose from extensions of the analytical work which led to the earlier advances.

IX. ANALYSIS OF SOURCE CHARACTERISTICS AND SCATTERING IN FIBER GYROS

The study of scattering in optical fibers has continued⁷ with effort to relate the inherent Rayleigh scattering in fibers to errors in optical fiber sensors, particularly the Sagnac interferometer. Error signals may arise from fluctuations inherent in the optical source; secondary waves from regions near the center of a Sagnac loop which are substantially coherent with the primary waves; and waves scattered by inhomogenities which are substantially uncorrelated. The relative strength of the fluctuations depends upon the characteristics of the source, its coherence time/length, whether it has multi (longitudinal) modes or not, and whether it is gain-saturated (constant intensity) or not. Calculations indicate that very broadband multimode low coherence gain saturated lasers are a good, and perhaps best signal source for single pass optical fiber gyros. With such a source it is probable that the "incoherent" scatter provides the largest potential error, but is likely to be smaller than errors due to environmental effects. Further work is necessary to relate specific details of existing optical sources to specific interferometer designs, to determine the relevant time constants of scattering phenomena and to obtain quantitative evaluations of error. A study on the reduction of backscattering error⁵ has revealed that the use of short signal pulses or equivalent chirped pulses and suitable

modifications of the fiber loop can greatly reduce the error due to backscattering.

X. REFERENCES

1. Interim Scientific Report, Contract F49620-80-C-0040, Edward L. Ginzton Laboratory Report No. 3341, Stanford University (December 1981).
2. G. A. Pavlath and H. J. Shaw, "Re-entrant Fiber Optic Rotation Sensors," **Fiber Optic Rotation Sensors and Related Technologies**, Springer Series in Optical Sciences, Volume 32, edited by S. Ezekiel and H. J. Arditty, Springer-Verlag, Berlin, Heidelberg, New York, 1982, p. 364-367 (See Appendix).
3. G. A. Pavlath and H. J. Shaw, "Unpolarized Operation of Fiber-Optic Rotation Sensors," *CLEO* **81**, 126-127 (1981) (See Appendix).
4. R. A. Bergh, G. Kotler and H. J. Shaw, "Single-Mode Fiber-Optic Directional Coupler," *Electron. Lett.* **16**, 260-261 (1980).
5. P. R. Bevington, **Data Reduction and Error Analysis for the Physical Sciences**, (McGraw-Hill, New York, 1965), p. 204.
6. A. Papoulis, **Probability, Random Variables, and Stochastic Processes**, (McGraw-Hill, New York, 1965), p. 153.
7. C. C. Cutler, S. A. Newton and H. J. Shaw, "Limitation of Rotation Sensing by Scattering," *Opt. Lett.* **5**, 488-490 (1980).
8. R. A. Bergh, H. C. Lefevre and H. J. Shaw, "All-Single-Mode Fiber-Optic Gyroscope," *Opt. Lett.* **6**, 198-200 (1981).
9. E. Born and M. Wolf, **Principles of Optics: Electro-Magnetic Theory of Propagation Interference and Diffraction of Light**, (Pergamon Press, New York, 1980) 6th ed., p. 267.
10. G. A. Pavlath and H. J. Shaw, "Multimode Fiber Gyroscopes," **Fiber Optic Rotation Sensors and Related Technologies**, Springer Series in Optical Sciences, Volume 32, edited by S. Ezekiel and H. J. Arditty, Springer-Verlag, Berlin, Heidelberg, New York, 1982, p. 111-115 (See Appendix).
11. H. Arditty, H. J. Shaw, M. Chodorow and R. Kompfner, "Re-entrant Fiber-Optic Approach to Rotation Sensing," *Proc. Soc. Photo Opt. Inst. Eng.*, Vol. **157**, Aug. 1978, p. 138.
12. S. A. Newton, C. C. Cutler and H. J. Shaw, "Reduction of Backscattering Error in an Optical Fiber Gyro," *IEEE J. Quan. Elect.*, QE-17 (II), **44** (1981) (See Appendix).
13. H. C. Lefevre, R. A. Bergh and H. J. Shaw, "All-Fiber Gyroscope with Inertial Navigation Short-Term Sensitivity," *Opt. Lett.* **7**, 9, 454-456 (Sept. 1982).

XI. PUBLICATIONS AND REPORTS

Following is a list of publications and reports covering work done wholly or partly under Contract F49620-80-C-0040.

1. C. C. Cutler, S. A. Newton and H. J. Shaw, "Limitation of Rotation Sensing by Scattering," Edward L. Ginzton Laboratory Report No. 3150, Stanford University (July 1980); Opt. Lett. **5**, 11, 488-490 (November 1980).
2. G. A. Pavlath and H. J. Shaw, "Re-Entrant Fiber Optic Rotation Sensors," **Fiber Optic Rotation Sensors and Related Technologies**, Springer Series in Optical Sciences, Volume 32, edited by S. Ezekiel and H. J. Arditty, Springer-Verlag, Berlin, Heidelberg, New York, 1982, p. 361.
3. G. Pavlath and H. J. Shaw, "Unpolarized Operation of Fiber Optic Rotation Sensors," Digest of Conference on Lasers and Electro-Optics (CLEO '81), Washington, D. C. (June 10-12, 1981).
4. G. A. Pavlath and H. J. Shaw, "Multimode Fiber Gyroscopes," **Fiber Optic Rotation Sensors and Related Technologies**, Springer Series in Optical Sciences, Volume 32, edited by S. Ezekiel and H. J. Arditty, Springer-Verlag, Berlin, Heidelberg, New York, 1982, p. 111.
5. S. A. Newton, C. C. Cutler and H. J. Shaw, "Reduction of Backscattering Error in an Optical Fiber Gyro," Digest of Conference on Lasers and Electro-Optics (CLEO '81), Washington, D. C. (June 10-12, 1981).
6. G. A. Pavlath and H. J. Shaw, "Birefringence and Polarization Effects in Fiber Gyroscopes," Appl. Opt. **21**, 10, 1752-1757 (15 May 1982).
7. R. A. Bergh, C. C. Cutler, H. C. Lefevre, S. A. Newton, G. A. Pavlath and H. J. Shaw, "The All-Fiber Gyroscope: A Practical Alternative for Rotation Sensing," Invited paper for the Sixth Topical Meeting on Integrated and Guided Wave Optics, Asilomar, California (January 6-8, 1982).
8. Technical Report excerpt from G. A. Pavlath, "Fiber-Optic Rotation Sensors: Alternate Configurations and Modes of Operation," Edward L. Ginzton Laboratory Report No. 3551, Stanford University (March 1983).
9. "Work Progresses on Fiber Optic Gyro," Aviation Week & Space Technology (December 7, 1981), p. 64.
10. G. A. Pavlath and H. J. Shaw, "Stability of Fiber Optic Rotation Sensors Under Various Polarization Conditions," Edward L. Ginzton Laboratory Report No. 3163, Stanford University (August 1980).
11. Interim Scientific Report for Contract F49620-80-C-0040, Edward L. Ginzton Laboratory Report No. 3341, Stanford University (December 1981).

APPENDIX

This appendix contains reprints of publications on work done wholly or partly under Contract F49620-80-C-0040 during the period of January 1, 1981 through April 30, 1982.

RE-ENTRANT FIBER OPTIC ROTATION SENSORS

G. A. Pavlath and H. J. Shaw
Edward L. Ginzton Laboratory
Stanford University
Stanford, CA 94305

A recirculating fiber optic rotation sensor is described which employs multiple transits of pulsed light around a closed coil of optical fiber. An all-fiber implementation of this re-entrant rotation sensor is presented. The experimental results verify the basic operation of the device.

Present fiber optic rotation sensors propagate cw light once around an N-turn optical fiber coil. In re-entrant rotation sensors, [1] the N-turn optical fiber coil is closed so that pulsed light can propagate many times around the coil. The Sagnac phase shift is increased proportionally to the number of recirculations of the light around the optical fiber coil. Thus, in effect, the length of the fiber is increased by the factor N.

Fig.1 shows the schematic of the present re-entrant rotation sensor. It is constructed in all-fiber form, without splices, using single-mode fiber components.

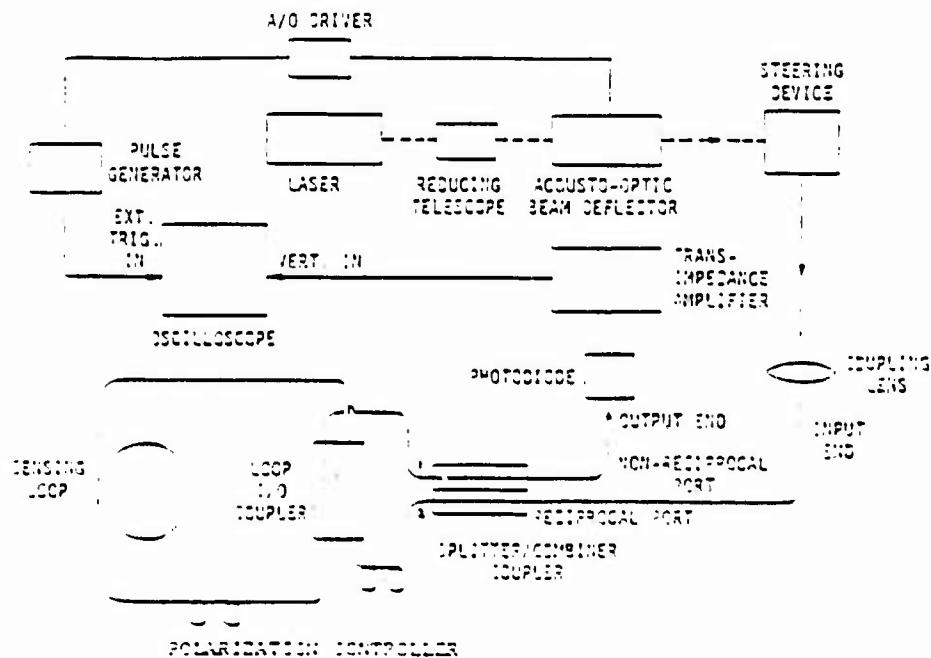


Fig.1 All fiber optic, passive, reentrant rotation sensor schematic

An optical pulse obtained from a Nd:YAG laser by an acousto-optic beam deflector is coupled in to the fiber by a coupling lens. This pulse propagates to the splitter/combiner coupler, which is a fiber-to-fiber evanescent field coupler, [2,3] where it is split into two equal parts. These pulses

APPENDIX

This appendix contains reprints of publications on work done wholly or partly under Contract F49620-80-C-0040 during the period of January 1, 1981 through April 30, 1982.

propagate to the loop I/O coupler where portions of the pulses are injected into the loop in opposite directions. This coupler is adjusted for a coupling coefficient near unity. The pulses propagate around the loop many times. After each transit around the loop, a portion of each pulse is coupled out. These sampled pulses are recombined by the splitter/combiner coupler and detected by a germanium photodiode. The polarization controllers [3,4] compensate for birefringence in the fiber, and allow the interferometer to be easily balanced at zero rotation rate.

We have found in practice that the requirements of this interferometer, namely efficient and balanced injection of pulses into the sensing coil together with efficient and balanced reinjection of pulses after each circulation, are difficult to satisfy with bulk optics components external to the fiber requiring a large number of alignments and adjustments which are not independent. The present all-fiber version involves no alignments and contains only four adjustments (two coupler and two polarization controllers) which are non-interacting and very easily made and maintained, leading to excellent performance of the interferometer.

Each input pulse gives rise to a train of pulses at the photodiode with pulse spacing equal to the loop transit time (Fig.2). The envelope of the

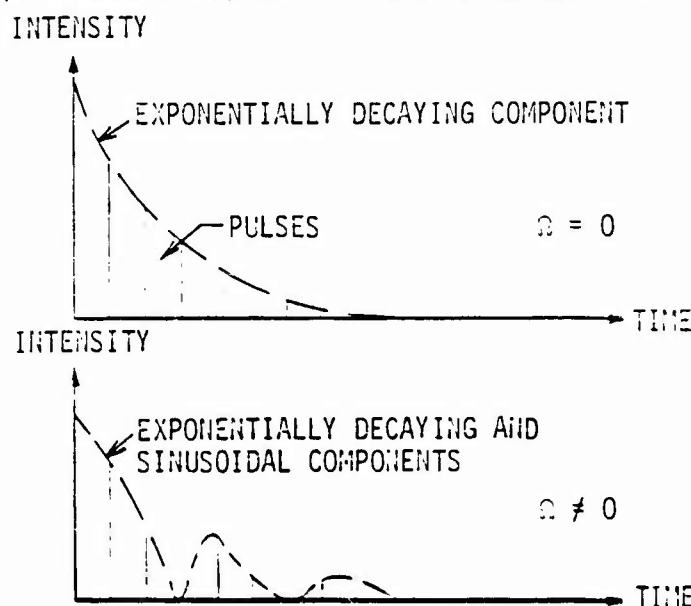


Fig.2 Detected pulse trains at rest and during rotation

pulse train has an exponentially decaying component due to loss in the sensing loop and a sinusoidal component whose frequency is proportional to the rotation rate. The latter occurs because the Sagnac phase shift increases linearly with the number of transits around the loop while the pulse height is proportional to the cosine of the Sagnac phase shift.

For a circular sensing loop of diameter D , the frequency, F , of the sinusoidal component of the pulse train envelope is

$$F = \frac{D}{\lambda} \Omega \quad (1)$$

where λ is the wavelength and Ω is the rotation rate. The accumulated phase $\phi(t)$ of the sinusoidal envelope component in a time T is proportional to the angle turned through $\theta(T)$ as

$$\phi(T) = \int_0^T F(g) dt = \frac{D}{\lambda} \phi(T) \quad (2)$$

Thus with a re-entrant rotation sensor the integration which yields the angular position change is accomplished optically.

Fig.3 shows the measured pulse trains at various rotation rates for the

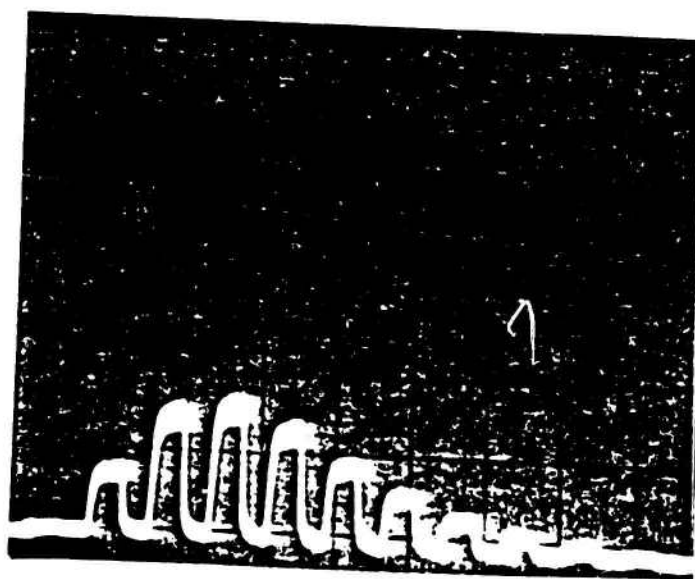
5 μ s/div

5 mV/div



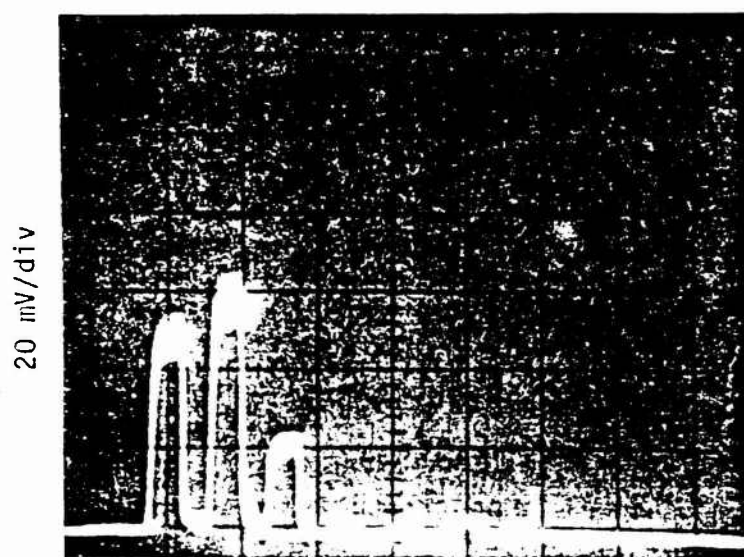
$\Omega = 0$ rad/sec

5 mV/div

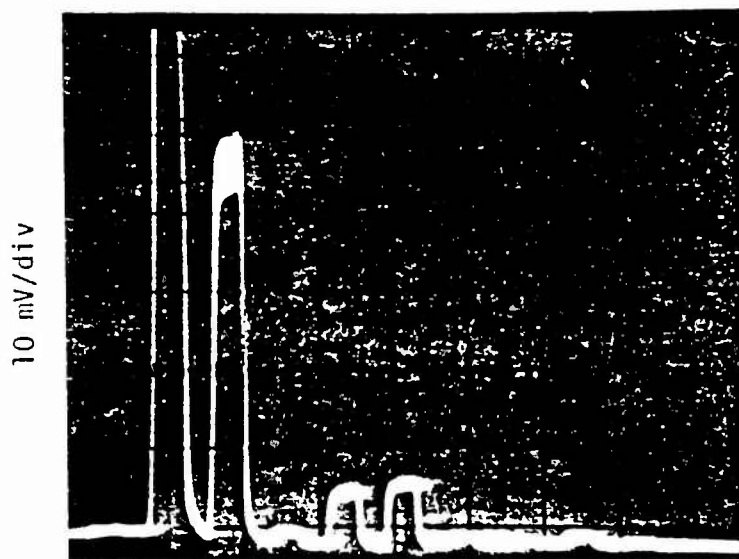


$\Omega = 0.16$ rad/sec

re-entrant rotation sensor depicted in Fig.1. The sensing loop was an 830 meter length of Corning single-mode fiber wound on a circular form of 15 cm diameter. The attenuation of the fiber was measured at 1.3 dB/km at 1.06 μ m. At rest a 180 degree phase shift, which results from the splitting/recombining process, exists between the counterpropagating pulses. This results in a straight base line as the output if the rotation sensor is properly balanced. The thickness of the line is due to the thermal noise of



$$\Omega = 0.58 \text{ rad/sec}$$



$$\Omega = 0.82 \text{ rad/sec}$$

Fig.3 Experimental output pulse trains

the detector and corresponds to 50 nW of optical power.

When the sensor is rotated, the envelope of the pulse train is a decaying sinusoid. The rotation rates in Fig.3 were chosen to give approximately 1, 2, and 3 cycles of the sinusoidal component. The measured pulse trains are in agreement with theory.

In conclusion, an all-fiber re-entrant rotation sensor has been constructed. It has shown that pulses can be recirculated many times (10) and that the Sagnac phase shift accumulates for multiple transits of the sensing. An optical amplifier will be placed in the sensing loop to compensate for loss in order to extend the number of recirculations by a very large factor.

The potential of reentrant systems for sensing very small rotation rates will be evaluated, including the use of large diameter sensing loops where

the use of such loops is applicable. This reentrant system is also a good vehicle for studying the effects of Rayleigh backscattering in fiber optic rotation sensors.

- ¹H. J. Arditty, H. J. Shaw, M. Chodorow, and R. Kompfner, "Re-entrant Fiber Optic Approach to Rotation Sensing," Proc. Soc. Photo-Opt. Instrum. Eng. 157, 138-148 (1978).
- ²R. Bergh, G. Kotler, and H. J. Shaw, "Single-mode Fiber-optic Directional Coupler," Electronics Letters 16, 260-261 (1980).
- ³M. Digonnet and H. J. Shaw, "Analysis of a Tunable Single Mode Optical Fiber Coupler," to be published in the April 1982 issue of IEEE Journal of Quantum Electronics.
- ⁴H. Lefevre, "Single-mode Fiber Fractional Wave Devices and Polarization Controllers," Electronics Letters 16, 778-780 (1980).

This work was supported by the Air Force Office of Scientific Research under Contract F49620-80-C-0040.

UNPOLARIZED OPERATION OF FIBER OPTIC ROTATION SENSORS

G. Pavlath and H. J. Shaw

Edward L. Ginzton Laboratory
Stanford University
Stanford, CA 94305

415 + 497-0203

ABSTRACT

Reciprocal operation of a fiber optic rotation sensor using unpolarized light is presented. The existence of stable operating points which are unaffected by slow environmental changes, to which the sensor can be biased is shown.

UNPOLARIZED, RECIPROCAL OPERATION OF FIBER OPTIC ROTATION SENSORS

G. Pavlath and H. J. Shaw

Edward L. Ginzton Laboratory
Stanford University, Stanford, California 94305

(415) 497-0203

SUMMARY

A non-rotationally induced differential phase shift is present in fiber optic rotation sensors if the polarization in the optical fiber is not conserved or controlled. This phase shift is caused by residual birefringence in the optical fiber. It can be quite large and very sensitive to the environment. It has been shown¹ that this phase shift can be eliminated by correct usage of a polarization analyzer. There still remain environmentally produced amplitude variations. Work is being done in various laboratories to develop polarization conserving fibers and active polarization control to limit these effects.

A new method is presented by which the non-reciprocal phase shift can be eliminated without the use of polarization conserving fibers, active polarization control, or polarization analyzers. Figure 1 shows a bare, basic fiber optic rotation sensor. The light source is unpolarized. At any instant of time the electric field can be represented by its components along the x and y (transverse) directions. The phaser between E_x and E_y is randomly distributed over the interval $[-\pi$ to $\pi]$. The instantaneous intensity incident on the detector contains both reciprocal and non-reciprocal terms. Some of the non-reciprocal terms are caused by cross products of E_x and E_y . These cross-product terms are averaged to zero in the detector. The remaining non-reciprocal terms combine on an intensity basis to eliminate the non-reciprocity.

If the optical fiber and other components of a rotation sensor are modeled as birefringent elements using Jones' matrices,² the normalized, detected intensity is

$$I_{\text{det}} = 1/2 + 1/2 (1 - |t(X1,Y2) - t(Y1,X2)|^2) \cos \theta_s \quad (1)$$

where θ_s is the Sagnac phase shift and $t(X1,Y2)$, $t(Y1,X2)$ are the off-diagonal elements of the Jones' matrices describing the birefringence of the fiber. These elements are environmentally sensitive. Figure 2 shows plots of I_{det} versus θ_s for several values of these elements. Note how the curves expand and contract about their average value. This causes the detected intensity to be independent of environmental fluctuations for Sagnac phase shifts which are odd multiples of $\pi/2$. By placing a non-reciprocal phase shifter in the loop, it is possible to bias the rotation sensor to one of these points at rest. The detected intensity will now be stable at rest. These stable operating points are coincident with the points of maximum sensitivity.

Figure 3 shows curves of I_{det} versus θ_s obtained experimentally using the rotation sensor shown in Fig. 1. The experimental results are in agreement with theory.

It has been shown that a rotation sensor, operated with unpolarized light is reciprocal without the use of polarization conserving fibers, polarization analyzers or active polarization control. In addition there exist stable operating points where the detected intensity is insensitive to the environment.

REFERENCES

1. H. Arditty, H. J. Shaw, M. Chodorow, and R. Kompfner, Proceedings of the Society of Photo-Optical Instrumentation Engineers, Volume 157, p. 138 (1978).
2. R. Ulrich and M. Johnson, Optics Letters 4, 152 (1979).

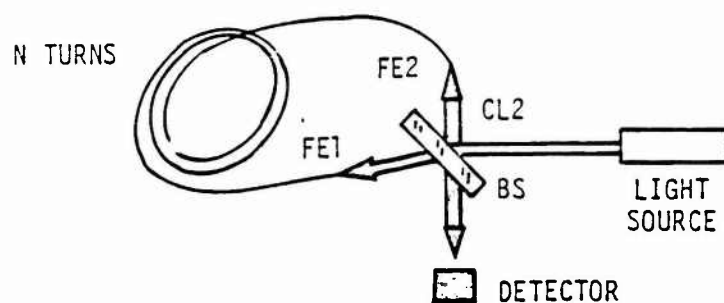


Figure 1 - FORS schematic: FE1, FE2, fiber ends one and two, CL1, CL2, coupling lenses one and two, BS beam splitter.

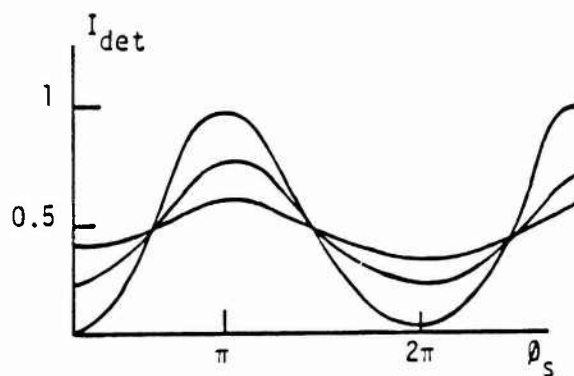


Figure 2 - Computer normalized detected intensity (I_{det}) vs. Sagnac phase shift (ϕ_s) for various environmental conditions.

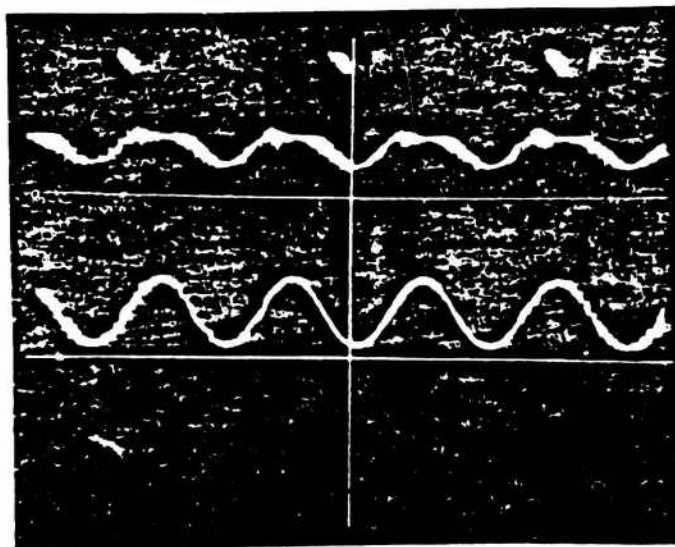


Figure 3 - Detected intensity vs. Sagnac phase shift for various environmental conditions.

MULTIMODE FIBER GYROSCOPES

G.A. Pavlath and H.J. Shaw
Edward L. Ginzton Laboratory
Stanford University
Stanford, CA. 94305

We have recently shown [1] that the basic reciprocity requirements [2,3] for sensitive fiber gyros can be met in single mode systems in which the usual polarized light source is replaced by an unpolarized source, and that certain other operational features also result which are of interest. In the present paper we extend the analysis of both polarized and unpolarized gyros to the case of gyros using multimode fibers, and show that there are interesting features in these cases also.

The electric field in the multimode fiber is expanded in the modes of the fiber as

$$E(x,y,z) = \sum_{k=1}^N a_k(z) M_k(x,y) \quad (1)$$

where $M_k(x,y)$ is the k^{th} mode and $a_k(z)$ is a complex number representing the amplitude and phase of the k^{th} mode. For quasi-monochromatic light, the correlation between the modes must be specified along with the power in the mode. This is accomplished mathematically by a generalized coherence matrix (4) which is $N \times N$. The kl^{th} term is

$$J_{kl} = \langle a_k(z) a_l^*(z) \rangle \quad (2)$$

where the asterisk (*) and the brackets ($\langle \rangle$) denote the complex conjugate and the infinite time average respectively. The generalized coherence matrix has the same properties as the 2×2 coherence matrix described in Ref. [4].

The optical fiber is modeled as a $2N$ port linear system. The ports are identified with the fiber modes at either end of the fiber. The fiber is described by two transfer matrices T^{21} and T^{12} which characterize propagation from end 1 to 2 and vice versa. The kl^{th} element of these matrices is

$$T_{kl}^{21} = r_{kl}^{21} e^{j(\phi_{kl}^{21} + \phi_s/2)} \quad (3a)$$

$$T_{kl}^{12} = r_{kl}^{12} e^{j(\phi_{kl}^{12} - \phi_s/2)} \quad (3b)$$

where ϕ_s is the Sagnac phase shift, r_{kl} is the fraction of the light incident at one end in mode k which exits the other fiber end in mode l , and ϕ_{kl} is the phase shift along the path connecting modes k and l . Reciprocity is assumed to hold at rest thus $T_{kl}^{21} = T_{lk}^{12}$. The transfer

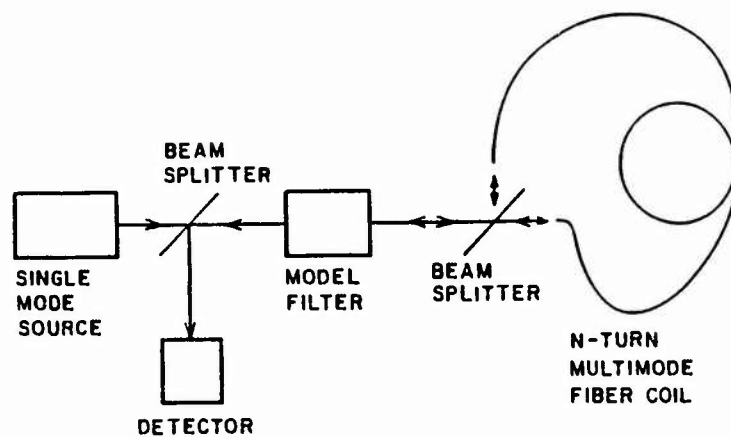


Fig. 1(a) Multimode polarized, fiber optic gyroscope configuration.

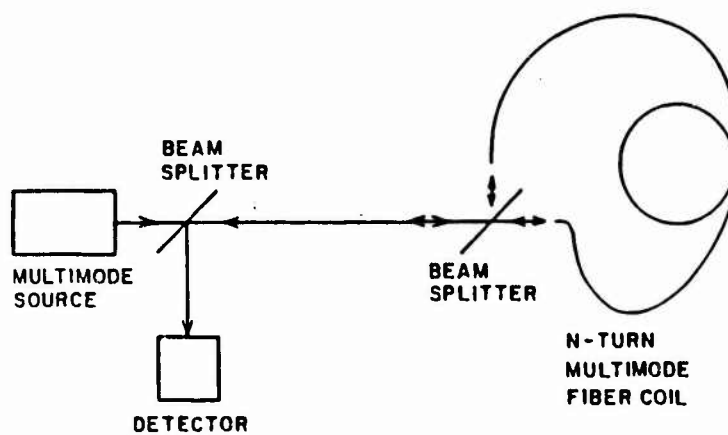


Fig. 1(b) Multimode, unpolarized, fiber optic gyroscope configuration.

matrices are unitary if the fiber is lossless. A transfer matrix for the gyroscope can be written in terms of the transfer matrices of the components. The $T_{k\ell}$'s are environmentally sensitive.

We consider two configurations of multimode fiber gyros, one using polarized light (Fig. 1(a)) and the other using unpolarized light (Fig. 1(b)), where polarized and unpolarized are defined in terms of the general coherence matrix. For polarized light all of the power is in one mode (i.e., $J_{k\ell} = \delta_{mk}\delta_{m\ell}$), while for unpolarized light the power is evenly divided among the modes and the modes are uncorrelated (i.e., $J_{k\ell} = 1/N \delta_{k\ell}$).

The normalized power assuming ideal components is calculated to be

$$I_{\text{polarized}} = 1/2(r_{mm})^2(1 + \cos \phi_s) \quad (4a)$$

$$I_{\text{unpolarized}} = 1/2 \left[1 + \left\{ \frac{1}{N} \sum_{k=1}^N (r_{kk}^{12})^2 - \frac{1}{N} \sum_{k=1}^N \sum_{\substack{\ell=1 \\ \ell \neq k}}^N (r_{k\ell}^{12})^2 \cos(\phi_{k\ell}^{12} - \phi_{\ell k}^{12}) \right\} \cos \phi_s \right] \quad (4b)$$

The above formalism reduces to the case for single mode fibers by setting $N = 2$.

Response curves (I versus ϕ_s) for multimode fibers are shown in Fig. 2 for various values of $T_{k\ell}$. Note that the response curves are sinusoidal with the positions of the maxima and minima of each curve independent of $T_{k\ell}$. This indicates reciprocal behavior. For the polarized gyro, the value of the minima are fixed while the value of the maxima depends on $T_{k\ell}$. In the unpolarized gyro, the average value of the curves is constant, while the maxima and minima expand or contract uniformly about the average value depending on $T_{k\ell}$. Thus the behavior of polarized and unpolarized multimode gyros has the same basic characteristics as for polarized and unpolarized single mode gyros.

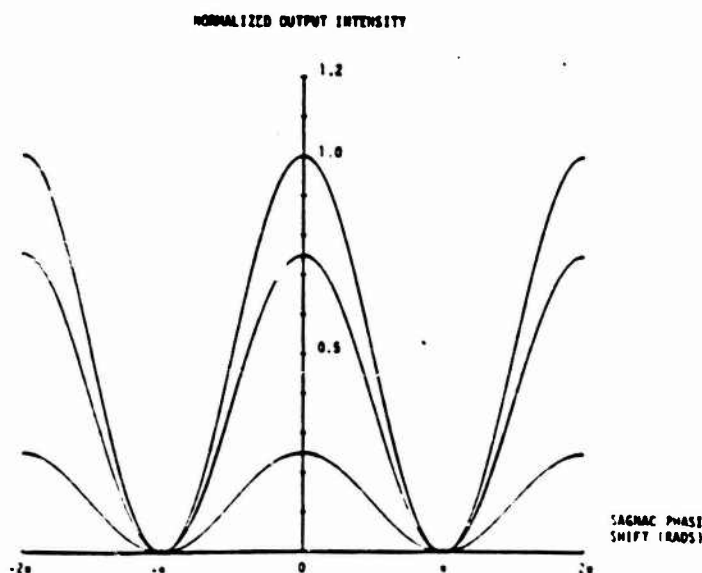


Fig.2(a) Response curves of polarized, multimode fiber optic gyroscope for various values of the scattering coefficients ($T_{u\ell}$).

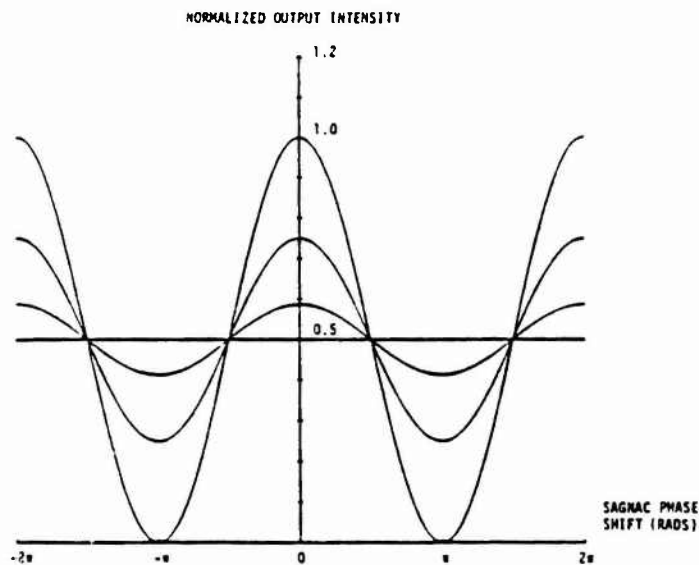


Fig.2(b) Response curves of unpolarized, multimode fiber optic gyroscope for various values of the scattering coefficients ($T_{u\lambda}$).

For the polarized gyro, Fig. 1(a), the insertion loss can be large if the optical fiber scatters the incident power uniformly over the N modes. However, individual modes are sometimes well preserved, which would result in reduced insertion loss. The insertion loss of the unpolarized gyro, Fig. 1(b), is expected to be low due to the absence of mode selective components. All N modes are detected. The large numerical apertures of multimode fibers allow more optical power to be coupled into them than into single mode fibers. This can be important in reducing the effects of detector noise. Low cost LED's can be used with multimode fibers. Relaxed alignment tolerances and cheaper fiber are further advantages. Also coherent backscattering and environmental sensitivity are expected to be lower because of averaging over the modes.

In conclusion, we see that reciprocal operation of gyros with multimode fiber is theoretically possible in both polarized and unpolarized forms and that there are some prospective advantageous tradeoffs over single mode gyros.

- ¹G. Pavlath and H.J. Shaw, "Unpolarized Reciprocal Operation of Fiber-optic Rotation Sensors," Technical Digest, Conference on Lasers and Electro-Optics, (Washington, D.C., 1981) 126-127.
- ²H. Arditty, H.J. Shaw, M. Chodorow, and R. Kompfner, "Re-Entrant Fiber-optic Approach to Rotation Sensing," Proceedings of the Society of Photo-Optical Instrumentation Engineers, Vol. 157 (August 1978) 138.
- ³R. Uirich and M. Johnson, Optics Letters 4, (1979) 152.
- ⁴M. Born and E. Wolf, *Principles of Optics*, Pergamon Press, 5th Edition, (1975), 544-553.

This work was supported by the Air Force Office of Scientific Research under Contract F49620-80-C-0040.

REDUCTION OF BACKSCATTERING ERROR IN AN OPTICAL FIBER GYRO

S. A. Newton, C. C. Cutler, and H. J. Shaw

Edward L. Ginzton Laboratory

Stanford University, Stanford, California 94305

(415) 497-0203

ABSTRACT

Coherent Rayleigh backscattering can be a source of significant error in Sagnac fiber rotation sensors. By using appropriate methods of signal modulation and by modification of the sensing loop, this error can be greatly reduced.

REDUCTION OF BACKSCATTERING ERROR IN AN OPTICAL FIBER GYRO

S. A. Newton, C. C. Cutler, and H. J. Shaw

Edward L. Ginzton Laboratory

Stanford University, Stanford, California 94305

(415) 497-0203

SUMMARY

Rayleigh backscattering has recently been recognized as an important factor which may limit the sensitivity of optical fiber Sagnac rotation sensors.¹ Each of the primary waves that counterpropagate around the sensing loop excites small scale inhomogeneities in the fiber which in turn act as induced dipole radiators.² The fiber captures a portion of the scattered radiation and guides it in the reverse direction. The contributions from each of the scatterers add vectorially to constitute a total backscattered field in each direction, which has an amplitude and phase that are stable in time if the loop is not perturbed.

Since the scatterers are randomly distributed along the fiber we can only estimate the r.m.s. amplitude of each backscattered wave in terms of the total backscattered power, and the phase of each wave cannot be predicted. These waves possess some degree of coherence with the two primary waves and add vectorially at unpredictable phases that are in general not identical for both waves (Fig. 1). The result is a component of phase shift due to backscattering that is, for any single measurement, indistinguishable from that induced by rotation.

In general, the error due to backscattering can be minimized either by reducing the coherence between the primary and the scattered waves or by reducing the magnitude of the detected backscattering itself. The former

may be accomplished in a number of ways, notably by phase modulating the primary waves, thereby randomizing the phases of the backscattering waves. Other factors such as environmental changes and finite source coherence length also play a role in reducing the effect of backscattering. Even with these factors and with intentional modulation the uncertainty due to scattering can be of the same order of magnitude as that of the best operation yet reported.³

The magnitude of the detected backscattering can be reduced significantly by using signal pulses that are of short duration relative to the transit time τ around the loop. This reduction is due to the fact that at any given time a short pulse is localized in a correspondingly short segment of the fiber path. As a result, only a fraction of the total backscattered light is able to arrive at the output in coincidence with the direct signal pulse (Fig. 2). The non-coincident backscattering can be removed by gating. Similar results can be obtained using chirped pulses that are spectrally equivalent to the short pulses but require lower peak powers.

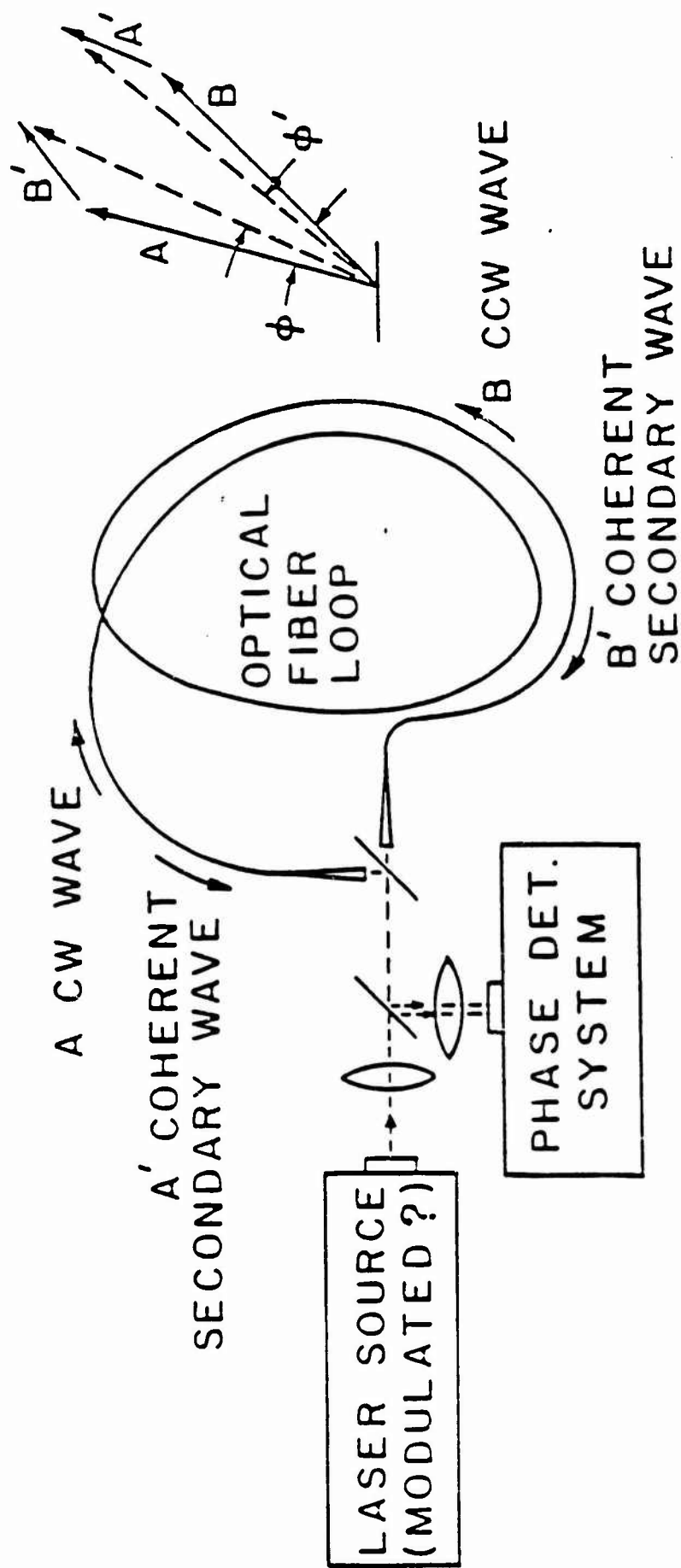
The use of short pulses not only reduces the coincident backscattered power by a large factor (1000 if $\Delta t = 5$ ns in a 1 km loop), it also defines the segment of the fiber where it originates. The backscattered power detected during the interval $\tau - \Delta t/2 \leq t \leq \tau + \Delta t/2$ (and thus in coincidence with the direct pulse) originates solely from scatterers located within a corresponding segment of fiber halfway around the loop in the interval $L/2 - v\Delta t/2 \leq z \leq L/2 + v\Delta t/2$, where L is the loop length and v the group velocity of the pulse. Thus if the input pulse is made shorter, the sources of the unwanted backscattered power are reduced in number and

are restricted to a shorter segment of the fiber $\Delta z = v\Delta t$ (e.g., if $\Delta t = 5$ ns, then $\Delta z = 1$ m). Since its location is known, such a segment can be identified and physically isolated from the rest of the system. By reducing the backscattering from only this short segment of the loop, a further improvement in rotation sensitivity will result. There are several methods of accomplishing this.

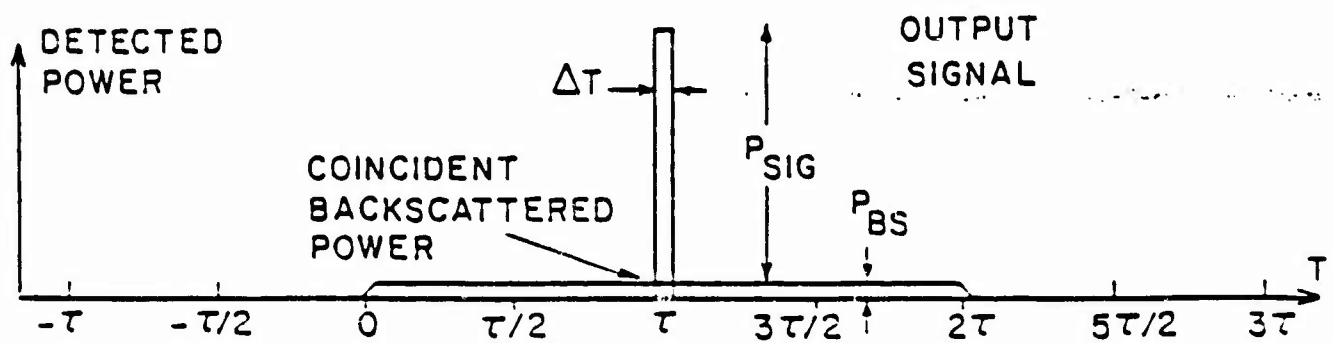
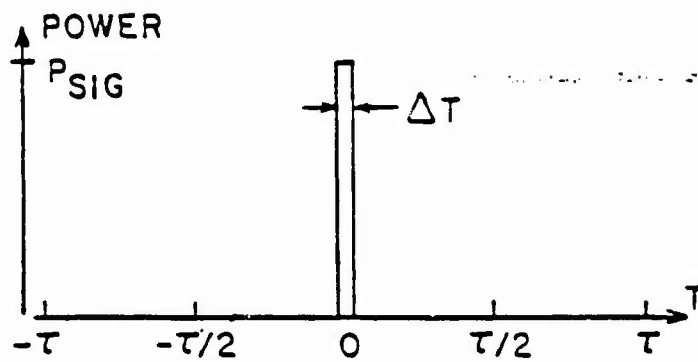
In summary, it appears that through the use of short signal pulses or equivalent chirped pulses and suitable modification of the fiber loop, the error due to backscattering can be greatly reduced.

REFERENCES

1. C. C. Cutler, S. A. Newton, and H. J. Shaw, Opt. Lett., 5, 488 (1980).
2. E. Brinkmeyer, Electron. Lett., 16, 329 (1980).
3. See, for example, R. Ulrich, Opt. Lett. 5, 173 (1980).



INPUT SIGNAL



Birefringence and polarization effects in fiber gyroscopes

G. A. Pavlath and H. J. Shaw

A formalism is presented for treating birefringence and polarization in fiber optic sensors. This formalism is applied to study theoretical characteristics of fiber gyroscopes which are operated with various states of polarization of the input light including nonpolarized and partially polarized light, which have potentially useful characteristics. Measurements supporting the theoretical predictions are described.

I. Introduction

It is recognized today that polarization plays an important role in the operation of many kinds of fiber optic sensors. The monomode optical fibers which form the sensors are birefringent. This birefringence enters during fiber manufacturing either deliberately as in polarization maintaining fibers or accidentally. Birefringence can also be induced in a fiber by bending or twisting and by external stress, electric, magnetic, and acoustic fields.¹⁻³ This birefringence is extremely sensitive to the environment of the fiber. Changing birefringence can cause substantial variations in the signals from fiber optic sensors, which can be indistinguishable from the signals caused by the physical field being measured.

This paper will focus on cw single-pass fiber optic gyroscopes. A new method is presented by which the effects of fiber birefringence are reduced. It consists of operating the gyroscope with unpolarized light and removing any polarization selective elements from the system. This method assures reciprocal operation and provides stable operating points at which the gyroscope can be operated without being affected by reciprocal changes in fiber birefringence.

To understand how this method works a formalism will be presented which quantifies the fiber birefringence and treats its effects for any state and degree of polarization on the performance of fiber optic sensors in general. Previous formalisms^{4,5} were applicable only

to completely polarized (monochromatic) light. This formalism, which is applicable to light of any degree of polarization (quasi-monochromatic), is applied to several methods of operating a fiber optic gyroscope including the unpolarized method. Experimental results are given which support the theoretical predictions.

II. Theory

A. Coherence Matrix Representation of Polarization

To represent the state and degree of polarization, the coherence matrix formalism⁶ will be used. Choose any two orthogonal polarization states as the basis for the coherence matrix. Let E_K and E_L be the projections of the electric field of a light wave on this basis. The coherence matrix J of the light wave is then

$$J = \begin{pmatrix} \langle E_K E_K^* \rangle & \langle E_K E_L^* \rangle \\ \langle E_L E_K^* \rangle & \langle E_L E_L^* \rangle \end{pmatrix} \quad (1)$$

where the brackets $\langle \cdot \rangle$ signify the infinite time average. In the rest of this paper the basis states are chosen as linearly polarized along the x and y axes.

The coherence matrix defined by Eq. (1) is Hermitian. The degree of polarization P is determined by the eigenvalues (λ_1, λ_2) , and the intensity I is given by the trace. These properties can be stated mathematically as

$$J_{KL} = J_{LK}^* \quad (2a)$$

$$P = |\lambda_1 - \lambda_2| / (\lambda_1 + \lambda_2) \quad (2b)$$

$$I = \text{Tr} J \quad (2c)$$

If a light wave passes through a linear birefringent system, characterized by a Jones matrix S , the input and output coherence matrices are related as follows:

$$J_{\text{out}} = S J_{\text{in}} S^* \quad (3)$$

The coherence matrix of a linear superposition of light waves is the sum of the coherence matrices of the light waves. These properties will be used extensively.

The authors are with Stanford University, Ginzton Laboratory, Stanford, California 94305.

Received 12 June 1981.

0003-6935/82/101752-06\$01.00/0.

© 1982 Optical Society of America.

B. Birefringent Model of Optical Fiber

The optical fiber will be modeled as a general birefringent element using Jones matrices.^{4,7,8} A Jones matrix S_{12} will describe propagation from fiber end 2 to fiber end 1. A second Jones matrix S_{21} will describe propagation in the opposite direction. The fiber is assumed lossless. Hence the Jones matrices are unitary. This means that the sum of the absolute squares of the elements in a row or column equals unity. The Jones matrices can be written in general as

$$S_{12} = \begin{pmatrix} t(X1,X2) & t(X1,Y2) \\ t(Y1,X2) & t(Y1,Y2) \end{pmatrix}, \quad (4a)$$

$$S_{21} = \begin{pmatrix} t(X2,X1) & t(X2,Y1) \\ t(Y2,X1) & t(Y2,Y1) \end{pmatrix}, \quad (4b)$$

where the $t(k,l)$'s are complex numbers which represent the scattering coefficients of a general four-port linear system. The ports represent the x and y linear polarizations at the ends of the fiber as in Fig. 1. If the fiber is reciprocal, the complex scattering coefficients are related as

$$t(k,l) = t(l,k). \quad (5)$$

A more detailed form of the Jones matrices will be derived by considering the length of fiber shown in Fig. 2.

The propagation constants β_x and β_y for the two polarizations are shown explicitly. First consider a model in which, at some point z along the fiber, some power is exchanged between the two polarizations, while at all other points in the fibers the two polarization modes are uncoupled. The Jones matrices (which are 2×2) can now be written

$$S_{12} = \exp(j\bar{\beta}L) \times \begin{pmatrix} \cos\theta \exp\left(j\frac{\Delta\beta L}{2}\right) & \sin\theta \exp\left[-j\Delta\beta\left(\frac{L}{2} - z\right)\right] \\ -\sin\theta \exp\left[j\Delta\beta\left(\frac{L}{2} - z\right)\right] & \cos\theta \exp(-j\Delta\beta L/2) \end{pmatrix}, \quad (6a)$$

$$S_{21} = \exp(j\bar{\beta}L) \times \begin{pmatrix} \cos\theta \exp\left(j\frac{\Delta\beta L}{2}\right) & -\sin\theta \exp\left[j\Delta\beta\left(\frac{L}{2} - z\right)\right] \\ \sin\theta \exp\left[-j\Delta\beta\left(\frac{L}{2} - z\right)\right] & \cos\theta \exp(-j\Delta\beta L/2) \end{pmatrix}, \quad (6b)$$

where $\bar{\beta} = (\beta_x + \beta_y)/2$ and $\Delta\beta = \beta_x - \beta_y$. The parameter θ is the angle through which the input state of polarization is rotated by the fiber.

In general in a length of optical fiber there exist many points where the two polarization modes are coupled. The Jones matrices for this general fiber can be obtained by dividing the fiber into lengths which contain only one point of coupling, then taking the matrix product of the Jones matrices of each section. These matrices have the general form of those in Eq. (6). These general matrices can be written

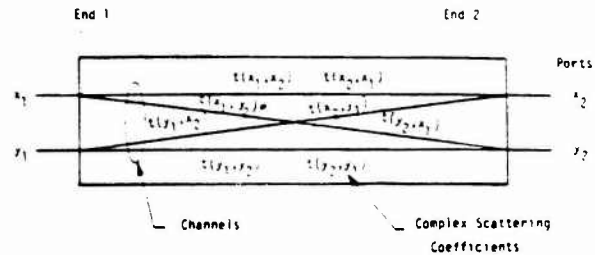


Fig. 1. Four-port linear system model of a single-mode fiber. The ports are x_1, x_2, y_1, y_2 corresponding to linear polarizations. The channels between the ports are shown schematically along with their complex scattering coefficients.

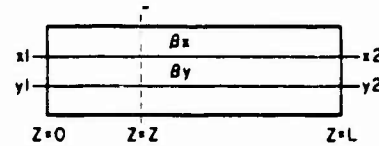


Fig. 2. Model of a single-mode fiber in which the two polarization modes are coupled at a point Z and are uncoupled at all other points.

$$S_{12} = \exp[j\bar{\phi}(L)] \begin{pmatrix} \cos\theta(L) \exp[j\xi(L)/2] & \sin\theta(L) \exp[-j\phi(L)/2] \\ -\sin\theta(L) \exp[j\phi(L)/2] & \cos\theta(L) \exp[-j\xi(L)/2] \end{pmatrix}, \quad (7a)$$

$$S_{21} = \exp[j\bar{\phi}(L)] \begin{pmatrix} \cos\theta(L) \exp[j\xi(L)/2] & -\sin\theta(L) \exp[j\phi(L)/2] \\ \sin\theta(L) \exp[-j\phi(L)/2] & \cos\theta(L) \exp[-j\xi(L)/2] \end{pmatrix}, \quad (7b)$$

In these equations $\bar{\phi}$ is the average phase shift along the fiber, ξ represents the change in ellipticity of the input state of polarization, θ is the total polarization rotation, and ϕ represents the reciprocal phase shift of the fiber (which can mask the Sagnac phase shift in a fiber optic rotation sensor). All the parameters in Eqs. (7) depend on the length of the fiber.

If the fiber is used in the sensing loop of a fiber gyroscope, the Jones matrices in Eqs. (7) are modified as follows to allow for the Sagnac rotationally induced phase shift ϕ_s .

$$S_{12} = \exp(j\phi_s/2) S_{12}, \quad (8a)$$

$$S_{21} = \exp(-j\phi_s/2) S_{21}. \quad (8b)$$

C. Jones Matrix Representations of Polarizers Beam Splitters, and Gyroscopes

The remaining components of a basic fiber gyroscope are beam splitters and a polarizer. These components will be assumed ideal, since the major focus of this paper is the effect of the state and degree of polarization of the fiber sensing loop. The Jones matrix representations for ideal polarizers orientated to pass the x linear polarization and the y linear polarization are

$$P_x = \begin{pmatrix} 1 & 0 \\ 0 & 0 \end{pmatrix}, \quad (9a)$$

$$P_y = \begin{pmatrix} 0 & 0 \\ 0 & 1 \end{pmatrix}. \quad (9b)$$

The beam splitter is represented by two Jones matrices, one for transmission and one for reflection:

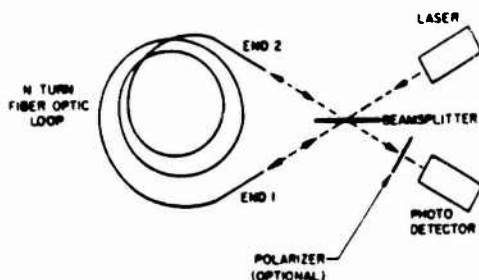


Fig. 3. Schematic of the fiber optic rotation sensor, which is analyzed.

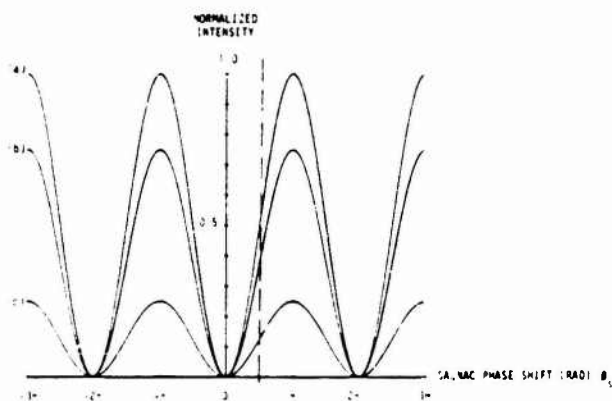


Fig. 4. Normalized intensity vs Sagnac phase shift for polarized input. The polarizer passes the input polarization. The parameter θ is (a) 0, (b) 30, (c) 60.

$$T = \frac{\exp(j\pi/4)}{\sqrt{2}} \begin{pmatrix} 1 & 0 \\ 0 & 1 \end{pmatrix}. \quad (10a)$$

$$R = \frac{\exp(-j\pi/4)}{\sqrt{2}} \begin{pmatrix} 1 & 0 \\ 0 & 1 \end{pmatrix}. \quad (10b)$$

The Jones matrix which describes the rotation sensor can be expressed in terms of the Jones matrices of the components as given in Eqs. (7), (8), (9), and (10). Figure 3 shows the schematic for the rotation sensor which will be used in the following analysis. This rotation sensor is reciprocal only if the beam splitter is ideal.⁹ The Jones matrix G of the fiber optic gyroscope is

$$G = P_j(RS_{12}R + TS_{21}T), \quad (11)$$

where P_j represents either P_x or P_y in cases where a polarizer is needed.

D. Analysis of Specific Cases

1. Copolarized

In the first case to be analyzed the laser is linearly polarized along the x axis, and the polarizer is orientated to pass the x linear polarization. The coherence matrix of the input light is

$$J_{in} = \begin{pmatrix} 1 & 0 \\ 0 & 0 \end{pmatrix}. \quad (12)$$

Using the coherence matrix given above in Eq. (12) with the Jones matrix G given by Eq. (11), the normalized detected intensity is

$$I = \frac{1}{2} \cos^2 \theta (1 - \cos \phi_s). \quad (13)$$

This intensity depends on the Sagnac phase shift ϕ_s , and the fiber birefringent parameter θ , which describes the rotation of the state of polarization by the fiber. If θ is 90° , the detected intensity is zero. Figure 4 shows computer plots of Eq. (13). The curves are parametrized by θ . This set of curves shows that this mode of operation is reciprocal by exhibiting no translation of the curves along the ϕ_s axis as the birefringent parameters are varied. Also note in Fig. 4 that the zero minima of all the curves are at zero, while the maxima of the curves vary with θ .

The sensitivity to rotation of the fiber optic gyroscope shown in Fig. 3 is zero at rest, and a nonreciprocal phase bias element must be included in the optical sensing loop to move the operating point at rest to a point of maximum sensitivity. The value of this nonreciprocal phase bias is an odd multiple of $\pi/2$ rad. The operating point shown in Fig. 4 by the dashed line is of most interest. When the rotation sensor is at rest, the detected intensity varies with the fiber birefringent parameter, θ , which again is a function of the environment. This intensity variation represents an error which must be dealt with. Techniques for this are polarization maintaining fibers, electronic polarization control, or certain types of modulation.

2. Cross-Polarized

The next case to be considered has the polarizer orientated to pass the Y linear polarization. The source is still linearly polarized along the x axis with coherence matrix as given in Eq. (12). Using Eqs. (3) and (11) now results in the following form for the normalized detected intensity:

$$I = \frac{1}{2} \sin^2 \theta [1 + \cos(\phi_s + \phi)]. \quad (14)$$

The detected intensity now also depends on the fiber induced reciprocal birefringent dependent phase shift ϕ . Figure 5 shows plots of Eq. (14) in which the curves are parametrized by θ and ϕ . This mode of operation is nonreciprocal. This is seen in Fig. 5 where the curves exhibit translation along the ϕ_s axis as the reciprocal birefringent dependent phase shift ϕ is varied. This

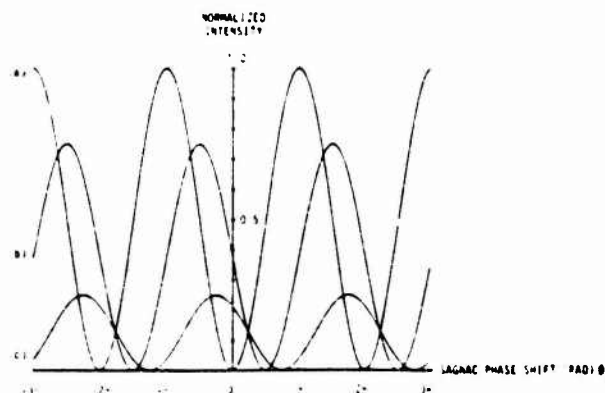


Fig. 5. Normalized intensity vs Sagnac phase shift for polarized input. The polarizer rejects the input polarization. The parameters θ and ϕ are (a) (90,180), (b) (60,90), (c) (30,45).

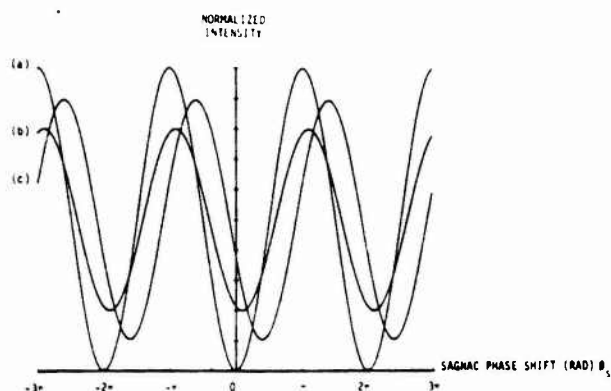


Fig. 6. Normalized intensity vs Sagnac phase shift for polarized input. No polarizer is used. The parameters θ and ϕ are (a) (0,0), (b) (30,45), (c) (60,90).

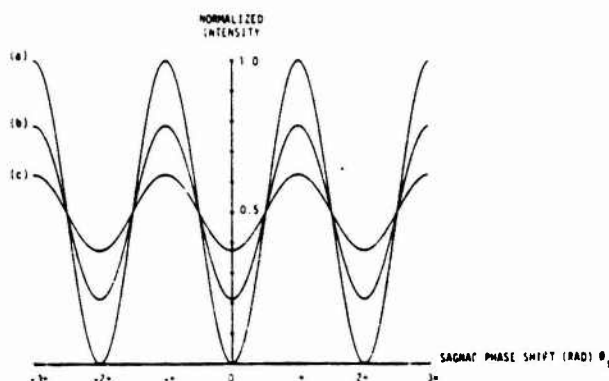


Fig. 7. Normalized intensity vs Sagnac phase shift for completely unpolarized input. No polarizer is used. The parameters θ and ϕ are (a) (0,0), (b) (30,45), (c) (60,90).

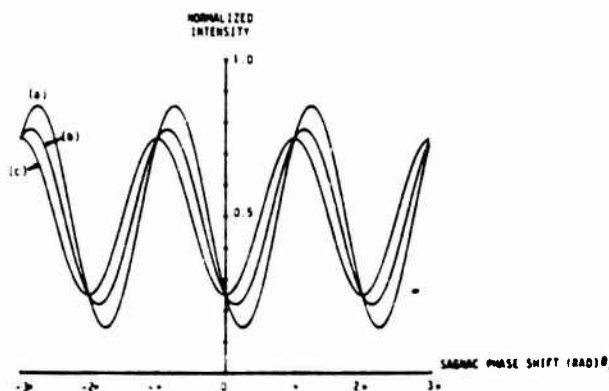


Fig. 8. Normalized intensity vs Sagnac phase shift for partially polarized input. No polarizer is used. The parameters θ and ϕ are (45,90). The degree of polarization is (a) 1, (b) 0.5, (c) 0.

fiber induced reciprocal birefringent dependent phase shift is indistinguishable from the rotation induced phase shift. The minima of the curves are fixed at zero again, while the maxima again depend on the environment through θ , the state of polarization rotation parameter.

3. No Polarizer

The last case to be considered for completely polarized input light is that in which no polarizer is used before the detector. The input light is still linearly polarized along the x axis as before. In this case it is apparent that the normalized detected intensity is the sum of the detected intensities for the cases in which the polarizer is orientated along the x and y axes [Eqs. (13) and (14)]:

$$I = \frac{1}{2}[1 - \cos^2\theta \cos\phi_s + \sin^2\theta \cos(\phi_s + \phi)]. \quad (15)$$

The detected intensity again depends on θ , the rotation of the state of polarization, and on ϕ , the fiber induced reciprocal birefringent dependent phase shift. From the form of Eq. (15) it can be seen that the average value of the detected intensity is independent of θ and ϕ . This is shown in Fig. 6, which shows plots of Eq. (15) for various values of θ and ϕ . The maxima and minima of the curves expand or contract about the average value of the detected intensity. This mode of operation is also nonreciprocal as evidenced by the translation of the curves along the ϕ_s axis. The independence of the average value of the detected intensity is due solely to the lack of a polarizer before the detector. This property will be quite useful in the next case examined.

4. Unpolarized

Let the light source in Fig. 3 be unpolarized. The coherence matrix of this light wave is given as

$$J_{in} = \begin{pmatrix} 1/2 & 0 \\ 0 & 1/2 \end{pmatrix}. \quad (16)$$

Using this coherence matrix in Eq. (3) with the Jones matrix of the rotation sensor given by Eq. (11), the normalized detected intensity is found to be

$$I = \frac{1}{2}[1 - (\cos^2\theta - \sin^2\theta \cos\phi) \cos\phi_s]. \quad (17)$$

The detected intensity again depends on θ and ϕ . The average value of the detected intensity is again constant due to the absence of a polarizer. Figure 7 shows plots of Eq. (17). The curves are parametrized by the birefringent parameters θ and ϕ . This mode of operation is reciprocal because the curves do not translate along the ϕ_s axis with changing values of θ and ϕ . Physically part of the nonreciprocity is eliminated due to the incoherence of the two polarizations. The remaining nonreciprocity is exactly canceled when the two orthogonal polarizations add in the photodetector. Notice the behavior of the curves when the Sagnac phase shift is an odd multiple of $\pi/2$. The detected intensities

at these points are independent of the fiber birefringence. The sensitivity to rotation at these points is also a maximum. If the rotation sensor in Fig. 3 were biased to one of these points at rest, the detected intensity at rest would be independent of changing birefringence in the fiber. The rotation sensor would be stable at rest. The scale factor would still depend on the fiber birefringence. Other methods must be used to stabilize it.

5. Partially Polarized

In general optical components have some degree of polarization selectivity, and most light sources have a small nonzero degree of polarization. The terms in the coherence matrix are infinite time averages of the products of the phasors of the electric field. When these terms are measured with a detector with a finite integration time, a nonzero degree of polarization may be obtained for an unpolarized source. Because of these observations the performance of the fiber optic rotation sensor in Fig. 3 must be examined for partially polarized light.

Equation (18) shows the coherence matrix for a light wave with degree of polarization P along the x axis:

$$J_{in} = \begin{pmatrix} (1/2)(1+P) & 0 \\ 0 & (1/2)(1-P) \end{pmatrix}. \quad (18)$$

This light wave can be expressed as a sum on an intensity basis of a completely polarized light wave and a completely unpolarized light wave:

$$J_{in} = \begin{pmatrix} P & 0 \\ 0 & 0 \end{pmatrix} + \begin{pmatrix} (1/2)(1-P) & 0 \\ 0 & (1/2)(1-P) \end{pmatrix}. \quad (19)$$

The normalized detected intensity of the rotation sensor shown in Fig. 3, using a light source with the above coherence matrix, is the weighted sum on an intensity basis of the detected intensities for polarized and unpolarized inputs [Eqs. (15) and (17)]. The normalized detected intensity is

$$I = \frac{1}{2}[1 - (\cos^2\theta - \sin^2\theta \cos\phi) \cos\phi_s] - \frac{P}{2} \sin^2\theta \sin\phi \sin\phi_s. \quad (20)$$

The detected intensity now depends on θ , ϕ , and P , the degree of polarization. In Fig. 8 plots of Eq. (20) are shown for various values θ , ϕ , and P . From this figure it is seen that this mode of operation is nonreciprocal by an amount proportional to the degree of polarization. If the nonreciprocity can be made small enough, this mode of operation can be used in a practical rotation sensor. The degree of polarization is approximately equal to the minimum detectable phase shift.

III. Experimental Evidence

The rotation sensor shown in Fig. 3 was constructed on a rotating table. The sensing loop was formed from 600 m of ITT single-mode fiber wound about an area of 1 m² with 150 turns. A randomly polarized 1-mW He-Ne laser was used as an unpolarized source. The degree of polarization was measured as 5%. This laser

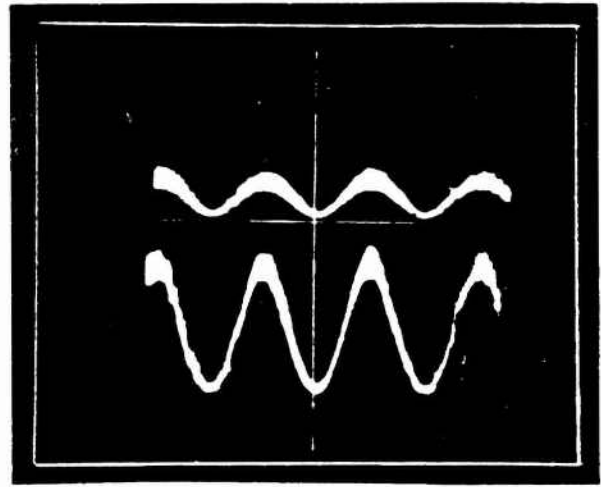


Fig. 9. Measured intensity vs Sagnac phase shift using polarized input light with polarizer passing the input polarization for different birefringent conditions in the fiber.

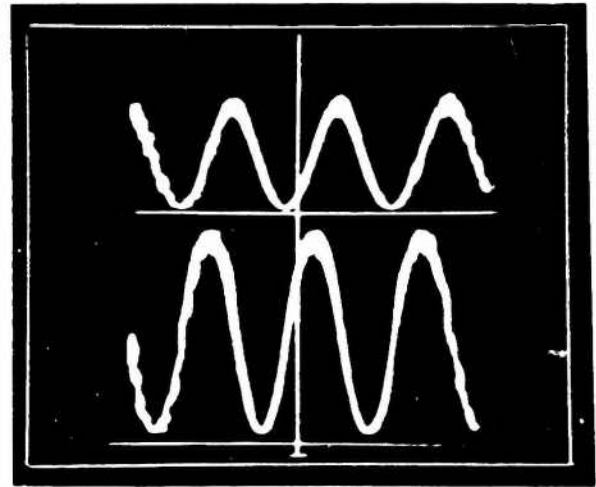


Fig. 10. Measured intensity vs Sagnac phase shift using polarized input light with polarizer rejecting the input polarization for different birefringent conditions in the fiber.

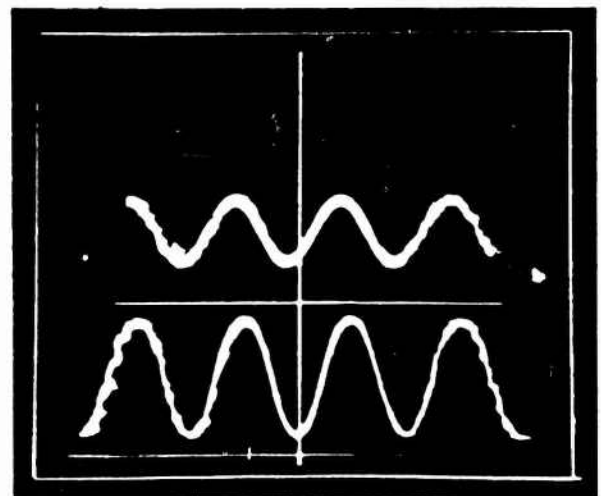


Fig. 11. Measured intensity vs Sagnac phase shift using polarized input light with no polarizer for different birefringent conditions in the fiber.

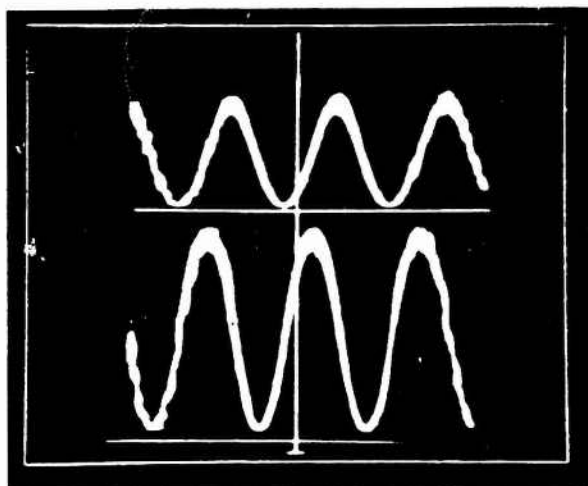


Fig. 12. Measured intensity vs Sagnac phase shift using input light of 5% degree of polarization for different birefringent conditions in the fiber.

emitted at a wavelength of 632.8 nm. A second 50-mW laser was used to give polarized light at the same wavelength. A plate-type beam splitter was used to split and recombine the light waves.

A photomultiplier tube was used to detect a portion of the spatial fringe pattern of the recombined light waves. The photomultiplier output was displayed on the vertical channel of a storage monitor. The rotating table has rotation rate transducers which give a voltage proportional to the rotation rate. This voltage was displayed on the horizontal axis of the storage monitor. As the rotation rate was swept through an appropriate range, an electrical fringe pattern of detected intensity vs Sagnac phase shift was traced on the storage monitor. This measured response curve was taken for various birefringent parameters and compared with the theoretical response curves calculated previously. The birefringence of the fiber was mechanically changed by twisting and bending the fiber.

Figures 9, 10, and 11 show the measured detected intensity vs Sagnac phase shift for polarized input light with an output polarizer passing the input polarization, an output polarizer rejecting the input polarization, and no polarizer, respectively. Comparing Figs. 9, 10, and 11 with the theoretical plots in Figs. 4, 5, and 6, respectively, it is seen that experimental and theoretical curves agree very well. The main difference between the two sets of figures is the reduced fringe visibility of the measured electrical fringes. This is due to uneven power flow around the loop in opposite directions, which is caused by the beam splitter having a 60:40 power splitting ratio. A less obvious difference is the small variation of the mean of the electrical fringes in Fig. 11. This variation is attributed to laser power fluctuations and fluctuations of the coupling of the spatial beam into the fiber.

Figure 12 shows the electrical fringes for nearly unpolarized input light ($P = 5\%$) when no polarizer is used. Comparison of this figure with Fig. 7 shows that theory and experiment are in good agreement again. The differences are again caused by the same factors as above.

IV. Conclusions

We have developed a formalism which describes the birefringence of an optical fiber and the effect of the birefringence on the performance of fiber optic sensors. This formalism was checked by measurements made on a single-pass cw fiber optic rotation sensor. It was shown that unpolarized input light leads to reciprocal operation of the rotation sensor. It was also shown that by using unpolarized input light, the rotation sensor could be made stable (independent of reciprocal fiber birefringence changes) at rest if a suitable nonreciprocal phase shift (odd multiples of $\pi/2$ rad) was applied to the loop.

References

1. R. Ulrich and A. Simon, *Appl. Opt.* 18, 2241 (1979).
2. R. Ulrich, S. C. Rashleigh, and W. Eickhoff, *Opt. Lett.* 5, 273 (1980).
3. V. Ramaswamy, R. H. Stolen, M. D. Divino, and W. Pleibel, *Appl. Opt.* 18, 4080 (1979).
4. R. Ulrich and M. Johnson, *Opt. Lett.* 4, 152 (1979).
5. G. Franschetti and C. Smith, *J. Opt. Soc. Am.* 71, 1487 (1981).
6. M. Born and E. Wolf, *Principles of Optics* (Pergamon, London, 1975), p. 544-553.
7. R. Ulrich, *Opt. Lett.* 5, 173 (1980).
8. E. Kintner, *Opt. Lett.* 6, 154 (1981).
9. If the beam splitter is not ideal, two beam splitters must be used to guarantee reciprocity.

This work was supported by the Air Force Office of Scientific Research under contract F49620-80-C-0040.

The All-fiber Gyroscope: A Practical Alternative for Rotation Sensing

R. A. Bergh, C. C. Cutler, H. C. Lefevre,
S. A. Newton, G. A. Pavlath, and H. J. Shaw

Edward L. Ginzton Laboratory
Stanford University
Stanford, California 94305

Optical fibers are of great potential importance for sensor systems, because they are environmentally sensitive and because they can be used in interferometers for measurement of very small phase shifts. Fiber gyroscopes, like their predecessors the ring laser gyros, are based on the Sagnac effect,^{1,2} whereby light traveling around a closed path experiences a phase shift proportional to the rotation rate in inertial space. The detected phase shift represents an optical path difference that may be less than one thousandth of an angstrom in length.

The emergence of the fiber ring interferometer as a practical alternative to existing rotation sensors began³ with the development of very low-loss optical fibers. It was soon recognized that such fiber rotation sensors had the potential to rival the sensitivity of ring laser gyros, and ultimately that of the best mechanical gyros. However, early attempts to observe the Sagnac effect in fiber interferometers were disappointing because of parasitic propagation phenomena and because of limitations in the measurement of phase.

In the past few years, many of these limiting effects have been identified and greatly reduced by improving the construction of the interferometer and the treatment of the optical signal. These improvements include optical reciprocity with polarization control,⁴⁻⁷ synchronous detection,^{5,7} and reduction of the error due to coherent Rayleigh backscattering.^{7,9}

The development of single mode fiber components for manipulating the guided optical signals was a crucial step toward greater sensitivity. A

low-loss directional coupler¹⁰ and polarizer¹¹ were demonstrated. Fiber devices analogous to bulk retardation plates were developed in the form of adjustable polarization controllers which make use of the birefringence induced by fiber bends.¹² Phase modulation was accomplished by wrapping turns of fiber around voltage driven PZT expanders.¹³

These components have made possible a rotation sensor in which the optical signals remain guided in a single mode along the entire path in an unbroken fiber. Perhaps the greatest advantage of such a system is its very low loss - a parameter of prime importance since the sensitivity is now approaching the quantum detection limit. Besides a substantial reduction of loss, the absence of bulk optical components and joints eliminates severe alignment problems as well as unwanted back reflections.

An all-fiber rotation sensor has been constructed in which all components are fabricated directly on a single 580 meter length of single mode fiber wound on a 7 cm radius (Fig. 1). The response for a rotation of 3 degrees/hour is shown in Fig. 2 and indicates a noise equivalent rotation rate of less than one hundredth of the rotation rate of the earth.

As these and other recently reported results¹⁴ indicate, fiber gyro sensitivity has rapidly progressed to the point where it is within an order of magnitude of that of the ring laser gyro. It is expected that the use of an optical isolator to protect the light source, the use of polarization preserving fiber, and the use of longer fibers will improve the sensitivity much further.

An integrating rate gyro, using a pulsed reentrant mode of operation, has also been demonstrated (Fig. 3). Two optical pulses, which counterpropagate around the sensing loop many times, are nondestructively sampled after each transit. The envelope of the resulting pulse train at the detector

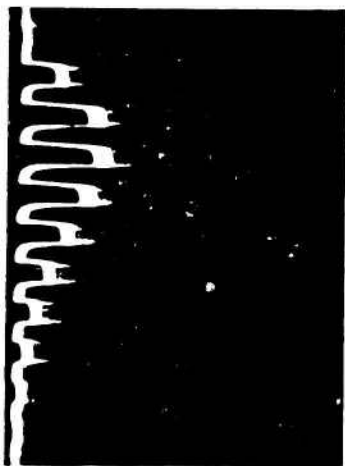
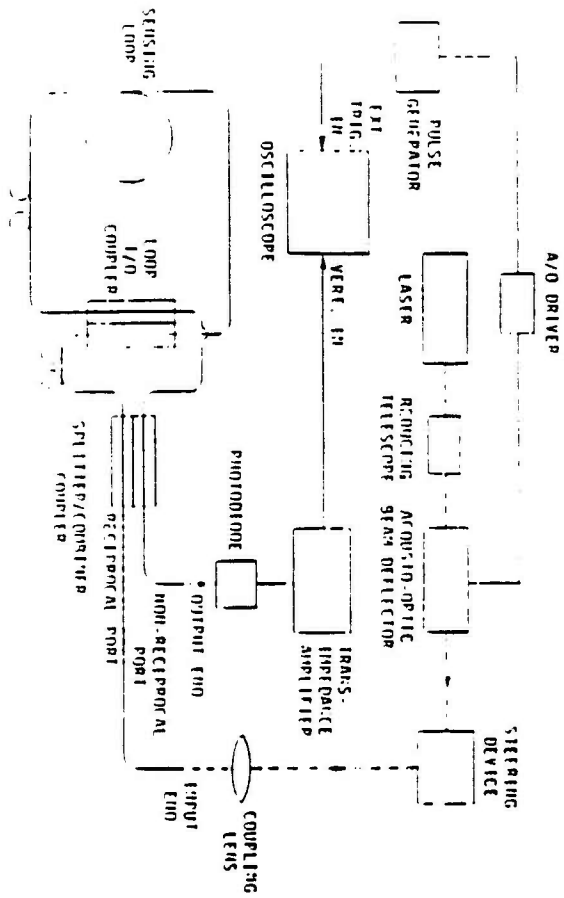
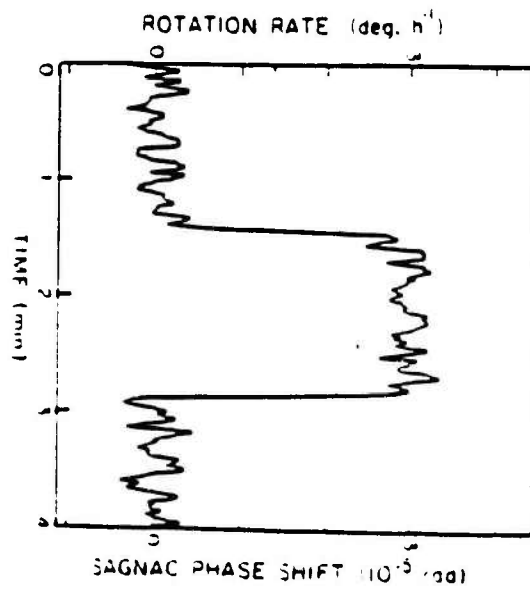
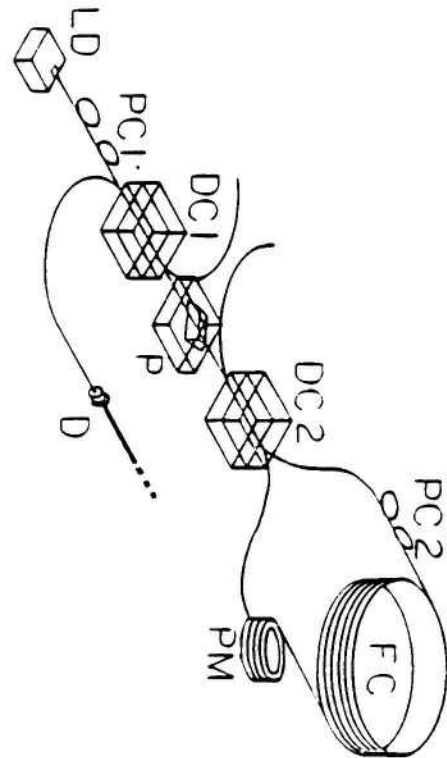
is sinusoidal, with the frequency of the sinusoid being proportional to the angular velocity.

Fiber gyros are relatively simple instruments; compact, light weight and rugged, requiring little maintenance, and featuring strapdown mounting and rapid turn-on. Presently, they have the sensitivity required for a variety of navigational sensing tasks in the area of guidance, control and navigation. Linearity and stability of the scale factor, and dynamic range, are further items of importance for practical applications, and work is in progress in these areas. If the rate of advancement in sensitivity is any indication of future progress, the optical fiber rotation sensor will emerge as the instrument of choice for inertial navigation in the not too distant future.

This work was supported by the Air Force Office of Scientific Research under Contract F49620-80-C-0040 and the Atlantic Richfield Company.

References

1. E. J. Post, Rev. Mod. Phys. 39, 475 (1967).
2. H. J. Arditty and H. C. Lefevre, Optics Letters 6, 401 (1981).
3. V. Vali and R. W. Shorthill, Proc. SPIE Conf., Reston, Virginia (1976).
4. H. J. Arditty, H. J. Shaw, M. Chodorow, and R. Kompfner, Proc. SPIE 157, 138 (1978).
5. H. J. Arditty, M. Papuchon, C. Puech, and K. Thyagarapan, Conf. Digest, OSA, Washington, D.C. (1980).
6. R. Ulrich, Optics Letters 5, 173 (1980).
7. K. Böhm, F. Russer, E. Weidel, and R. Ulrich, Optics Letters 6, 64 (1981).
8. C. C. Cutler, S. A. Newton, and H. J. Shaw, Optics Letters 5, 488 (1980).
9. R. A. Bergh, H. C. Lefevre, and H. J. Shaw, Optics Letters 6, 502 (1981).
10. R. A. Bergh, G. Kotler, and H. J. Shaw, Electronics Letters 16, 260 (1980).
11. R. A. Bergh, H. C. Lefevre, and H. J. Shaw, Optics Letters 5, 479 (1980).
12. H. C. Lefevre, Electronics Letters 16, 778 (1980).
13. D. E. N. Davies and S. A. Kingsley, Electronics Letters 10, 21 (1974).
14. J. L. Davis and S. Ezekiel, Optics Letters 6, 505 (1981).



FIBER OPTIC ROTATION SENSORS
ALTERNATE CONFIGURATIONS AND MODES OF OPERATION

George Attila Pavlath, Ph.D.
Stanford University, 1982

This is a theoretical and experimental study of rotation sensors which utilize the Sagnac effect in ring interferometers fabricated from optical fibers.

The effects of fiber birefringence and polarization of light on the performance of such sensors are of great importance and these effects have been investigated using a mathematical formalism particularly suited for treating these properties. This formalism has been applied to a variety of polarization conditions and to various kinds of phase modulation techniques. The predictions of this formalism are compared with experiment in certain cases and are found to be in good qualitative agreement.

Based on these results, a new type of phase modulated rotation sensor which uses two modulation frequencies is proposed to overcome some of the problems characteristic of some kinds of operation.

The principles of operation of reentrant pulsed fiber rotation sensors have also been examined. This is the case where a single pulse circulates around the fiber many times. Considerations of system optimization for various cases are treated and presented.

Experimental results obtained with with two types of such reentrant rotation sensors are presented and discussed. Mathematical formulas

have also been derived for the rotation rate error in single pass and reentrant rotation sensors in terms of the uncertainties in the system parameters due to noise. In the case of reentrant rotation sensors, several mathematical algorithms for processing the signal have been treated. Computer calculations have been made on the rotation error as a function of the rotation rate and the number of recirculations, for a passive reentrant rotation sensor which uses a cycle counting detection algorithm. The rotation rate error as a function of recirculations and also for low rotation rates has been calculated and proposals have been made for reducing these errors. The theory should also be capable of treating other conditions of operation for a rotation sensor.

CONTENTS

I.	INTRODUCTION	1
II.	ROTATION INDUCED PHASE SHIFTS.	6
III.	POLARIZATION AND BIREFRINGENCE IN OPTICAL FIBERS	11
	A. Necessary Conditions for Reciprocity	14
	B. Polarization	16
	C. Birefringence	18
IV.	SINGLE PASS, CW, FIBER OPTIC ROTATION SENSORS.	23
	A. Unmodulated, Single-pass Fiber Optic Rotation Sensor	23
	1. Co-Polarized	24
	2. Cross Polarized	25
	3. No-Polarizer	26
	4. Unpolarized	27
	5. Partially Polarized	29
	B. Single Frequency Modulated, Single Pass, Fiber Optic Rotation Sensor	33
	1. Co-Polarized	35
	2. Cross-Polarized	36
	3. No-Polarizer	37
	4. Unpolarized	38
	5. Partially Polarized	39

C. Two Frequency Modulated, Single Pass, Fiber Optic Rotation Sensor	41
1. Co-Polarized	42
2. Cross Polarized	43
3. Unpolarized	43
4. Partially Polarized	45
5. Signal Processing	45
V. PASSIVE REENTRANT FIBER OPTIC ROTATION SENSORS.	53
A. Theory of Operation	53
B. Polarization Analysis of Reentrant Fiber Optic Rotation Sensor	60
1. Co-Polarized with External Polarizer	63
2. Cross Polarized with External Polarizer	66
3. No Polarizer	67
4. Co-Polarized with Internal Polarizer	68
5. Unpolarized	69
6. Partially Polarized	71
C. Experimental Results	76
1. Hybrid Reentrant Pulsed Fiber Optic Rotation Sensor	76
a. Description of Rotation Sensor	76
b. Spatial Alignment	78
c. Modematching of Input and Alignment Beams	81
d. Non-reciprocity of Hybrid Reentrant Rotation Sensor	84
e. Experimental Results	85

2. All Fiber Optic, Reentrant Pulsed Rotation Sensor	89
a. Design Consideration	89
b. Description of Rotation Sensor	92
c. Alignment Procedures	95
i. Spatial Beam Alignment	95
ii. Loop I/O Coupler Alignment	95
iii. Splitter/Combiner Coupler Alignment	96
iv. Input Polarization Controller Alignment	99
v. Loop Polarization Controller Alignment	99
d. Experimental Design and Technique.	99
e. Results	102
VI. NOISE IN FIBER OPTIC ROTATION SENSORS.	106
A. Propagation of Noise in Single Pass, CW, Fiber Optic Rotation Sensors.	108
B. Noise Sources	110
1. Light Source	110
2. Input Coupling	112
3. Optical Fiber Birefringence Noise	113
4. Linear Single Scattering Noise	114
5. Detector Noise	120
6. Post Detector Noise	121
7. Miscellaneous Noise Sources	122
C. Propagation of Noise in Passive Reentrant Pulsed Fiber Optic Rotation Sensors.	122

VII.	ACTIVE REENTRANT PULSED FIBER OPTIC ROTATION SENSORS.	132
A.	Amplifier Noise	133
B.	Noise due to Incoherent Backscattering	138
C.	Amplifier Non-reciprocity	143
D.	Higher Order Rotation Induced Phase Shifts	149
VIII.	CONCLUSION	152
IX.	APPENDICES	
A.	Effects of Finite Integration Times on the Performance of Fiber Optic Rotation Sensor Operated with Unpolarized Light	156
B.	Modematching of Input and Recirculating Spatial Beams in Hybrid Reentrant Rotation Sensors.	164
C.	Computer Program for Evaluation of Mean and Standard Deviation of the Number of Zero-crossings for Passive Reentrant Rotation Sensor	166
D.	Multi-Fiber Rotation Sensor	170
X.	REFERENCES	173

I. INTRODUCTION.

Navigation can be defined as a method of guiding an object or person between two points. The navigational problem has three components. First, the present location then the direction and distance to the destination must be determined, and finally, the required direction must be set and maintained. The second component of this problem depends on the geometry of the space containing the two points and on the coordinate system used. It will be not be discussed in this paper.

Determining present location and direction can be accomplished with or without reference to external objects. Location can be determined from landmarks, stars, or radiosignals. Direction can be determined from landmarks, stars, or the earth's magnetic field. These are examples of the use of external references.

The process of not using external references is called deadreckoning or inertial navigation. This process requires that an initial position and direction be known. The present position is then obtained by integrating the velocity vector to obtain the position change with respect to the initial position. Until quite recently, this has been typically achieved by using accelerometers, mechanical gyroscopes and atomic clocks. Mechanical gyroscopes, which depend on the principle of conservation of angular momentum, are required for the determination of both the position change and the present direction. The highest quality mechanical gyroscopes achieve rotation sensitivities of 10^{-2} to 10^{-3} degrees/hour. They, however, require much maintainance to function properly.

In 1913, a French scientist, Sagnac, published a paper(1) demonstrating the first optical rotation sensor. The rotation sensor operates because of a rotation induced phase shift (Sagnac phase shift) between lightwaves which counterpropagate around a closed optical path. Chapter II of this paper deals with the Sagnac effect. This original rotation sensor had poor sensitivity and remained a laboratory curiosity until quite recently.

In the late 1960's, the ring laser gyroscope* was first demonstrated. This is an optical rotation sensor which uses the Sagnac effect in a slightly altered way. A rotation dependent frequency difference between light waves which counterpropagate around an active closed optical path is used instead of a phase shift. The early laser gyroscopes suffered from the phenomenon known as lock-in where the frequency difference between the counterpropagating light waves goes to zero when the rotation rate drops below some threshold value and no rotation rate information is available. Since, in practice this region is quite wide, the ring laser in its basic form is not useful as a rotation sensor.

Much time and money have been invested in understanding and overcoming the problem of lock-in. The locking is due to coupling of the waves by backscattered radiation, mostly from the mirrors which form the closed cavity. The solution to this problem is to use better mirrors and a dithering technique which keeps the gyroscope outside of the lock-in region. Currently, mechanical dithering is used in production gyroscopes, although

* The term "gyroscope" is commonly used in discussing Sagnac rotation sensors, i.e. ring lasers, fiber loop sensors, etc. This is strictly speaking a misnomer, but is a convenient term. I shall follow standard practice and use it also.

magnetic and optical dithering have been used in laboratory models. The stability of the dither can be a limiting factor in the rotation sensitivity of laser gyroscopes, which is equal to that of mechanical gyroscopes.

Due to the problems of lock-in and the problems associated with the stability of the dither, attention has again turned to the Sagnac (external signal) type of rotation sensor. Two technological developments were crucial: the low loss optical fiber and the laser. The availability of low loss fiber in long lengths in the mid 1970's, allowed the fabrication of closed optical loops with a large multiplicity of turns. The Sagnac phase shift increases in proportion to the number of turns. Thus phase shifts which were 2 to 3 orders of magnitude larger than those in Sagnac's original sensor, could be obtained for a given rotation rate. The laser provided a light source of high intensity which could efficiently (90%) be coupled into the fiber. Thus small rotation rates could be measured more easily than in the Sagnac experiment.

As in the development of any device, unforeseen problem arose which had to be overcome to make the device practical. Two major sources of problems are the birefringence in the optical fiber and backscattered radiation. These problems can limit the rotation sensitivity of the fiber optic rotation sensor.

In Chapter III, a mathematical formalism is presented which models the birefringence of the optical fiber, the polarization properties of light, and their effect on fiber optic rotation sensors. In Chapter IV, this formalism is applied to single pass, CW, fiber optic rotation sensors.

The predictions of this formalism are compared qualitatively with experiment for unmodulated rotation sensors. The agreement is good. The formalism is then used to examine phase modulated rotation sensors. A new type of phase modulated rotation sensor, using two modulation frequencies, is proposed. Its behavior under various conditions is studied.

Chapter V covers passive reentrant, pulsed fiber optic rotation sensors. The principles of operation, the effects of optical fiber birefringence, and design considerations and tradeoffs are discussed. Experimental work on two such rotation sensors, a hybrid system containing bulk optical components and fiber optics, and an all fiber system is described and compared with theory. The results indicate that the only practical implementation of this configuration of rotation sensor is an all fiber optic version.

In Chapter VI, the effects of noise on fiber optic rotation sensors are considered. Formulas are developed which relate the uncertainty in the measured rotation rate to the uncertainties in the parameters of the rotation sensor for both single pass and reentrant rotation sensors. The uncertainties in the rotation sensor parameters, due to noise, are quantified. This method is applied to a passive reentrant rotation sensor which uses a cycle counting detection algorithm to study the uncertainty in the measured rotation rate as a function of the rotation rate and the number of recirculations. It is found that the rotation rate accuracy does not increase beyond some number of recirculations because of the exponentially decreasing signal to noise ratio. The rotation rate accuracy

decreases between counts because of the digitization process and at low rotation rates due to the low signal to noise ratio. Methods for reducing these errors are discussed.

An active (amplifier in fiber loop), reentrant pulsed fiber optic rotation sensor is examined in Chapter VII. The performance of the rotation sensor is calculated in the presence of amplifier noise, incoherent backscattering, and amplifier non-reciprocities. System tradeoffs are considered and numerical predictions are made.

It is hoped that the reader will develop an appreciation for the depth and diversity of fiber optic rotation sensors.

September 1981

Aviation Week & Space Technology

McGraw-Hill Publication \$3.00

HANSEN LABORATORIES



McDonnell Douglas DC-8 flight tests GE/Sheema CFM56 engines

0328 UIV949 99586 DEC83
STANFORD UNIVERSITY
LIBRARY
SERIALS RECORD DIV
STANFORD CA
94305

Work Progresses on Fiber Optic Gyro

By Philip J. Klass

Cambridge, Mass.—Encouraging progress during the past year in understanding the complex optical physics effects of the fiber optic gyro was reported here at a conference sponsored by the Massachusetts Institute of Technology's Research Laboratory of Electronics.

Despite progress, however, the sensor is not likely to be in operational military systems use until late in this decade, judging from the present state of the art and problems yet to be resolved (AW&ST Oct. 19, p. 55).

The more than 150 persons attending included many U.S. and European gyro manufacturers who were anxious to assess the current status and future prospects of the new sensor as a potential competitor both to ring-laser gyros and to more conventional spinning-wheel gyros.

Drift Rates Compared

Some experimental fiber optic gyros, much too large and fragile for avionic applications, have exhibited drift rates approaching 0.1 deg./hr., while compact, more rugged units, whose size is suitable for military use, exhibit drift rates of 50-100 deg./hr.

By comparison, current laser gyros typically exhibit drift rates of less than 0.01

deg./hr., permitting an aircraft inertial navigation system with accuracies better than 1 naut. mi. per flight hour.

The initial market for fiber optic gyros is expected to be in shorter-range tactical missiles, where drift rates of a few degrees per hour are acceptable.

But the new type of sensor will face competition for this market both from laser gyros and from more conventional types that use low-cost, molded-plastic components—a technology developed by Draper Laboratory, Cambridge, Mass., under USAF Avionics Laboratory sponsorship.

Potential advantages of a fiber optic gyro over its competitors include small size, ruggedness and the prospect of modest cost if it can be mass-produced using semiautomated techniques transplanted from microelectronics fabrication procedures.

The objective of an ambitious fiber optic gyro effort under way at France's Thomson-CSF is a three-gyro (three-axis) sensor, with 1 deg./hr. performance, in a 4-in. cube, at a price of \$3,000-6,000, according to H. J. Arditty, who directs the effort in corporate research laboratories.

Ironically, most of the current leaders in the fiber optic field are companies and

laboratories not now engaged in the manufacture of more conventional gyros. These include companies such as Martin Marietta/Orlando, McDonnell Douglas/Astronautics, West Germany's AEG-Telefunken and Thomson-CSF. However, more traditional gyro suppliers also are investigating the new technology.

These include such U.S. companies as Honeywell, Rockwell International and Lear Siegler, whose scientists presented papers here, as well as Germany's Teldix, which also presented a paper.

There is widespread activity in universities around the globe. In the U.S., research is centered at Stanford University, a recognized pioneer in the field, and the Massachusetts Institute of Technology.

Foreign universities include Britain's University of Southampton, West Germany's Technical University of Hamburg, Italy's University of Pavia, the University of Tokyo and Tsinghua University in the People's Republic of China.

On the surface, this global interest by companies and universities with no previous interest in gyros seems surprising—especially considering the modest near-term market for such sensors.

One reason is that the fiber optic gyro poses one of the most difficult challenges in the entire field of fiber optics.

Thus the technology developed for this device is certain to have a large payoff later for more demanding applications in telecommunications, such as greatly increased bandwidth (AW&ST Oct. 12, p. 44).

Worldwide Activity

This explains, at least partially, the motivation behind the efforts under way in the research laboratories of AEG-Telefunken and Thomson-CSF, as well as West Germany's Siemens and Britain's Standard Telephone Laboratories.

The great variety of designs and concepts reported here served to emphasize the broad spectrum of different technical approaches that can be employed for a fiber optic gyro.

All of them are adaptations of the Sagnac interferometer, first demonstrated nearly 70 years ago. The basic concept is that light from a single source, typically a laser, is split and one-half is injected into a coil of optical fiber and circulates in a clockwise direction while the other half is injected at the opposite end and circulates in the opposite direction.

If the coil of optical fiber is stationary, when the light beams emerging from opposite ends are compared, they should

General Electric Wins Computer Award

San Francisco—National Aeronautics and Space Administration has selected General Electric Co.'s Space Systems Div. as integration support services contractor for the proposed numerical aerodynamic simulator, a specialized computer that would be installed at Ames Research Center for advanced research in three-dimensional fluid flow. The contract will be on a cost-plus-award-fee basis, with a proposed estimated value of \$6.7 million for the basic 28-month performance period and a first 12-month option period.

Since the required support services are highly dependent on the computer development and construction plan, NASA will not complete negotiations and sign a contract with General Electric until after it has chosen the computer Phase C/D contractor. Competing Phase C/D proposals, from Burroughs Corp. and Control Data Corp., are due early in 1982, and NASA expects to select the winner next summer.

General Electric's role as integration support services contractor will be to assist NASA in program management and project control; perform independent verification and validation of the processing system, and render required support to test and integration, facility design and construction, and initial operations activities. The present plan contemplates a peak requirement for 28-29 people, but this number may change according to Phase C/D proposals.

The proposed computer could be 40 times as fast and have 50 times the memory capacity of the current generation of computers (AW&ST Sept. 14, 1980, p. 52).

The numerical simulator was removed from the Fiscal 1982 budget in accordance with the Administration ban on NASA new starts this year (AW&ST Feb. 23, p. 18), but the program is being supported at a low level from the aeronautical research and technology base.

General Electric was selected for the support role in competition with Computer Sciences Corp. of Mountain View, Calif., and Hughes Aircraft Co. of Culver City, Calif.

have the same phase since both traveled the same distance through a common medium.

When the fiber optic coil is rotated about an axis at the center of the coil, there will be a change in the relative phase of the beams emerging from the two ends. The amplitude of the phase shift will be proportional to the coil's angular velocity and the direction of the phase shift will indicate the direction of rotation.

When the fiber optic gyro was first demonstrated five years ago by two University of Utah scientists, it seemed to offer a number of attractive advantages over the laser gyro.

The sensitivity and accuracy of a conventional laser gyro varies directly with the area enclosed by its contrarotating laser beams, so that a small device can be obtained only at the price of decreased accuracy.

Number of Turns

With some—but not all—types of fiber optic gyros, the accuracy/sensitivity increases as a function of the number of turns of fiber in the sensing coil, in addition to being a function of the area enclosed by the coil.

Because optical fibers can be made in very small diameters, a sensor containing many turns for increased accuracy can be fabricated in a relatively small volume for overall sensor compactness.

The fiber optic gyro also has shown promise to overcome a problem encountered by the laser gyro because the optical path of its contrarotating beams also functions as the cavity in which the lasing action occurs.

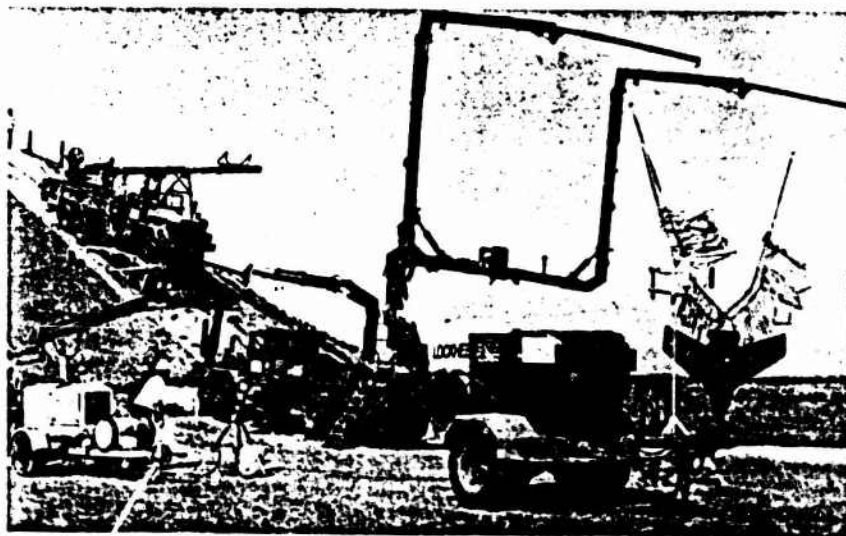
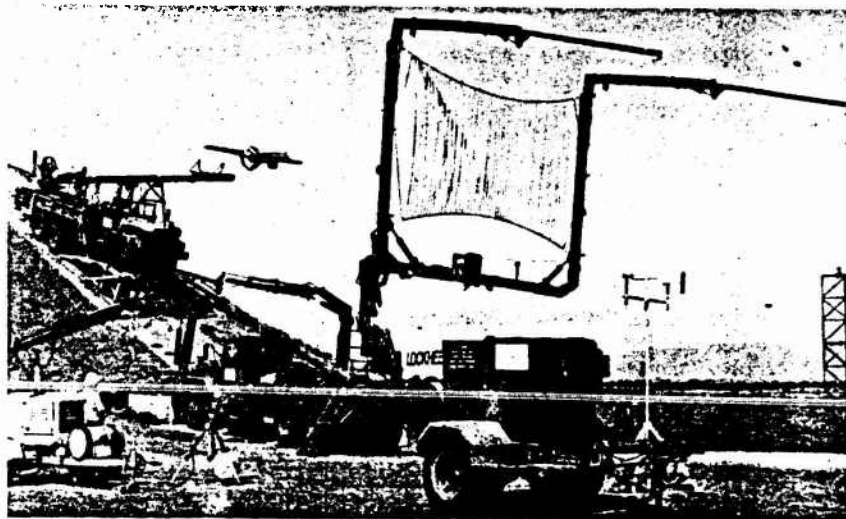
This leads to an unwanted interaction between the contrarotating beams, known as "mode locking," which makes the laser gyro insensitive at very small angular rates unless corrective design measures are taken.

To overcome this mode-locking problem, Honeywell, Litton Industries and Singer Kearfott oscillate the entire gyro through a very small angle at several hundred oscillations per second—known as "dither."

The fiber optic gyro does not encounter this problem because it uses an external laser, such as a light-emitting diode type, and the optic fiber serves only as a transmission medium. But when attempts were made to fabricate fiber optic gyros with usable accuracies, "we discovered that this seemingly simple device had a host of its own challenging problems, about which little was known," one scientist said.

For gyro applications, single-mode fibers usually are employed and light injected into the ends of the fiber coil usually is linearly polarized, i. e., horizontally or vertically.

As the light travels through the coil, it does not retain its initial polarization. For example, a vertically polarized beam will become horizontally polarized, then revert



Army's Aquila RPV in Launch and Retrieval Tests

Launch and retrieval of the Army/Lockheed Aquila remotely piloted vehicle (RPV) is demonstrated in this sequence photographed during tests at Lockheed Missile and Space Co.'s Sunnyvale, Calif., facility (Awast Jan. 7, 1980, cover and p. 54). The test vehicle was unpowered as it was hurled about 30 ft. from the launcher into the retrieval net. Flight tests of the Aquila, designed for reconnaissance and target-designating missions over the forward battle area, are scheduled to begin next year in Ft. Huachuca, Ariz. The initial contract covers 22 vehicles, which can send back live television pictures of the disposition of enemy vehicles and troops and then act as a laser-designator for artillery or air strikes. Aquila is designed to stay aloft more than 3 hr. at a speed of 110 kt. and altitude up to 12,000 ft. It can fly a programmed route or be controlled from the ground.

back to vertical, then back to horizontal, a phenomenon called "birefringence."

Because vertically polarized waves travel at a slightly different velocity from those that are horizontally polarized, this polarization contamination creates an uncertainty, or "noise," in making the required phase comparison measurements.

According to E. C. Kintner of Draper Laboratory, "Polarization-induced drift is a serious problem." A 20-db. improvement in polarization stability is needed to achieve a 10-fold improvement in sensor performance, he said.

Output Efficiency

Another challenging problem is to couple efficiently the output from an external laser into a single-mode optical fiber coil whose inner diameter (transmission medium) typically is only a few microns. Light reflected into the laser can degrade its spectral purity, creating additional noise within the sensor.

A great deal of interest here focused on techniques for improving the polarization stability of single-mode fibers, i. e., achieving very low birefringence.

One approach is to make the fiber core elliptical instead of round, a technique being explored by Andrew Corp., which expects soon to offer samples of the new fiber, according to the company's R. B. Dyott. The elliptical core measures 1×2.5 microns.

One significant disadvantage, however, is that propagation losses run quite high, around 40 db./km. Dyott said the loss appears to be "very dependent on the drawing tension during manufacture," and he expressed hope that the attenuation could be reduced.

Another technique is to use the cladding material which encapsulates a circular core to apply a stress that introduces a controlled strain. Japan's Hitachi recently made significant advances in such polarization-stable fibers, according to Ivan Kaminow of Bell Laboratories.

Still another approach to easing the problem, which involves twisting the optical fibers, was described by Ferdinand Gauthier of Thomson-CSF and by D. N. Payne of the University of Southampton. Gauthier showed photographs of a company facility that is being used to apply up to 28 twists of fiber per meter length.

Temperature Variations

Unlike the elliptical core, however, which exhibits a polarization stability relatively unaffected by ambient temperature variations, the stability of both the prestressed and spun-fiber techniques is affected by temperature.

Polarization also is affected by magnetic fields, which means that a fiber optic gyro must be shielded against, or compensate for, magnetic fields.

Still other effects that can adversely affect performance were cited by MIT

Fiber Optic Gyro Interest Rises Rapidly

Cambridge, Mass. — The large turnout of gyro manufacturers for the recent conference on fiber optic gyros is in sharp contrast to industry's relative indifference to the laser gyro immediately following its invention by Sperry in the early 1960s (AW&ST Feb. 11, 1963, p. 98).

The fiber optic gyro first was demonstrated about five years ago by two University of Utah scientists. At the corresponding time after the Sperry laser gyro disclosure, only Honeywell had shown sufficient interest to enter the field, although Rockwell subsequently did so.

In the mid-1970s, when the laser gyro began to emerge as a favorite for many civil and military inertial navigation system applications, companies such as Litton Industries and Singer Kearsott launched crash programs to catch up, while others concluded it was too late for them to enter the field.

This explains the large turnout of both U. S. and West European companies for the recent fiber optic gyro conference held by the Massachusetts Institute of Technology. U. S. companies included Honeywell, Lear Siegler, Litton Industries, Northrop, Rockwell, Raytheon, Singer Kearsott and Sperry. European companies in attendance included France's Sagem and Sfen, West Germany's Teldix and Bodenseewerke, as well as British Aerospace.

professor Shaoul Ezekiel, who arranged the conference and served as co-chairman along with Arditty of Thomson-CSF.

For example, unless the laser output is divided precisely in half, the beam rotating in one direction will cause more heating than in the reverse direction, resulting in the lack of what is called "reciprocity." Ezekiel cautioned: "Complete reciprocity is essential because the effect we must measure is so small."

This internal heating problem is not

inconsequential, Ezekiel said, because of the very small diameter of the fiber core. For example, if the laser input is only 1 milliwatt (0.001 w.), with a 3-micron-dia. core this corresponds to a power density of 10 kw./sq. cm.

An experimental phase-nulling optical gyro that measures only 2.5 in. in diameter and 0.65 in. thick was described by Eric Udd of McDonnell Douglas/Astronautics. The device was developed using company funds and was first tested late

Now, a Clear and Precise Analysis of U.S.-Soviet Military Balance

U.S.-Soviet
Military Balance



The Issue: Survival.

The Conclusion:

The United States has reached a breakpoint in national security... America is either going to change direction and retain its relative strength—or accept a position of inferiority.

- A necessary reference for every member of Congress.
- Must reading for the entire defense establishment, both governmental and military.
- Mandatory background information for the news media, and for the contractors and subcontractors who serve the defense establishment.
- An incisive, impartial and immensely comprehensive text that should be read by every intelligent American who pretends to base his or her opinion on facts, rather than scattered pieces of information embroidered with emotion.

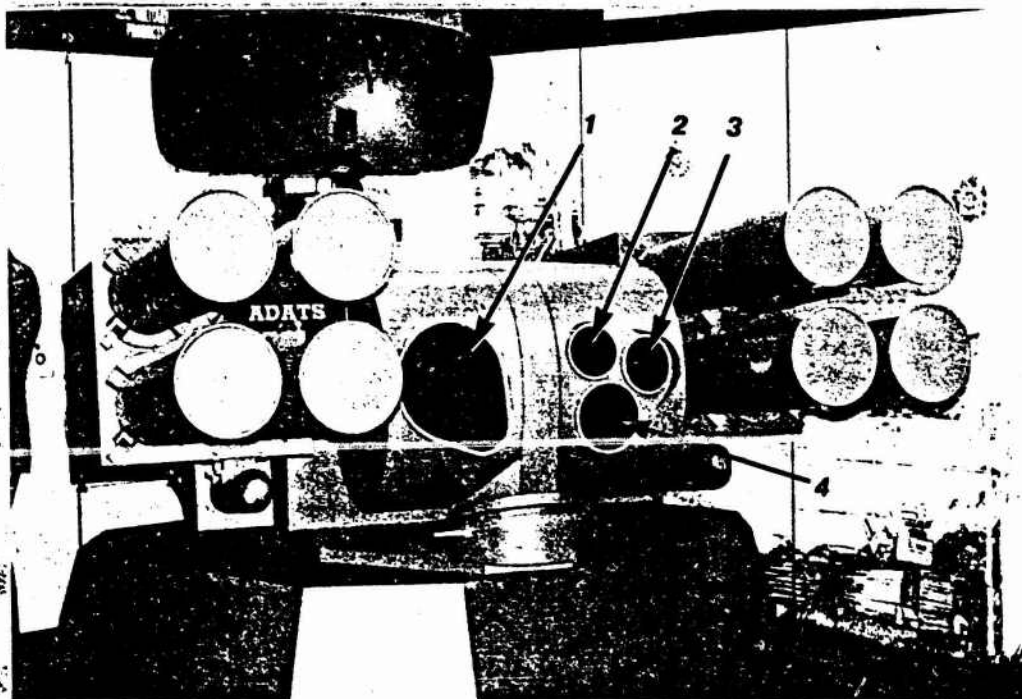
Now get the facts—all the facts—upon which to base your best judgment. U.S.-Soviet Military Balance is available by mail through the Aviation Week & Space Technology Book Club, McGraw-Hill, Inc., 1221 Avenue of the Americas, New York, New York 10020. Write, send in coupon or call 212-997-3289.

Another Tool of the Trade from
Aviation Week & Space Technology
Aviation Week & Space
Technology Book Club
1221 Avenue of the Americas
New York, New York 10020



Please send me _____ copies of U.S.-Soviet Military Balance at \$23.95 per copy. All orders under \$25.00 must be prepaid. Orders received from outside the U.S. must have checks drawn against a U.S. bank in U.S. currency. Check or money order is enclosed.

Name _____
Address _____
City _____
State _____ Zip _____
Add local sales tax where applicable
Allow 4 to 6 week delivery



Martin Marietta Developing Turret

Turret for the mobile Oerlikon-Bührle combination Air Defense Antitank System (ADATS), being developed by Martin Marietta/Oriando, is armed with eight laser beam-riding missiles that can be used against either aircraft or tanks. Antenna of the pulse-Doppler air-target acquisition radar is visible above. Four electro-optical windows visible below include (1) imaging infrared sensor for night target acquisition and tracking, (2) television camera for daytime use, (3) laser range finder, and (4) laser for beam-riding guidance of missiles. The system is in early testing.

last year. The device exhibits a drift rate of about 50-100 deg./hr., but McDonnell Douglas is under contract to USAF's Armament Laboratory, Eglin AFB, Fla., to develop a fiber optic gyro with drift rates in the 0.1-10 deg./hr. range.

Additionally, the company recently won a contract from USAF's Avionics Laboratory to develop technology and components that may ultimately permit a fiber optic gyro to exhibit drift rates of 0.01 deg./hr. Udd believes it will be five years before such performance can be demonstrated in the laboratory.

Unlike some other fiber optic gyro designs, the phase-nulling approach used by McDonnell Douglas provides a direct digital output, similar to a laser gyro. Its accuracy is independent of the number of turns in the fiber optic coil, although sensitivity does increase with the length of the fiber.

Army-Sponsored Design

Martin Marietta's J. M. Martin described a two-year-old design of a fiber optic gyro, developed under Army sponsorship, that used a single-mode fiber 1,200 meters (3,936 ft.) in length in a coil that is 30 cm. (11.8 in.) in diameter.

The device exhibited a drift rate of approximately 36 deg./hr. after warmup and a random noise corresponding to 0.06 deg. per square-root-hour, Martin said.

The Martin Marietta design approach, like that used by McDonnell Douglas, uses an opto-acoustic modulator to change slightly the frequency/wavelength of the

light rotating in one direction from that in the opposite direction, providing a digital sensor output.

A new approach to fiber optic gyro design, called a pulsed reentrant type, was described by George Pavlath of Stanford University.

In the new reentrant type, Pavlath said, "we close the optical loop upon itself and let the light circulate around many times, thereby increasing sensitivity." By comparison, in more conventional designs the beam of light circulates through the sensor

coil only once and emerges at the opposite end.

Using a continuous-wave laser, the output is chopped into a pulse whose length (time-duration) is less than a single transit time of light through the sensor coil.

This pulse is split in half, with one segment being injected into the sensor coil to circulate in a clockwise direction while the other circulates in the opposite direction.

Because the sensor coil ends are joined, the two contrarotating pulses continue to circulate. An optical amplifier must be inserted between the two joined ends to compensate for losses in the optical fiber and rejuvenate the pulses.

"With each transit through the endless loop, the Sagnac phase shift will increase," Pavlath said. "The Sagnac phase shift between pulses will vary linearly with time. When these pulses are sampled and combined, after suitable filtering, we obtain a sinusoidally modulated pulse train. The rotation information is contained in its envelope.

"If one filters some more so that only the envelope of the pulse train remains, the [sinusoidal] envelope frequency will be proportional to sensor rotation rate much like a ring-laser gyro," Pavlath said. This provides a convenient digital output.

He said an experimental pulsed reentrant fiber optic gyro has been constructed at Stanford University that "is extremely easy to adjust and to use."

Honeywell's Joel G. Hanse described an experimental device, called dual-polarization fiber gyro, in which the helium-neon laser beam is given a 45-deg. polarization.

Cost Determined B-1B Avionics Choice

Cost was the deciding factor in the selection of Westinghouse Defense and Electronics Systems Center as supplier of the offensive radar system for the USAF/Rockwell International B-1B long-range combat aircraft (Avast Nov. 23, p. 29).

From both a technical and managerial standpoint, the competing Westinghouse and Hughes proposals were "extremely close," according to Gerald B. Gimness, manager of the LRCA avionics program at Boeing Military Airplane Co. Boeing could have worked with either supplier without problems, Gimness said.

The present state of development of Westinghouse's AN/APG-66 radar, and the growth potential it offers through the addition of line replaceable units, were important factors in the selection, a USAF official said. The LRCA radar will differ considerably from the APG-66 version currently in use on the USAF/General Dynamics F-16, but this configuration is more economical and meets requirements for the new bomber.

An extensive development program is planned to add the LRCA requirements to the baseline configuration. New requirements include:

- High-resolution ground-mapping, which will be achieved through Doppler beam sharpening and synthetic aperture radar technology.
- Terrain-following and terrain-avoidance capability.
- Air-to-ground ranging.

The offensive radar system includes the function of the multirole radar and the radar terrain sensor.

This is the equivalent of injecting both horizontally and vertically polarized waves into both ends of the fiber sensing coil.

Hanse said this provides an order of magnitude improvement in performance over more conventional homodyne-type optic gyro designs and a 2:1 improvement in scale factor, as well as minimizing the effects of temperature variations on the fiber sensor.

An experimental dual-polarization device built by Honeywell, using a 150-meter (492-ft.) long fiber, yielded a gyro with a long-term drift rate of about 50 deg./hr., and with a short-term drift rate of as low as 1.6 deg./hr., Hanse said.

Fabrication Possibilities

There is a wide range of opinion concerning the fabrication technique that will prove best for manufacturing fiber optic gyros when the technology reaches that state of maturity.

Most of the current experimental devices are made with a variety of discrete optical components to facilitate testing and adjustment.

For defense and aerospace applications, the device will need to be rugged and to be able to operate in both an adverse temperature and a shock/vibration environment. The characteristics of optical fibers themselves are very susceptible to such environmental effects.

Most of those working in the field believe that to achieve both ruggedness and low cost it will be necessary either to use integrated optics fabrication techniques, adapted from microelectronics technology, or to devise means that will enable a single piece of optical fiber to provide a variety of optical functions in addition to serving as the sensing coil.

Stanford University, with partial sponsorship by Arco, Inc., a petroleum-based conglomerate, is focusing on the development of an all fiber optic type sensor. Others, like Hughes Aircraft, are exploring integrated optics techniques.

Waveguide Devices

Hughes Research Laboratories' O. G. Rainer described several integrated optic waveguide devices the company has fabricated using photolithography under sponsorship of the Jet Propulsion Laboratory and the Air Force, including a four-spot optical switch delivered earlier this year to USAF.

"Sooner or later we must face the crucial question of how to mass-produce devices to tolerances measured in microns, with alignments measured in angstroms," one scientist said following the recent conference.

"This is fundamental to the future success of the device," he said.

The scientist added, "Integrated optics has for some time been a clever idea looking for a challenging problem it could solve. With the fiber optic gyro, I think it finally has found the problem." □

Filter Center

Companies to develop new Mk. 15 identification friend/foe (IFF) system for triservice use and potential North Atlantic Treaty Organization applications are being sought by USAF's Aeronautical Systems Div. Present plan is to issue a draft request for proposal early next year. Expression of interest must be submitted by Dec. 19 to attention of Code ASD/AEKAC, Wright-Patterson AFB, Ohio 45433.

Goodyear Aerospace has been selected to supply the digital scene-matching area correlator for terminal guidance of the Navy/USAF/General Dynamics Tomahawk cruise missile by McDonnell Douglas Astronautics Co., the guidance system contractor. Goodyear is to deliver the first three prototype area correlator systems by early 1983. The system will correlate imagery from a missile television camera with prestored data of landmarks in the target area.

USAF's Electronic Systems Div. has reorganized into three major mission-oriented groups. Brig. Gen. M. H. Alexander is new deputy for strategic systems, which includes the Boeing E-4 airborne command post, missile and air surveillance radars. Maj. Gen. John T. Buck, new deputy for tactical systems, previously director of the Boeing E-3A AWACS program office, takes on additional programs such as Pave Mover airborne radar, secure communication systems and the Joint Tactical Information Distribution System (JTIDS). Col. D. J. Kutyna, named deputy for mission support services, will be responsible for the Cobra Judy shipboard ICBM reentry vehicle tracking radar, traffic control and landing systems, physical security systems and environmental surveillance systems.

USAF is seeking prospective contractors for a program to upgrade the capabilities of its Ballistic Missile Early Warning System (BMEWS) facility at Thule, Greenland. The plan is to select multiple contractors for six-month design studies, followed by selection of one for implementation. Upgrading will include the surveillance and tracking radars, data processing and communication systems if funds permit. Expressions of interest are due this week to attention of Code ESD/PKY, Hanscom AFB, Mass. 01731.

Computerized fly-by-light control system for helicopters will be designed, developed and demonstrated in flight by Boeing Vertol under a four-year contract for approximately \$20.5 million awarded by the Army Aviation Research and Development Command's Applied Technology Laboratory, Ft. Eustis, Va. The system, to be developed under the Advanced Digital Optical Control System Flight Demonstrator Program, will be installed on an Army UH-60A Black Hawk helicopter at Boeing's facility near Philadelphia. The system includes a multi-axis sidarm control stick that replaces conventional helicopter controls, an onboard digital computer that monitors pilot control inputs and positions helicopter rotor actuators in response to those inputs and an optical fiber network to link system elements. Army-Boeing Vertol flight tests are expected to begin in late 1984.

USAF test facility for turbine engine fuel controls at Kelly AFB, Tex., will be modified by Hamilton Standard Div. of United Technologies Corp., incorporating changes expected to cut energy use by 66% and save almost \$2 million annually. Hamilton Standard is modifying 49 fuel control test stands that test the fuel control on Pratt & Whitney F100 engines that power USAF/McDonnell Douglas F-15s and General Dynamics/Ft. Worth F-16s. Coupling stands in groups of three, together with use of a refined computer program, is expected to effect economies in quantities of fuel used for testing. The stands have used 65,700 megawatts of power a year, a figure the new system is expected to reduce to 21,852 megawatts. The project will be performed by Hamilton Standard and Pratt & Whitney's Government Products Div.